A new additive manufacturing technique for layered metal-composite hybrid structures

Vom Promotionsausschuss der
Technischen Universität Hamburg
zur Erlangung des akademischen Grades
Doktor-Ingenieur (Dr.-Ing.)
genehmigte Dissertation

von

Rielson Miler Moreira Falck

aus
Salvador

2020

Gutachter:

Univ.-Prof. Dr.-Ing. Sergio de Traglia Amancio Filho

Prof. Dr.-Ing. Benedikt Kriegesmann

Vorsitzender des Prüfungsausschusses:

Prof. Dr.-Ing. Dieter Krause

Tag der mündlichen Prüfung:

11. September 2020

Acknowledgements

I would like to express my gratitude to the following people who supported this work:

- My deepest appreciation to Univ.- Prof. Dr.-Ing. Sergio de Traglia Amancio Filho for his support, encouragement, patience, and guidance during the time of the research. His guidance helped me in every step throughout the process of writing this thesis.

- Besides my advisor, I would like to thank Prof. Dr.-Ing. Benedikt Kriegesmann for accepting to review this PhD work and for his contribution to the examination process.

- Prof. Dr.-Ing. Norbert Huber for giving me the opportunity to work at Helmholtz-Zentrum Geesthacht (HZG) and for his recommendations.

- All members of the department of solid state joining processes (WMP) for their professional support. I wish to express my especial thanks to Dagmar Koschek, Dr. Lucian Blaga and Dr. Jorge F. dos Santos for the support and recommendations.

- Several colleagues from HZG, particularly for the members of workshop for their great work on the development of the heating system and customizing the printing bed, Jürgen Knaack and Kay Erdmann for their assistance with the fatigue testing, Dr. Maria Serdechnova and Anissa Bouali for their support on the XRD measurements, Margarethe Fritz for the FTIR measurements, and Dr. Seyed Goushegir and Dr. Paula O. Guglielmi for their help on the nanoindentations experiments and fruitful discussions.

- My sincere and especial thanks to my great friends Natalia Manente, and specially to Natascha Zocoller, and Dr. Eduardo Feistauer for their support and encouragement.

- Conselho Nacional de Desenvolvimento Cientificio e Tecnológico – CNPq (Brazil) for supporting the project and sponsoring my PhD scholarship.

- For my parents and brother (written in Portuguese): *Meu irmão, Tailan, por estar sempre torcendo pelas minhas conquistas e pelo apoio. Obrigado! Palavras são poucas para agradece-los, meus pais, Arlindo e Cleyse, que sempre se doaram e renunciaram aos seus sonhos para que eu pudesse realizar os meus. Muito obrigado pelo incentivo incondicional!*

- My wife Mirjam for her never-ending support. While I was impatient and times were far from easy, she has been incredibly patient and encouraged me throughout this journey. Along with her, I would like to thank my son Levi, for his great source of love and unlimited happiness. I love you both!

Abstract

Substitution of conventional metals by lightweight materials is inevitable. However, employment of multi-materials in a structure presents a challenge and choosing the right materials, design, and manufacturing technique is essential in the development of any engineering structural application. New joining and additive manufacturing techniques complement the successful integration of materials, design, and production. Conventional joining methods, such as adhesive bonding and mechanical fastening, face technological limitations when used to join dissimilar materials, such as metals and composites. The relatively long curing time of an adhesive is also a significant drawback for adhesive bonding. In recent years, new joining techniques have been investigated to develop hybrid joints that overcome the limitations of traditional joining methods.

There is an increased interest in recent advances in the field of additive manufacturing (AM). These offer the flexibility to produce complex geometric parts, such as sandwich structures with AM honeycomb cores. Combining the principles of joining and polymeric AM is the main aim of the present doctoral thesis, which introduces AddJoining, a new technique that was co-invented by the author (patent application by HZG, DE 102016121267A1, 2018) to contribute to the manufacturing options for joining multi-material parts. The process was inspired by additive manufacturing and joining technology principles, and this new technique uses polymer 3D printing, e.g., fused filament fabrication, FFF (also known as fused deposition modeling, FDM), to add layers of polymer or composite to a metal substrate. The AddJoining process has a potential to produce structures with geometric flexibility, such as honeycomb cores. As an early phase of this technology this PhD work was devised to understand and develop the fundamentals of the AddJoining process by joining transportation grade lightweight aluminum 2024-T3 with a combination of unreinforced polyamide 6 (PA6) and carbon-fiber reinforced polyamide 6 (CF-PA6).

To understand the process-induced changes in the selected material combination (aluminum 2024-T3 and the composite $[PA6/CF\text{-}PA6]_{4S}$), three combinations of process parameters were selected. The optimized process parameters with coating temperature (CT) at 229 °C and heating bed temperature (HBT) at 77 °C were kept constant. Moreover, the optimized HBT was fixed and the minimum and maximum values of CT selected at 20 °C and 150 °C, respectively. Intimate contact of polymer-to-polymer was promoted purely by temperature, which led to strong adhesion and influenced polymer bond formation. From a microstructural aspect, it was shown that strengthening occurred close to the interface of the aluminum 2024-T3 by reprecipitation of particles once solubilized, due to exposure to high processing temperatures. Within the composite $[PA6/CF\text{-}PA6]_{4S}$ the process induced a global modification of the polymer, the effect of HBT slightly changed the thermal properties of the composite part. However, to better understand the local changes on the polymer, a stepwise approach was carried out to combine the phase-identification of the polymer and nanohardness investigations. The results offered a more comprehensive understanding of the local variations in material properties by means of the phase-changes in each layer while it indicates the presence of two polymorphs of α-PA6 and γ-PA6. Thus, it is associated with the presence of a thermal history of AddJoining, which can affect the crystallinity locally and decrease the hardness. From the hybrid joint mechanical performance, the influence of heating bed temperature on secondary bending could be an indication of low stiffness in the composite part caused by a variation in its crystal structure. This indicates that changes to PA6 phases could have led to a variation in hybrid joint's ductility and strength.

The mechanical performance of AddJoining hybrid joints was assessed by a wide range of mechanical tests. An interfacial intralaminar failure mode was observed with quasi-static loading. Compared to adhesively bonded joints there was a significant increase in ultimate lap shear force (ULSF). In addition, the S-N curves obtained from fatigue testing indicated outstanding results and the hybrid joints produced reached their fatigue limits (10^6 cycles) with loading levels corresponding to 30 % of ULSF. By monitoring stiffness degradation, it was seen that damage evolution was dominated mostly by fiber rupture throughout fatigue life due to the high stiffness stability of hybrid joints.

To summarize, this PhD work has been successful in fulfilling its objectives, namely describe the AddJoining process fundamentals and mechanical behavior. Moreover, this work shows the potential for the AddJoining technique in the manufacturing of future complex multi-material parts for structural applications with tailored design aspects to improve damage tolerance and load-bearing carrying.

Zusammenfassung

Der Einsatz von Multimaterialien in ein- und derselben Struktur ist eine große Herausforderung, und die Auswahl der richtigen Materialien, des passenden Designs und entsprechender Fertigung ist für die Entwicklung von jeglicher Konstruktionsstruktur ohnehin unerlässlich. Neue Verbindungstechnologien und additive Fertigungstechniken ergänzen die erfolgreiche Integration von Materialien, Design und Herstellungstechniken. Konventionelle Verbindungsmethoden wie Kleben und mechanisches Befestigen unterliegen bei der Anwendung technologischen Einschränkungen, wenn sie genutzt werden, um ungleiche Werkstoffe wie Metalle und Verbundwerkstoffe zu verbinden. In den vergangenen Jahren sind neue Verbindungstechniken untersucht worden, um Hybridverbindungen zu entwickeln, die die Einschränkungen herkömmlicher Verbindungsmethoden überwinden.

Das Interesse an den jüngsten Fortschritten auf dem Gebiet der additiven Fertigung (AF) ist gestiegen. Diese Methoden bieten die Flexibilität komplexe geometrische Bauteile zu produzieren wie beispielsweise Sandwichstrukturen mit AF-Wabenkernen. Die Prinzipien des Verbindens und der polymeren AF zu kombinieren ist das Hauptziel der vorliegenden Doktorarbeit, in der AddJoining vorgestellt wird, eine neue Verbindungsmethode, die vom Autor miterfunden wurde (Patentanmeldung der HZG, DE 102016121267A1, 2018), um zur Weiterentwicklung der Fertigungsmöglichkeiten zum Verbinden von Teilen aus mehreren Materialien beizutragen. Der Prozess wurde durch Prinzipien der additiven Fertigung und Fügetechnologie inspiriert. Diese neue Technik verwendet Polymer-3D-Druck, z.B. Fused Filament Fabrication (FFF), auch bekannt als Fused Deposition Modeling (FDM), um einem Metallsubstrat Schichten aus Polymer oder Verbundstoff hinzuzufügen. Durch die AddJoining-Methode können geometrisch flexible Strukturen wie Wabenkerne erzeugt werden. Diese Doktorarbeit hat zum Ziel, die frühe Phase der AddJoining-Technik zu beleuchten und die Grundlagen zu entwickeln und zu verstehen. So werden die Haftmechanismen, Veränderungen der Mikrostruktur sowie die mechanischen Eigenschaften der Verbindungen Aluminium 2024-T3 mit einer Kombination aus unverstärktem Polyamid 6 (PA6) und kohlefaserverstärktem Polyamid 6 (CF-PA6) untersucht.

Um die Prozessbedingten Veränderungen in der gewählten Materialkombination (Aluminium 20-T3 und Verbundwerkstoff $[PA6/CF\text{-}PA6]_{4S}$) zu verstehen sowie den gesamten Prozess zu untersuchen und optimieren wurde die statistische Versuchsplanung und -analyse (DoE) angewendet. Des Weiteren wurden drei Kombinationen von Prozessparametern ausgewählt; die optimierten Prozessparameter mit einer Beschichtungstemperatur (CT) bei 229 C und einer Heizbetttemperatur (HBT) bei 77 C wurden gehalten. Darüber hinaus wurde die optimierte HBT festgelegt und der minimale und maximale CT-Wert ausgewählt, um die Auswertung der Ergebnisse bei 20 C bzw. 150 C zu erleichtern. Der enge Kontakt von Polymer zu Polymer wurde lediglich durch die Temperatur herbeigeführt, was zu einer starken Adhäsion führte und die Polymerbindungsbildung beeinflusste. Aus mikrostruktureller Sicht konnte nach Anwendung einer Mikrohärteprüfung gezeigt werden, dass die verstärkungsfördernde Präzipitation von Partikeln, die nach dem Auflösen durch die Entwicklung hoher Verarbeitungstemperaturen gebildet werden, vor allem nahe der Grenzfläche des Aluminiums 2024-T3 auftrat. Innerhalb des Verbundwerkstoffes $[PA6/CF\text{-}PA6]_{4S}$ veranlasste dieser Prozess eine globale Veränderung des Polymers, der Effekt der HBT führte zu einer geringfügigen Veränderung der thermischen Eigenschaften des Verbundteils. Um dabei die lokalen Veränderungen des Polymers besser verstehen zu können wurde ein schrittweiser Ansatz verfolgt, um die Phasenanalyse der Polymer- und Nanohärtung zu kombinieren. Das Resultat bot ein umfassenderes Verständnis der lokalen Variationen der Materialeigenschaften durch die Phasenänderungen in jeder Schicht, während es außerdem das Vorhandensein von zwei Polymorphen von α-PA6 und γ-PA6 anzeigt. Demzufolge kann der thermische Einfluss von AddJoining die Kristallinität lokalen beeinträchtigen und die Härte des Polymers verringern. Aufgrund des mechanischen Verhaltens der Hybridverbindung könnte der Einfluss der Temperatur des Heizbetts auf die sekundäre Biegung ein Hinweis auf eine geringe Steifheit des Verbundteils sein, die durch eine Variation seiner Kristallstruktur verursacht wird. Die weist darauf hin, dass die Änderungen der PA6-Phasen zu einer Veränderung der Duktilität und Festigkeit des Hybridgelenks geführt haben könnten.

Die mechanische Leistung von AddJoining-Hybridverbindungen wurde anhand eines breiten Spektrums an mechanischen Untersuchungen bewertet. Bei quasistatischer Belastung wurde ein intralaminarer Grenzflächenversagensmodus beobachtet. Verglichen mit Klebeverbindungen war ein signifikanter Anstieg der endgültigen Zugscherfestigkeit zu verzeichnen. Außerdem zeigten die S-N-Kurven, die aus Ermüdungstests bezogen wurden hervorragende Ergebnisse, und die hergestellten Hybridverbindungen erreichen ihre Ermüdungsgrenzen (d. H. 10^6 Zyklen) mit einem Belastungsgrad von 30% des ULSF. Durch Überwachen der Verschlechterung der Steifheit wurde festgestellt, dass die Schädigungsentwicklung aufgrund der hohen Steifheitsstabilität hauptsächlich durch Faserbruch während der Ermüdungslebensdauer dominiert wurde.

Zusammenfassend ist festzuhalten, dass diese Doktorarbeit ihre Ziele, nämlich die Grundlagen des AddJoining- Prozesses und das mechanische Verhalten zu beschreiben, erreicht hat. Darüber hinaus zeigt diese Arbeit das Potenzial der AddJoining-Technik bei der Herstellung zukünftiger komplexer Multimaterialteile für strukturelle Anwendungen mit maßgeschneiderten Designaspekten zur Verbesserung der Schadenstoleranz und der Tragfähigkeit.

List of Abbreviations

2-P WD	Two-parameter Weibull distribution
µAFP	Micro automated fiber placement
ABS	Acrylonitrile butadiene styrene
AFP	Automated fiber placement
ALT	Alternate refers to CF-PA6 distribution
AM	Additive manufacturing
ANOVA	Analysis of variance
ASTM	American Society for Testing and Materials
ATP	Automated tape placement
ATR	Attenuated total reflection
BM	Base material
CDS	Characteristic damage state
CF	Carbon fiber
CF-PA6	Carbon-fiber reinforced polyamide 6
CF-PEEK	Carbon-fiber reinforced poly-ether-ether-ketone
CF-PEKK	Carbon-fiber reinforced poly-ether-ketone-ketone
CF-PPS	Carbon-fiber reinforced polyphenylene sulphide
CFRP	Carbon-fiber reinforced polymers
CSM	Continuous stiffness measurement
CT	Coating temperature
DA	Direct assembly
DaB	Displacement at break
DIC	Digital image correlation
DIN	Deutsches Institut für Normung e.V.
DoE	Design of experiments
DSC	Differential scanning calorimetry
DTG	Difference thermogravimetry
EASA	European Aviation Safety Agency
EDS	Energy-dispersive X-ray spectroscopy
FDM	Fused deposition modeling

FFF	Fused filament fabrication
FEM	Finite element method
FML	Fiber metal laminate
FTIR	Fourier-transform infrared spectroscopy
FRP	Fiber-reinforced polymer
HCF	High cycle fatigue
IJP	Ink jet printing
ISO	International Organization for Standardization
LCF	Low cycle fatigue
LOM	Laminated object manufacturing
LSCM	Laser scanning confocal microscopy
MPB	Mid-plane bottom refers to CF-PA6 distribution
MPT	Mid-plane top refers to CF-PA6 distribution
Nd:YAG	Neodymium-doped yttrium aluminum garnet
NH	Amide II (functional group)
NDT	Non-destructive testing
OFAT	One-factor-at-time
PA	Polyamide
PEEK	Poly-ether-ether-ketone
Prepregs	Pre-impregnated fibers
RLOM	Reflected-light optical microscopy
RTM	Resin transfer molding
SB	Secondary bending
SEM	Scanning electron microscopy
SIMP	Solid isotropic material with penalization method
SLA	Stereolithography
TGA	Thermogravimetric analysis
ULSF	Ultimate lap shear force
VARI	Vacuum-assisted resin infusion
VMH	Vickers microhardness
XRD	X-ray powder diffraction

List of Symbols

a, b, c, d	Fatigue regression parameters
Adj MS	Adjusted mean squares
Adj SS	Adjusted sum of squares
CV	Coefficient of variance
e_m	Edge metal
e_c	Edge composite
E	Stiffness/elastic per fatigue cycle
E_0	Initial stiffness/elastic modulus
E_{11}	Elastic modulus in the longitudinal direction
E_{22}	Elastic modulus in the transverse direction
D	Damage
f	Frequency
f(x)	Probability density function
F	Applied cyclic force
F_{max}	Maximum force
F_{mean}	Mean force
F_{min}	Minimum force
F_p	Critical linearity index
F_x	Axial tensile force
F_z	Hoop tensile force
G_{12}	In-plane shear modulus
M	Bending moment
MR	Bernard's median rank
MTTF	Mean time to failure
N	Normal force
N_f	Fatigue life (number of cycles)
N_{Rx}	Predicted fatigue life
n_t	Total number of load levels (cyclic load)
n_i	Number of fatigue samples
$P_f(x)$	Probability of failure function

Q	Shear force
R	Fatigue stress ratio
R^2	Coefficient of determination
$R^2_{(adj)}$	Adjusted coefficient of determination
$R^2_{(pred)}$	Predicted coefficient of determination
R_a	Arithmetic mean value
R_x	Reliability level
R_z	Maximum peak-to-valley distance
SD	Standard deviation
t	Time
T_{cc}	Crystallization temperature
T_d	Onset thermal decomposition temperature
T_g	Glass transition temperature
T_m	Melting temperature
w	Weight fraction
X_c	Degree of crystallinity
X_T	Tension strength in longitudinal direction
Y_T	Tension strength in transverse direction
α	Weibull's shape Parameter
β	Weibull's scale Parameter
ΔH°	Enthalpy of melting temperature
$\Delta H°_m$	Enthalpy of melting for 100% crystallinity

Contents

Chapter 1. Introduction

1.1 Motivation

Countries are working hard to reduce emissions of greenhouse gases in all sectors over the coming decades [1]. A reduction of emissions will require efforts beyond the energy sector, including the use of efficient materials and products [2,3]. The substitution of conventional metals with lightweight multi-material structures is an attractive strategy for weight saving, and consequently to influence positively the reduction in CO_2 emissions [4]. The employment of multi-materials in a structure can bring essential benefits, but it is a challenge to combine dissimilar materials due to their differing physicochemical properties [5,6].

Traditional joining methods, such as adhesive bonding and mechanical fastening, face technological limitations when it comes to joining dissimilar materials, such as metals and composites. In addition, the relatively long curing time of an adhesive is a significant drawback of adhesive bonding. In recent years new joining techniques have been investigated to develop multi-materials and overcome the limitations of traditional joining methods [6]. These include friction riveting [7], friction spot joining [8,9], injection clinching joining [10,11], ultrasonic joining [12,13], ultrasonic welding [14,15], and induction-heated joining [16].

The demand for lightweight metal-polymer multi-material structures and the limitations of traditional joining techniques are motives driving the development of these alternative methods. Moreover, the possibility of using a wide range of materials and their combinations to additively manufacture hybrid structures with complex internal geometries, has also gained the attention of industry.

1.2 Objectives

A fusion of joining principles and additive manufacturing techniques has great potential to assist the manufacturing of complex multi-material parts. In this context, this PhD thesis introduces a new technique called AddJoining that was devised within its scope. The technique has a patent application (DE 102016121267A1) and it was developed at Helmholtz-Zentrum Geesthacht (Germany) (see Appendix A.1). The process was inspired by both additive manufacturing and joining technology principles, and the new technique uses polymer 3D printing, e.g. fused filament fabrication (FFF), to add layers of polymer or composite to a metal substrate [17]. The AddJoining process has an interesting potential to produce structures with geometric flexibility, such as honeycomb cores. Moreover, it has the potential to manufacture hybrid structures with a wide range of material combinations and that is one of major advantages of the technique.

The PhD thesis presented herein aims to introduce the AddJoining concept and its main features, demonstrating its use with commercially available materials. The objectives of this PhD thesis were established to:

a) Introduce the AddJoining concept and impart an understanding of its fundamental principles and process parameters, investigating the bonding formation involved in hybrid joints.

b) Evaluate the mechanical performance of hybrid joints and understand their damage initiation

and evolution under quasi-static shear testing.

c) Investigate the mechanical performance of the hybrid joints by fatigue testing under cyclic load.

1.3 Thesis structure

This thesis is structured in chapters. The PhD thesis starts by describing the motivation and primary objectives of this work (Chapter 1). Chapter 2 reviews the literature giving a brief introduction to polymeric composite materials and the main damage phenomena that occur with composite materials. Moreover, the major advanced methods of metal-composite manufacturing are presented. In addition, recent scientific and technological joining methods that are used to produce metal-composite hybrid structures are explored. At the end of Chapter 2 the chief characteristics of the base materials used during the development of the AddJoining concept are presented.

The experimental approach used in this work is described in Chapter 3, as well as its development phases for this thesis. Chapter 4 goes on to discuss the materials and methods applied during this PhD work. The properties of the base materials and the manufacturing procedure are described in detail. Moreover, along with a description of the materials, characterization techniques applied are addressed.

In Chapter 5, the new manufacturing method is introduced and the fundamentals of AddJoining are discussed, prior to a detailed discussion of the experimental results. In this part of the thesis, the principles of processes, parameters, and variants are explored, as well as their main advantages, limitations and potential application.

Moreover, the experimental results obtained in this work are presented in three further chapters. Chapter 6 is dedicated to understanding the technique based on bonding mechanisms, microstructural changes, physical-chemical properties, and a phase identification devoted to understanding the process-induced changes in the selected material combination (aluminum 2024-T3 and the composite $[PA6/CF\text{-}PA6]_{4S}$). Also in this chapter, an optimization of AddJoining hybrid joints is addressed, as well as the parameters used with respect to their mechanical performance.

In Chapter 7, the mechanical properties of the AddJoining hybrid joints are evaluated. In addition, the ultrasonic C-scan non-destructive method was used to assess damage evolution and correlated with the microstructural analysis. Also in this chapter, an exploratory study evaluates the effect of mechanical properties at different testing temperatures on the quasi-static mechanical behavior of the AddJoining hybrid joints. The finite element method (FEM) was applied to assess stress concentrations and the failure region using Hashin criteria to depict the stress distribution and identify fracture mechanisms.

Chapter 8 is devoted to the results of fatigue performance testing of AddJoining hybrid joints. S-N curves are employed to characterize the fatigue resistance of hybrid joints, obtained as results from a number of fatigue tests. Furthermore, a fatigue life assessment was performed using a two-parameter Weibull distribution. It is interesting to note that this method was used to evaluate fatigue data scattering as well as predict the S-N curves under different reliability levels. Stiffness degradation was monitored to help understand the fatigue damage development during fatigue cycling. Moreover,

a failure analysis of the AddJoining hybrid joints and their typical fracture surface features under cyclic loading is provided.

This PhD work contributes to the development of hybrid structures, based on a fusion of joining principles and additive manufacturing techniques. For this reason, Chapter 9 summarizes the main results and conclusions of this scientific investigation. Finally, Chapter 10 offers recommendations for future scientific and technological investigation to contribute further to the manufacturing of complex multi-material parts.

Chapter 2. Literature review

This chapter briefly reviews the common types of composite materials with a focus on polymeric composite materials. Furthermore, the chapter summarizes recent developments in advanced methods for producing thermoplastic composites: automated fiber/taper placement (AFP/ATP) and fused filament fabrication (FFF). The emphasis on this two manufacturing techniques was intentionally set as AddJoining relies on concepts and fundamentals of both technologies for continuous fiber reinforced thermoplastics. These concepts and fundamentals are important to support the discussion of the results in this work. Focus is given on the correlation between process parameters and printed part's mechanical performance. In addition, this chapter gives a brief overview of alternative and recent developments in the production of metal-composite joints. Finally, a basic understanding of the base materials used in this work are presented towards the end of the chapter. As most of the microstructural and physico-chemical transformatinos occur in the polymer and polymer composite during AddJoining, a more detailed review on polymide 6 and carbon-fiber reinforced polyamide 6 is provided.

2.1 Composite materials and their fundamental classifications

Composites are widely applied and often thought of as replacements for traditional structural materials, e.g. metals. Their unique properties has opened up a new class of structural applications, for example, high performance applications for space and aerospace [18,19]. The classic definition of a composite is "*the combination of two or more distinct phases at the macroscopic level to make an improved or superior material*" [18,20]. The purpose of using composite materials is to produce a synergistic effect that reduces costs and improves the mechanical properties. Another advantage of composites is the wide range of materials available makes tailored design principles possible [19].

In general, composite materials are composed of a reinforcement phase and a matrix phase. The first is marked by high stiffness, and could be fibrous or particulate in form [21]. Its reinforcement provides the composite material with load transferability and toughening. The matrix phase is mostly a ductile and weaker constituent of the composite material, except for in a metal-matrix composite [22]. Composite materials are classified according to the reinforcement used and this can be subdivided into the following categories:

a. Fibrous refers to a composite using reinforcement in the form of fibers and these can either be continuous or discontinuous in a matrix material. The most commonly used fibers are carbon, aramid, boron and glass [20]. The difference between the two kinds of reinforcement is related to their geometric aspects, where continuous fibers have a high length-to-diameter ratio and composites containing them are generally stiffer than the bulk matrix [18,20,21]. Known as prepregs they are formed by either a unidirectional fiber (1D) or two woven fibers (2D) in a matrix material. In the case of 2D the fiber bundles are wound onto a mandrel to form sheets stacked in different orientations [23]. Unlike prepregs, discontinuous fibers are short, also termed chopped fibers, having a length-to-diameter ratio of $5 < \frac{l}{d} < 1000$ [21].

b. Particulate is composed of particles that are dispersed throughout the matrix. There are no constraints on the shape or configuration of particles. Such a composite is usually selected

for applications that demands low strength properties. In this context, a recent development of nanoparticle composites with carbon nanotubes [24–27], has the potential to change the generally applicability of particulate composites for structural applications.

A third category called *layered composites* was developed at the end of the 1970s to allow for optimization of aerospace applications [28,29]. A layered metal-composite has captured the attention of industry by combining a conventional fiber reinforced polymer (FRP) with thin metal interlayers. Furthermore, this hybrid composite material has opened up new opportunities for improving the tolerance of impact damage in aircraft structural applications [30]. Inspired by this category, the technology introduced in this PhD work was developed, based on the principles of additive manufacturing technology and joining method [17]. The purpose of this new technology is to offer an alternative technique for manufacturing layered hybrid structures.

There are three common damage phenomena that occur in composite materials (Figure 2-1): matrix cracking, delamination and fiber failure. These damage mechanisms can occur under quasi-static and cyclic loading [31]. The damage is first observed as a single crack in metals that propagates during service life. However, the failure modes for composite materials are more complex than those for isotropic materials [20,32]. The damage mechanisms in composites are usually based on interaction between matrix failure and fiber failure.

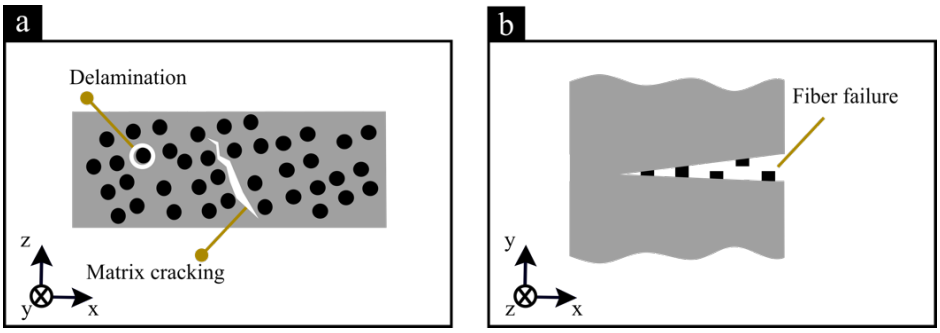

Figure 2-1 Typical damage in composites: (a) matrix cracking, delamination, and (b) fiber failure.

Composite material is expected to perform multiple tasks and damage can occur while in service. Matrix cracking is the first type of damage to appear. This can start at a fiber-matrix interface or in a region with a high content of resin. Another possible location is in regions that have stress concentrations or imperfections inside the laminate. It is common for cracks to start along the fiber direction. However, cracks can evolve perpendicular to the plane of the composite in cases of dominance in transverse tension and/or longitudinal shear stresses. It is interesting to note that the tips of matrix cracks often become initiation points for delamination and fiber failure [33]. Delamination is a failure mode that occurs due to high out-of-plane normal and shear stresses. This failure mode is characterized by separation of an adjacent reinforced layer (also known as lamina) of the composite material. During loading, this significantly influences the compressive stiffness, where a buckling effect can occur locally in the composite material [34]. Delamination can occur in a composite by eccentricities in the load path, which can lead to out-of-plane normal stress, for example in a single lap joint configuration [35]. The last stages of the damage mechanisms occur by fiber failure. Such damage only happens when the fiber strength inside the composite is exceeded. Fiber failure is not only limited by mechanical loading, but also by the chemical interaction between the polymer and the environment, e.g. presence of water or oxygen. Damage in these circumstances has

been reported for biodegradable composites [36]. Furthermore, the damage takes place at locations of local stress concentrations, where the fibers themselves are weaker [37]. Thus, fiber failures change local stiffness and strength dramatically. Therefore, in the transportation industry the structural design is defined to ensure the integrity of the entire structure and this covers certain types of damage observed in this material characterization. Hence, the design specifies material tolerances from the results obtained by mechanical testing to cover the component's life and peak loads while in service [38,39].

The major advantages of using composite materials are considered their strength-to-weight superiority compared to conventional materials [23,29]. Their current main drawback is the cost associated with the manufacture of composite materials. There are several possible manufacturing techniques available. This PhD work will also cover recently developed advanced methods, such as automated processes of additive manufacturing (Section 2.2) and contemporary joining techniques (Section 2.3).

2.2 Advanced methods of metal-composite manufacturing

Innovative manufacturing technologies can help to meet the demands of advanced industries, such as aerospace, to reduce fuel costs and emissions. A further advantage is to circumvent the time and labor of manually intensive techniques. It also enables engineers to use advanced interface design and hybrid materials to improve complex structural applications. The following sections present three technologies that have potential for manufacturing metal-composite structures, such as automated tape placement and automated fiber placement, described in Section 2.2.1, and additive manufacturing in Section 2.2.2. Together with the advanced methods described in these sections, the focus will be on thermoplastic based composites and the main controllable variables for these techniques.

2.2.1 Automated processing technique

Automated techniques such as automated tape placement (ATP) and automated fiber placement (AFP) are well known. Both techniques are interchangeable and can be described together due to the similarity of their processes. The only difference between the techniques is the geometry of the material laid down. Their process concept is similar to that of additive manufacturing, where the part is built up by successively adding material. Figure 2-2 illustrates the general set-up in an ATP/AFP process with a heating source.

In the case of ATP a prepregs tape is laid down that is between 75 mm and 300 mm in width [40], but for AFP the material geometry laid down has an average width of 3.2 mm minimum and 12.7 mm maximum [41]. The deposition speed varies from 0.83 m/s to 1 m/s [40]. An ATP process is used for simpler geometries and can cover larger areas at a relatively high speed. AFP demands a longer processing time, but can manufacture a more complex geometry, such as a fuselage section with window cutouts [40–42]. Compaction is activated by a roller that guarantees a pressure of 0.1 MPa for a thermoset tape 75 mm in width. This pressure is applied by the compaction device as shown in Figure 2-2. An increase in compaction force can result in less void formation and this improves the mechanical strength. The material selected for making the compaction device is commonly steel. Recent research has replaced the steel by introducing a silicone rubber roller, which proves to have a

better pressure distribution and longer contact that promotes high quality bonding [43,44]. The diameter of the roller also exerts a direct influence on the stress distribution that is induced. According to Sarrazin and Springer [45], the authors reported that a diameter smaller than 50 mm is impractical and strongly influences the stress distribution. However, Schäfer *et al.* [46] reported the importance of a smaller roller diameter, because it enables the manufacturing of complex geometry parts.

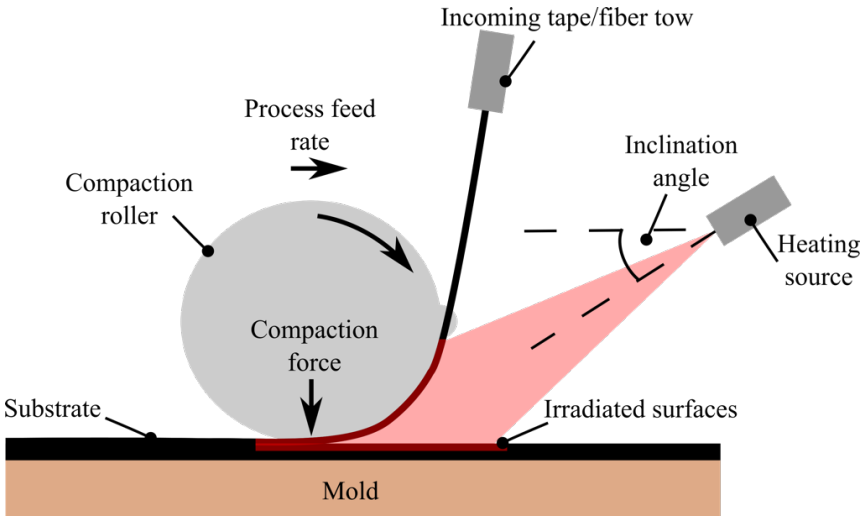

Figure 2-2 Schematic of the principles of automated tape placement (ATP) or automated fiber placement (AFP) with an in-situ heating source.

During the layup of the fiber or tape, the compaction roller transfers an additional pressure to help in the consolidation. For thermoplastic tape, the pressure necessary is between 1.4 MPa [47] and 3.6 MPa [48]. The literature reports three different heating sources to produce in-situ consolidation [49] by: (1) infrared [47,50], (2) laser [43,51], and (3) hot gas torch [52,53]. Their purpose is to apply the energy needed to heat up the deposited substrate or tape, and the incoming tape. Important for in-situ consolidation is to reach the melting temperature of the polymer, promoting a bonding formation. This avoids the additional time and energy consumed using a post-consolidation step such as an autoclave. However, the presence of a highly viscous resin is the main disadvantage with the high processing thermoplastics of ATP/AFP. The reason for this is their fast heating and cooling rates, combined with only a short time to apply pressure. According to the contemporary literature, it is possible for an AFP process to use ultrasonic techniques to achieve consolidation [54]. Ultrasonic consolidation uses a sonotrode device, which converts a high frequency alternating current into high frequency vibrations. In this process the sonotrode applies both pressure and vibration to form a welding interface [54].

Polyether ether ketone (PEEK) is a semi-crystalline thermoplastic that is most commonly used with carbon fiber (CF) reinforcement for ATP methods [45,47,48,51–53,55,56]. The high performance of such a thermoplastic is preferred for advanced applications. However, other materials are also being further investigated, such as CF with a different matrix: polyphenylene sulfide (CF-PPS) [57], polyamide 6 (CF-PA6) [43,58], and polyether ketone ketone (CF-PEKK) [48,52]. Much of the current literature is a validation by repeating studies of other investigations, as the materials available for ATP are limited. Therefore, to consider the applicability of an ATP process fully, a wide range of materials still needs to be investigated.

In the past, a hot gas torch was often employed, due to its lower capital investment. However, with the development of more efficient heating sources the hot gas torch tends to be replaced by other heating sources, such as laser or infrared. The application of a laser as the heat source can increase the capability of focusing a higher heat intensity on precise regions [59]. Moreover, it minimizes the formation of local residual stress and the possibility of inducing delamination in the consolidated material [40,59]. A carbon dioxide laser is absorptive and can cause oxidation of the material surface, affecting the adhesion of the fiber-matrix interface [60]. Moreover, there is a high risk of burning the material [61]. However, neodymium-doped yttrium aluminum garnet (abbreviated Nd:YAG) is a type of solid-state laser preferable for a carbon fiber reinforced thermoplastic. The thermally conductive carbon fiber allows controllable heating by absorption of laser light. Thus, the heating mechanism promotes a more uniform heating of the thermoplastic and thus diminishes the changes caused by destroying the polymer material [62,63]. In this regard, the third category of heating sources is used to allow an in-situ consolidation during the ATP process. Infrared uses a laser with a short wavelength and the heat affects a large and homogeneous area [47,50]. The quality of bonding is controlled by a uniform and progressive heating distribution across the material surface. This heating source is known for its reliability, low maintenance and efficiency [49].

The literature reports that a gap of between 0.5 mm to 1 mm is inevitable in ATP to allow the layup variation [40]. The presence of a gap is one of the reasons for its inferior mechanical performance compared to using an autoclave process. However, the impact of a different heating source can change the mechanical properties compared to an autoclave curing process. The mechanical performance of ATP using a hot gas torch is 45 % less than with autoclave processing [53]. The lack of post-processing with ATP hinders an improvement in the mechanical properties. However, an alternative to hot gas torch can achieve up to 90 % of the mechanical properties that are achieved by a standard autoclave process cycle [64,65]. Using a laser, Comer *et al.* [66] obtained results superior in interlaminar toughness of up to 134 % higher than from autoclaves using CF-PEEK material. However, the authors did report a reduction in flexural strength (68 %) and interlaminar shear strength (70 %). These results were also similarly reported by Ray *et al.* [55], where the authors discussed that the lower crystallinity attributed for the lower mechanical strength and stiffness values. Furthermore, Stokes-Griffin and Compston [67] discussed the influence of process parameters on the mechanical properties. The authors found that at 100 m/s it seems to be independent of process temperature. The literature reports that it is challenging to obtain comparable mechanical properties to an autoclave [55]. As well as the mechanical properties, ATP has problems in achieving a desirable degree of crystallinity in semi-crystalline thermoplastics and poor fiber-matrix bonding issues [45,68]. The mechanical properties are not reported in the literature available for ATP with infrared as the heating source.

In the case of AFP, the method has the possibility to combine a number of process parameters, but some material-related challenges. AFP can improve the production of components and the processing of the material. According Lukaszewicz *et al.* [40], the productivity of AFP is higher for all part sizes compared to an ATP process. The reason for this is the capability of an AFP process to accelerate and decelerate during layup with high levels of steering control of the deposited material. Besides these advantages AFP has limitations for producing complex geometries free from gaps or overlaps (Figure 2-3). Croft *et al.* [69] reported a reduction of up to 13 % of the in-plane shear strength due to the presence of an overlap. However, the authors also reported an insignificant change in tensile strength was observed, compared with the base material (free of defects). Surprisingly, Sawicki and Minguet [70] reported that the presence of smaller gaps (0.8 mm in width) decreased the interlaminar

shear strength by up to 27 % compared to the baseline. Furthermore, Sawicki and Minguet [70] also reported that larger gaps (2.5 mm in width) have insignificant influence on the interlaminar shear strength. The unexpected low influence of larger gaps is not well explained as it is claimed that a sharp variation in internal stress distribution is observed with small gaps. Woigk *et al.* [71] carried out an experiment that combines the effect of gaps and overlaps. The authors reported a tension and compression strength reduction of 7.4 % and 14.7 % respectively, compared to the base material. An interesting investigation has been recently published by Rakhshbahar and Sinapius [72]. The authors evaluated the influence on filling in the gaps caused by an AFP process. To perform this homogenization, the authors reported a combination of 3D printing with a carbon-fiber reinforced thermoplastic to manufacture hybrid AFP laminates. The authors reported an improvement in tensile strength, interlaminar shear strength and flexural strength of 13 % compared to the AFP laminate.

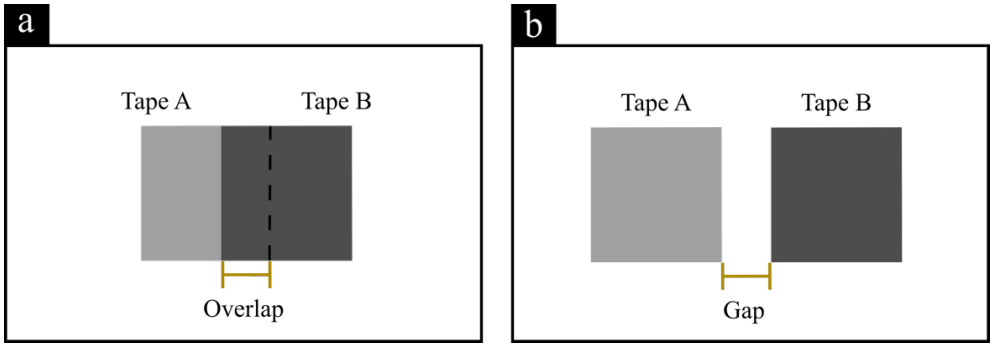

Figure 2-3 Typical manufacturing non-conformities in AFP/ATP process: (a) presence of overlap and (b) presence of gaps.

By using ultrasonic consolidation in the AFP process, Rizzolo and Walczyk [54] investigated the flexural stiffness and strength of flat samples using two materials, in their trial carbon-fiber polyethylene terephthalate (CF-PET) and glass-fiber high density polyethylene (GF-HDPE). By changing the process speed from 34 mm/s to 102 mm/s, the authors reported that the stiffness and strength of GF-HDPE decreased by 20 % and 40 %, respectively. For the CF-PET, the authors also reported a decrease of 65 % in stiffness and 49 % in strength when the speed was tripled from 34 mm/s to 102 mm/s. The authors reported high energy transfer at lower speeds, where ultrasound seems to be efficient.

According the literature, Stokes-Griffin *et al.* [43] carried out a study on the application of unidirectional CF-PA6 tapes on mild steel substrates by means of an ATP process. The authors reported bonding strength by means of lap shear tests. An ultimate lap shear strength of 25 MPa was achieved using a PA6 film to promote bonding of CF-PA6 on the metal surface by laser heating. The authors adapted the lap shear geometry to a total length of 70 mm instead of 140 mm, thus secondary bending effect was not reported and it avoided early failure.

The relevant works published that have investigated in-situ consolidation with different heating sources are presented in Table 2-1 and Table 2-2, for ATP and AFP, respectively.

Table 2-1 Selected works carried out on automated tape placement (ATP).

Authors	Process variant	Material	Description
Colton *et al.* [47]	Infrared	CF-PEEK	Proof of feasibility of an automated process for flat CF-PEEK and arbitrary ply configurations.
Janssen *et al.* [50]		CF-PA6	Feasibility study on combining CF-PA6 tape joining 3D printed structures by thermoforming process.
Clancy *et al.* [51]	Laser	CF-PEEK	Investigation into the manufacturing of two laminates with variable angle to improve stress distribution and laminate performance.
Grouve *et al.* [57]		CF-PPS	Assess the bonding strength of CF-PPS and correlate with the process parameters of laser-assisted ATP.
Brecher *et al.* [58]		CF-PA6 CF-PEEK	Evaluation of the process route to manufacture a tailor-made composite with different types of thermoplastic.
Lamontia *et al.* [52]	Hot gas torch	CF-PEEK CF-PEKK	Evaluate the manufacturing of cylinders and the impacts of void formation and ply waviness defects on the mechanical properties.
Qureshi *et al.* [53]		CF-PEEK	Investigate the influence of process parameters on the mechanical properties of continuous rings and laying tape onto pre-consolidated CF-PEEK laminates.
Khan *et al.* [73]		CF-PEEK	Correlate the results from modeling the effects of parameters on the quality of consolidation according to the bonding mechanism used.

Table 2-2 Selected works carried out on automated fiber placement (AFP).

Authors	Process variant	Material	Description
Rajan *et al.* [74]	Infrared	CF-PEEK	Evaluation of the formation of defects in curved samples by understanding strain measurements during the manufacturing process.
Arhant *et al.* [75]	Laser	CF-PA6	Investigation into manufacturing of pressure vessels from thermoplastic composite for deep sea applications. The study also compared the compression properties of CF-Epoxy produced by wet filament winding.
Van Hoa *et al.* [76]	Hot gas torch	CF-PEEK	Investigation into the manufacturing of flat laminates and a comparison with conventional autoclave molding.
Lamontia *et al.* [52]		CF-PEEK CF-PEKK	Evaluate the manufacturing of cylinders and the impacts of void formation and ply waviness defects on the mechanical properties
Rizzolo and Walczyk [54]	Ultrasonic	CF-PET GF-HDPE	Feasibility study on ultrasonic consolidation for AFP using flexible thermoplastic-based composites.

2.2.2 Polymeric additive manufacturing

Major industries are constantly searching for new technologies. This is key to the development of efficient products, such as lightweight vehicles to reduce fuel consumption. Additive manufacturing, also known by its acronym AM, is one such innovative technique even though it can actually be considered a relatively old process, it has only recently gained attention for industrial application. Many manufacturing processes modify the geometry of a part by removing material mass until the desired shape is obtained, for example by milling [77]. By definition AM is the opposite principle to this subtractive technique, adding material layer upon layer to form the desired shape. Based on ASTM F2792-12a [78], AM is also known by many names, such as generative manufacturing, rapid prototyping, 3D printing, and other terms.

Table 2-3 divides polymer AM into four categories. A description of each process is available in a work by Kruth *et al.* [77]. They all have in common the use of Computer Aided Design (CAD) to define the part to be produced. These techniques differentiate between the process of adding successive layers, whether that is liquid, powder, or sheet material [79]. For example, stereolithography (SLA) uses a laser technology to cure layer by layer of photopolymer, and when it is exposed to light such a polymer changes its properties. In a similar way to SLA, the fused filament fabrication (FFF) technique builds parts by extruding polymer through a nozzle onto a platform [77,80].

There are different methods of 3D printing, but the most widely used is FFF. This technique uses a thermoplastic feedstock, which is heated to a temperature above the melting point of semi-crystalline polymers or the glass transition point of amorphous polymers. The material is deposited layer by layer to create the finished part [81]. FFF technology has undergone rapid growth since 2009 after expiration of the trademarked patent held by Stratasys (U.S. 5121329) [82]. Prior to patent expiration 3D printers were too expensive. The technology is changing the standard methods of manufacture that are used in a traditional company. One case study of its use is from the German automotive company BMW, in which they improved productivity of automotive parts, such as jigs and fixtures, on the assembly line. Using the FFF method, BMW was able to reduce costs by up to 60 % compared to traditional machining methods [83].

Table 2-3 List of additive manufacturing processes for polymers. Adapted from [77].

Supply	Process	Material addition method
Liquid	Stereolithography (SLA)	Liquid layer deposition
	Ink jet printing (IJP)	Drop-on-demand deposition
Powder	3D printing	Layer of powder and binder printing
	Selective laser sintering (SLS)	Layer of powder
	Laser cladding	Continuous injection of powder
Solid	Fused filament fabrication (FFF)	Continuous extrusion and deposition
	Laminated object manufacturing (LOM)	Deposition of sheet material
Gas	Selective laser chemical vapor deposition	Condensation of gas

Fused filament fabrication (FFF) is also known under the trademarked term as fused deposition modeling (FDM). In this PhD work, FFF is used due to its popularity in the engineering community. FFF is an additive manufacturing technology that develops parts with complex geometries by the layering of extruded materials. A representation of the process is depicted in Figure 2-4. The main components of an FFF machine are: (1) extrusion head, (2) printing platform, and (3) filament material spool. The first component is the backbone of an FFF machine, where the physical process of fabrication occurs. It can be divided into drive wheels, heating element and extrusion nozzles [84,85]. The raw material is available on the market in the form of flexible filament that is fed through a heating element called a liquefier, where the viscosity of the material decreases with increasing temperature. The heat input must be sufficient to bring it to a semi-molten state, which allows it to flow through the extrusion nozzle. The nozzle has resistive heaters that are responsible for keeping the polymer at a specific temperature, e.g. above the melting point of a semi-crystalline polymer [81,84]. Thus, material flows easily through the nozzle and forms a layer in the XY-plane. The polymer begins to harden immediately after flowing from the nozzle, but bonds to the layer below. After each layer is built the platform lowers down and another layer is deposited, and so on until the 3D part is finished [86]. Usually an FFF machine contains a second nozzle to extrude supporting material for any structure that has an overhang angle of less than 45° from the horizontal by default [87].

FFF technology is steered similar to other additive manufacturing techniques [78], taking the information from a CAD file. This file has all the data in a 3D representation and such information is converted into an STL file, which stands for standard tessellation language. This means that it approximates a model for triangles and slices that contain the information layer by layer until the final shape is reached [81,84]. During the additive process a secondary material is usually necessary to support overhanging geometries, holes or cavities, which leads to waste material, because this is removed after the part is finished [84]. On the other hand, the part can be manufactured as multi-material from a variety of materials in one component, because the filament can be easily changed. The process also requires no additional material to help with the curing process [81]. Advantages of the FFF process include the use of available thermoplastics, which can manufacture models with good structural properties similar to the final production model. However, the FFF process requires several factors to achieve a high-quality finish. The nozzle diameter and movable build platform have an influence on the layer thickness and vertical dimensional accuracy, which can vary from 0.2 mm to 0.4 mm [88]. Górski *et al.* [89] observed that the overall dimension in FFF parts can achieve a 2 % deviation compared to other technology used to form polymers. Other parameters also have an effect on the surface quality, such as longer printing time, road thickness, orientation, and road angle [90–92]. Aside from the surface quality and dimension accuracy, the process parameters have a significant effect on the final mechanical properties and the presence of air gaps, also known as voids or internal flaws [93]. These are represented by an incomplete filling of the area inside the perimeter of FFF parts and can act as local stress concentrations, reducing the global strength of the component [94,95]. Further information on the FFF-process-parameters/printed-part properties correlations can be found in a recent manuscript [96] co-published by author of this PhD thesis.

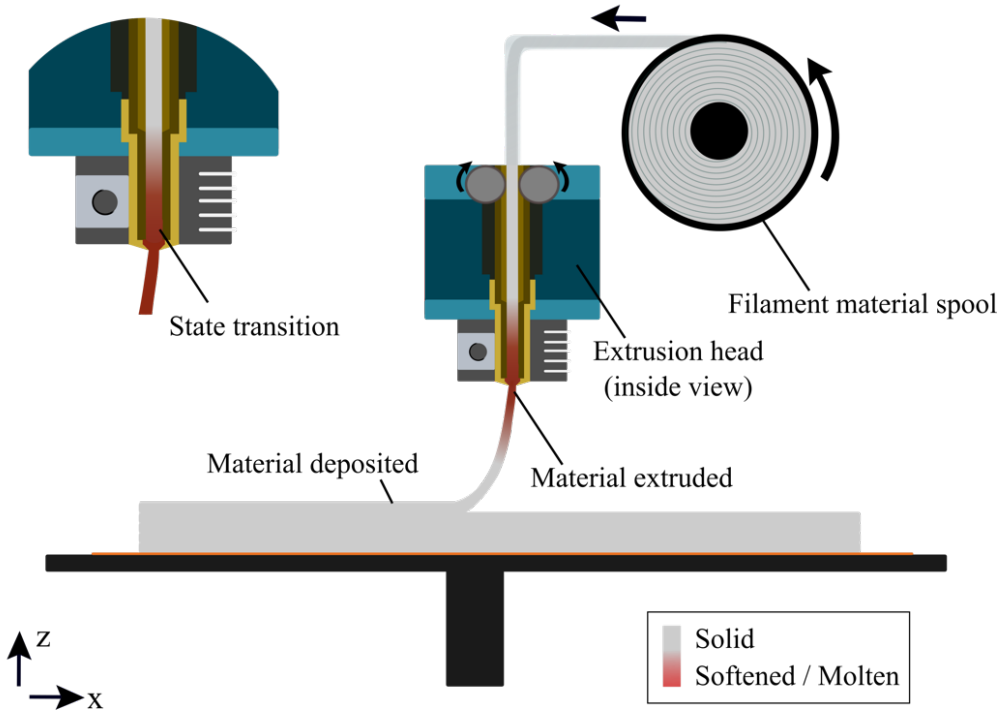

Figure 2-4 Schematic of the fused deposition modeling (FFF) process and its main components.

The material extruded by the heated head of the extruder in FFF is deposited in the form of a thin layer of material. The dimensions of this layer are therefore controlled by the material flow rate. The dimensions of the road's thickness and width, along with the speed of the extrusion head determine the flow rate of the material extruded from the nozzle [97]. The thickness of the road is defined by the operation system and can be between 0.1 mm and 0.3 mm [90,98].

Figure 2-5 depicts the main geometrical parameters used in FFF. A short description of each parameter is summarized in the following:

i. Raster orientation: also known as build strategy, associated with orientation in the print bed.
ii. Raster angle: direction of filament deposition, relative to the x-axis of the build platform.
iii. Road thickness: depends on the nozzle used, which influences the thickness of the layer deposited.
iv. Road width: refers to the width of the filament deposited that is used to build the part.
v. Air gap: is the gap between the raster in the same layer.

Some investigations have considered whether the air gap affects the strength and stiffness of the final part [87,99]. Other researches have observed that the road width [100], raster angle [87,101–103] and raster orientation [104,105] play roles that affect the mechanical performance of the FFF part. In this PhD work, *road* was selected as a synonym for *raster* for simplification.

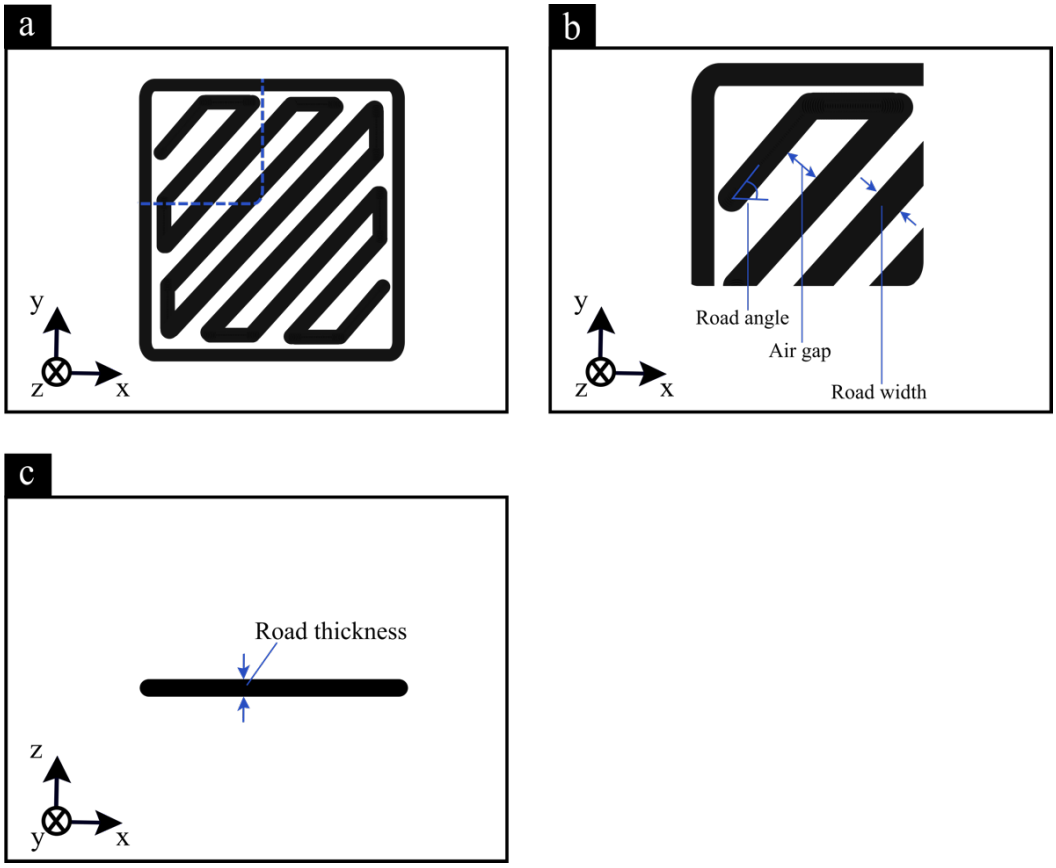

Figure 2-5 Representation of the (a) top view of an in-fill pattern with a detail view to highlight the main geometrial parameters of FFF process: (b) road angle, air gap, road width, and (c) road thickness. Adapted from [106].

Ahn *et al.* [87] observed that the effect of a negative air gap increases the packing density of the material and consequently exhibited an increase in strength, even if the strength did not increase by much with a negative air gap. However, the orientation $[45^{o} / -45^{o}]_{6}$ exhibited a large increase in tensile strength. Fatimatuzahraa *et al.* [95] obtained similar tensile strength for ABS, focusing only in one parameter variation in build orientation, $[0^{o} / 90^{o}]$ and $[45^{o} / -45^{o}]$. An interesting observation was obtained by Sood *et al.* [92,100], who determined the surface methodology that correlated with different process parameters and mechanical tests, for example tensile and bending. They found that the maximum strength is reached with a combination of minimum layer thickness (0.127 mm) and maximum road angle (60°). However, higher road angle means that the roads are inclined along the direction of loading and result in a reduction in bending performance. They concluded that an air gap of zero can be a benefit in terms of diffusion, which reduces the chance of stress accumulation due to efficient heat dissipation. Pan *et al.* [107] studied the influence of nozzle speed and layer thickness on strength with polylactide (PLA). They concluded that increasing the speed and the road thickness help to improve the adhesive strength. However, the road thickness has a greater influence on mechanical performance than the nozzle speed. As the heat loss with a larger road thickness is slow, it keeps the fused filament in a wet state for longer, which it is important for the interlayer bonding. Ning *et al.* [108] performed a similar study on chopped carbon fiber investigated the influence of process parameters on the mechanical properties. They observed that the nozzle speed and road thickness significantly influence the mechanical properties of ABS reinforced with a mass fraction of 5 % chopped carbon fiber. The mechanical properties became optimal at 25 mm/s and after this

point an increase in nozzle speed had negative effects on properties. They explained that as the deposition time is shorter it results in less bonding between the adjacent roads. The reason for continuous reduction in mechanical performance with increasing road thickness is associated with poor consolidation of bonding between the layers. The road thickness that gave the best properties was 0.15 mm with 1.1 GPa, 36.8 MPa and 24.4 MPa, for elastic modulus, tensile strength and yield strength, respectively. Wu *et al.* [109] also evaluated the influence of road thickness with ABS and PEEK. They observed that the mechanical performance of FFF parts are inferior by approximately 30 % compared to injection molding, likewise for ABS and PEEK. The authors reported fracture of PEEK road that were fully melted, which leads to significantly bonding. They also studied the effects of road angle and road thickness on PEEK. They obtained tensile strength and bending strength with a magnitude of 56 MPa for PEEK with a road thickness of 0.3 mm and road angle of 0° / 90°.

An interesting study performed by Sun *et al.* [91] investigated the influence of filament deposition approaches and process conditions on improving the bonding quality between the deposited filament. Their findings showed that the extrusion temperature has an impact on the filament neck growth (Figure 2-6) – i.e. the creation of a ligament between adjacent deposited filaments. A similar observation has been reported by Rodriguez *et al.* [99] and Bellehumeur *et al.* [98], where the neck formation among the adjacent roads is larger when an extrusion temperature is maintained near or above the glass transition temperature. Although the authors did not report directly a correlation between neck growth and mechanical properties of 3D-printed parts, they investigated the heat transfer and thermal mechanisms. However, Sun *et al.* [91] reported that by increasing the amount of deposited layers a significant effect on the bond formation on the bottom layers could be observed due to autohesion. Such phenomena is a fundamental concept that explains interface bonding, where the maintenance of extrusion temperature for a specific printing time promotes binding of the polymer interface by intermolecular diffusion [110,111].

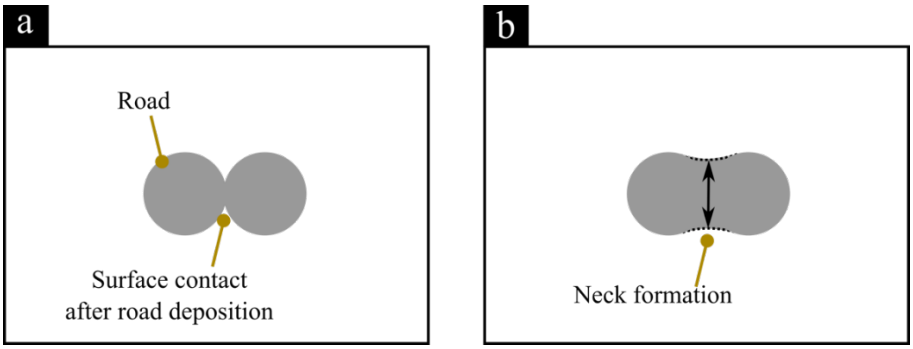

Figure 2-6 Representation of the main mechanisms of FFF process: (a) surface contact after road deposition and (b) neck formation among the adjacent roads. Adapted from [91,99].

Other researchers have focused on an improvement of the mechanical properties of FFF parts using reinforcement. New materials for FFF technology are necessary to increase its range of applications. One method has been studied by a small number of researchers to incorporate fibers or metal particles [108,112]. This concept allows a gain in mechanical performance of FFF based parts. For example, Zhong *et al.* [113] introduced short glass fibers to improve the mechanical properties of ABS. They increased the glass fiber volume fraction by 13 % and reached a tensile strength nearly 34 % more than the unfilled ABS. Shofner *et al.* [114] investigated a different approach to enhance the mechanical properties. They combined vapor-grown carbon fibers into ABS. This reinforcement increased the tensile strength by more than 45 % over the raw material.

Recently, two methods of FFF printing reinforced thermoplastics have been developed (Figure 2-7). Prüss and Vietor [115] named these *embedding before the printing process* and *embedding in the extrusion head* as illustrated in Figure 2-7(a) and Figure 2-7(b), respectively. The method with continuous fiber reinforced thermoplastic (Figure 2-7(a)) as the base material is commercially available by MarkForged [116]. A desktop 3D printer can produce continuous reinforced polyamide 6 (PA6) made of carbon, glass, and aramid. Therefore, it is limited to this material selection. However, its advantage is a constant and high fiber volume ratio. The second variant (Figure 2-7(b)) remains at the research level, with fiber embedding mostly taking place within the extrusion head. This variant is the subject of a patent application by Fischer *et al.* [117]. The fiber is available as dry bundles and the thermoplastic is added separately to the extrusion head as conventional filament. There is no literature available with mechanical properties from the second variant. Fischer *et al.* [118] have only briefly published the concept of the extrusion head for embedding fiber into the thermoplastic inside the extrusion head. However, Rakhshbahar and Sinapius [72] reported that its volume content is not comparable to commercially available fiber reinforced thermoplastic filaments. Nonetheless, the second variant does give freedom to combine a wide range of fibers and thermoplastics and to adjust the fiber volume.

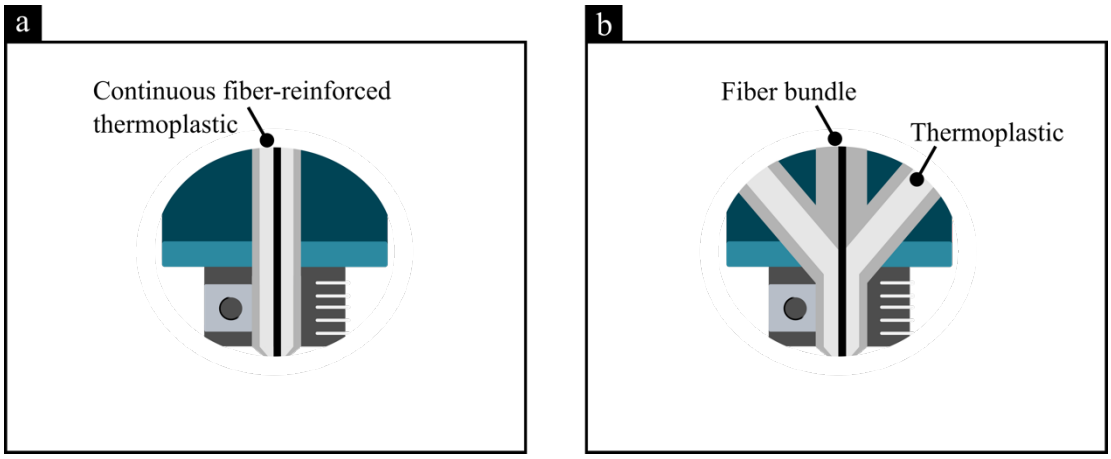

Figure 2-7 FFF printing variants for continuous fiber reinforced thermoplastics: (a) fiber reinforced thermoplastic coaxially extruded, and (b) fiber inserted into the thermoplastic within the extrusion head. Adapted from [72,119].

Recently, Desktop Metal launched a new 3D printer, Fiber™, with its printing head working as micro automated fiber placement (µAFP) [120]. The process can manufacture high resolution parts with continuous fiber thermoplastic materials. The company claims comparable industrial grade similar to AFP processes and reports outstanding performance of parts with porosity less than 1% [120–122].

2.3 Recently developed alternative methods for producing metal-composite lightweight structures

There are several approaches that have been proposed for joining metal-polymer or metal-composite hybrid structures in overlap configurations. Adhesive bonding [123,124] and mechanical fastening [125] are the most popular conventional joining techniques for different types of material. A combination of both techniques [126–129] is also widely used in the aerospace industry to improve load transferability. Various welding joining processes [14,130,131] have also gained attention for

producing overlap joint configurations. According to the literature, new concepts have addressed the possibility of direct assembly of the composite on a metal surface, e.g. 3D printing of a composite on a surface structured metal. It opens up a new range of possibilities for joining strategies, such as joint designs that can be applied to improve the load transfer between the materials in the overlap area. A combination of these individual techniques is known as a hybrid joining technology. The use of metal-polymer hybrid structures and various joining techniques is a response to the increased demand of the transport industry to produce lightweight structures. In recent works, Amancio-Filho and dos Santos [132] and Amancio-Filho and Blaga [6] have classified the joining technologies for metal-composite structures that are available into four groups, as illustrated by the diagram in Figure 2-8. Note that the techniques presented here are only a few examples. Furthermore, these technologies offer alternative process variants that are unspecified to keep the diagram fairly compact.

Adhesive bonding is the first group referred to in Figure 2-8. It is an established joining technology that has been extensively applied in several types of application for joining similar and dissimilar materials in structural configurations, e.g. metal-metal and metal-composite [133–135]. Mechanical fastening is also well-known and commonly applied in structural applications, for example riveting, screwing, clinching, and staking technologies [136], as well as more recently developed technologies such as friction-based injection clinching joining [137] and FricRiveting (friction riveting) [138,139]. The limitations of traditional joining technologies, such as adhesive bonding and simple mechanical fastening, have promoted the development of alternative methods for joining metals with composites. A good example is the development of new welding technologies to mitigate the process limitations of conventional technologies. For example, an intrinsic disadvantage of adhesive bonding is the long curing time and mechanical fastening can cause a stress concentration in the material around the fastener and imposes a weight penalty due to the fastener. To overcome these issues, a number of welding technologies have been proposed to join hybrid structural parts and thoroughly investigated. However, the low thermal resistance reported of the thermoplastic in most polymers can be an issue. There is literature on investigations into: ultrasonic [14,15], induction [140], resistance [141], laser welding [142,143], and friction spot joining [8,144] of metal-composite hybrid spot joints.

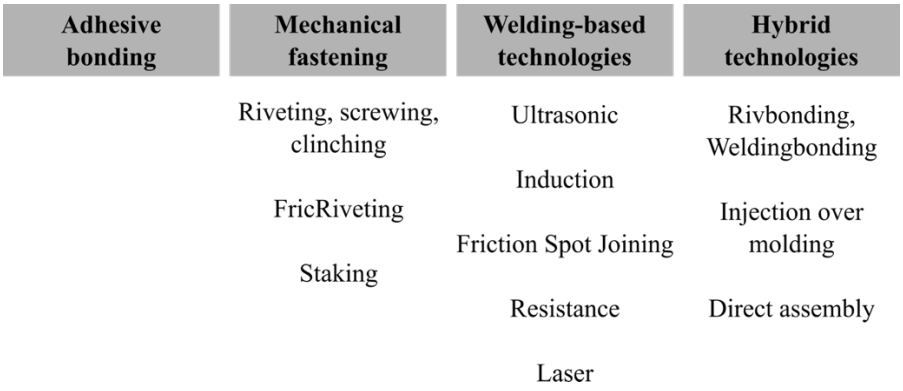

Figure 2-8 Available joining technologies for metal-composite hybrid structures. The techniques are divided into four main groups according to Amancio-Filho and dos Santos [132].

The hybrid technologies are shown in the last group and it is a variant to combine different joining methods. Thus, it leads to novel approaches to join structural parts and developed to produce high-performance hybrid joints. It has been reported the combination of rivet and adhesive called as Rivbonding, spot weld and adhesive called as Weldingbonding [145]. Also, injection over molding [146] and direct assembly [147].

Direct assembly (DA) is a new concept for producing hybrid joints and it is a subject increasingly investigated by the scientific community. There are several methods for joining the metal part with FRP parts using the DA approach and various processes can be employed to assemble the composite. These include autoclave-assisted technologies and non-autoclave concepts such as resin transfer molding (RTM) and vacuum-assisted resin infusion (VARI). In most cases this can be achieved by a completely manual procedure, such as hand layup and spray-up [148]. However, closed mold concepts such as RTM and VARI are preferred, as they improve the quality of the working environment [148,149]. These closed mold processes are also preferred because less void formation in the composite part is achieved, thereby improving the mechanical performance of metal-composite hybrid joints. Alternatively, it is also possible to use additive manufacturing as recently introduced by Falck *et al.* [17] to produce high performance hybrid joints. This method is the subject of thorough discussion in this PhD work.

2.4 Material used in this work

2.4.1 Aluminum 2024-T3

Aluminum alloys are widely used by several industries. It is the material of choice for large fuselage skin sheets and for applications with advanced joining technologies. Aluminum 2024 is applied in critical aerospace components, such as primary structures, e.g. fuselage, wing tension components, shear webs and also ribs [150]. Aluminum 2024 is a heat-treatable alloy and is part of the 2000 series. Such a material is a precipitation hardening aluminum alloy, where copper and magnesium are the main alloying elements. The presence of these elements increases the mechanical performance of the alloy, especially its strength and toughness [151]. The presence of copper also influences positively its corrosion resistance, as copper is the most cathodic alloy element and is less affected by galvanic reactions [152]. The formation and precipitation of secondary particles during the aging process provides the alloy with high mechanical performance [151,153]. The alloy's main mechanical and physical properties are further discussed in Section 4.1.1.

According to the literature, success with 2000 series aluminum alloys and conventional fusion welding processes has been limited [154]. The main problems associated with fusion welding of aluminum 2xxx are solidification cracking and porosity [155]. In contrast, alternative solid-state welding processes, such as friction stir welding [156,157] and friction spot welding [158], have been successfully used to weld 2xxx aluminum alloys. They mitigate the problems associated with solidification in fusion welding processes. The alloy is also preferred in metal-composite hybrid structures, such as fiber metal laminate (FML) [30].

In recent years, further new joining techniques have been investigated using aluminum 2024-T3 to develop hybrid joints. These include friction riveting [7], friction spot joining [8,9], and recently Falck *et al*. [17] have studied the feasibility of AddJoining hybrid joints. The results obtained are within the scope of this PhD work and are discussed in the following chapters.

2.4.2 Polyamide 6 (PA6) and carbon-fiber reinforced polyamide 6 (CF-PA6)

Polyamide (PA) is a semi-crystalline thermoplastic, which is commercially known under the trade name Nylon and was invented for Du Pont by the American chemist W. H. Carothers in 1935. Types

of PA are widely used as engineering polymers. Their excellent properties have made them a considerable part of the world engineering polymers market [159]. Currently used composite structures are based on thermosets. However, there is an increasing interest in replacing the thermoset with a thermoplastic material, because thermoplastic composites can be reprocessed and are easily recycled [160,161]. They also present excellent cost effectiveness and short process cycles when compared to the long processing times of thermoset composites [160,162].

Polyamide can be divided into two main categories: aromatic and aliphatic [163]. There is also a variety of combined aromatic and aliphatic Nylon, often called aramides. PA has high toughness under a wide range of temperatures along with excellent impact and abrasion resistance, lubricity, and good resistance to organic solvents [163]. The presence of a repeating amide group as represented by -CO-NH- in the chain is the main characteristic of PA [164]. Such a polymer type is conventionally identified by the number of carbon atoms present in the monomer. PA6 is characterized as a *caprolactam monomer* with six carbon atoms (Figure 2-9). Whereas PA66 is comprised of two monomers *hexamethylenediamine* and *adipic* acid, each with six carbon atoms.

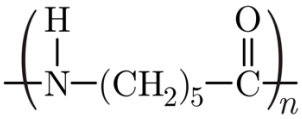

Figure 2-9 Polyamide 6 (PA6) chemical structure. Adapted from [164]

The presence of moisture has a plasticizing action, which changes the mobility of the amorphous phase present in PA6 [165–167], thus exposing the material to a worsening in mechanical and thermal properties [167,168]. This is caused by the polar characteristic of PA6 monomer, which implies interactions between chains and its surroundings can occur. Therefore, absorption of moisture is dependent on the temperature and environment. At room temperature with 50 % relative humidity, PA6 can absorb water up to 2.75 % [163,164,169].

Carbon-fiber reinforced polyamide 6 (CF-PA6) is a thermoplastic composite that offers advantages in manufacturing lightweight structures. The material has potential applications in the automotive industry and sport sector [170]. It is suitable for injection molding and thermoforming applications. Botelho *et al.* [162] compared the mechanical behavior of CF-PA6 and CF-PA66 composites. Their mechanical properties improved with increasing fiber content. A similar observation has also been reported for 3D printed composites [171,172]. The increased popularity of additive manufacturing has opened up the possibility for production of reinforced polymer, such as continuous CF-PA6, as recently published [173,174]. The fiber diameter, volume fraction and distribution can influence the mechanical properties of a 3D printed composite [171,172]. An interesting investigation into the influence of fiber orientation, fiber type and volume fraction in a composite was evaluated by Dickson *et al.* [175] with continuous reinforced PA6. Their results indicated a six-fold increase in the tensile strength of the composites compared with that of non-reinforced PA6.

PA6 has a melting temperature between 210 °C and 220 °C [164]. Typically, CF-PA6 is reported as having a melting temperature up to 220 °C [176]. CF-PA6 starts to degrade at around 470 °C and PA6 at 450 °C [176–178]. Li *et al*. [179] reported the effects of the thermal histories on the interfacial properties of continuous CF-PA6 material, which improves adhesion with the fiber content. An *et al.* [176] reported the influence of continuous carbon fiber content on the thermal properties of CF-PA6.

The recrystallization temperature increased by up to 180 °C compared to unreinforced PA6 and the melting temperature was not significantly influenced by the fiber content. However, the presence of fiber did influence the thermal stability of the thermoplastic, which caused an improvement in the thermal properties of CF-PA6 in comparison with PA6 [176,180]. The effects of nucleation and growth of PA6 crystals is affected by the presence of carbon fibers [181]. Typical CF-PA6 processing temperatures are between 230 °C and 250 °C, and it can be processed by injection molding [182] as well as more recently by additive manufacturing with temperatures up to 263 °C [175]. For PA6 processing the temperatures are 227 °C and 288 °C for injection molding [183,184] whereas for additive manufacturing the temperatures are between 245 °C and 265 °C [175,185].

Chapter 3. Experimental approach

This is the first scientific work to develop and study the fundamentals of the AddJoining process. The experimental concept of this PhD work is divided into four main phases (Figure 3-1). In the first phase, the feasibility of AddJoining was demonstrated, using fused deposition modeling with a single lap hybrid joint configuration. The author and collaborators showed the relevance of the process-induced changes on the quasi-static mechanical properties of hybrid join of aluminum 2024-T3 with acrylonitrile butadiene styrene (ABS) [17,186]. The exploratory investigation showed the potential of AddJoining to produce metal-polymer by layering; ABS was investigated and its relevance for the progress of the PhD work were important for understanding the fundamentals of the AddJoining process variants reported for each variant on [187]. Furthermore, this work was concentrated on a high performance material combination. In this regard, hybrid joints were thoroughly investigated by combining aluminum 2024-T3 with alternate layers of polyamide 6 (PA6) and carbon-fiber reinforced polyamide 6 (CF-PA6) as shown in Figure 3-1.

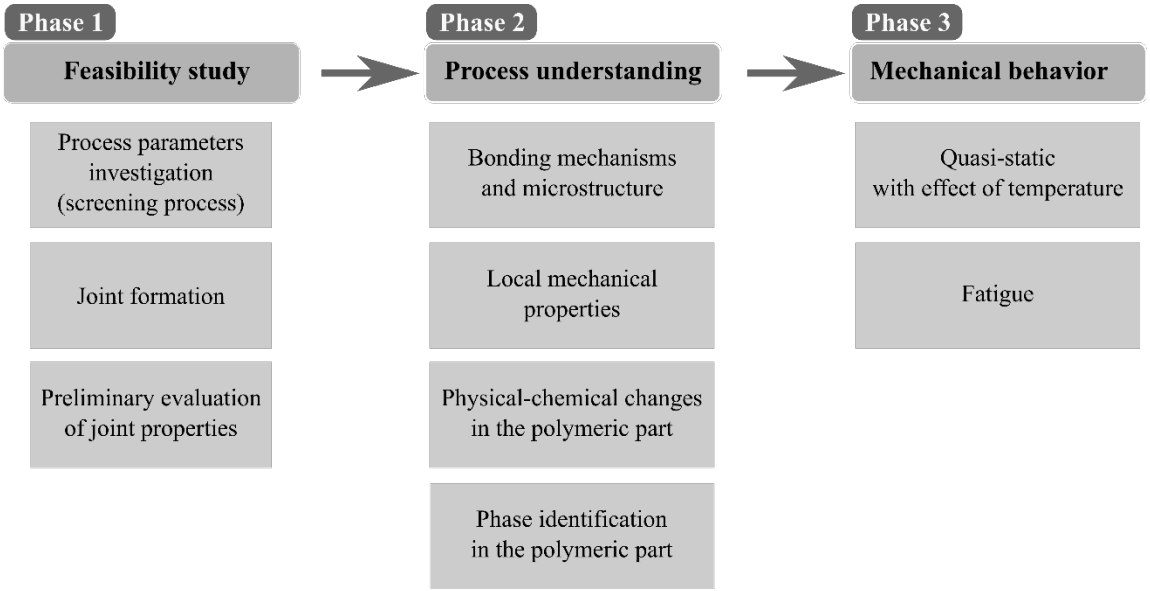

Figure 3-1 Experimental approach used in this PhD thesis.

After defining a range of process parameters, one material combination (Aluminum 2024-T3 and PA6 / CF-PA6) was selected for process understanding and optimization. For the second phase of this work, a full factorial design of experiments (DoE) was employed using statistical analysis and analysis of variance (ANOVA). One response, ultimate lap shear force (ULSF), was evaluated and the optimized parameters obtained by this study were used to increase the mechanical performance of the material combination, which is further studied in this work. These results are presented in Appendix A.4. The optimized joining condition obtained was used for the subsequent phases. Furthermore, a detailed analysis of the joints was investigated. Three joining conditions were selected for comparison purposes in the second phase, where the bonding mechanisms and an analysis of the joint microstructure were evaluated. Local mechanical properties were measured by instrumented nanoindentation at the interface between the metal part and the composite part. Thus, the changes caused by process parameters were correlated by thermal analysis using differential scanning calorimetry (DSC) and thermogravimetric analysis (TGA). To further support this, powder X-Ray

diffraction (XRD) was used to evaluate possible phase identification and transformation in the composite parts influenced by changes in process parameters.

In the third phase, using the knowledge gathered by process understanding, the mechanical behavior was assessed. For this phase, a wide range of mechanical testing was performed to better understand the mechanical behavior of the metal-composite hybrid joints produced by AddJoining as follows:

1. A digital image correlation system (DIC) was linked to the single lap shear test and applied to evaluate the strain field during loading, to understand damage initiation and evolution by the switching of direction of strain variations. Loading and unloading experiments were performed to evaluate damage initiation and propagation during the test. To support this evaluation, non-destructive ultrasonic measurements were carried out to determine the damage size. In addition, a finite element model was employed and validated experimentally. This model assisted in gaining a comprehension of the joint failure mechanisms.
2. Mechanical performance under cyclic loading was studied. In this step, a fatigue life analysis of the hybrid joints was established, using three statistical models for the experimental data obtained. Moreover, monitoring of stiffness degradation was carried out to identify the degradation phase in the hybrid joints under cyclic load.

For all cases in phase three, the failure mechanisms of the corresponding AddJoining hybrid joints (single lap) were investigated using scanning electron microscopy (SEM).

Chapter 4. Materials and methods

4.1 Base materials

4.1.1 Aluminum 2024-T3

The aluminum alloy 2024-T3 used in this work was a rolled sheet with a thickness of 2 mm obtained from Constellium, France [188]. This metal alloy was selected thanks to its excellent mechanical properties and applicability to the transportation industry. Such a material belongs to the 2xxx series of precipitation hardening aluminum alloys, where copper and magnesium are the major alloying elements. Table 4-1 depicts the nominal chemical composition of the aluminum 2024-T3 used in this work. The alloy is used for applications requiring a high strength to weight ratio and good fatigue resistance [189]. The main mechanical and physical properties of the alloy are given in Table 4-2.

Table 4-1 Nominal chemical composition range of aluminum 2024-T3 [189]**.**

Element	Al	Cr	Cu	Fe	Mg	Mn	Si	Ti	Zn
wt%	90.7 – 94.7	≤ 0.1	3.8 – 4.9	≤ 0.5	1.2 – 1.8	0.3 – 0.9	≤ 0.5	≤ 0.15	≤ 0.25

Table 4-2 Physical and mechanical properties of aluminum 2024-T3 at room temperature [189]**.**

Coefficient of thermal expansion [(µm/m)/°C]	Thermal conductivity [W/(m·K)]	Melting temperature range [°C]	Elastic modulus [GPa]	Ultimate tensile strength [MPa]	Elongation at break [%]
24.7	121	500-638	70	480	21

The aluminum alloy microstructure is possible to observe elongated grains in longitudinal direction (Figure 4-1(a)) which appear as equiaxed grains in the transverse direction (Figure 4-1(b)). The formation of secondary hardening particles (Al_2CuMg and $CuAl_2$) phases can occur in the aluminum alloy selected in this work, where it is visible as black spots in the microstructure [190,191].

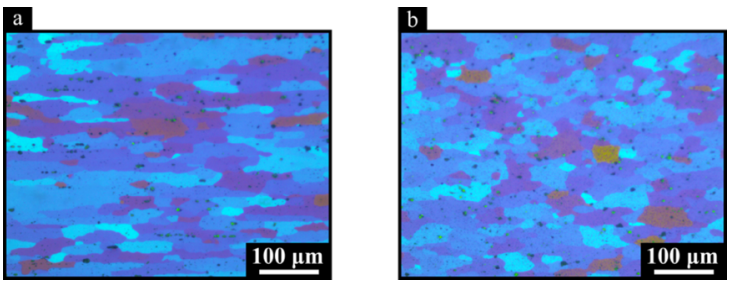

Figure 4-1 Microstructure of aluminum 2024-T3 (a) in longitudinal and (b) in transverse directions according to the alloy rolling direction.

4.1.2 Carbon-fiber reinforced polyamide 6 (CF-PA6)

CF-PA6 filament bundles of 0.38 ± 0.02 mm diameter were acquired at MarkForged [192]. Its carbon fiber bundles have 47 ± 1 % fiber volume fraction and are infused with a semi-crystalline polyamide 6 resin (Figure 4-2(a)). A total amount of 970 ± 22 individual fibers of 6 ± 1 µm diameter were measured inside the filament. During the manufacturing of fiber filament, a lack of matrix infusion between conglomerates of fibers can occur (Figure 4-2(b)). This is believed to be caused by the PA6 resin being polymerized during the fiber impregnation process, which creates a barrier to its infiltration into the fiber bundles, causing a non-uniform fiber distribution as pointed out in [193].

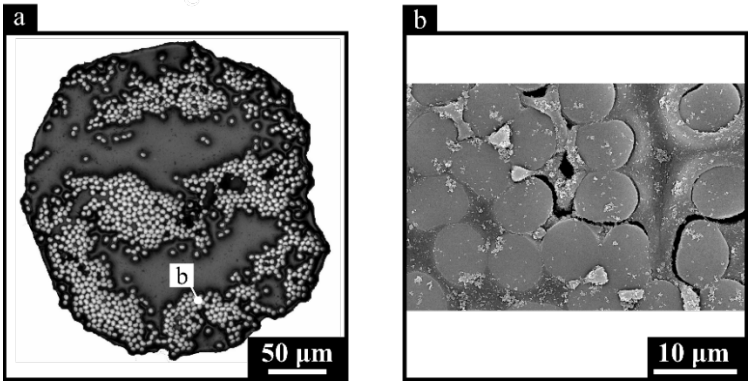

Figure 4-2 CF-PA6 base material: (a) cross-section, and (b) individual fibers.

Further characterization of the base material is presented in Appendix A.2. The relevant physical and mechanical properties of CF-PA6 are presented in Table 4-3. CF-PA6 presents outstanding mechanical performance and thermal stability in comparison with unreinforced PA6 [182,194]. The thermal degradation temperature of CF-PA6 is 4 % higher than PA6, and its recrystallization temperature is 10 % lower for the materials used in this work.

Table 4-3 Physical and mechanical properties of CF-PA6 at room temperature.

Crystallization temperature (DSC) [°C]	Glass transition temperature (DSC) [°C]	Melting temperature (DSC) [°C]	Onset thermal decomposition (TGA) [°C]	Elastic modulus [GPa]	Ultimate tensile strength [MPa]	Elongation at break [%]
157 [b]	57 [b]	233 [b]	476 [b]	54 [a]	700 [a]	1.5 [a]

(a) Data from the literature [192]
(b) Experimentally obtained

4.1.3 Polyamide 6 (PA6)

Spools were acquired from MarkForged (USA) for unreinforced polyamide 6 (PA6) filament [192]. The PA6 had a 1.74 mm filament diameter with absent void density (Figure 4-3(a) and Figure 4-3(b)). PA6 is known to be hygroscopic, due to the presence of hydrogen bonds, and any moisture content affects its strength, stiffness and elongation [195,196]. Therefore, to prevent moisture absorption, a

Pelican 1430 dry box was installed beside the 3D printer for use while printing and prevent moisture absorption (Figure 4-4). The PA6 stored in the dry box was dried every three months to keep the moisture content below a mass fraction of 1.3 %. [169,197]. Further characterization of this base material is presented in Appendix A.2.

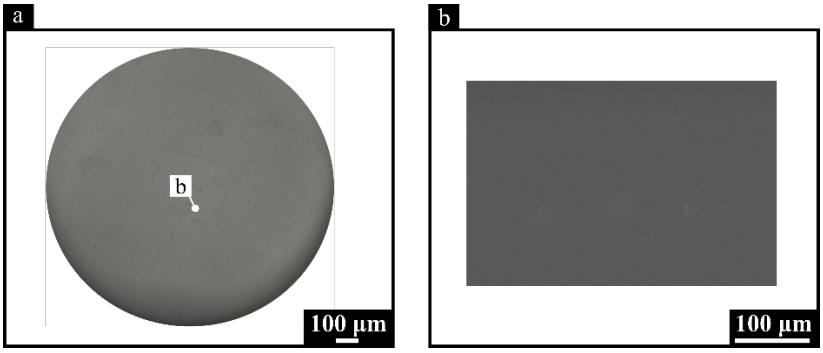

Figure 4-3 PA6 base material: (a) filament cross-section, and (b) visual absence of voids.

The relevant physical and mechanical properties of PA6 are presented in Table 4-4. PA6 is a high-performance semi-crystalline polymer widely used in the transportation industry and has a melting temperature around 201 °C and thermal decomposition starts at 456 °C. The elastic modulus and ultimate tensile strength are relatively low compared to CF-PA6, at 98 % and 92 % respectively. However, PA6 can undergo high plastic deformation before failure with an elongation at break that is 173 % higher than CF-PA6.

Table 4-4 Physical and mechanical properties of PA6 at room temperature.

Crystallization temperature (DSC) [°C]	Glass transition temperature (DSC) [°C]	Melting temperature (DSC) [°C]	Onset thermal decomposition (TGA) [°C]	Elastic modulus [GPa]	Ultimate tensile strength [MPa]	Elongation at break [%]
153 [b]	56 [b]	201 [b]	456 [b]	0.94 [a]	54 [a]	260 [a]

(a) Data from the literature [192]
(b) Experimentally obtained

4.2 Equipment

4.2.1 Mark Two 3D printer

The AddJoining process was investigated using a commercially available 3D printer, the Mark Two (MarkForged, USA) [116]. The Mark Two 3D printer produces reinforced polymer with continuous fibers using the FFF method (Figure 4-4). It is a desktop 3D printer with a maximum printing size of 320 mm by 132 mm by 154 mm, length, width and height, respectively. The extruder head has two nozzles - one nozzle for printing the PA6 material and the other nozzle to print the CF-PA6 material. As a non-open source 3D printer the printing parameters are constrained by structural parameters. Process parameters such as the printing temperature (270 °C), road thickness (125 µm) and deposition speed (average 40 mm/s) are fixed and cannot be changed by the user. Software called Eiger (version

1.10) that is provided by MarkForged was used to define structural parameters such as CF-PA6 distribution, the number of CF-PA6 layers within the composite part and the CF-PA6 orientation. By varying these control parameters, an optimum combination of structural parameters was obtained and this is discussed in Chapter 6 and presented in Appendix A.4.

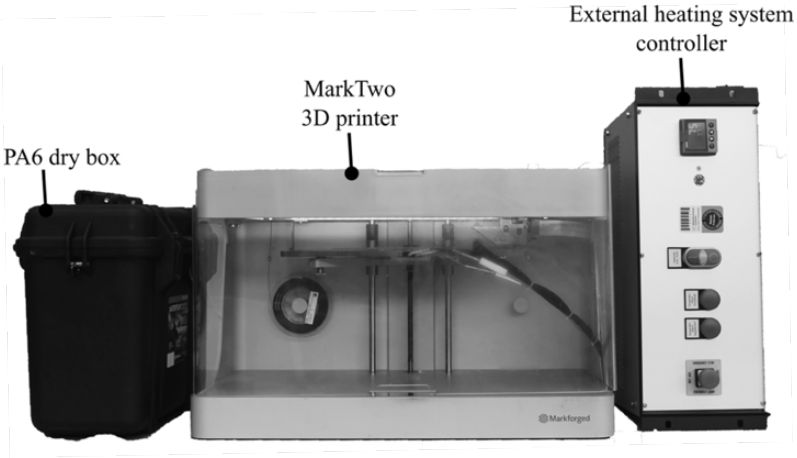

Figure 4-4 AddJoining equipment set-up with a PA6 dry box connected to the Mark Two (MarkForged 3D printer) and a customized external heating system controller connected to the printing bed surface.

4.2.2 Direct heating control system

A customized heating control system was specially developed for this purpose at Helmholtz-Zentrum Geesthacht (HZG). The system has a customized printing bed surface made of mica paper sold under the tradename K-Therm® AS600M (AGK GmbH, Germany) impregnated with silicone resin. The printing bed surface that was developed has 320 mm by 200 mm by 7 mm, length, width and height, respectively (Figure 4-5).

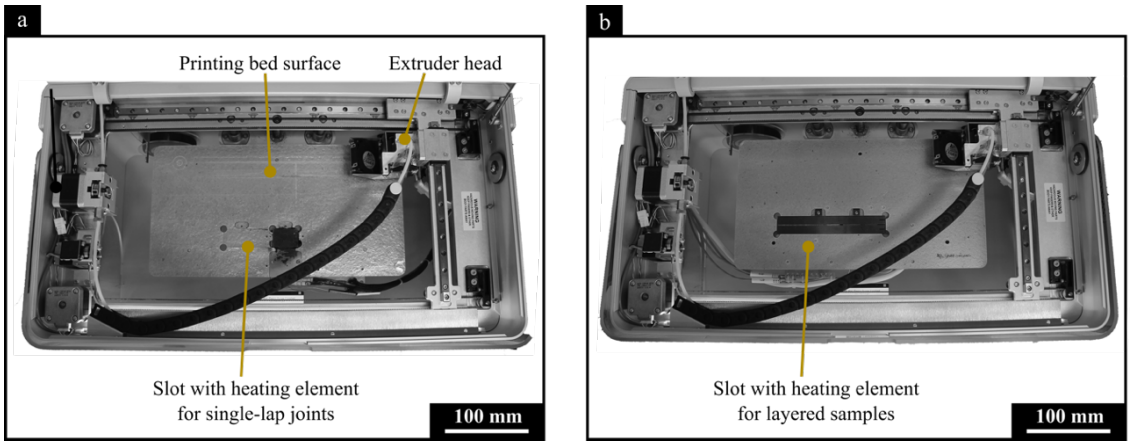

Figure 4-5 Top view of the Mark Two (Markforged) 3D printer highlighting the main components for (a) single lap joint configuration, and (b) layered sample configuration.

Two printing bed surfaces were developed with different slot geometries and manufacturing constraints. The first configuration (Figure 4-5(a)) was applied for single lap joint samples with a slot of 100 mm by 25 mm by 2 mm, length, width and thickness, respectively. For the investigated configuration, Figure 4-5(a), the heating element was positioned underneath the aluminum alloy

sample with two thermocouples connected to the controller. The controller allows adjustment of the temperature from 20 °C to 270 °C. For safety reasons a cut-off temperature was set at 300 °C. Second configuration (Figure 4-5(b)) was applied for layered samples. Nevertheless, this is out of the scope of this work.

4.3 Methods

4.3.1 Aluminum surface pre-treatment

The metal surface was first mechanically abrading by sandblasting, and the aluminum surface was further treated to increase its roughness for better adhesion between the joining parts (Figure 4-6), as presented in Section 5.1

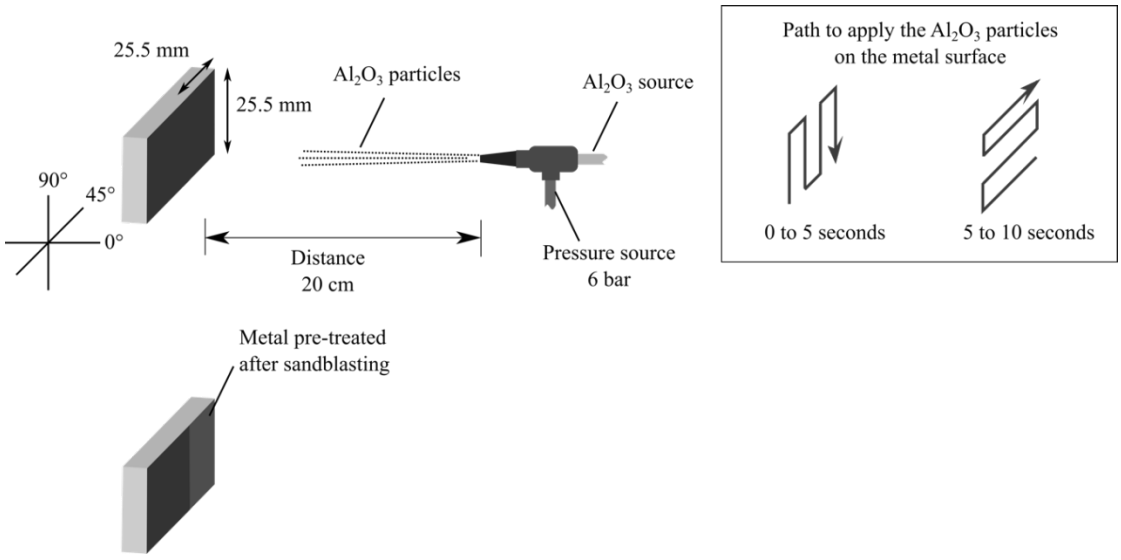

Figure 4-6 Schematic of the pretreatment applied to the Aluminum 2024-T3 surface.

An illustration of the surface pretreatment used on the metal surface is shown in Figure 4-6. The metal was sandblasted with corundum (Al_2O_3), with particle sizes ranging from 100 µm to 150 µm and a pressure of six bar. The metal was positioned at an angle of 45 degrees from the blasting nozzle and a working distance of 200 mm was used. Surface pretreatment was applied to the overlap area (25.5 mm x 25 mm) for 10 seconds. The parameters of the preprocessing and their control are crucial for assuring the consistency of surface roughness. For the metal used in this PhD work, the surface roughness of the as-received aluminum 2024-T3 is shown in Figure 4-7(a) and after sandblasting in Figure 4-7(c). The average maximum peak-to-valley distance (R_z) measurements of the aluminum 2024-T3 corresponded to 7 ± 0.8 µm (see Figure 4-7(b)). After applying the surface treatment described here, surface roughness was up to 91 % higher than the as-received alloy, 89 ± 0.3 µm (see Figure 4-7(d)). Increased surface roughness aids the formation of micromechanical interlocking [6]. To avoid subsequent formation of an oxide layer, the pretreated samples were cleaned using pressurized air and then immersed in ethanol for three minutes in an ultrasonic bath.

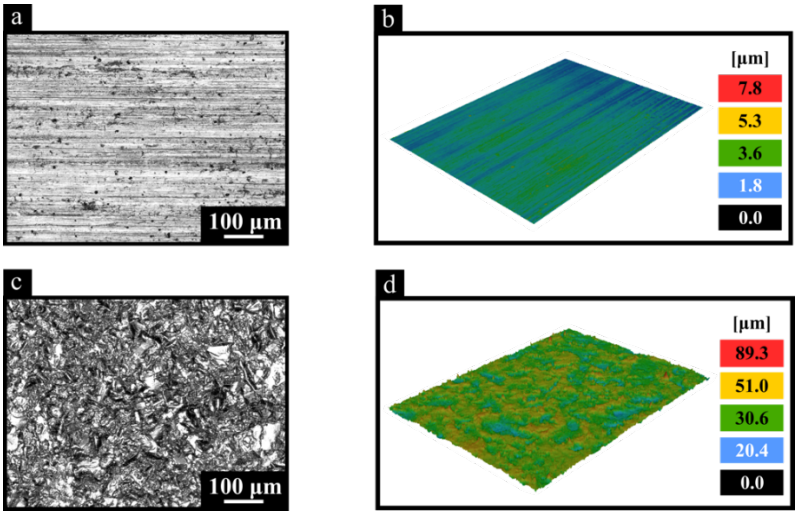

Figure 4-7 Surface roughness measurements of (a) the as-received and (c) sandblasted aluminum 2024-T3 parts; with (b) and (d) 3D reconstruction image of the surfaces of the part obtained by LSCM.

4.3.2 Manufacturing procedure of the samples

In the preferred process variant, using fused filament fabrication (FFF), the AddJoining manufacturing route is divided into three steps. In the first step, the aluminum alloy substrate is fixed to the build platform by placing it into a slot. To produce the hybrid joints, the aluminum 2024-T3 sample with dimensions 100 mm by 25 mm by 2 mm in length, width and thickness, is first placed on the printing bed surface (Figure 4-5(a)). Then the PA6 filament is melted by the extrusion head and deposited by a nozzle to form a coating layer on the metal substrate. Next, further polymer layers (CF-PA6 or PA6) are deposited until the desired thickness and stacking sequence of the polymeric part is achieved, in which layers of unreinforced and reinforced polymer are intercalated, in this case PA6 and CF-PA6, respectively. When producing the layered samples, the aluminum 2024-T3 sample with dimensions 150 mm by 25 mm by 2 mm in length, width and thickness, is first fixed to the printing bed surface (Figure 4-5(b)) and the same procedure is applied to deposit the polymeric composite on the metal substrate, as described above. It is interesting to note that the AddJoining process is introduced by this work and its development is described in detail in Chapter 5 and Chapter 6, respectively.

4.3.3 Statistical modeling of joining parameters and process understanding

To better understand and optimize a new manufacturing processes, it is usually necessary to use a statistical approach that is used for designing and evaluating an experiment, such as a design of experiments (DoE) [6]. This method makes it possible to gain a better understanding of the influence of control variables (process parameters) to improve the response (e.g. mechanical performance) [198].

In an early phase of developing the AddJoining process, a DoE was proposed to improve the mechanical performance of the single lap joints produced. The DoE was employed during process development and the experiments were proposed according to a three-level full factorial design. Two factors were considered for the DoE, coating temperature (CT) and heating bed temperature (HBT). The selected factors were varied over the three levels shown in Table 4-5.

Table 4-5 AddJoining process parameters (two factors) used in the three-level full factorial design.

Factor	Abbreviation	Unit	Level 1	Level 2	Level 3
Coating temperature	CT	°C	20	85	150
Heating bed temperature	HBT	°C	200	235	270

There were nine experimental combinations of process parameters tested for the selected design approach (Table 4-6). Although this table is presented in sequential order, the runs was adequately randomized using Minitab software (version 11) (Minitab, Inc., USA) before the manufacturing of the single lap joints. The purpose of this is to ensure that observations and errors are independently distributed and not influenced by uncontrolled variables [198]. In this table, the factors are represented by numbers and normalized factors for low, intermediate and high are denoted with "-", "0" and "+", respectively. In total 27 single lap joints were manufactured to investigate their ultimate lap shear force (ULSF). This response is measured by mechanical testing, as described in Section 4.3.8.1. Therefore, for each DoE condition, three replicates were made and their ULSF was averaged.

Table 4-6 Three-level full factorial design with two-factor matrix for the AddJoining process

Experimental	Factors		Normalized factors	
	CT [°C]	HBT [°C]	CT [°C]	HBT [°C]
1	200	20	-	-
2	235	20	0	-
3	270	20	+	-
4	200	85	-	0
5	235	85	0	0
6	270	85	+	0
7	200	150	-	+
8	235	150	0	+
9	270	150	+	+

The effect of each of the process parameters on the response (ULSF) was determined using analysis of variance (ANOVA). The statistical analysis was conducted by using an F-test, carried out by Minitab 14 software (Minitab Inc., USA). This method allows for the rejection of null hypothesis for factors that have no statistically significant effect on the response. Using this technique, a p-value of less than 0.05 (i.e., a confidence level of 95%) was chosen to indicate the significance of a parameter and the F-value was used to evaluate the effect of the process parameters [198,199]. Details of the statistical analysis of controlled parameters are shown in Table 4-6 and are further discussed in Appendix A.4.

4.3.4 Microstructural analysis

To analyze the microstructure of the hybrid joints a cross-section of the joints was cut. This was then mounted, and polished, following standard metallographic methods to obtain a smooth surface. The aluminum 2024-T3 microstructure was revealed by electrochemical etching (30 V for 120 s at room temperature) in a Barker's solution of water and fluoroboric acid (200 ml H_2O and 5 ml H_3OBF_4) and examined by reflected-light optical microscopy (RLOM) using a Leica DM IRM optical microscope (Leica Microsystems, Germany).

The fracture surfaces were analyzed using scanning electron microscopy (SEM) using a Quanta^{TM} 650 FEG (Thermo Fischer Scientific Inc., USA). The measurements were carried out at 10 kV, with a spot size of 3.5, working distance of 10 mm, and vacuum level between 10^{-4} Pa and 10^{-3} Pa, combining secondary and backscattered electrons. Before analyzing the fracture surface the samples were gold sputtered using a Q150R ES coating system (Quorum Technologies Ltd., England) with a current of 60 mA for 30 s.

The surface roughness of as received aluminum 2024-T3, with sandblasting treatment, and with the presence of a polymeric coating, were characterized by laser scanning confocal microscopy (LSCM) using Keyence (VK-9700, Japan). The non-contact surface roughness measurements were performed with a 20x magnification lens and the data processed with VK Analyzer software (version 3.8.0.0). According to ISO 4287: 1997 [200], two parameters were selected to analyze the surface roughness of the specimens (average roughness: R_a, and peak-to-valley roughness: R_z).

4.3.5 Thermal analysis of the polymeric parts

The physicochemical variations induced by processing in the composite parts were evaluated using differential scanning calorimetry (DSC) and thermogravimetric analysis (TGA). Samples were extracted with the aid of diagonal cutting pliers and a scalpel from the full thickness of the composite $[PA6/CF\text{-}PA6]_{4S}$ part. The influences of the joining process on its properties were characterized by DSC and TGA.

4.3.5.1 Differential scanning calorimetry (DSC)

DSC analysis was carried out using the heat flux in a DSC 200 F3 Maia (Netzsch, Germany). Under an inert atmosphere of nitrogen, samples of 15 ± 0.1 mg were placed in an aluminum crucible. The samples were heated from 20 °C to 270 °C at a rate of 10 K/min and kept at that temperature for 5 min, they were then cooled to 20 °C again at the same cooling rate of 10 K/min [201,202]. The purpose of the first heating and cooling cycle is to eliminate any thermal history left behind by manufacturing of the base material filaments used in the AddJoining process. After keeping them at 20 °C for 5 min, the samples were heated to 270 °C and cooled again. In this way the samples were submitted to two heating and cooling cycles to evaluate the temperatures of melting point (T_m) and crystallization (T_{cc}) [201]. The exothermic and endothermic curves were recorded, and the degree of crystallinity (X_c) was calculated from the melting enthalpy values using the following equation:

$$X_c = \frac{\Delta H_m}{(1-w)\Delta H_m^o} \quad (4\text{-}1)$$

In the case of CF-PA6, w is the weight fraction of carbon fiber within the composite. With pure PA6, w is equal to zero. The melting enthalpy is ΔH_m while ΔH_m^o is the enthalpy value of 100% crystalline PA6, which is estimated to be 230 J/g [203,204].

4.3.5.2 Thermogravimetric analysis (TGA)

In order to identify the thermal stability of the polymer, the onset temperature of thermal decomposition was identified by TGA. This experiment was conducted using a TG 209 F3 Tarsus (Netzsch, Germany). The samples each weighing 12 ± 1 mg were placed in alumina crucibles at a heating rate of 20 K/min from 20 °C to 700 °C. The samples were heated under an inert atmosphere of nitrogen.

4.3.6 Phase identification

X-ray diffraction (XRD) was used for phase identification within the polymeric part. These patterns were collected using a Bruker D8 Advance (Bruker, Germany). This XRD equipment has a Cu-Kα radiation (1.5418 Å) source and SSD160 silicon compound strip detector. The position and intensity of diffraction peaks were recorded at an angular scanning speed of 0.02°/min and the diffraction range was from 10° to 35° [182,205]. The samples used for testing were prepared from selected stop-action stages during the printing process. The purpose of this was to identify any phase changes as the first three layers were 3D printed in each of the three joint conditions, and this is discussed in detail in Chapter 6.

4.3.7 Local mechanical properties

4.3.7.1 Microhardness

Local modifications were investigated by microhardness mapping using a Vickers hardness tester (Zwick/Roell, Germany). Measurements were made on the aluminum 2024-T3 at the cross-section of the joints and base materials as described in Section 4.3.4. Microhardness mapping followed the ASTM E384 standard, applying 2 N with an indentation time of 10 s [206]. Hardness mapping was made for half of the cross-section with a total of 250 indentation points. The distance between indents and rows was 300 µm.

4.3.7.2 Nanohardness

The size of the microhardness indenter was relatively large, which can lead to inaccurate values of hardness. For that reason, nanoindentation was also employed, mainly for the composite $[PA6/CF\text{-}PA6]_{4S}$ at the cross-section of the joints and base materials as described in Section 4.3.4. To avoid any interaction with the fibers in polymer matrix in the CF-PA6 layers, the nanoindentation was measured only in the PA6 layers for the composite $[PA6/CF\text{-}PA6]_{4S}$ part. Moreover, it was also carried out in the PA6 coating, i.e. the interface between metal and composite.

Nanoindentation was performed using a Nano indenter® XP (MTS Systems Corporation, USA) that uses the continuous stiffness measurement (CSM) technique. This method was employed to monitor changes to the mechanical properties while the indenter was driven into the specimen. The indenter reached a depth of 1000 nm into the surface with a displacement rate of 10 nm/s [207]. As results of the experiments, hardness and elastic modulus were obtained [208]. All nanoindentation tests were conducted with a Berkovich diamond indenter at room temperature.

Four regions of the joint were selected for the measurement (Figure 4-8). Rows of nine indentations separated by 50 µm between the nanoindents were made in each region [209,210]. The first region was in the aluminum 2024-T3, close to the PA6 coating. The second region corresponds to the interface of the metal with the composite $[PA6/CF\text{-}PA6]_{4S}$ directly on the PA6 coating (Figure 4-8), and the third region and fourth region were positioned in the first and last layers of PA6, respectively.

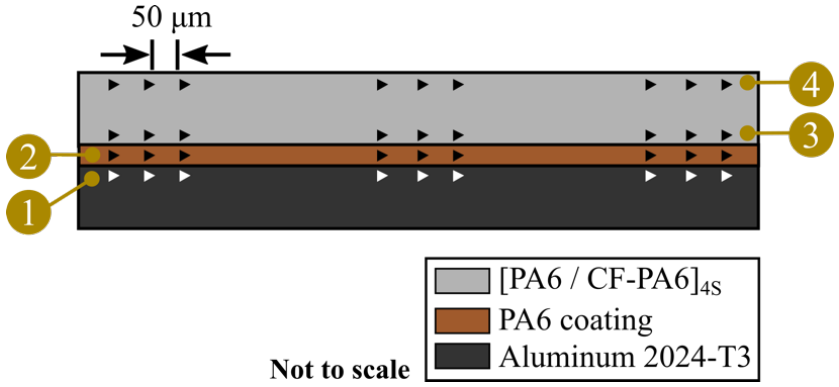

Figure 4-8 Schematic of the three nanoindentation regions (1) in the aluminum 2024-T3 part close to the PA6 coating, and (2) in the PA6 coating, (3) in the first and (4) last PA6 layers of the composite part.

4.3.8 Global mechanical properties

4.3.8.1 Single lap joint

Single lap joint geometry is widely used to evaluate the mechanical performance of joints. Figure 4-9 shows the sample geometry of the joints and the dimensions used in this work. Quasi-static (under room temperature and at different temperatures) and fatigue lap testing were performed to understand the global mechanical performance of these single lap joints.

From the applied DoE, (see Appendix A.4, Figure A.15(a) and Figure A.16(a)), the composite configuration was selected based on the on maximum mechanical performance response. The stacking sequence are $[PA6/CF\text{-}PA6/\ PA6/CF\text{-}PA6/\ PA6/CF\text{-}PA6/PA6/\ CF\text{-}PA6]_S$ and $[+45°/0°/\text{-}45°/0°/+45°/0°/\text{-}45°/0°]_S$ and corresponds to material and orientation, respectively. In this regard, PA6 layer are orientated at +45° in relation to the loading direction, but all the CF-PA6 layers are unidirectional with 0° orientation to the loading direction. According to the stacking sequence described here, the composite is designated by using the material stacking as "$[PA6/CF\text{-}PA6]_{4S}$" in this PhD thesis.

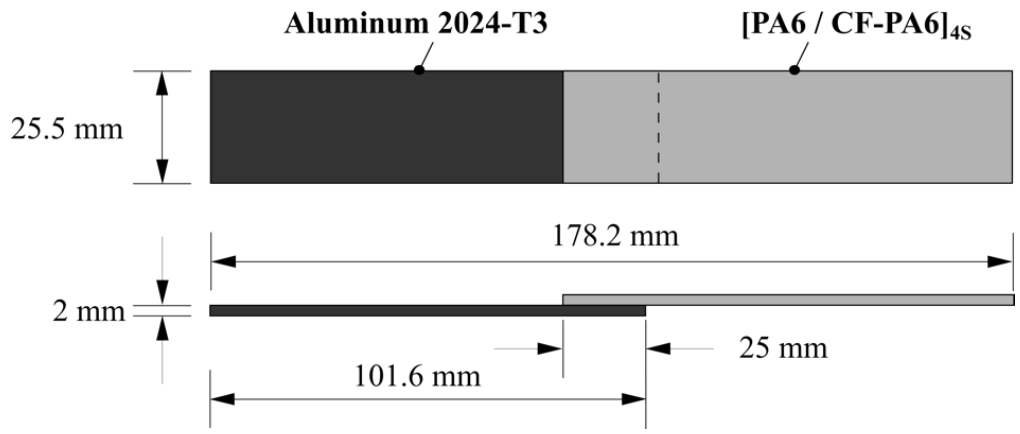

Figure 4-9 Schematic of the specimen geometry of the AddJoining hybrid joints.

Quasi-static lap shear testing

The strength of the single lap joints was evaluated under quasi-static loading to assess their mechanical performance. Based on ASTM D3163-01 [211], single lap shear tests were performed in a Zwick/Roell universal testing machine with a load capacity of 100 kN. The constant crosshead speed was 1.27 mm/min and the tests were performed at room temperature. The AddJoining hybrid joint configuration has a specimen geometry of 101.6 mm by 25.5 mm by 2 mm in length, width and thickness, respectively (Figure 4-9). The overlap area of the joints is 25 mm by 25.5 mm. For mechanical testing, the sample was clamped with a 25 mm grip distance, leaving a free length of 128.2 mm (Figure 4-10). Three replicates were used to obtain the average ultimate lap shear force (ULSF) of the joints. ULSF is the maximum force that a joint can bear before final failure.

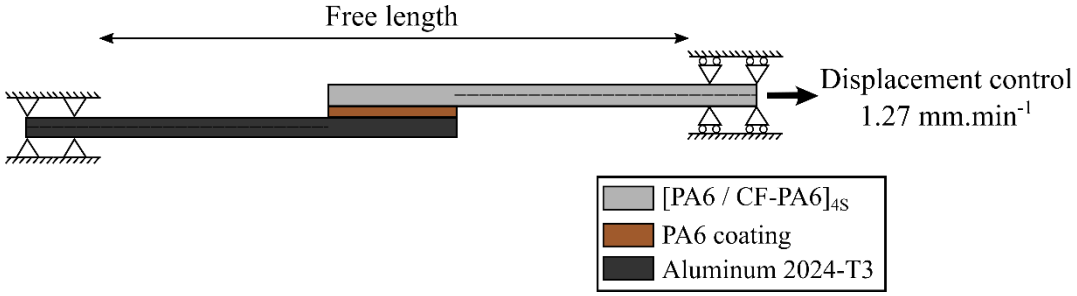

Figure 4-10 Schematic of the boundary conditions for single lap shear testing.

To fully understand the mechanical performance of AddJoining samples, a digital image correlation (DIC) system ARAMIS 4M (GOM, Germany) was used to assess the strain fields of single lap joints. The back-face strain of the aluminum 2024-T3 and the composite [PA6/CF-PA6]$_{4S}$ were measured under loading in a Zwick/Roell universal tensile testing machine with a load capacity of 100 kN. A 4M camera with a focal length of 50 mm was positioned and trigger signals were sent for an acquisition rate of two pictures per second. ARAMIS software was used to analysis the data. In addition to strain evolution, loading and unloading experiments were performed with three loading levels (10 %, 50 %, and 90 % of ULSF). At each load level the sample was submitted to non-destructive testing to quantify the damage (see Section 4.3.9.1). Each sample was also prepared for

damage characterization analysis by RLOM and LSCM. Sample preparation follows the description in Section 4.3.4.

As well as testing at room temperature, the effects of different temperatures levels were evaluated. The quasi-static test parameters were kept the same as described above. The single lap joint was clamped inside a chamber using a Zwick/Roell universal tensile testing machine with a 50 kN load capacity. This was coupled with a resistance heater and linked to a nitrogen tank to provide heating and cooling environments, respectively. Samples were tested at three temperature levels, -55 °C, 70 °C and 120 °C. Prior to mechanical testing, the target temperature was set and the sample heated or cooled at an incremental rate of 5 °C/min. The test was only started when the target temperature stabilized and was kept at this for a holding time of 5 min to allow uniform temperature distribution inside the sample. During mechanical testing the target temperature deviated ±8 °C.

Fatigue testing

To contribute to an understanding of how joints using the AddJoining technique would mature in service, an S-N curve was employed to characterize fatigue resistance of the single lap joints, obtained from the results of a number of fatigue tests. The fatigue testing was performed in accordance with the ASTM E466 standard [212] with the same geometry of quasi-static single lap joints (Figure 4-9). The tests were performed at five different load levels until final failure with three replicates at each load level. A servo-hydraulic fatigue testing machine was used with a load capacity of 63 kN. Prior to starting these experiments, the fatigue test parameters were characterized by the mean force (F_m) that was calculated from the following equation:

$$F_m = \frac{F_{max} + F_{min}}{2} \tag{4-2}$$

Where maximum force (F_{max}), and minimum force (F_{min}) are obtained from the stress ratio. Before starting the cyclic loading phase, a monotonic phase was set to reach the mean force within 15 s (Figure 4-11). Furthermore, the cyclic loading varied from maximum to minimum force with a load ratio of 0.1. This is often used for aircraft component testing, and corresponds to a tension-tension cycle with a sinusoidal loading form and frequency of 5 Hz [213].

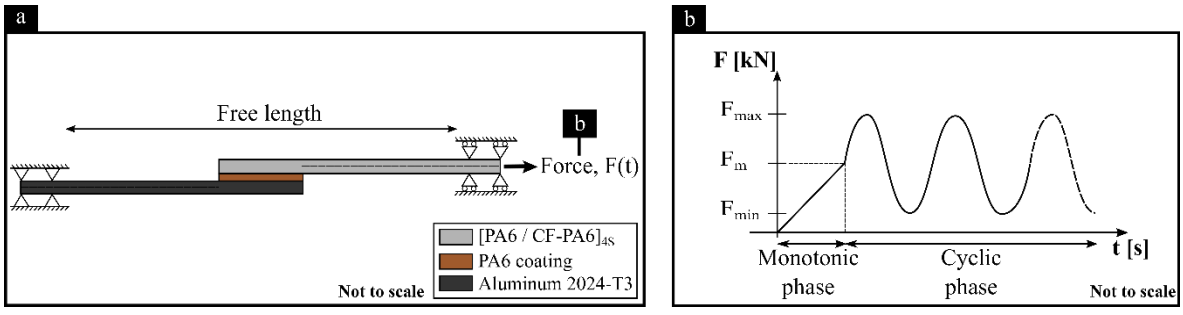

Figure 4-11 Schematic of the characteristic levels of load cycles for single lap fatigue testing.

The fatigue data were statistically analyzed according to the ASTM E739 standard [214]. To measure failure probability a deterministic two-parameter Weibull distribution approach was used, according to the DIN 50100 standard [215]. Three experiments at low load level were stopped after 10^6 cycles without failure, known as run-outs [213]. These joints were tested under quasi-static conditions, as explained previously, to measure their residual strength.

4.3.9 Damage assessment method

The types of damage in the composite $[PA6/CF\text{-}PA6]_{4S}$ and their influence on mechanical performance is quite complex. As is the case with other composites, $[PA6/CF\text{-}PA6]_{4S}$ does not accumulate damage by crack growth of a single defect, rather by the initiation of several small matrix defects. These can eventually lead to the development of delamination, whether due fatigue loading or quasi-static loading. As investigation and understanding damage development is highly dependent on the assessment method, two different methods were used to quantify the defects and characterize their influence on the mechanical performance of the single lap joints.

4.3.9.1 Non-destructive testing method

The damage in the single lap joints subjected to mechanical testing was characterized in this work. An ultrasonic testing technique was employed using a USPC 3040 DAC C-scan system (Dr. Hilger Ingenieurbüro, Germany) with a resolution of 20 MHz. A schematic of the C-Scan set-up is shown in Figure 4-12(a). The single lap joint was placed on supports inside a water tank. This is a standard procedure to allow for uniform coupling of the ultrasonic transmission between the transducers and the sample [216]. The overlap is the critical area of a single lap joint. Therefore, the region between the aluminum 2024-T3 part and composite $[PA6/CF\text{-}PA6]_{4S}$ part was chosen for damage monitoring (Figure 4-12(b)).

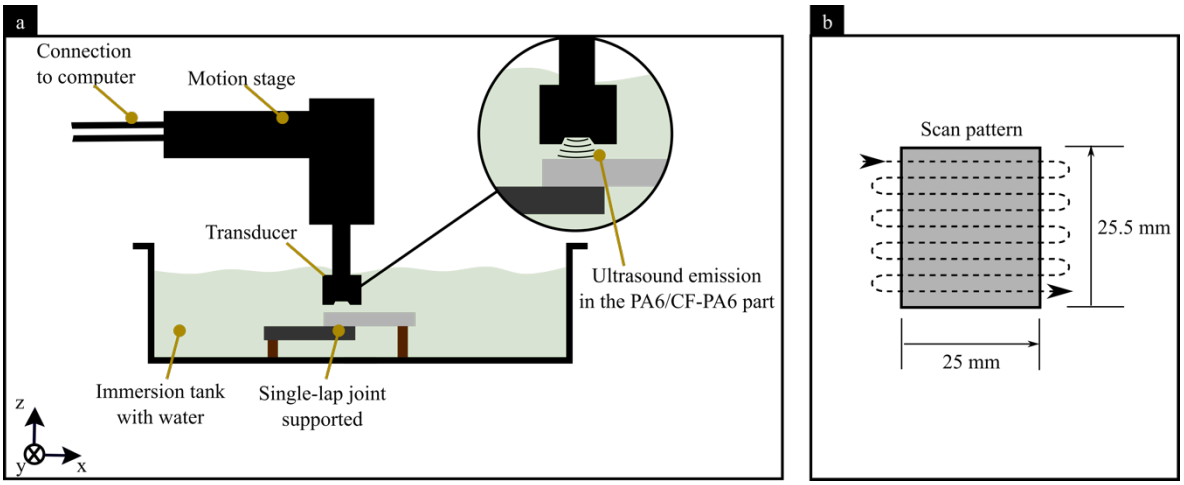

Figure 4-12 Schematic of the C-Scan measurements (a) setup, and (b) scan pattern in the single lap joint overlap area.

The aluminum 2024-T3 was placed as backing element, i.e. signal from this region were not measured. The defect depth was considered as 0.0 mm as the interface of aluminum 2024-T3 and PA6 coating / $[PA6/CF\text{-}PA6]_{4S}$ (Figure 4-13(a)). The maximum defect depth is the composite $[PA6/CF\text{-}PA6]_{4S}$ final thickness of 2 mm. An example of the typical defect's depth measurement on the composite $[PA6/CF\text{-}PA6]_{4S}$ is shown in Figure 4-13(b) with the depth scale. Furthermore, as PA6 is sensitive to moisture, the sample was dried at 80 °C for 22 hours before further testing in accordance with ASTM D570 [197].

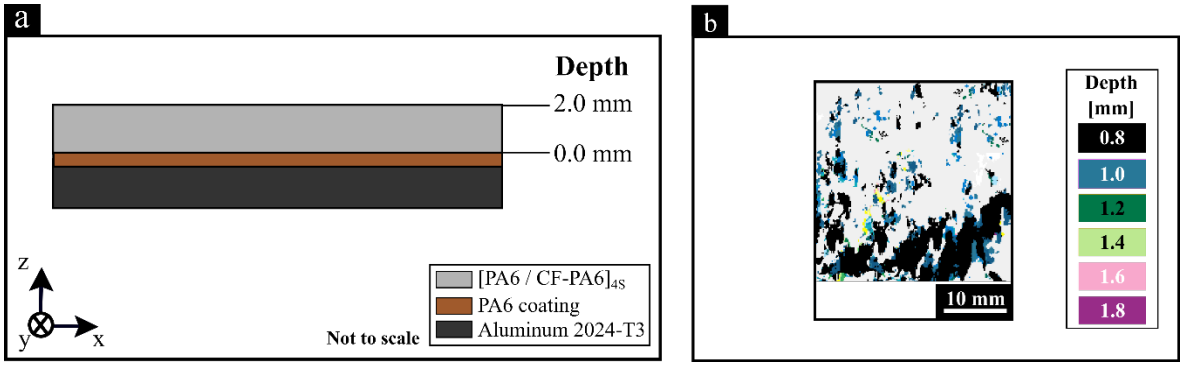

Figure 4-13 (a) Schematic to highlight the region of the C-Scan measurements and (b) an example of a C-Scan measured sample showing the defect depth.

4.3.9.2 Stiffness degradation testing method

During fatigue cycling, the degradation of stiffness can be used as an analogue to monitor damage development. The stiffness degradation tests were carried out using a servo-hydraulic testing machine from Instron/Schenk with a load capacity of 100 kN. A load ratio of 0.1 and sinusoidal loading was applied with a test frequency of 5 Hz until failure.

The stiffness reduction during fatigue loading was monitored at four loading levels (70 %, 60 %, 50 % and 35 % of ULSF). The secant elastic modulus was used, due to the non-linear behavior of the stress-strain curve under fatigue loading [217]. Three replicates were tested to obtain the average secant elastic modulus of the joints.

A stop-action series was carried out for loading level 47 % ULSF (at 10^5 cycles), to quantify the damage evolution at three levels of fatigue life (N_f) 10 %, 60 % and 80 %. The samples were scanned using the C-Scan technique (as described in Section 4.3.9.1) and a delamination area was evaluated in each sample.

Chapter 5. Introduction to AddJoining

A new technique for producing layered hybrid structures called AddJoining is introduced in this chapter. The concept was developed during this PhD work and patent applied for (see Appendix A.1). This chapter is divided into four sections. The first section is dedicated to introducing the principles of the process. The second section briefly discusses the main process parameters. The third section shows the possible process variants that have been identified and explored for the current technique. The last section highlights the advantages, limitations and potential applications of using the method that is introduced here.

5.1 Principles of the process

This section will introduce the current principles and steps of AddJoining based on the common practice and procedures adopted in this work. At the beginning of the process, preprocessing is usually necessary before AddJoining parts. It is important to clean and prepare the metal surface beforehand, to ensure there is a good interlocking between the metal and polymer. Although not implemented in this work, depending upon project requirements or type of composite polymeric matrix 3D-printed, an additional surface pretreatment may be applied to the metal to improving adhesion forces, such as chemical conversion, anodizing and application of primers [218].

For the AddJoining method, Mark Two was used to produce the 3D printed composite parts, layer by layer on the surface of the aluminum alloy substrate as introduced in Section 4.3.1. In preparation for AddJoining the CAD software's 3D data is sliced into layers. The first phase starts by positioning the metal substrate in the slot located on the printing bed surface (Figure 5-1(a)) as was presented in Section 4.2.2. To promote adhesion of the polymer to the metal, an initial coating layer is 3D printed on the metal surface. The polymeric layer referred to here as the polymer coating is directly 3D printed. Figure 5-2(a) shows the polymer coating 3D printed on the aluminum 2024-T3 surface with dimensions 26 mm by 25 mm by 0.2 mm in length, width and thickness, to produce an AddJoining hybrid joint. While the polymer coating is 3D printed, a control temperature is set on the external heating system. The control temperature can vary from 20 °C to 270 °C. After the polymer coating is finished a consolidation time to form the coating of ten minutes was selected. In fact, this consolidation time is an additional parameter of the AddJoining process. However, for this PhD work it is important to note that this consolidation phase was intentionally overestimated, to reduce the number of process variables and thereby simplify experimental investigation, in this case five minutes was overestimated to allow temperature stabilization of the metal substrate. On the heating control system, a new temperature is now selected and the metal substrate, already coated with a thin layer of polymer, is repositioned in the slot located on the printing bed. The new temperature can range from 20 °C to 150 °C.

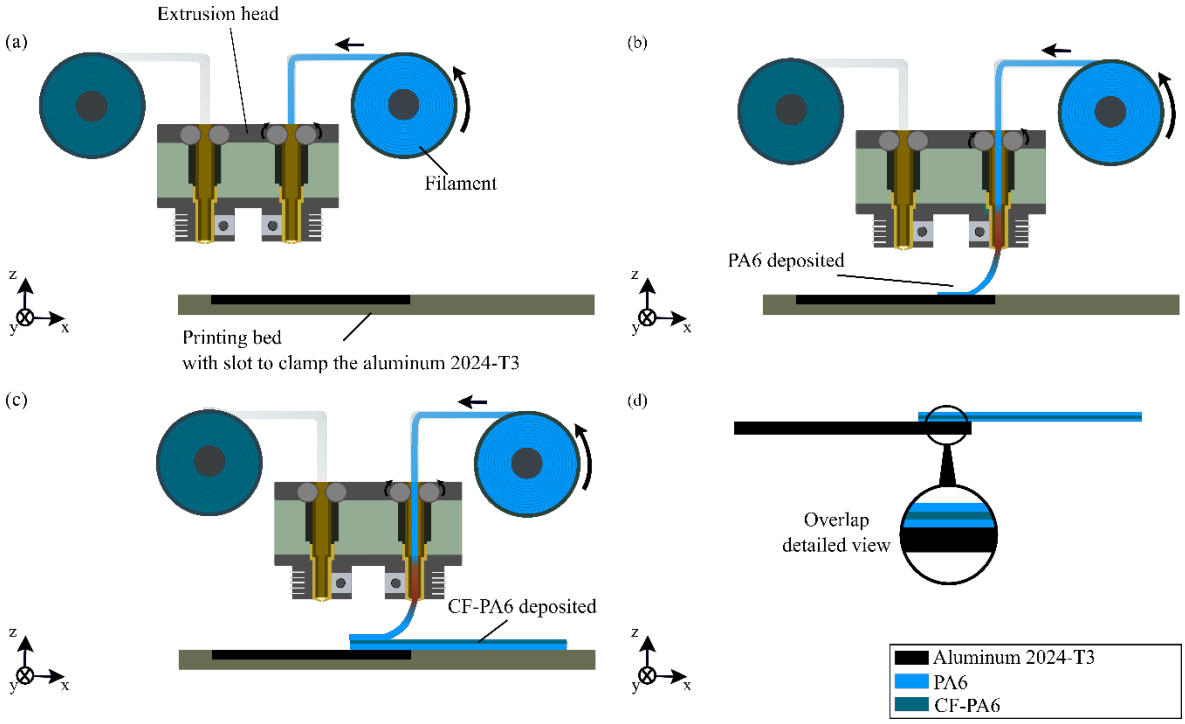

Figure 5-1 Schematic of the AddJoining process for layered metal–polymer composite hybrid structures: (a) initial setup, (b) deposition of the first polymer layer on the metal substrate, (c) deposition of the subsequent polymer layers, (d) final layered metal-polymer hybrid structure. Reproduced from [17].

3D printing of the composite part now starts. The unreinforced polymeric filament uncoils slowly and is guided to the extrusion head, where a resistive heater is located close to the nozzle. The filament is heated there to 270 °C, above the polymer's melting temperature, which decreases the material's viscosity. At this point, the softened or molten material flows smoothly through the extrusion nozzle, and the polymer is deposited to form a full layer on top of the metal substrate (Figure 5-1(b)). When each layer has completed the build platform is lowered by the thickness of one layer. The platform only moves in the Z-direction, while the extrusion head moves in a horizontal plane (X-Y). Whenever a layer of reinforced thermoplastic filament is required in the sample, the alternative filament uncoils and is guided to the second extrusion head, in a similar matter to that described for the unreinforced polymeric filament. However, if the reinforcement has continuous fibers, as soon as enough reinforced thermoplastic material is extruded to complete the current layer a cutter (inside the extruder head) is automatically activated inside the extruder head, which cuts through the fibers (Figure 5-2(b)). This process is repeated, adding polymer layers on top of the previously consolidated polymer successively, until the final thickness of the polymeric part is achieved (Figure 5-1(c)). Finally, the AddJoining hybrid joint is removed from the build platform (Figure 5-1(d)). Additional steps after 3D printing e.g., thermomechanical treatment, such as hot isostatic pressing, may be applied to reduce or eliminate any intrinsic voids in the layered composite component. Note that no post-processing was performed in this work.

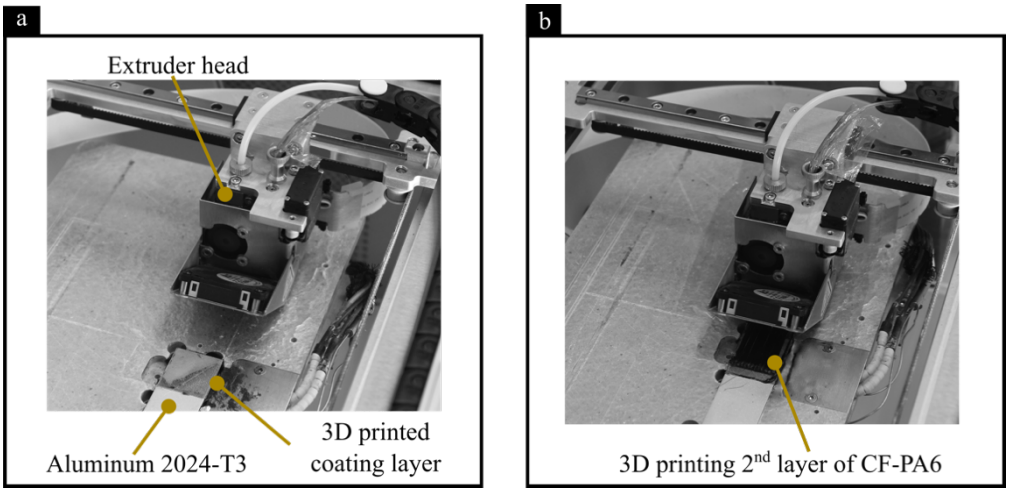

Figure 5-2 AddJoining process for layered metal-polymer hybrid joints: (a) 3D printing the coating layer, and (b) 3D printing the CF-PA6 layer.

5.2 Process parameters

The AddJoining technique has a wide range of controllable process parameters, depending on the 3D printer selected. The author and collaborators have reported the importance of five controllable parameters that influence the mechanical performance of hybrid joints with two well-established material combinations of aluminum 2024-T3 and acrylonitrile butadiene styrene (ABS) [186]. Four of these controllable parameters are printing temperature (PT), road thickness (RT), deposition speed (DS), and number of contours (NC). Falck *et al.* [186] also identified a fifth controllable parameter named after the polymer as ABS coating concentration (AC). The AC in that case represented a homogeneous coating layer of the respective unreinforced filament material, which is used to promote better adhesion between the metal and subsequent printed polymer layers. The five controllable process parameters are summarized as follows:

a) Printing temperature (PT) is the working temperature of the extruder head (Figure 5-3(a)), which must be above the glass transition temperature or melting temperature, respectively, for amorphous and semi-crystalline thermoplastics.

b) Road thickness (RT) is the thickness of the consolidated layer, the vertical distance between each layer (Figure 5-3(b)).

c) Deposition speed (DS) means the speed of the extruder head while printing (Figure 5-3(c))

d) ABS concentration (AC) is the polymer concentration applied as a coating on the metal surface.

e) Number of contours (NC) refers to the enclosed loops of road deposition in the filled perimeter region (Figure 5-3(d)).

These five controllable parameters were in fact not applicable with the desktop 3D printer selected for this work, as introduced in section 4.2.1. The chosen 3D printer had these parameters fixed to a printing temperature of 270 °C, a road thickness of 0.125 mm, and an average speed of 40 mm/s for the deposition. No polymeric concentration was applied for the coating in this PhD work, as the process variant selected is based on a heating control method, as is further discussed in Section 5.3.

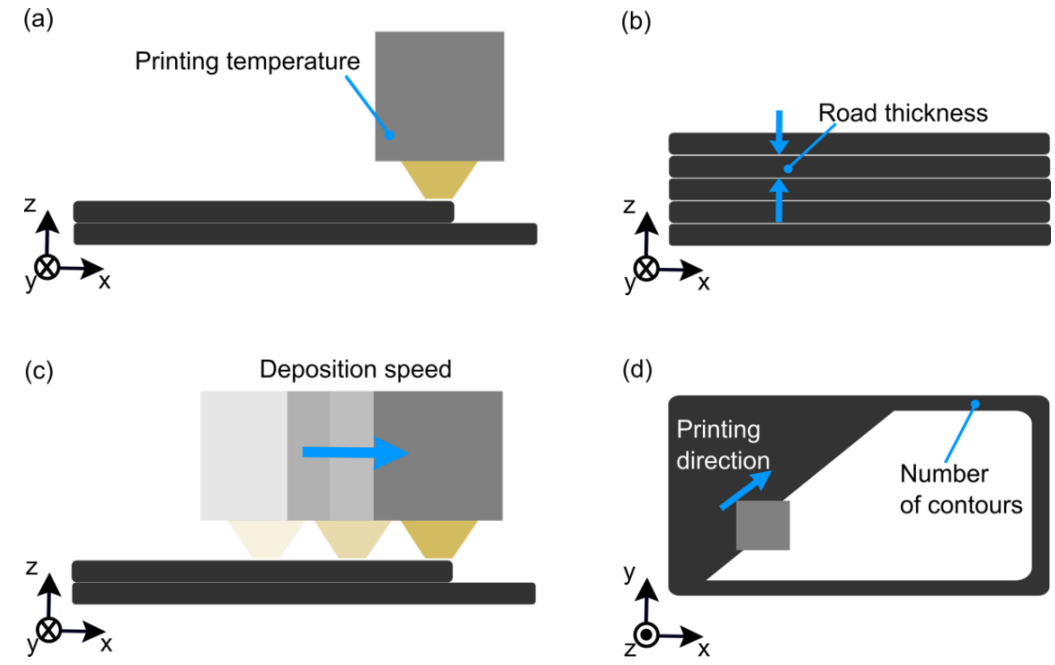

Figure 5-3 Representation of the AddJoining process parameters based on standard FFF.

For the selected material used in this PhD work, a desktop 3D printer was used to define the core set of composite structural parameters: (1) the CF-PA6 distribution, (2) the number of CF-PA6 layers within the composite part, and (3) the CF-PA6 orientation. The first structural parameter, CF-PA6 distribution, is defined as the symmetry of layers around the mid-plane, where the three feasible configurations identified are alternate, mid-plane bottom and mid-plane top (Figure 5-4). The alternate configuration means that the layers of PA6 and CF-PA6 in the layup are intercalated one upon another. The mid-plane bottom is where all of the CF-PA6 layers are located below the mid-plane in the composite cross-section. The mid-plane top is the reverse of the mid-plane bottom. For all CF-PA6 distributions, a final layer of PA6 is printed on the top composite surface for protection of the CF-PA6 layers.

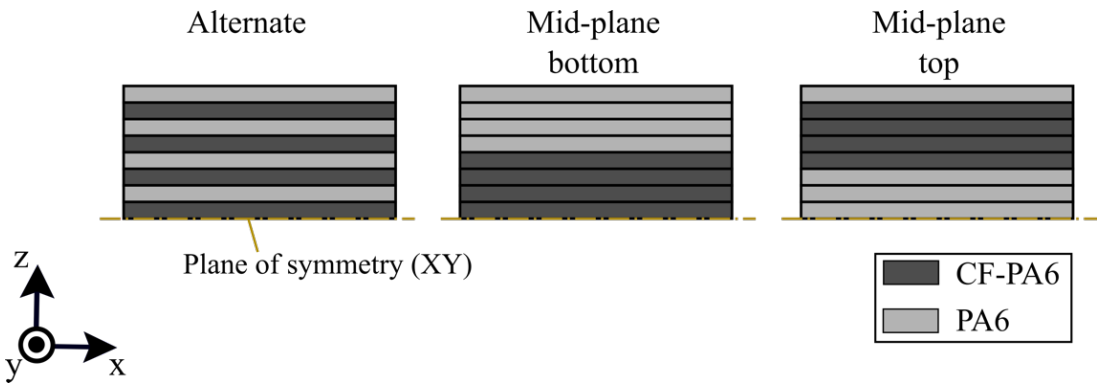

Figure 5-4 Schematic of the three possible CF-PA6 distributions identified in this PhD work.

The second structural parameter, the number of CF-PA6 layers, represents the amount of reinforced thermoplastic in the composite (Figure 5-5). The number of CF-PA6 layers is constrained by the total thickness of the composite part, as previously described in Section 4.3.8. The minimum and

maximum numbers of CF-PA6 layers were determined for the three CF-PA6 distributions identified. These structural parameters are therefore dependent on each CF-PA6 distribution. Thus, for a composite that is 2 mm thick, the minimum and maximum CF-PA6 layers are four and eight layers, respectively.

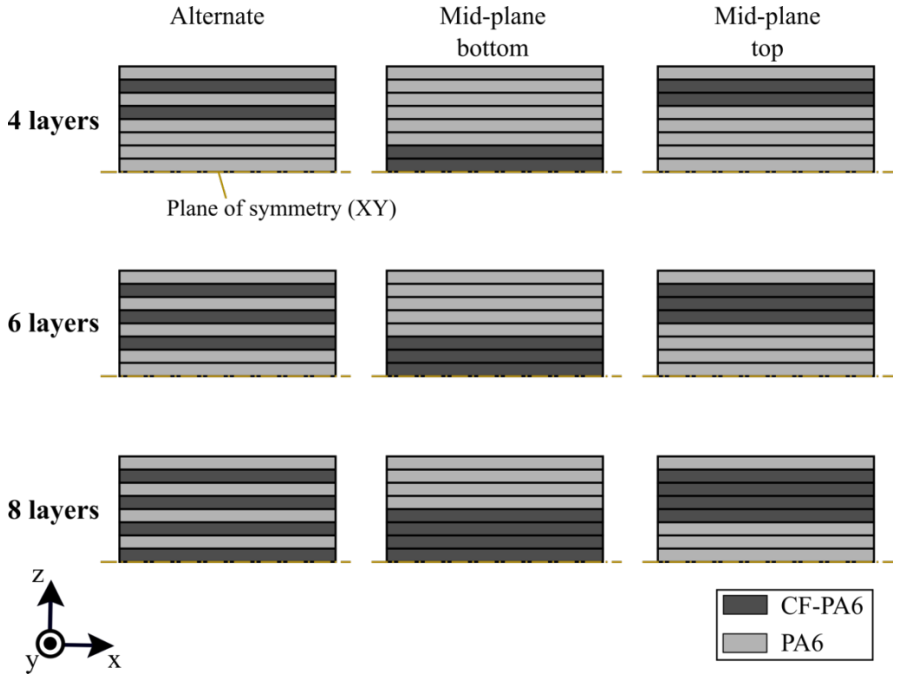

Figure 5-5 Schematic of the three possible numbers of CF-PA6 layers for each CF-PA6 distribution identified in this PhD work.

The third structural parameter, CF-PA6 orientation, is designed based on the carbon fibers orientated on the long Y-axis and here shown as 0°, i.e. in the loading direction (Figure 5-6). The four orientations chosen represent 45° steps in a clockwise direction from -45° to 90°. The anisotropic feature of unidirectional fiber composites means fiber orientation plays a significant role in their mechanical performance.

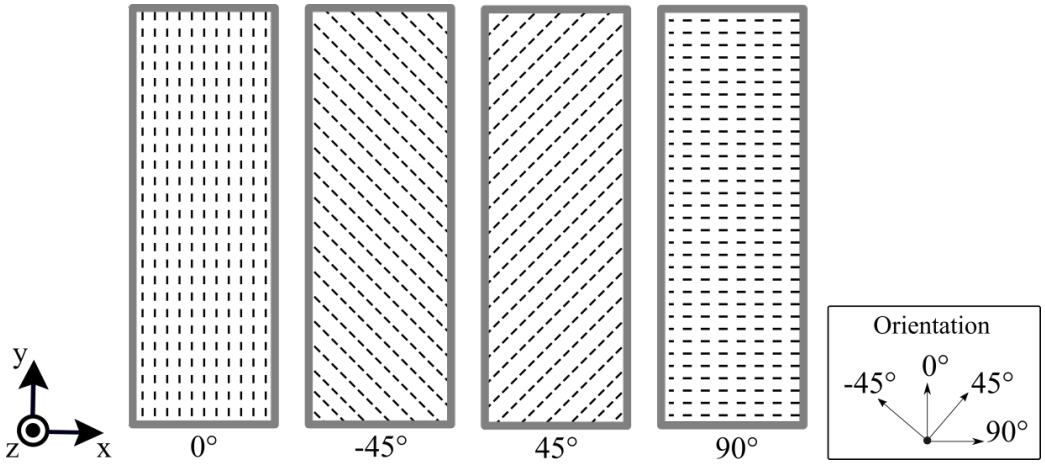

Figure 5-6 Schematic of the four CF-PA6 orientations used in this PhD work.

These combinations of structural parameters and the process variant of the heating control gave an opportunity to thoroughly investigate the mechanical behavior of AddJoining hybrid joints. In fact with the heating controls it was possible to identify two process parameters: Coating Temperature (CT) and Heating Bed Temperature (HBT). CT is defined as the temperature that allows the polymer to form the initial coating layer on the metal surface. HBT is the main function that controls the temperature of the bed during the whole printing process of the hybrid joints and the hybrid layered samples. For the material selected in this work, CT can range from 200 °C to 270 °C and HBT from 20 °C to 150 °C. HBT can affect the crystalline phase of the coating layer and the subsequent layers deposited on the coating.

The results obtained on the influences of the controlled structural parameters on the mechanical performance of the hybrid addjoints is discussed in Appendix A.4 as well as the statistical modelling of combinations of structural parameters and the process variant of the heating control.

5.3 Process variants

The desktop 3D printer chosen is commonly used to produce continuous fibers. Continuous fibers improve the stiffness and strength of a composite better than discontinuous fibers. However, the properties of the layered hybrid structures produced by AddJoining are also influenced by the process variants. There were three process variants investigated during the feasibility study of the AddJoining process by using the material combination aluminum 2024-T3 with acrylonitrile butadiene styrene (ABS) to test the adhesion of polymer on the metal surface in a single lap joint configuration.

The first variant was investigated by initially applying a commercially available adhesive and a custom tool was designed to spread the adhesive on the metal. The polymeric part was then 3D printed on the overlap area of the joint, as described in Section 4.3.2. Following the supplier's procedure, the adhesive joints were cured in a convection oven. The second variant was based on using a heating control system, as described in Section 4.2.2. The third variant was to form a thin polymeric coating, similar to an adapted dip-coating method, and for which a custom tool was designed to ensure a homogeneous coating with a nominal thickness of 100 µm. The sample was subsequently dried in a horizontal position for five minutes at room temperature. The author and collaborators have reported the overall mechanical performance of each variant on [187].

A fourth variant was also proposed, of directing a laser beam with a self-adjusting intensity control to reheat the polymer as it leaves the extruder head nozzle. This variant promised to provide a control of the internal bonding of the 3D printed layers and thereby diminish the presence of internal voids [219]. However, due to the early development stages of this technology, the fourth variant was not attempted, as it would demand extensive investigation and project development of laser and feedback instruments, such as optical and temperature sensors interconnected with the desktop 3D printer.

The use of a heating control variant was the preferred strategy as it opened up the possibility for development of AddJoining technique. This process variant was selected for further investigation and an explanation of the process. Such a variant proved the most promising in terms of mechanical performance and reproducibility of the first three variants mentioned and tested. The usage of a heating control makes it possible to elevate the temperature above the glass transition temperature or crystallization temperature. The objective was to influence bond formation between the 3D printed layers caused by the autohesion of the polymers [110,220]. Autohesion leads to the formation of

strong bonds across the interfaces between the polymers by entanglement of polymer chains across the interface. For the two process parameters identified, Coating Temperature (CT) and Heating Bed Temperature (HBT), their influence on bonding formation is discussed in Chapter 6 and Appendix A.4.

5.4 Current advantages, limitations and potential applications

Modern industrial requirements demand more cost-effective processes. The traditional approaches for producing hybrid layered metal-composites involve manual layup and tape laying [30,220]. However, such methods are time-consuming, generate high levels of waste material and are labor intensive. Those are the main driving force behind developing a more effective way to produce layered metal-polymer or metal-composite hybrid structures for lightweight structural applications.

AddJoining is a technique inspired mainly by these industrial requirements, it provides much manufacturing flexibility to produce parts with complex shapes, such as honeycomb cores. The AddJoining process is clean and the manufacturing process is integrated, without the need for a complicated assembly infrastructure. No cost studies have been performed, but the savings from one AddJoining final assembly could decrease the total cost of a structural part compared to conventional composite lamination technologies. Another advantage derives from the fact that good recyclability and reduction of waste can be achieved by the use of thermoplastic materials (the latter a non-exclusive advantage to the process). Furthermore, AddJoining has the potential to be easily automated and improves the reliability of a process by reducing the uncertainty associated with manual operations.

In terms of the limitations of AddJoining, the presence of voids in a 3D printed composite or polymeric part, which are presently unavoidable with the state-of-the-art of this technique. Voids may act as local stress concentrators in 3D printed FFF parts, decreasing the global strength of an additively manufactured component in comparison to injection molded parts [93,95,109]. However, additional post-printing steps, such as thermomechanical treatment, may be applied and are expected to eliminate the intrinsic voids in the layered component produced by the AddJoining technique.

In designs for aircraft and automotive, high performance lightweight structures can be applied. Therefore, the AddJoining concept promises the satisfaction of a wide range of potential applications for hybrid joints in this sector. However, it is imperative that the new layered hybrid structures present improved mechanical strength and damage tolerance. This can be achieved by combining two or more materials that have significantly different physical and chemical properties to produce a material with the specific advantages of characteristics from both components. This has the potential of building strong materials that are lighter and less expensive compared to traditional manufacturing methods. The inclusion of reinforced thermoplastic layers allows for redistribution of the load, thus avoiding a catastrophic failure in critical applications.

The flexibility to produce complex geometric parts, which are net-shaped with mechanical functionalities, is certainly achievable with the AddJoining technique. One potential example of these is a layered hybrid panel with internal honeycomb cores (Figure 5-7(a)). Among other possible applications, this is expected to be applied by the transportation industry for B pillars in automotive structures and for skin stringers in aircraft structures (Figure 5-7(b)). Other industrial applications are also envisaged, such as shipbuilding, infrastructure and medical (e.g. prosthetics). The transportation

sector is often fighting for every gram to reduce the weight of vehicles and aircraft. To achieve this the tendency is to replace traditional materials with lightweight materials. Since the advance of additive manufacturing, topology optimization has become an asset in reducing the weight of 3D printed parts and at the same time ensuring the desirable mechanical performance. As highlight of initial results, when considering potential applications using AddJoining principles, it is important to understand the methodology and limitations of the topology method. It demands a robust concept of material selection and considerations for the manufacturing of structures. An exploratory study presented to the engineering modelling community [221] was undertaken to assess the potential of AddJoining as promising technology for producing topology optimized hybrid structures. The net-shape demonstrator part was 3D printed with a 40 % of the volume fraction (Figure 5-7(d)), which can be used in future topology and strength-to-weight optimized aircraft under floor beams (Figure 5-7(c)). The topology is expected to carry a uniformly distributed load of 100 kg under quasi-static loading conditions. For future investigation, the convergence of the topology design has open questions regarding design shape according to mesh refinement and implementations of different load cases.

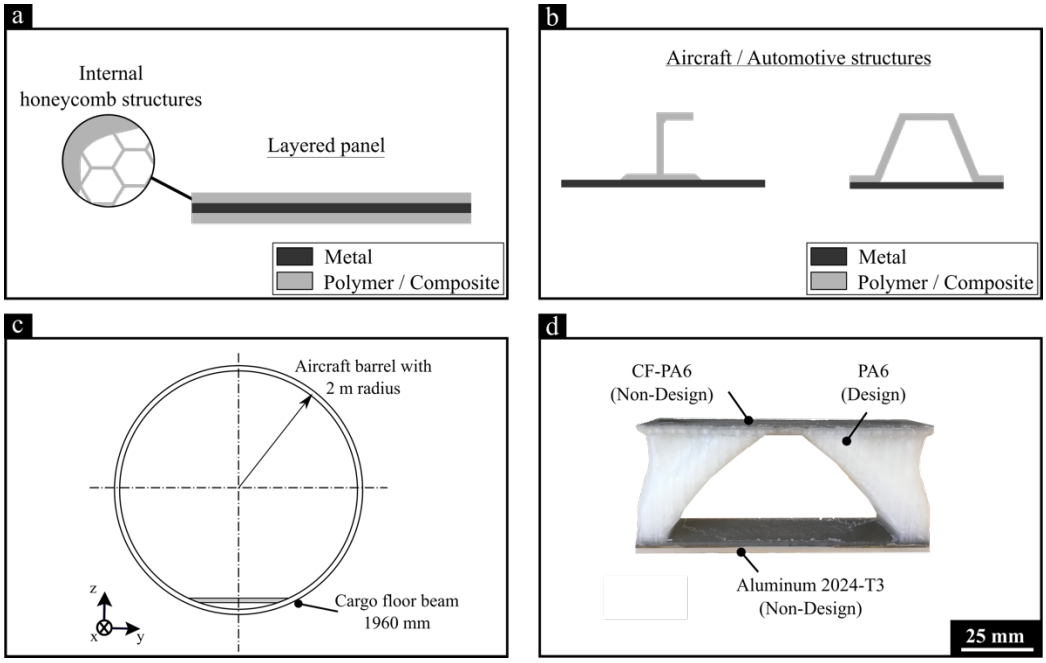

Figure 5-7 Examples of potential AddJoining applications the transportation industry for hybrid structures: (a) layered panel with internal honeycomb cores, (b) skin-stringer or B pillars for aicraft and automotive structures, respectively. Also, (c) schematic view of the fuselage barrel of a mid-size aircraft with (d) topology optimized 3D printed cargo floor beam (scale 1:20). Reproduced from [186].

Chapter 6. Development of AddJoining

As already mentioned, the process was inspired by a fusion of additive manufacturing (AM) and joining technology principles. Thus far in this PhD work, the author and collaborators have introduced the technique, and briefly discussed the main bonding mechanisms that occur during the process [17]. The current PhD thesis is dedicated to understanding the AddJoining technique variant using heating control. This process strategy was chosen, because it offered the possibility for further development of the technique. Another factor in the selection of this process variant was associated with its good reproducibility and promising hybrid parts' mechanical performance, as is discussed in detail in Appendix A.4. Briefly, the optimized process parameters were assessed by a full factorial design of experiments (DoE) and analysis of variance (ANOVA). This chapter further evaluates an understanding of the process by means of addressing bonding mechanisms, microstructural changes, thermal properties, and phase transformation, devoted to understanding the changes induced by the process in the selected material combination (aluminum 2024-T3 and composite $[PA6/CF\text{-}PA6]_{4S}$). Three combinations of process parameters were selected for the investigation by varying coating temperature (CT) and heating bed temperature (HBT). In this regard, from the DoE, the optimized CT at 229 °C and HBT at 77 °C were fixed and the minimum and maximum values of CT selected to help evaluating the results, at 20 °C and 150 °C, respectively (Appendix A.4, see Table A.5 and Figure A.21). Also, the final sections of the chapter are devoted to optimizing the mechanical performance of the AddJoining hybrid joints by adjusting the parameters used.

6.1 Process understanding

6.1.1 Bonding mechanisms and microstructure

6.1.1.1 Bonding formation during the AddJoining process

The relation between surface roughness and bonding formation is not straightforward for polymer-polymer bonding. The effectiveness of bonding is associated with intimate contact between the parts or layers. Zosel [222] reported that an intimate contact is not achievable on a rough surface with low contact forces. With the current state of the technology, the AddJoining process does not apply contact force during the manufacturing process. Therefore, intimate contact between the polymeric printed layers is promoted solely by the strong adhesion that is induced by temperature. Several authors have reported the influence of temperature on thermally-bonded polymer samples, based on the autohesion of polymers [110,220,223,224]. Such a phenomenon leads to the formation of strong bonding across polymer-polymer interfaces by entanglement of polymer chains across the interface.

A stepwise concept was adopted to help understand the bonding formation and surface roughness influencing at the interface between subsequently printed layers during the manufacturing of the AddJoining hybrid joints. The approach included four steps to identify possible changes in the joints, according to the selected process parameters. After each step, the sample remained fixed in the printer's heating bed slot for the remaining time at a constant HBT to simulate the full AddJoining process. It is important to point out that added effects of subsequent 3D printed layers were not possible to evaluate with the stepwise approach applied in this PhD work. However, it can provide

essential information about the bonding formation and possible phase changes during the AddJoining process. In this respect, at each step a surface image was analyzed by LSCM to identify irregularities and surface roughness. XRD was also applied to identify phase changes on the polymer (Section 6.1.4).

First of all, the stacking sequence is $[+45°/0°/-45°/0°/+45°/0°/-45°/0°]_S$, where the lowest layer on the PA6 coating is a PA6 layer at +45° orientation in relation to the loading direction, but all the CF-PA6 layers are unidirectional with 0° orientation to the loading direction. During application of the 3D printed PA6 coating, the optimized CT was applied to form the coating on the metal surface. After the consolidation phase, the HBT was set to one of the three temperatures, 20 °C, 77 °C and 150 °C and kept at this for the remaining 3D printing time (56 min for each set). Figure 6-1 summarizes the four steps adopted in the stepwise investigation of bonding mechanisms.

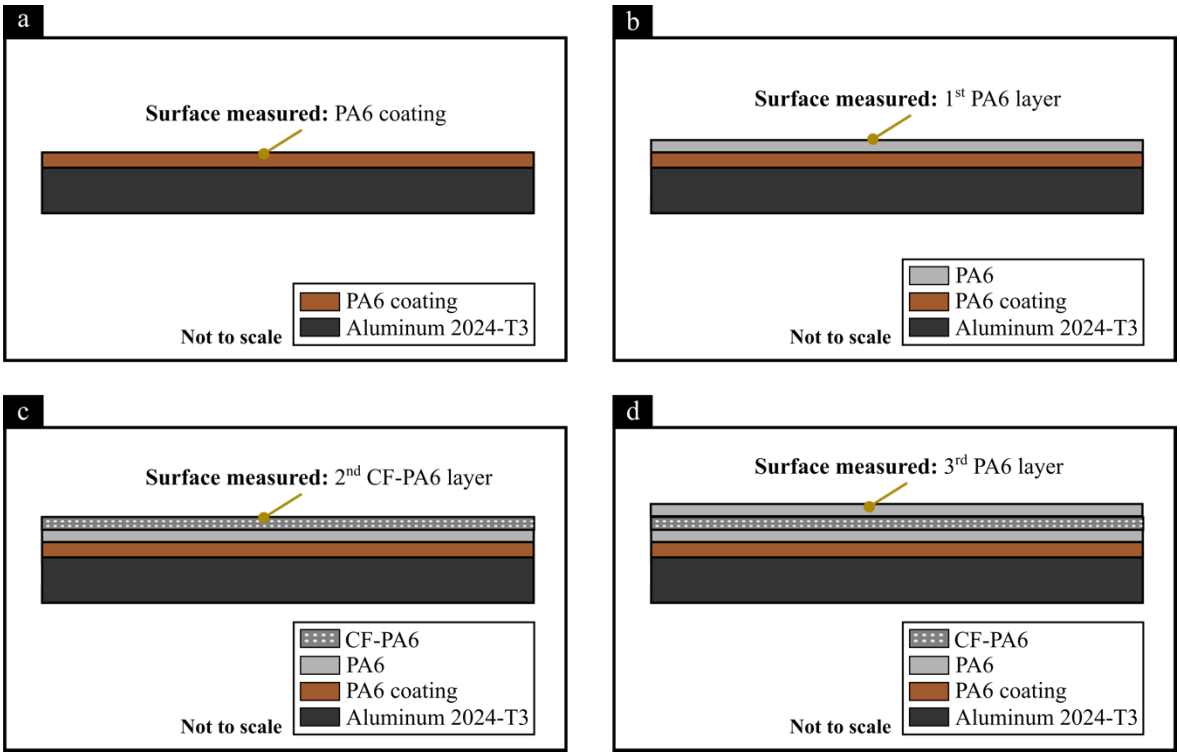

Figure 6-1 Four steps adopted in the stepwise investigation of bonding mechanisms: (a) PA6 coating, (b) 1st PA6 layer, (c) 2nd CF-PA6 layer, and (d) 3rd PA6 layer. Note that each stop-action layer was maintained at constant HBT for a period to resemble the length of the full AddJoining process cycle to print a 2mm composite part.

The first step is referred to here as *PA6 coating* (Figure 6-1(a)). The first layer of PA6 that is 3D printed as a coating layer on the metal substrate and kept for 56 min. The second step is known as *1st PA6 layer,* following the stepwise approach (Figure 6-1(b)). For this step, the samples remained fixed in the slot at each HBT for another 52 min. After 3D printing of the CF-PA6 layer as the second layer, referred to as *2nd CF-PA6 layer*, the sample remained for a further 49 min on the heating bed (Figure 6-1(c)). The last step produced the third layer, known as *3rd PA6 layer*, where a PA6 layer is 3D printed onto the previous CF-PA6 layer, each sample remained for a further 36 min fixed in the heating bed slot (Figure 6-1(d)).

From the overlap area, Figure 6-2 shows the surface image for each HBT defined in this study. It is not possible to identify any visible macrostructural change among the different HBTs. Except for the maximum HBT, i.e. 150 °C, where the printing of CF-PA6 layer led to misoriented carbon fiber reinforcement (Figure 6-2(c-iii)). For this case, the HBT used is above the T_g (57.1 ± 1.1 °C) and near to the crystallization temperature (152.7 ± 0.5 °C) of PA6. In this case, during the AddJoining process, the fiber nozzle drags the CF-PA6 as the previous 3D-printed PA6 layer used is in low viscosity due to the high temperature, thereby potentially inducing misorientation during the deposition of carbon fiber reinforced filaments.

The surface morphology of each step was further evaluated by LSCM, as shown in Figure 6-3. It can be observed that surface is rough at low HBT (20 °C) with peak-to-valley roughness (R_z) of 324 µm (Figure 6-3(a)). Higher temperatures promoted a decrease in surface roughness with maximums of 99 µm and 63 µm at 77 °C and 150 °C, respectively. This is further corroborated by the observations of this stepwise approach, where the polymer-polymer bond formation is controlled by temperature. It is possible to observe this with the deposition of the PA6 layer at 45° on the coating layer (Figure 6-3(b)). This image shows a similar smooth roughness map for HBT at 77 °C and 150 °C. At the lowest temperature of 20 °C the presence of black area indicates zero roughness. Moreover, it is the sign for an unmeasurable area, indicating possible voids or large gaps. Such gaps were further identified in the microstructure detail of the overlap joint shown in Figure 6-4 (highlighted with blue arrows). Once again, this suggests the importance of controlling the temperature to allow for a progressive autohesion process and fusion of the surfaces, by providing an adequate initial topography at the interface between layers, leading to a better spreading of the subsequent printed layer. Therefore, the lack of a smooth surface and the presence of fault lines at low temperature is presumed due to a lack of softening of the polymer and negatively influencing the polymer bond formation [91,222].

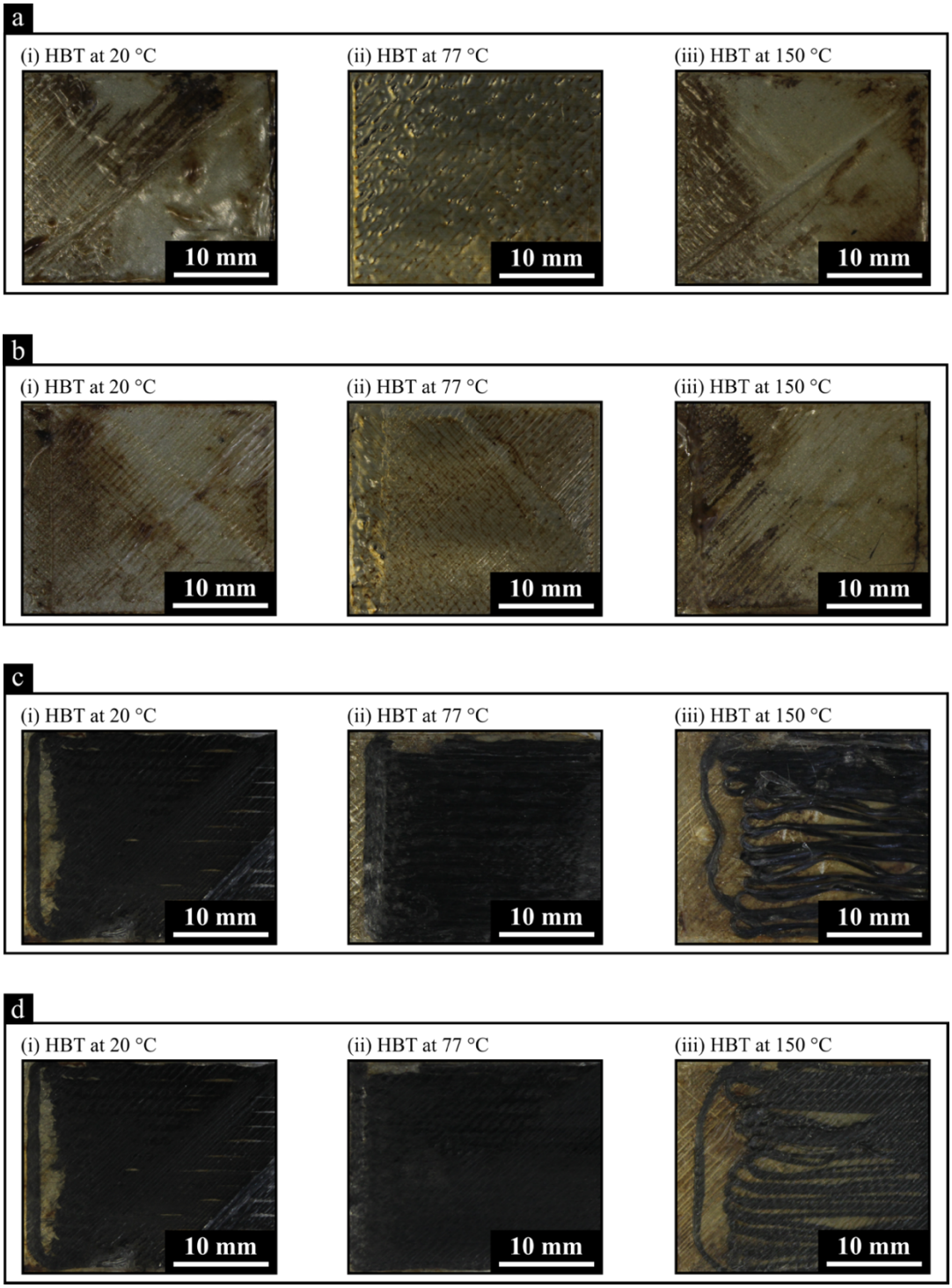

Figure 6-2 Surfaces of the overlap joints at three different heating bed temperatures (HBT) and highlighting the four different layers by stop-action during the AddJoining process obtained by digital camera: (a) PA6 coating, (b) 1st PA6 layer, (c) 2nd CF-PA6 layer, and (d) 3rd PA6 layer. Note that each stop-action layer was maintained at constant HBT for a period to resemble the length of the full AddJoining process cycle to print a 2mm composite part.

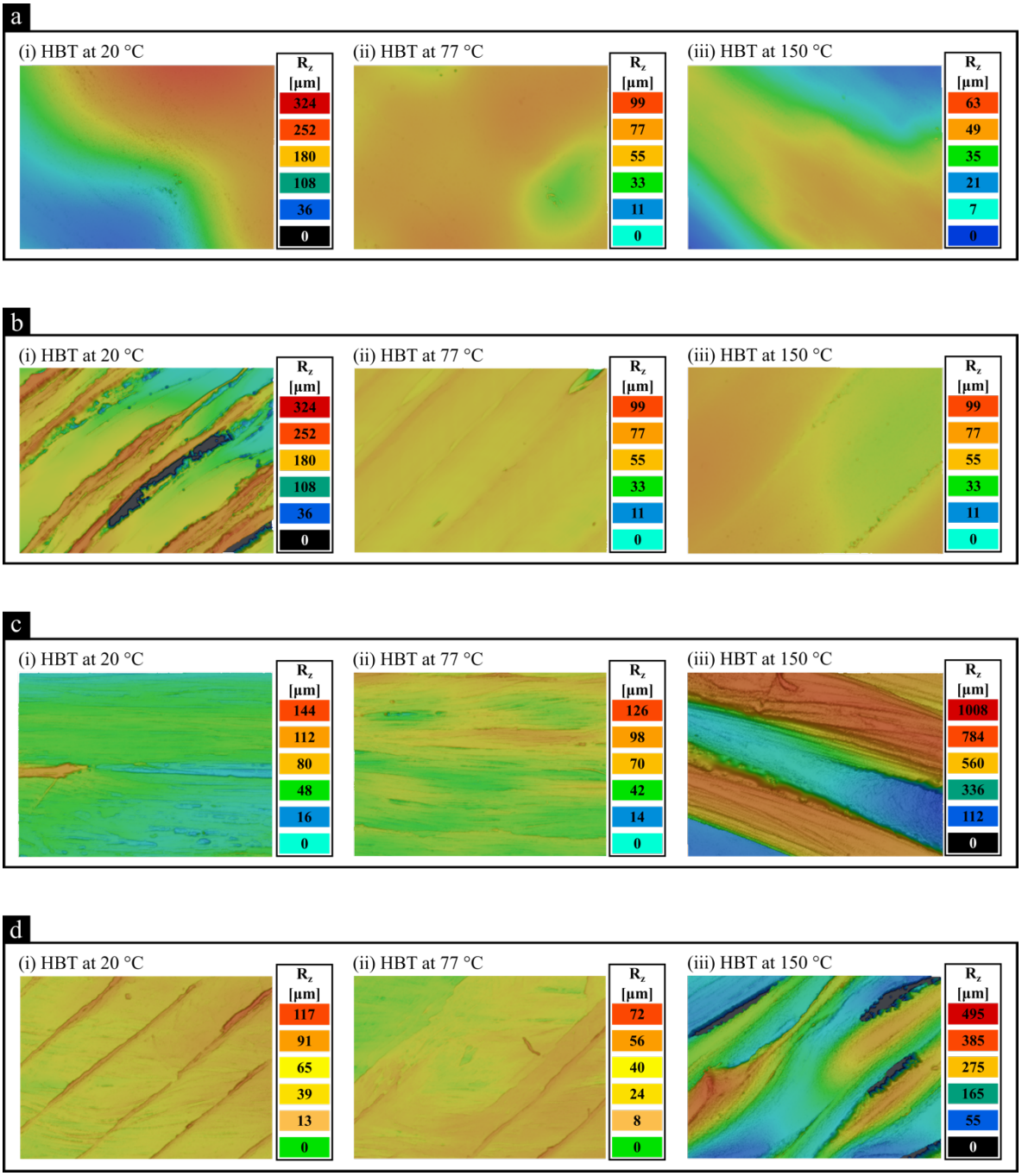

Figure 6-3 LSCM reconstructed 2D surface images of the center of the overlap joint at three different heating bed temperatures (HBT), highlighting four different layers of stop-action during the AddJoining process on: (a) PA6 coating, (b) 1st PA6 layer, (c) 2nd CF-PA6 layer, and (d) 3rd PA6 layer. Note that to resemble the full AddJoining process, each stop-action layer was further maintained at constant HBT for a period to resemble the length of the full AddJoining process cycle to print a 2mm composite part.

3D printing of the CF-PA6 layer orientated 0° in this example, resulted in a decrease in roughness at low temperature (20 °C) (Figure 6-3(c-i)). This significant decrease in roughness is associated with the presence of uniform carbon fiber bundles that resemble a thin ply placement. During the AddJoining process, the fiber nozzle slightly presses the CF-PA6 onto the surface, leaving a uniform surface. As the fiber nozzle is 25 µm vertically lower than the polymer nozzle, this difference in

height is calibrated for the chosen 3D desktop printer used for this PhD work. At the highest temperature, (Figure 6-3(c-iii)), low viscosity of the previous polymer layer leds to the fibre nozzle to drag the CF-PA6 causing a misalignment of the carbon fiber reinforcement as previously discussed.

In the last step of the stepwise approach, the third 3D printed layer shows three different scenarios for HBT (Figure 6-3(d)). At 20 °C with the lines of the PA6 road at 45° it has maximum roughness of 117 µm. For the optimum condition at 77 °C the lines of the PA6 road are difficult to distinguish from interface lines, suggesting homogenization between adjacent roads. At the highest temperature of 150 °C the previous layer and its high surface roughness led to the formation of fault lines, indicated by the black areas (Figure 6-3(d-iii)). The different HBT greatly varied the surface morphology and strongly influenced the quality of bonding formation as it will be discussed in the coming section.

6.1.1.2 Microstructure of the joined composite [PA6/CF-PA6]$_{4S}$ part

An experimental evaluation of the microstructure helps to better understand the overlap joint. The microstructures of the 3D printed composite [PA6/CF-PA6]$_{4S}$ is presented in Figure 6-4. For each HBT case, the microstructure of a cross-section in the hybrid joints was analyzed in three different regions: (1) [PA6/CF-PA6]$_{4S}$ last layer, (2) [PA6/CF-PA6]$_{4S}$ center, and (3) interface of aluminum 2024-T3 and the PA6 coating / [PA6/CF-PA6]$_{4S}$.

For all three cases, no visible microstructural changes were detected near the surface (Figure 6-4(1)) or at the center of the composite (Figure 6-4(2)). The presence of pores – intrinsic flaws related to the 3D printing FFF process - is visible. However, there are statistically no differences in the total porosity on average 12%. Van der Klift *et al.* [174] also reported the presence of pores in 3D printed FFF composites. In the base material used for this PhD work and in most of the fiber filament available in the market, during manufacturing of fiber filament a lack of matrix infusion between conglomerates of fibers can occur (Figure 4-2(c)). Despite this an intimate contact was possible between the PA6 coating layer and metal surface, as well as between the subsequently deposited PA6 layer and PA6 coating layer (Figure 6-4(3)). Therefore, the intimate contact between polymers was promoted by strong autohesion induced by the higher HBT. For HBT at 20 °C, gaps are visible (highlighted in blue) in Figure 6-4(3). This observation corroborates the results from the stepwise approach (Section 6.1.1.1). However, it is interesting to note that a bond line is visible at the interface between the coating and the deposited PA6 layer (highlighted with white arrows in Figure 6-4(3) for HBT at 20 °C and 77 °C. In contrast, at 150 °C, no bond line was detected between the deposited polymer and coating layers, suggesting intermolecular diffusion occurred at the interface [110]. The main drawback with this parameter (HBT at 150 °C) is the polymer mobility that causes a non-homogenous CF-PA6 oriented layer close to the coating layer (Figure 6-4(3)). This helps to support the observations obtained from the stepwise approach in Section 6.1.1.1.

This chapter further discusses the influence of the process parameters described above on the mechanical performance and other methods used to further understand the AddJoining process.

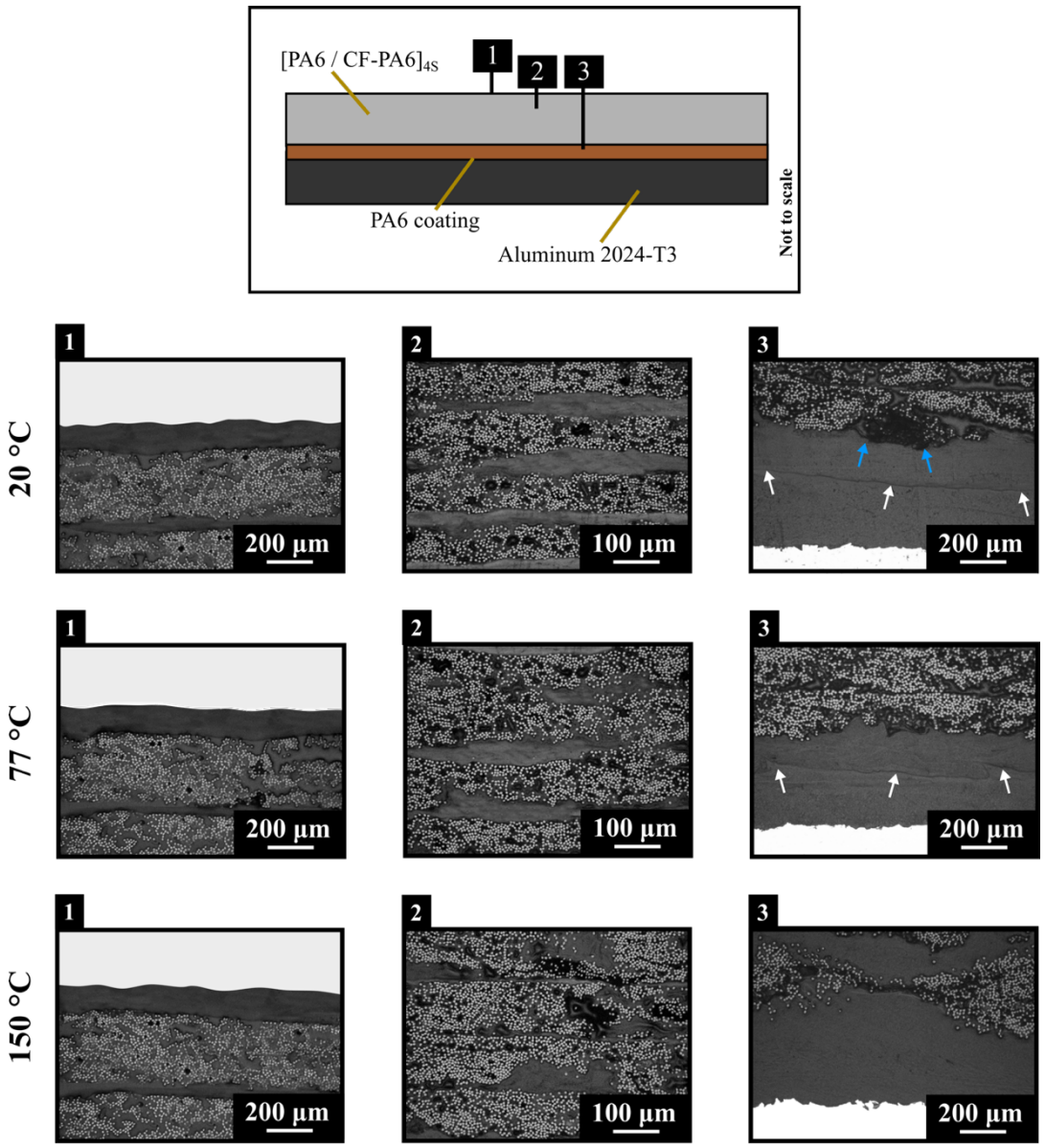

Figure 6-4 Microstructure detail of the overlap joint obtained by LSCM at three different heating bed temperatures (HBT), highlighting three different regions in each of (1) [PA6/CF-PA6]$_{4S}$ last layer, (2) [PA6/CF-PA6]$_{4S}$ center, and (3) interface of aluminum 2024-T3 and PA6 coating / [PA6/CF-PA6]$_{4S}$.

6.1.1.3 Microstructure of the joined aluminum 2024-T3 part

The microstructure of the aluminum 2024-T3 in the overlap joint was revealed by etching the samples as described in Section 4.3.4. The polarized optical micrographs reveal the grain distribution in the microstructure of the aluminum 2024-T3 in three different regions (Figure 6-5). These regions were intentionally chosen at (1) the interface of aluminum 2024-T3 and the PA6 coating / [PA6/CF-PA6]$_{4S}$, (2) aluminum 2024-T3 at the center of its thickness, and (3) the aluminum 2024-T3 bottom surface. The differences in color indicate the orientation of grains and boundaries. Huda *et al.* [225] reported that secondary hardening particles, such as Al_2CuMg (known as S-phase) and $CuAl_2$ (known as θ phase), are formed in the solid solution of copper and other alloying elements on the face-centered cubic lattice of aluminum crystals. These phase precipitates can occur in the aluminum alloy selected

in this work. Moreover, the literature [226] refers as secondary particles with similar composition as precipitate characteristics by their appearance as colonies of precipitates or as dispersion of fine precipitates in the microstructure, where it is visible as black spots. It is interesting to note that typical secondary particles dispersed throughout the microstructure are also visible in the base material (as shown in Figure 4-1, Chapter 4).

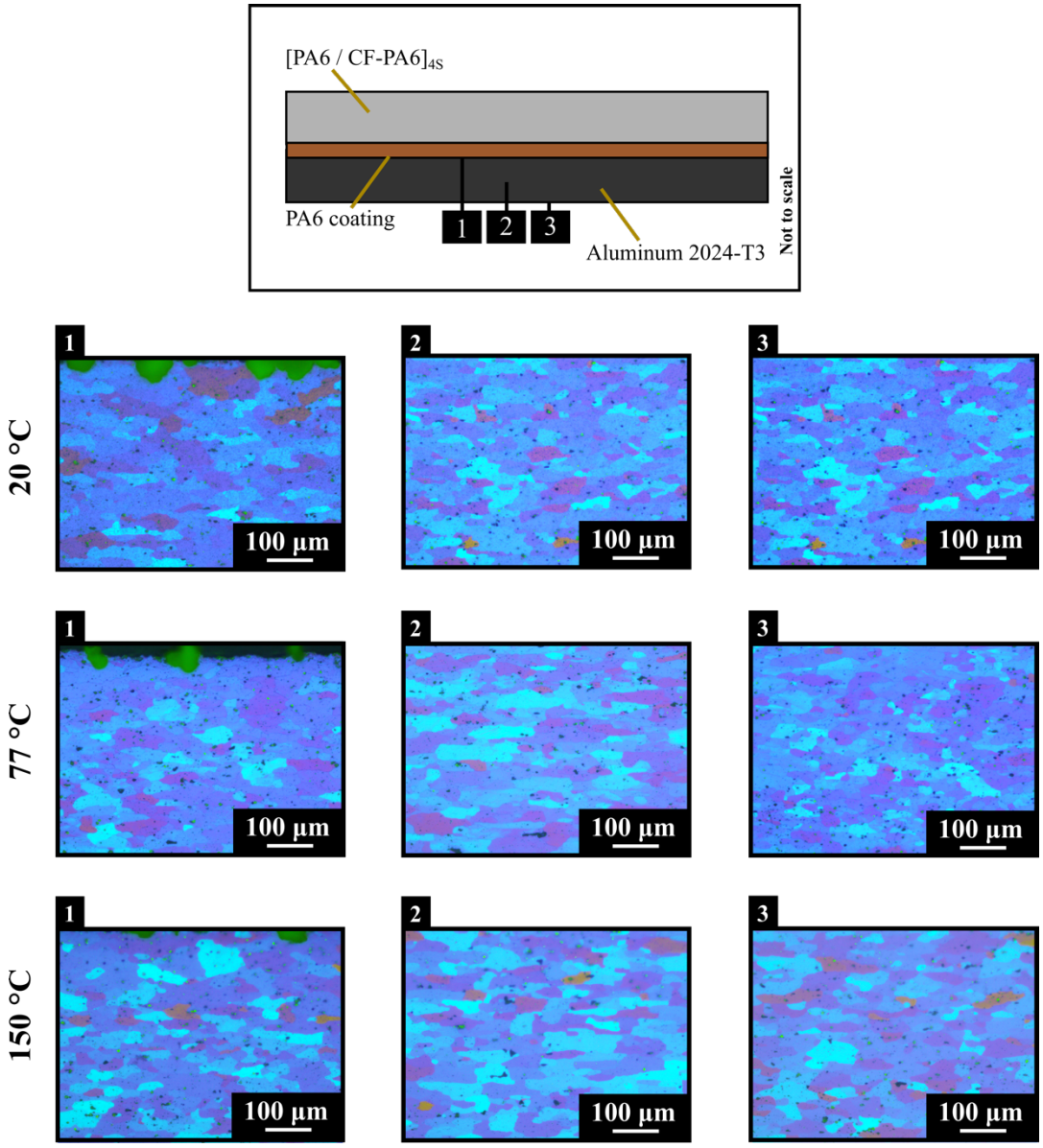

Figure 6-5 Microstructure of aluminum 2024-T3 on the overlap joint obtained by polarized optical microscope at three different heating bed temperatures (HBT) highlighting three different regions: (1) the interface of aluminum 2024-T3 and PA6 coating / [PA6/CF-PA6]$_{4S}$, (2) aluminum 2024-T3 at the center of its thickness, and (3) aluminum 2024-T3 bottom edge.

Although by visual inspection of microstructural aspects in Figure 6-5, it is very difficult to distinguish many differences between the three HBT. The changes in the local mechanical properties, e.g. microhardness (Section 6.1.2.1) and nanohardness (Section 6.1.2.2) were observed and correlated with the possible microstructural changes. According to Lin *et al.* [227], Al-Cu alloys can produce precipitate hardening, depending on the temperature and aging process. The literature also suggests

that by exposing the material to a temperature close to its GP (Guinier-Preston) solvus temperature can cause a variation in hardening [228–230]. For the material used in this work, the solvus temperature is on average 185 °C [231]. This low end of the GP zone is the first stage to form a fully coherent precipitate, whereas above the GP solvus temperature it can form an equilibrium phase of Al_2Cu precipitates [232].

6.1.2 Local mechanical properties

The AddJoining process could induce microstructural changes to the local properties of the joined materials. To study these the local mechanical properties were divided into aluminum 2024-T3 part and composite $[PA6/CF\text{-}PA6]_{4S}$ part. With the procedure explained in Section 4.3.7.1, microhardness was used to evaluate the local mechanical properties of the metal part. In addition, the local mechanical properties of the composite part were evaluated by nanohardness, as described in Section 4.3.7.2. To keep the evaluation systematic, this section is divided into two parts: first the local properties of the aluminum are discussed, followed by the local properties of the composite.

6.1.2.1 Aluminum 2024-T3

Figure 6-6 shows the Vickers microhardness (VMH) maps of aluminum 2024-T3. The VMH maps help assess the local mechanical properties of the aluminum 2024-T4 in the overlap joint at the three different HBT. In this investigation, hardness was considered symmetrical and so only half of the sample was evaluated. The horizontal axis represented here as width varies from 0 mm (at the edge) to 12.5 mm (half way across the overlap joint). The vertical axis represented as thickness varies from -0.1 mm, close to the interface with the coating layer, to -1.9 mm, near to the bottom surface of the overlap joint. For comparison, a VMH map of the base material was evaluated (Figure 6-6(i)). By comparing the hardness distribution, it is possible to observe process-related changes to the hardness. Such an observation was not possible to evaluate from the microstructural analysis in Section 6.1.1.3. Nonetheless, the discussion there on variation of temperature and possible precipitation hardening can help to understand the hardness differences in this section.

In the VMH maps presented in Figure 6-6(ii) to Figure 6-6(iv) it is possible to observe three distinct regions. The first region is close to the interface at a thickness of -0.1 mm. For HBT at 20 °C (Figure 6-6 (ii)), hardness was 3 % lower than that of the base material with (141.1 ± 3.2 HV) and (145.2 ± 2.7 HV), respectively. For HBT at 77 °C and 150 °C, hardness were 5 % higher at (152.3 ± 3.9 HV) and 6 % higher (154.2 ± 3.6 HV), respectively. These increases in hardening could be promoted by strengthening by precipitate particles that are formed by exposure of the material to temperatures approaching its solvus GP temperature (as discussed in Section 6.1.1.3). In the case of the bottom surface at a thickness of -1.9 mm, it shows that increasing HBT from 20 °C to 150 °C led to different hardness distributions. At 20 °C a decrease in hardness of 1 % (143.1 ± 2.9 HV) was observed compared to the base material (144.9 ± 5.2 HV), but the hardness distribution significantly increased with an average hardness of 150.5 HV at 77 °C and 154.7 HV at 150 °C. In the middle region at a thickness of -1 mm, the hardness distribution was 3 % lower for HBT at 20 °C with 138.9 ± 2.8 HV compared to the base material (142.9 ± 4.6 HV). For HBT at 77 °C and 150 °C hardness increased by 1 % (143.9 ± 2.2 HV) and by 2 % (146.1 ± 3.8 HV), respectively.

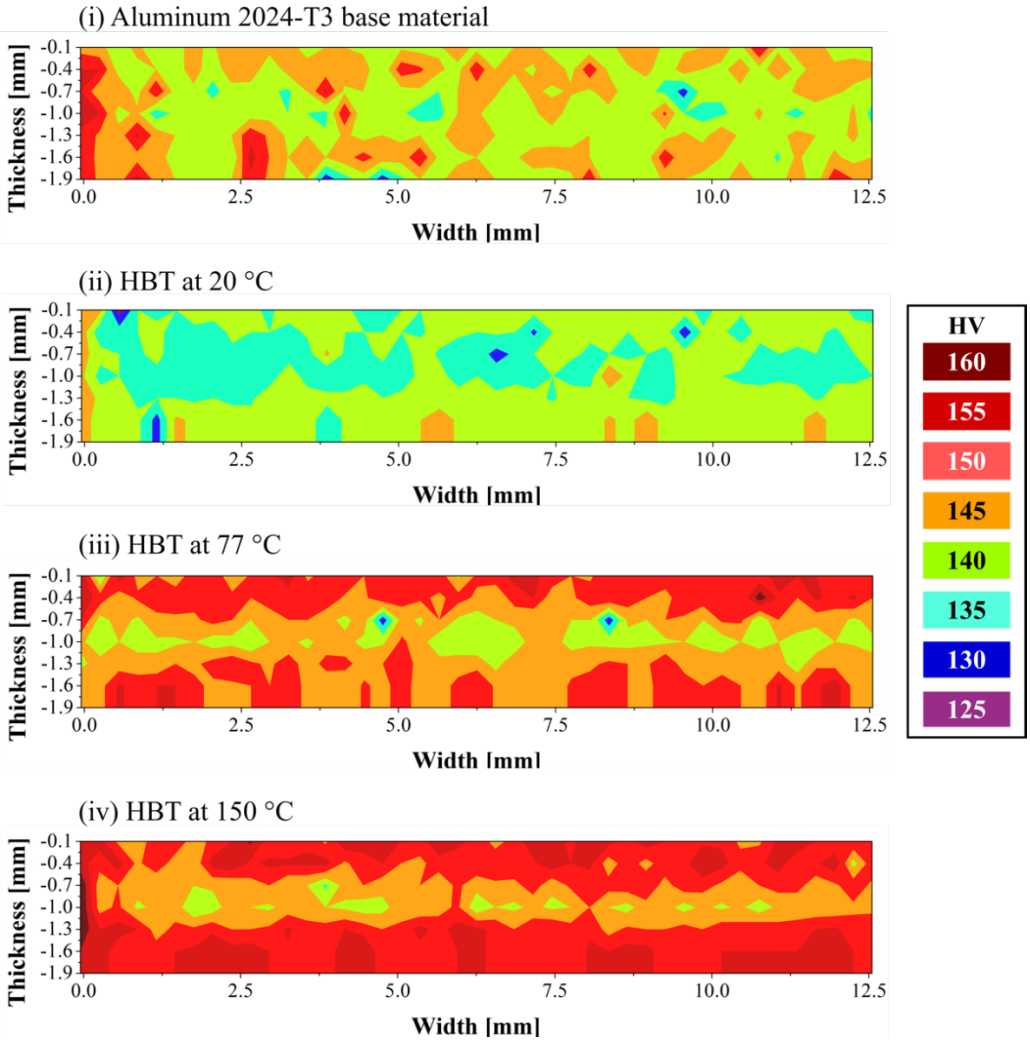

Figure 6-6 Vickers microhardness maps of the aluminum 2024-T3 in (i) the base material in the overlap joint, and after three heating bed temperatures (HBT) of (ii) 20 °C, (iii) 77 °C, and (iv) 150 °C, from the thickness between the edge of the sample (width=0 mm) and the middle of the joint (width=12.5 mm).

To summarize, hardness distributions of the metal part of the overlap joint configuration were evaluated. This region was exposed to a uniform heat distribution during formation of the polymeric coating in the first step of the AddJoining process. This means the metal part was affected by the heat of the process and due to its high thermal conductivity (121 W/(m·K) the heat was dissipated throughout a large area. For HBT at 77 °C and 150 °C, the temperature increased the hardness and this indicates a precipitation of strengthening particles occurred, as previously discussed. In contrast, for HBT at 20 °C, it is easier to observe the influence of the AddJoining process during the 3D printing process. HBT has no direct influence when is at room temperature, thus the reduction in hardness is caused exclusively by deposition of the polymeric coating in the first step and from further manufacturing steps of the 3D printed composite. It seems that the exposure to CT at 229 °C and the printing process time of 56 min caused a coarsening of the strengthening particles (i.e., lost in precipitate coherence) and consequently the reduction in hardness observed, compared to the base material. Similar coarsening of the strengthening particles has been reported in the heated affected zone with technologies involving a friction-based process [9,233,234] as well as metal additive manufacturing [235].

6.1.2.2 [PA6/CF-PA6]$_{4S}$ and interface of the overlap joint

Figure 6-7 are a schematic of four locations: (1) close to the interface of the aluminum 2024-T3 and PA6 coating, (2) PA6 coating, (3) PA6 first layer, and (4) PA6 last layer; thereby to perform the nanoindentation measurements. No measurements were made of the CF-PA6 layer, to avoid any interaction of fibers with the polymer matrix (i.e., possibly biasing the measurement). However, one may extent the interpretation of these results to the CF-PA6 as the layers were produced with same heat input. The average hardness (Figure 6-7) were obtained by evaluating the loading and unloading curves corresponding to nanoindentation measurements. The graphs are depicted in Appendix A.6.

The hardness measured by nanoindentation increased with increasing in HBT. For the first region, corresponding to the interface of the aluminum 2024-T3 and PA6 coating (Figure 6-7(1)). For HBT at 20 °C, the hardness was 7 % (1.84 ± 0.09 GPa) less than the base material (1.97 ± 0.07 GPa). This helps to support the observations from the Vickers microhardness tests (Section 6.1.2.1), where at lower HBT the exposure to CT at 229 °C caused lost in precipitate coherence consequently leading to decrease the hardness compare to the base material. On the contrary, higher HBT caused an improvement in the hardness by 6 % at 150 °C (2.09 ± 0.11 GPa). The exposure at higher HBT during the AddJoining process suggests that the uniform heat distribution throughout the metal during the formation of coating and 3D printing influenced the increasing in hardness compared to the base material. It appears that an increase of precipitate reinforcement took place, whereby precipitation of particles once solubilized in the base material (the base material alloy was only in T3 condition) may have taken place at higher HBT, thereby locally increasing hardness. Further studies, for instance by transmission electron microscopy should be carried in other to verify this assumption. Nevertheless, this is out of the scope of this work.

By comparing the results in the second region, corresponding to the PA6 coating, the average hardness (Figure 6-7(2)) drastically decreased compared to the base material, where at 20 °C a decrease of 53 % (0.037 ± 0.001 GPa) compared to the base material (0.079 ± 0.009 GPa) was observed. At the highest HBT the difference in hardness reduced by 28 % (0.057 ± 0.005 GPa) compared to the base material. In the measurements of the first layer of PA6, third region shown in Figure 6-7(3), it is difficult to distinguish any differences from the PA6 coating. The average hardness for first layer of PA6 (Figure 6-7(3)) is statistically similar to the PA6 coating values presented here. This observation correlates with the results presented in Section 6.1.3, where the phase changes in the polymer at PA6 coating and for the first layer of PA6 are similar. For example, for HBT at 150 °C the hardness is 0.057 ± 0.005 GPa (Figure 6-7(2)) and 0.058 ± 0.002 GPa (Figure 6-7(3)) for PA6 coating and first layer of PA6, respectively. On the contrary, by comparing the first layer of PA6 with the base material, for HBT at 150 °C hardness decreased 27 % (0.058 ± 0.002 GPa) compared to the base material (0.079 ± 0.009 GPa). For the last region, (Figure 6-7(4)), the last layer of PA6 has no significant difference within the selected HBT range, with an average of 0.04 GPa, corresponding to 49 % of the hardness of the base material.

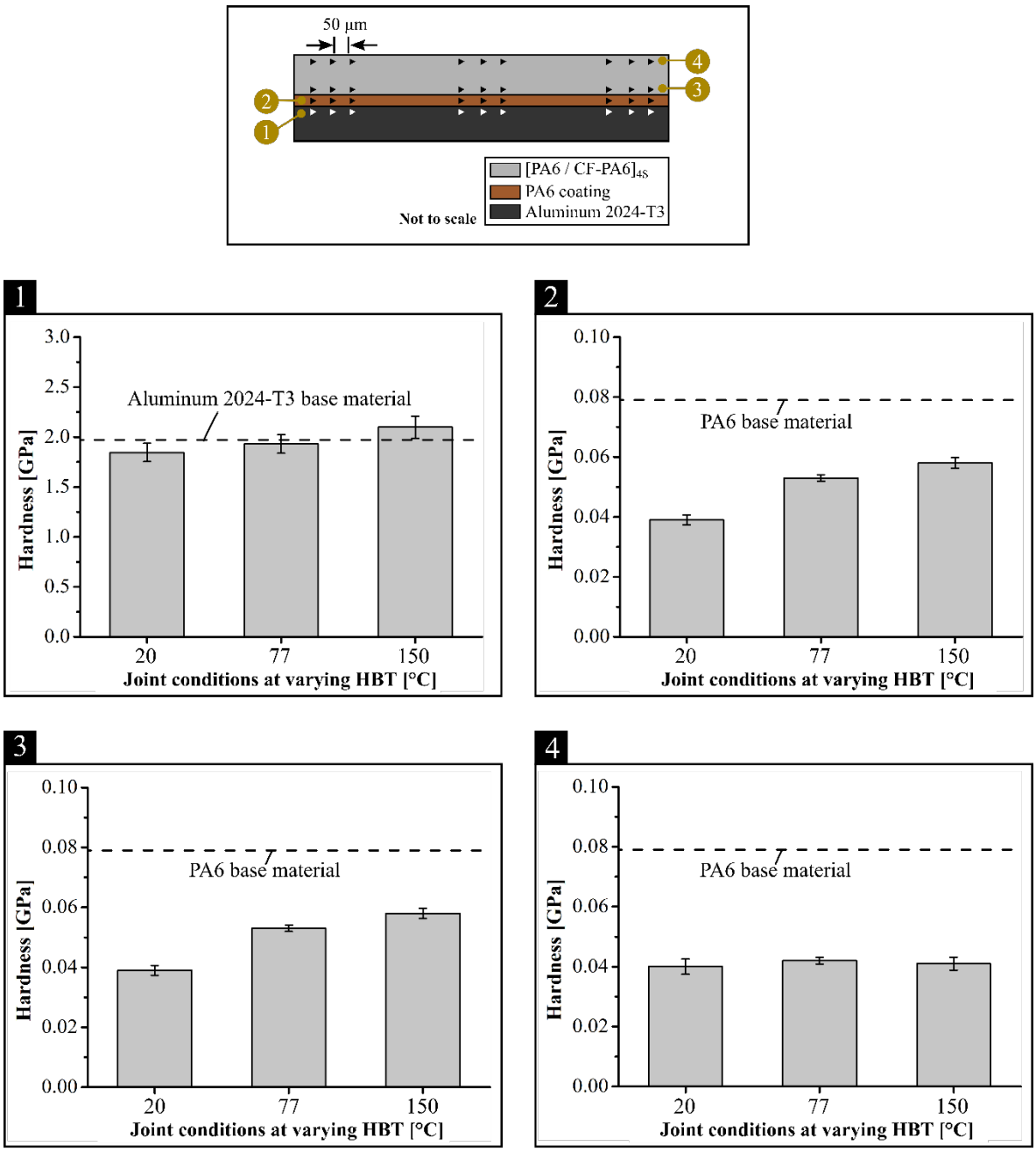

Figure 6-7 Schematic of nanoindentation measurement of the overlap joint locations on aluminum 2024-T3, on PA6 coating, and on composite [PA6/CF-PA6]$_{4S}$; average nanoindentation hardness of (1) aluminum 2024-T3 close to the interface with the PA6 coating / [PA6/CF-PA6]$_{4S}$, (2) PA6 coating, (3) PA6 first layer, and (4) PA6 last layer. Each at the three different heating bed temperatures (HBT).

Overall, this indicates that the heat factor used during the AddJoining process significantly influences the local mechanical properties closer to the metal surface, i.e. the PA6 coating and PA6 first layer. This follows, because during the AddJoining the PA6 coating is heated to a viscous state and cooled down to room temperature. The subsequent deposition of polymer in the AddJoining process can cause a change to the chain configuration from random (amorphous) to an ordered (crystalline). Therefore, it may be assumed at this point that the presence of a thermal history of AddJoining can affect the crystallinity and decrease in hardness. Engkvist [236] reported a study on the influence of

filling patterns of 3D printed PA6 samples on the microstructural and mechanical properties. The author observed a reduction of 8 % in crystallinity caused by polymer additive manufacturing. In this PhD work, the results observed in local mechanical properties are corroborated by phase changes in the polymer material (further discussed in Section 6.1.4).

6.1.3 Physicochemical changes in the polymeric parts

The composite $[PA6/CF\text{-}PA6]_{4S}$ part contains a total of 16 layers, i.e. 8 layers of CF-PA6 and 8 layers of PA6 layers. It leads to an equal volume fraction for PA6 and CF-PA6 layers. It is important to note that in this section, the base material filament PA6 and CF-PA6 used to produce the composite $[PA6/CF\text{-}PA6]_{4S}$ part using the AddJoining technique were not directly compared with the hybrid joints. The reason is to facilitate the interpretation of the rather complex thermal analysis results. Therefore, the results shown in this section address the hybrid joints subjected to HBT experiments discussed in Section 6.1.1.1.

Thermal analysis was carried out to explore the changes to properties in the composite $[PA6/CF\text{-}PA6]_{4S}$ part of the AddJoining hybrid joints, as described in Section 4.3.5. The thermal properties can be attributed to changes in molecular chain interactions and the formation of polymer thermal decomposition. As explained before, Section 4.3.5, this investigation examined samples extracted that cover the full thickness of the composite $[PA6/CF\text{-}PA6]_{4S}$ part. Changes in thermal properties were compared for the three HBT of 20 °C, 77 °C and 150 °C. Two thermal properties were obtained from the DSC heating curves, crystallinity (X_c) and melting temperature (T_m) (Figure 6-8(a)). The crystallinity was calculated according to Equation (4-1), as introduced in Section 4.3.5.1. In so doing the volume fraction of 50 % carbon fiber in the composite was considered. Next, the crystallization temperature (T_{cc}) was evaluated from the cooling curves (Figure 6-8(a)). Finally, the decomposition temperature (T_d) was obtained from the TGA curves (Figure 6-8(b)) to evaluate the thermal stability of the composite.

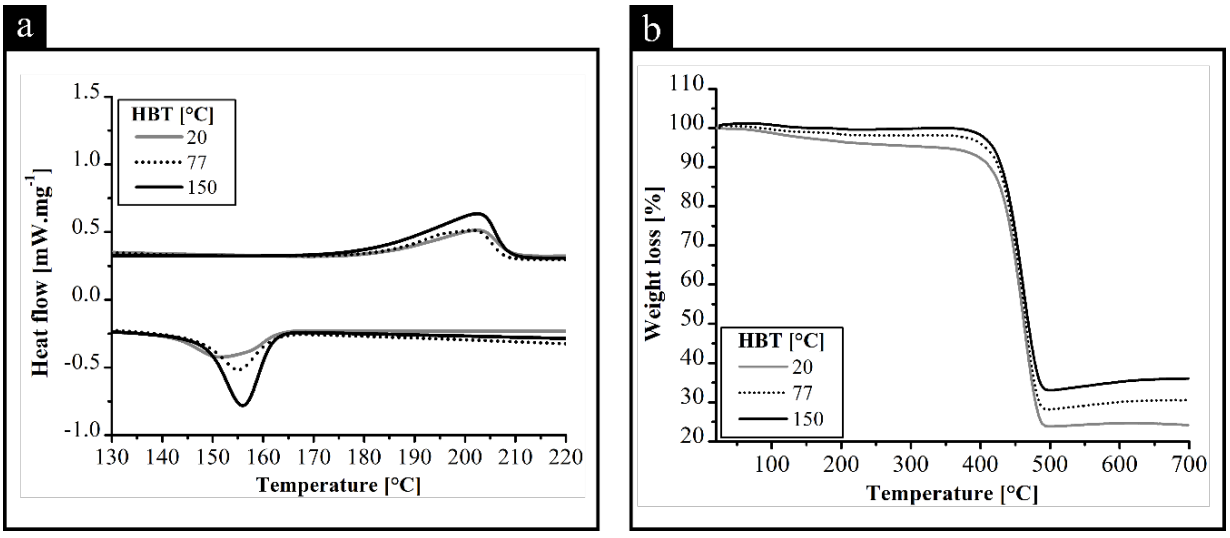

Figure 6-8. DSC curves for (a) heating and cooling, and (c) TGA curves; for three HBT at 20 °C, 77 °C and 150 °C for the composite $[PA6/CF\text{-}PA6]_{4S}$ part.

The glass transition temperatures are not shown in the depicted heating curves from DSC, which are between 40 °C and 50 °C. What is interesting here is the significantly endothermic average peak at 200 °C as illustrated in (Figure 6-8(a)). From the figure, only a single peak is observed at different HBT values existed from the heating and cooling curves. However, the presence of polymorphism was proven using first derivative on the heating and the cooling curves (shown in Appendix A.7). To better understand the polymorphism, a stepwise approach in Section 6.1.4 was carried out for phase-identification, which further helped to elucidate the phase changes during the AddJoining process. Melting temperature (T_m) and the crystallization temperature (T_{cc}) were evaluated from the heating and cooling curves from the DSC graphs (Figure 6-8(a)). Furthermore, the decomposition temperature (T_d) was obtained from TGA curves (Figure 6-8(b)). Therefore, Table 6-1 summarizes these main thermal properties calculated from Figure 6-8 for the composite $[PA6\text{-}CF\text{-}PA6]_{4S}$ part subjected to different HBT. For a quick comparison, the table also summarizes the thermal properties for the base material filament PA6 and CF-PA6 used to produce the composite $[PA6/CF\text{-}PA6]_{4S}$ part.

Table 6-1 Thermal properties for base material (PA6 and CF-PA6) and composite $[PA6/CF\text{-}PA6]_{4S}$ part

Thermal properties	Base material		Composite $[PA6/CF\text{-}PA6]_{4S}$		
	PA6 [a]	CF-PA6 [a]	HBT at 20 °C	HBT at 77 °C	HBT at 150 °C
X_c [%]	27.3 ± 0.9	1.3 ± 0.4	13.8 ± 0.4	15.7 ± 0.2	24.8 ± 0.3
T_g [°C]	55.9 ± 0.7	57.1 ± 1.1	56.7 ± 0.9	58.1 ± 1.1	58.3 ± 0.8
T_{cc} [°C]	152.7 ± 0.5	157 ± 0.7	151.5 ± 1.8	151.8 ± 1.4	155.9 ± 2.2
T_m [°C]	201.2 ± 1.2	233.1 ± 0.5	202.5 ± 0.8	201.3 ± 0.7	203.1 ± 0.4
T_d [°C]	456 ± 1.4	476 ± 2.5	464.5 ± 1.2	463.9 ± 2.3	461.3 ± 1.7

(a) Curves are available on Appendix A.2.

The melting temperature is virtually the same with a small variation of 0.6 % from 202.5 ± 0.8 °C with HBT at 20 °C to 201.3 ± 0.7 °C with HBT at 77 °C. Moreover, a slight increase by 0.2 % to 203.1 ± 0.4 °C with HBT at 150 °C could be seen. All in all, there was no drastic difference in thermal properties at different HBT and statistically no difference compared to the base materials. On the contrary, the crystallinity increased 14 % from HBT at 20 °C (13.8 ± 0.4 %) to HBT at 77 °C (15.7 ± 0.2 %). When exposure to HBT at 150 °C, the crystallinity index was 24.8 ± 0.3 %, which is 80 % higher than the crystallinity at the lowest HBT value. Figure 6-8(a) shows the exothermal curves that with peak temperature represent the crystallization temperature, where is considerable constancy between HBT at 20 °C with 151.5 ± 1.8 °C and HBT at 77 °C with 151.8 ± 1.4 °C. However, with HBT at 150 °C the crystallization temperature slightly increased by 3 % (155.9 ± 2.2 °C) compared with the lowest HBT value. According to Bureau *et al.* [237], an annealing effect can cause an increase in the crystallinity of PA6 by exposing the material to high temperatures. The author investigated the effect at 80 °C for 24 h. In this PhD work, the increase in crystallinity suggests chain mobility of the amorphous phase that induces an annealing effect of the polymeric crystallites [238].

As shown in Figure 6-8(b), thermal stability was caused by the presence of fiber. The steady decomposition temperature with an average temperature of 463 °C for the composite $[PA6/CF\text{-}PA6]_{4S}$ part decreased in 3% in comparison with CF-PA6 base material (476 °C) (Table 6-1). It could be an indication of thermal degradation, however a detailed evaluation of thermal changes in the

polymer structure by thermal analysis is out of the scope of this PhD work. Furthermore, it is interesting to note that has been reported that the presence of fibers improve the thermal stability of a composite, by acting as a physical barrier [239–241]. The curves show that there is only one degradation stage for all the HBT values evaluated in this investigation. It is interesting to confirm that the presence of carbon fiber in the composite improves the thermal stability, as shown in Appendix A.2 and Table 6-1. Moreover, it has been reported that presence of fibers can positively hinder the volatilization of small molecules [177]. The presence of fibers also decreases the rate of heat released during the process of thermal decomposition [242]. Another observation from the TGA curves is the reduction in mass during the first 100 °C, which is attributed to the escape of moisture present in the composite. In the region examined, a mass loss of 4.1 ± 0.8 % with HBT at 20 °C was followed by 1.2 ± 0.9 % at 77 °C. At the highest HBT value the mass loss reduced to 0.8 ± 0.1 %, because the manufacturing at the higher HBTs probably led to base material moisture release during the AddJoining printing process. Therefore, the mass losses during the first 100 °C for the TGA curves at 150 °C was relatively smaller compared to 20 °C and 77 °C.

To summarize, a partial conclusion can be drawn: the effect of HBT slightly changed the thermal properties of the composite. However, the results have given a basic understanding of the effects of HBT. Combining this investigation with phase-identification of the polymer (Section 6.1.4) can offer a more comprehensive understanding of the local variations in material properties by means of the phase-changes in each layer.

6.1.4 Phase identification in the polymeric parts

As previously described in Chapter 5, the AddJoining process is based on a polymeric additive manufacturing technique. The total volume of 3D printed composite is filled road-by-road and layer upon layer to form a full 3D printed part. Throughout the process of 3D printing, the polymeric material can undergo thermal changes with the deposition of each newly printed layer. As introduced in Section 6.1.1.1, a stepwise concept was applied to help understand the phase changes in the polymer. XRD patterns were used to measure the surface of the sample, as shown in Figure 6-2, according to the procedure described in Section 4.3.6. It is frequently observed and well-known that PA6 has different crystalline phases, such as α and γ [237,243]. Thus, an understanding of changes to these phases can constructively help to explain the effects of process changes on the mechanical performance. XRD patterns were analyzed for each HBT within the selected range. A set of schematics are presented in the figures that follow for each HBT that indicate the measurement location. For example, for HBT at 20 °C Figure 6-9(a) and Figure 6-9(b) point out the five locations that were used to measure XRD patterns: the PA6 coating, PA6 first layer, CF-PA6 second layer, PA6 third layer, and the PA6 last layer.

For HBT at 20 °C, the XRD pattern, corresponding to the PA6 coating (Figure 6-9(c)) shows a highly amorphous material with no regular peak [237]. As soon as the first layer is deposited (PA6 first layer the XRD pattern of the PA6 first layer shows a strong and sharp peak at 21.4° corresponding to γ-PA6 [243] (Figure 6-9(d)). Liu *et al* [244] reported that γ crystalline phase is metastable and is formed at low temperature, e.g. from 80 ° to 120 °C. The presence of carbon fiber in the second layer (Figure 6-9(e)) led to a decay in the shape of curve in first 10°. The presence of two broader peaks at 21.4° and at 23.4° is visible corresponding to γ-PA6. However, the formation of α-PA6 is also identified corresponding to the presence of a shoulder closer to 20° (highlighted with an arrow). According to

Yan [243], the presence of carbon fiber can enhance crystallization and form a stable α-PA6, a highly thermodynamically stable phase that consists of anti-parallel packed hydrogen-bonded chains as reported by Liu [244]. The author also reported that γ-PA6 is an unstable phase and a conversion from γ-PA6 to α-PA6 can occur with temperature. The next PA6 layer (Figure 6-9(f)) has a similar XRD pattern to the previous CF-PA6 layer (Figure 6-9(e)), where it did not affect the phase change. It indicates that with HBT at 20 °C these phase changes are purely associated with the AddJoining 3D printing process rather than the heating bed. In the last PA6 layer (Figure 6-9(g)) a peak is visible at 21.4° corresponding to γ-PA6 phase and the presence of a shoulder closer to 20° suggesting the formation α-PA6 (highlighted with an arrow). According to the literature [245], the plasticity of PA6 is driven by crystal slip parallel to the hydrogen-bonded sheets, where changes in mechanical properties are expected related to the crystalline phase. Overall, in this work, it indicates that the two polymorphs of α-PA6 and γ-PA6 can impact the local mechanical properties influenced by variation on HBT. This supports the explanation regarding the reductions in hardness, i.e. resistance to local plastic deformation (discussed in Section 6.1.2).

The intense peaks in the XRD patterns for HBT at 77 °C (Figure 6-10) and at 150 °C (Figure 6-11) indicate an enhancement in the degree of crystallinity [246]. The XRD patterns for HBT at 77 °C show no sign of unique amorphous phase. Figure 6-10(c) shows the XRD pattern from the PA6 coating. There is one significant peak at 21.4° corresponding to γ-PA6 and two shoulder evolves (highlighted with arrows) closer to 20° and 23.4° corresponding to a weak content of α-PA6 and γ-PA6, respectively. The subsequent PA6 layer (Figure 6-10(d)) shows a sharp peak at 21.4° corresponding to the unstable γ-PA6. In the same image the presence of a weak peak at 11° also corresponds to γ-PA6. After deposition of the CF-PA6 layer (Figure 6-10(e)), the peak at 11° disappears and the formation of three sharp peaks are visible. The peaks at 21.4° and 23.4° indicate a strong content of γ-PA6, and the formation of α-PA6 at 20°. The literature [247,248] suggests that as a metastable phase, it can transform further into γ-PA6 or α-PA6 by means of mechanical stress or be thermally induced. As previously discussed, the presence of carbon fiber can enhance crystallization and form stable α-PA6 [243]. The subsequent PA6 layer (Figure 6-10(f)) has a similar XRD pattern compared with the previous CF-PA6 layer, except that the peaks have inverted in strength representing by strong peak at 21.4° that corresponds to the γ-PA6. Some fraction of amorphous phase can form a crystalline phase during the heating process, forming γ-PA6 [244]. Finally, the last layer at 77 °C (Figure 6-10(g)) has a similar XRD pattern to that with HBT at 20 °C (Figure 6-9(g)). Once again, the similarity corroborates the results (i.e., an overall decrease in local properties in comparison to base material) obtained for hardness by nanoindentation within the selected HBT range.

For HBT at 150 °C there is no presence of unique amorphous phase. Figure 6-11(c) shows the XRD pattern from the PA6 coating. The temperature gradually triggers the formation of α-PA6 phase with visible peaks at 20°. The presence of γ-PA6 phase can be observed, represented by two characteristic peaks at 21.4° and 23.4°. The literature has reported that γ-PA6 phase is crystallized and can be stable at temperatures close to 150 °C, also causing a partial transformation of α-PA6 [249]. An interesting XRD pattern is shown in Figure 6-11(d) after deposition of the PA6 layer. Strong peaks at 13.5° and at 23.4° are visible, representing γ-PA6, with further peaks at 20° that indicate a strong content of α-PA6. As previously discussed, a metastable phase from 11° to 14° can be transformed to γ-PA6 or stable α-PA6 by means of mechanical stress or be thermally induced [247,248]. HBT at 150 °C induced distribution of phase crystallization, represented by the peak at 21.3° and 23.4° for γ-PA6,

as well as a peak at 20° representing α-PA6 (Figure 6-11(e)). With deposition of the third PA6 layer (Figure 6-10(f)), the formation of three sharp peaks are non-visible. A transition of PA6 phases is clearly observed in this XRD pattern, a sharp peak at 21.4° that corresponds to the γ-PA6 is visible. Moreover, the XRD pattern is similar compared to third PA6 layer at 77 °C (Figure 6-10(f)). Thus, a mixed phase of α-PA6 and γ-PA6 exists, caused by a thermally induced increase and possible transformation of a fraction of amorphous phase into crystalline phases. Figure 6-10(g) shows the XRD pattern from the last layer of PA6 at 150 °C. The last layer once again has a similar shape compared to HBT at 20 °C and 77 °C, as there is no strong influence of the HBT, which confirms the similarity in local mechanical properties discussed in Section 6.1.2.2.

To summarize, the presence of two polymorphs of α-PA6 and γ-PA6 were observed and it helped to support the interpretation of the variation in local mechanical properties for the composite part. It suggests that the subsequent deposition of polymer in the AddJoining process caused a change to the chain configuration from random (amorphous) to an ordered structure (crystalline). Therefore, these results helped to further understanding the decrease in hardness in comparison with the base material, which it is caused by the presence of a thermal history of AddJoining.

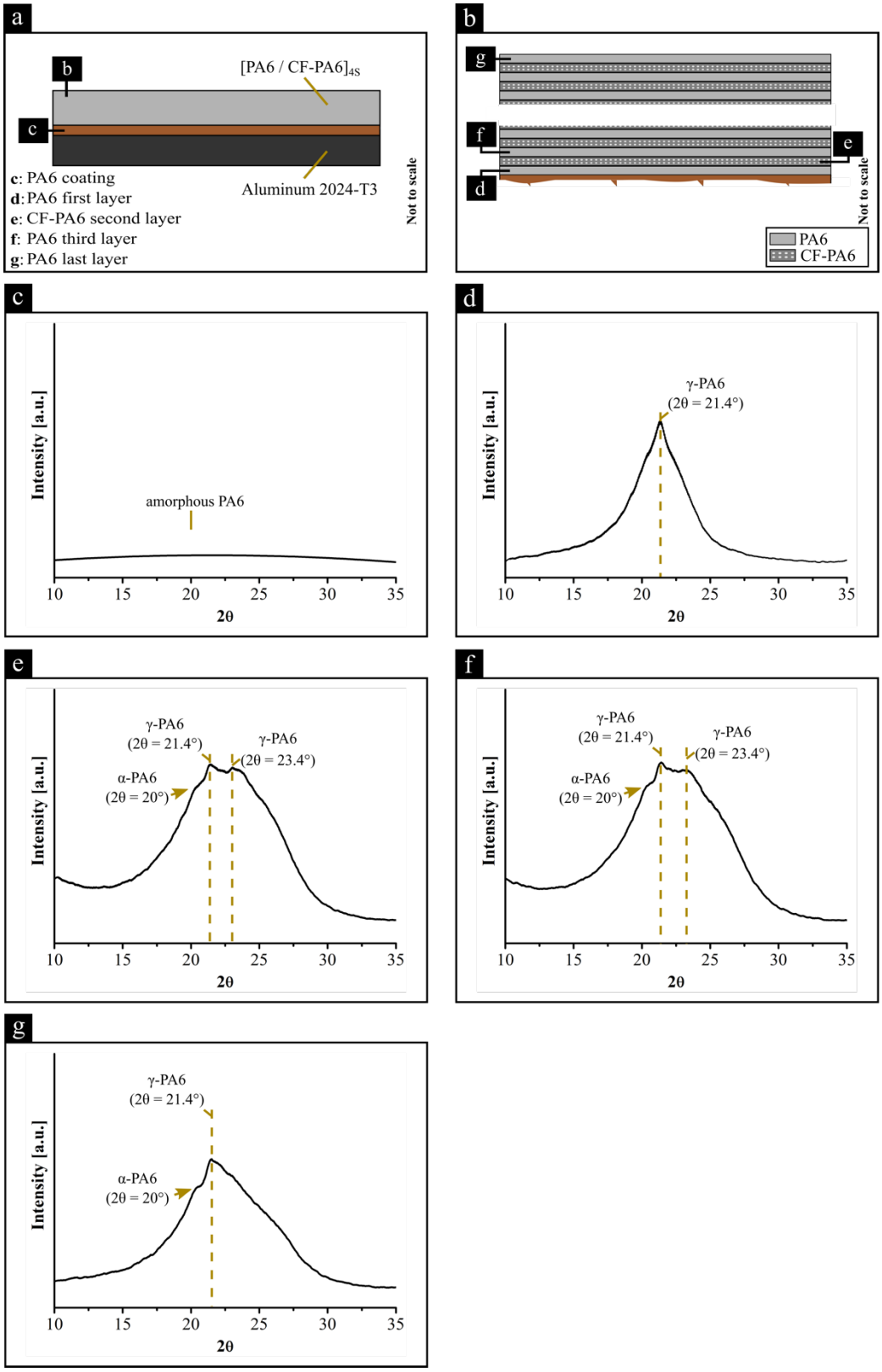

Figure 6-9 Schematic of XRD measurements of the overlap joint locations for HBT at 20 °C, with detail of (a) aluminum 2024-T3, (b) composite PA6/CF-PA6]$_{4S}$; XRD pattern for (c) PA6 coating, (d) PA6 first layer, (e) CF-PA6 second layer, (f) PA6 third layer, and (g) PA6 last layer.

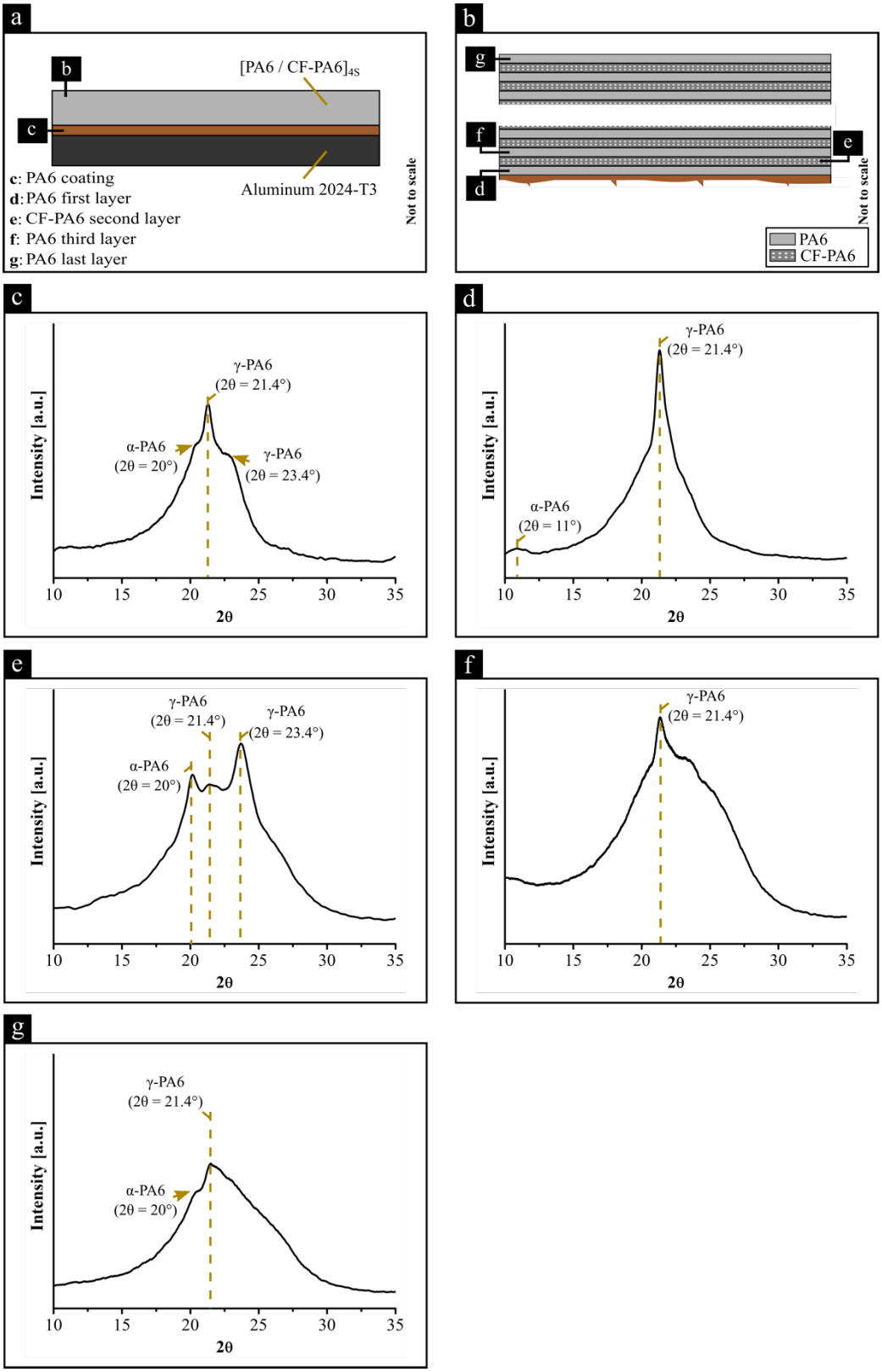

Figure 6-10 Schematic of XRD measurements of the overlap joint locations for HBT at 77 °C, with detail of (a) aluminum 2024-T3, (b) composite PA6/CF-PA6]$_{4S}$; XRD pattern for (c) PA6 coating, (d) PA6 first layer, (e) CF-PA6 second layer, (f) PA6 third layer, and (g) PA6 last layer.

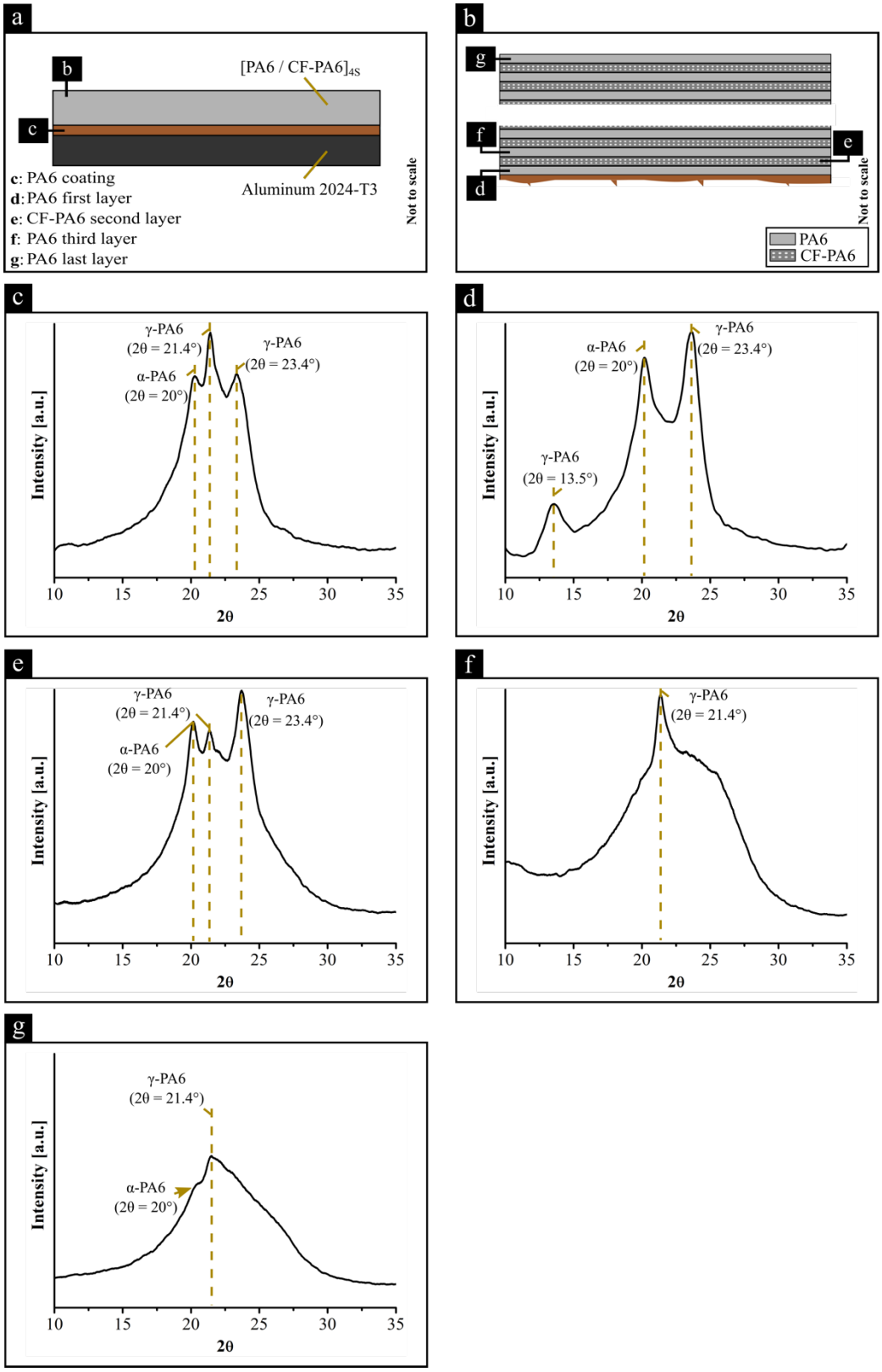

Figure 6-11 Schematic of XRD measurements of the overlap joint locations for HBT at 150 °C, with detail of (a) aluminum 2024-T3, (b) composite PA6/CF-PA6]$_{4S}$; XRD pattern for (c) PA6 coating, (d) PA6 first layer, (e) CF-PA6 second layer, (f) PA6 third layer, and (g) PA6 last layer.

6.1.5 Mechanical performance

Secondary bending (SB) was compared for the three HBT values with a common loading level of 5 kN. The out-of-plane displacements shown in Figure 6-12 were evaluated by a digital image correlation (DIC) system. A dissimilarity in material stiffness can be seen in the maximum out-of-plane displacements measured during the test. A summary of the out-of-plane displacement is depicted on Table 6-2. For HBT at 77 °C, the maximum out-of-plane displacement was -0.51 ± 0.19 mm for the composite $[PA6/CF\text{-}PA6]_{4S}$ part and 0.11 ± 0.08 mm for the aluminum 2024-T3 part. With HBT at 20 °C, the out-of-plane displacement was 21 % higher for the composite $[PA6/CF\text{-}PA6]_{4S}$ part and 18 % higher for the aluminum 2024-T3, compared to the performance with HBT at 77 °C of 0.13 ± 0.06 mm and -0.62 ± 0.15 mm. The effect of SB is even higher with HBT at 150 °C, where increases of 45 % (0.16 ± 0.05 mm) and 46 % (-0.74 ± 0.11 mm) were observed for the composite $[PA6/CF\text{-}PA6]_{4S}$ part and for the aluminum 2024-T3, respectively. The effect of SB is relatively low for HBT at 77 °C, and this low out-of-plane displacement corresponds an improvement in mechanical performance. In this section, the variation in the global mechanical performance is discussed by considering the changes in the microstructure of the joined composite $[PA6/CF\text{-}PA6]_{4S}$ part (Section 6.1.1.2). As previously reported in Section 6.1.1.2, a lack of bonding between the deposited polymers and coating layers as well as misalignment of fiber for 20 °C and 150 °C, were observed, respectively. This is a valuable result useful to explain the variation of SB owing to HBT. The effect of SB is thoroughly discussed in Chapter 7.

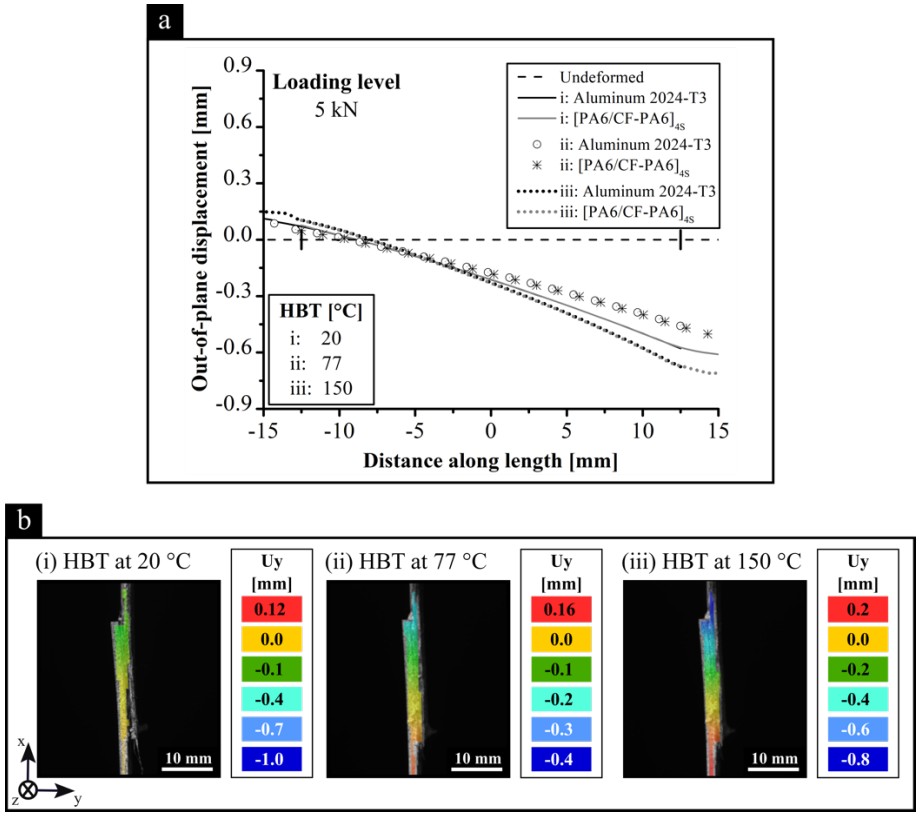

Figure 6-12 Out-of-plane displacement measured by a digital image correlation (DIC) system with HBT at 20 °C, 77 °C and 150 °C, highlighting (a) the profile, and (b) the image under lap shear quasi-static loading.

Table 6-2 Summary of the out-of-plane displacement results for the AddJoining hybrid joints measured on aluminum 2024-T3 and composite $[PA6/CF\text{-}PA6]_{4S}$ parts for HBT at 20 °C, 77°C and 150 °C under quasi-static loading.

HBT [°C]	Out-of-plane displacement [mm]	
	Aluminum 2024-T3 [a]	Composite $[PA6/CF\text{-}PA6]_{4S}$ [a]
20	0.13 ± 0.06	-0.62 ± 0.15
77	0.11 ± 0.08	-0.51 ± 0.19
150	0.16 ± 0.05	-0.74 ± 0.11

(a) Data from Figure 6-12

The overall mechanical performance is shown in Figure 6-13 for the chosen HBT range. The force-displacement curves for the different process variants showed a linear elastic behavior and similarity in stiffness prior to failure (Figure 6-13(a)). An exception is observed for HBT at 20 °C, where a change in slope of the curve (i.e. change in stiffness) is observed prior to failure. Such behavior may be related to the presence of gaps in the composite (refer to Section 6.1.1.2, Figure 6-4(3)) for HBT at 20 °C, which could play a role on decreasing the hybrid joint mechanical performance. For HBT at 77 °C, the ultimate lap shear force (ULSF) is 12.3 ± 0.1 kN (Figure 6-13(b)) with a displacement at break (DaB) of 2.48 ± 0.05 mm (Figure 6-13(c)). At 20 °C the mechanical performance decreased by 21 % in strength with ULSF (9.7 ± 0.2 kN, Figure 6-13(b)) and increased by 1 % in DaB (2.51 ± 0.07 mm, Figure 6-13(c)) and thus in ductility compared to HBT samples at 77 °C. With HBT at 150 °C the mechanical performance slightly decreased by 30 % in strength and 23 % in ductility compared to the HBT at 77 °C with ULSF of 8.6 ± 0.4 kN (Figure 6-13(b)) and DaB of 1.92 ± 0.15 mm (Figure 6-13(c)), respectively.

As a partial conclusion one can say that it is complex to compare these variations in mechanical performance by evaluating the local mechanical (i.e., hardness in Section 6.1.2) and physical-chemical changes (in Section 6.1.3) and phase changes in the PA6 (in Section 6.1.4). When external force is applied, the PA6 phase can change between α-PA6 and γ-PA6 or vice versa. The transition has been reported by Dencheva *et al.* [245], where the authors investigated the relationship between crystalline structure and mechanical behavior. The authors reported that γ-PA6 phase has a strong contribution to ductility and the presence of α-PA6 phase an increase in stiffness. To perform a similar comparison in this PhD work would be a difficult task, because the complexity increases when evaluating the mechanical performance of AddJoining hybrid joints, due to the effect of secondary bending. The mechanical performance of AddJoining hybrid joints is not only influenced by the crystalline structure of the polymer, but also by bonding formation, the presence of pores and secondary bending effects. This has been previously discussed in this chapter and is further discussed in Chapter 7 and the appendices (Appendix A.3 and Appendix A.4). Nonetheless it seems that a reduction in secondary bending influenced by the strong bonding formation on the joined composite part is a reasonable explanation to the higher quasi-static mechanical performance of AddJoining hybrid joints with HBT at 77 °C, as it leads to lower levels of out-of-plane displacements thus possibly leading to lower levels of stress in out-of-plane direction.

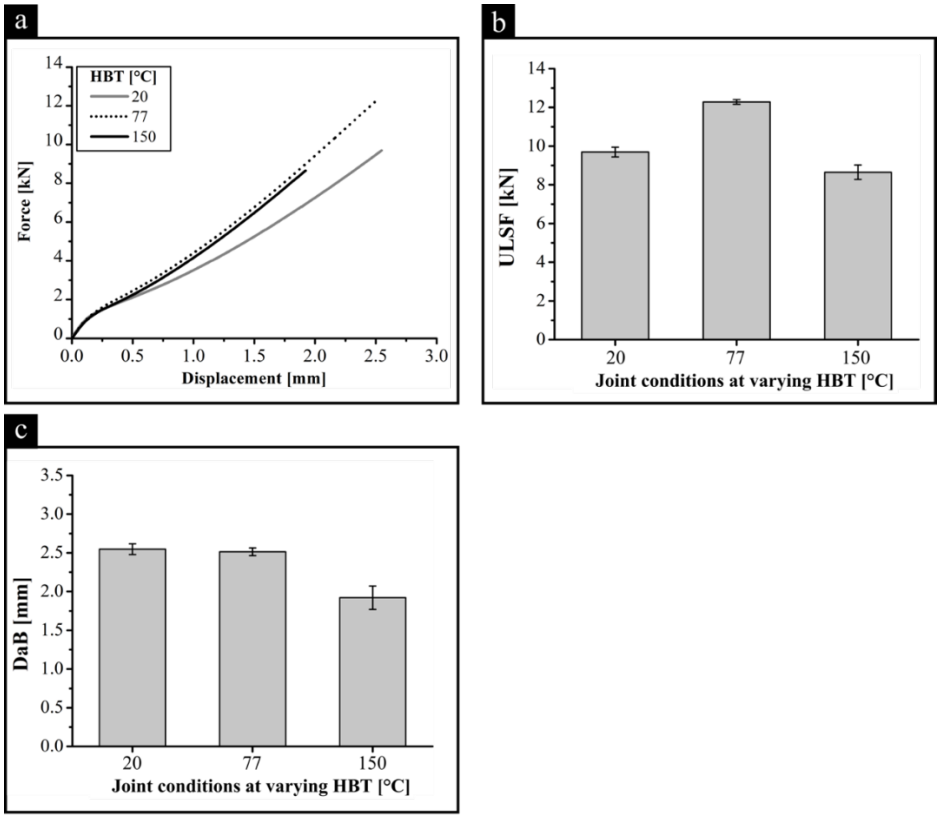

Figure 6-13 Mechanical performance of the AddJoining hybrid joints as a function of the selected HBT: (a) representative force-displacement curves, (b) average ultimate lap shear force, ULSF, and (c) displacement at break, DaB.

6.2 Process optimization for mechanical performance

By applying a derivative equation to the regression Equation (A-1) (see Appendix A.4) it is possible to obtain the maximum response. Furthermore, the set of optimized process parameters thus obtained corresponds to HBT at 77 °C and CT at 229 °C. The responses obtained by the statistical modeling of the AddJoining process, it corresponds to the point of maximum (Figure A.20 and Figure A.21, see Appendix A.4). In addition, this set of optimized process parameters was used for the investigation on Chapter 7 and Chapter 8. To conclude, in Figure 6-14 there is a comparison of the optimized joint condition and adhesively bonded reference joints produced with the same material combination and overlap length (12.5 mm). It shows an improvement of 76 % in ULSF on average, with 7.24 ± 0.4 kN and 5.5 ± 0.8 kN for the optimized joint and the adhesively bonded joint, respectively. As well as a 45 % improvement in DaB, with (2.1 ± 0.2) mm and (1.2 ± 0.2) mm for the optimized joint and the adhesively bonded joint, respectively. By comparing the optimized process parameters with those previously published by the author and collaborators in [17], there is an average improvement of 6 % in strength, which reflects the gain in mechanical performance due to the optimization procedure. Note that for the further investigations carried out and reported in Chapter 7 and Chapter 8, the overlap length was changed to 25.5 mm, based on the maximum ULSF response presented in Appendix A.5. The purpose of this was to reduce the number of variables within the process and structural parameters in this PhD work. According to the ASTM D3163 [211], it is permissible to change the single lap joint geometry in order to investigate possible variations in the failure mode.

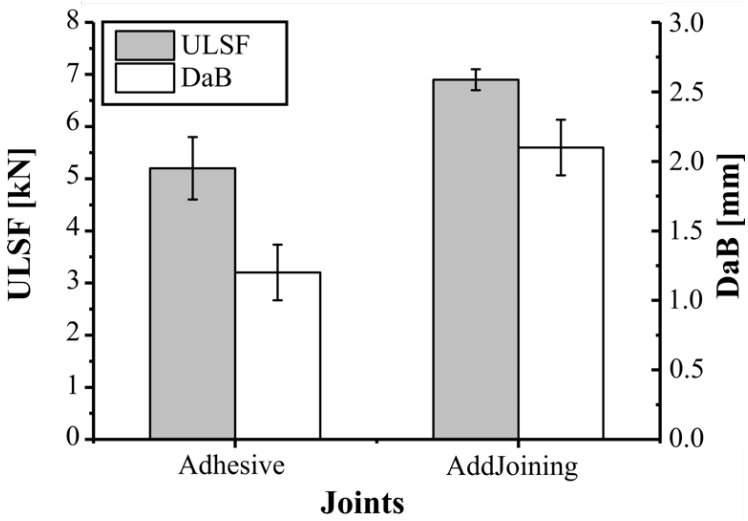

Figure 6-14 Mechanical performance of adhesively bonded joint and AddJoining hybrid joints, comparing average ultimate lap shear force, ULSF and displacement at break, DaB.

A comparison of the microstructures is depicted in Figure 6-15. Gaps are present between the adhesive and the first 3D printed layer of PA6 and the final thickness of adhesive is on average 32 µm, as shown in the microstructure in Figure 6-15(a). An ideal bond line thickness using structural adhesive is on average between 200 µm and 500 µm. Boutar *et al.* [250] reported that interface stresses are higher with a thin bond line adhesive thickness, which might reduce the load-carrying capability of the adhesive [250,251]. These results are corroborated by the investigation into other AddJoining process variants described in Appendix A.3 and published by the author and co-authors [187] using commercially available adhesive and a material combination of aluminum 2024-T3 and acrylonitrile butadiene styrene (ABS). As shown in Figure 6-15(b), close contact was achieved between the coating layer and the surface of the aluminum, and between the deposited polymer and coating layer. Therefore, the AddJoining hybrid joint shows that the primary bonding mechanisms between the printed layers are by thermal fusion and interlayer bonding. Keeping the temperature above the glass transition temperature assures good bonding between successively deposited layers. Hence, the result clearly demonstrates the effectiveness of the optimization procedure in finding the best set of joining parameters for the material combination used in this PhD work.

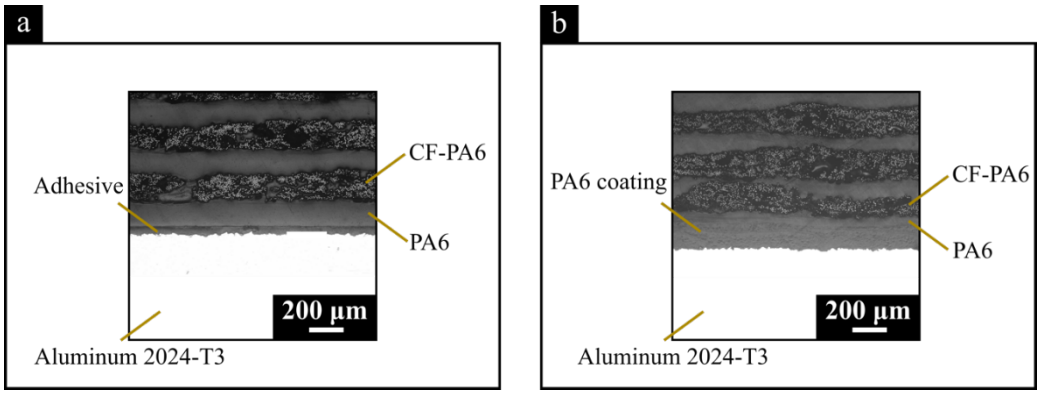

Figure 6-15 Microstructure of the overlap joint obtained by RLOM from (a) adhesively bonded joint, and (b) AddJoining hybrid joints.

To summarize, this chapter presented a thorough investigation of the bonding mechanisms of the materials used to form the AddJoining hybrid joints. The stepwise approach (Section 6.1.1.1) helped to support the understanding of the bonding mechanisms, which influenced the microstructural of the addjoined composite part (Section 6.1.1.2). For instance, the lack of smooth surface and presence of fault lines for HBT at 20 °C led to formation of gaps on the AddJoining hybrid joints. Another example is the misalignment of the carbon fiber reinforcement for HBT at 150 °C, where during the AddJoining process the fiber nozzle drags the previously deposited fiber bundles, due to low viscosity of the previous polymer layers. Such observation supports the variation in the mechanical performance discussed in Section 6.1.5. As previous discussed in this chapter, it is complicated to compare the variations in mechanical performance by evaluating the local mechanical (i.e., hardness in Section 6.1.2) and physical-chemical changes (in Section 6.1.3) and phase changes in the PA6 (in Section 6.1.4). However, physical-chemical and phase changes were correlated to further understand the AddJoining process and the importance on controlling the HBT. The heat factor used during the AddJoining process significantly influenced the local mechanical properties closer to the metal surface, i.e. the PA6 coating and PA6 first layer. The subsequent deposition of polymer in the AddJoining process caused a change to the chain configuration from random (amorphous) to an ordered (crystalline) structure. This observation was supported by phase changes in the PA6 (in Section 6.1.4), where it indicates the presence of two polymorphs of α-PA6 and γ-PA6. Such variation of polymer phase, it is associated with the presence of a thermal history of AddJoining, which affects the crystallinity and decrease in hardness of the case-study materials. Towards the end of the chapter, the mechanical behavior of a DoE/ANOVA optimized AddJoining hybrid joint (joint optimization in Appendix A.4) was compared with conventional adhesive bonding showing the potential of AddJoining in comparison to the state of the art manufacturing technology.

This thesis will further evaluate the mechanical properties of the AddJoining hybrid joints under quasi-static (Chapter 7), and fatigue loading (Chapter 8).

Chapter 7. Quasi-static behavior of hybrid joints

The mechanical properties of the AddJoining hybrid joints are further evaluated in this chapter. The overlap joint configuration was mechanically tested under lap shear quasi-static loading, as described in Section 4.3.8.1. In addition, damage evolution was assessed by a non-destructive method and this was correlated by microstructure analysis. This chapter will investigate in an exploratory study the effect of temperature on the mechanical behavior of the AddJoining hybrid joints. The finite element method (FEM) is applied to assess the stress concentration and failure regions using Hashin criteria to depict stress distribution and identify fracture mechanisms. The criteria are briefly presented in Appendix A.8.

7.1 Mechanical properties under lap shear loading at room temperature

Composite is well known for its outstanding in-plane properties, but it suffers from low transverse strength and shear stiffness in a single lap joint configuration [252]. This also applies to the 3D printed composite $[PA6/CF\text{-}PA6]_{4S}$ used in the AddJoining hybrid joints obtained after process optimization. The stacking sequence is $[+45°/0°/-45°/0°/+45°/0°/-45°/0°]_S$, where the lowest layer on the PA6 coating is a PA6 layer at +45° orientation in relation to the loading direction, but all the CF-PA6 layers are unidirectional with 0° orientation to the loading direction. Any change to CF-PA6 orientation modifies the AddJoining mechanical performance (presented in Appendix A.4), which directly affects the load transferability to the PA6 coating and thus the failure mode.

7.1.1 Secondary bending effect

In the present investigation, AddJoining hybrid joints are affected by the eccentricity of the load path under lap shear quasi-static loading, as illustrated in Figure 7-1(a). It follows by the PA6 coating in the overlap area transmits the load from the aluminum 2024-T3 component to the composite $[PA6/CF\text{-}PA6]_{4S}$ component. With an increase in tensile loading, the stress analysis of the single lap joint becomes highly nonlinear due to large deflections [253]. The maximum peaks of bending, peel and shear stresses occur at the ends of the aluminum 2024-T3 and composite $[PA6/CF\text{-}PA6]_{4S}$, as shown in Figure 7-1(a), represented by the overlap edges e_m and e_c respectively. From equilibrium and static calculations, the normal force (N), shear force (Q) and bending moment (M) can each result in stress components (Figure 7-1(b)). Hence, the state of the stress in the AddJoining hybrid joints is not purely axial stress, but also shear and peel stresses, as illustrated in Figure 7-1(c).

In this regard, the eccentricity of the load path and differences in material stiffness produce bending moments, in addition to tension in the overlap joining area [254,255]. This results in a phenomenon known as secondary bending (SB), which is defined as the ratio of bending strains to axial strains [256]. It is also approximately related to the lateral deformation of the neutral line, which is also known as out-of-plane displacement. Schijve [257] reported the importance of secondary bending predictions using a neutral line model and its applicability for design principles against fatigue [258]. However, it is beyond the scope of this PhD work to develop a neutral line model for the AddJoining hybrid joints.

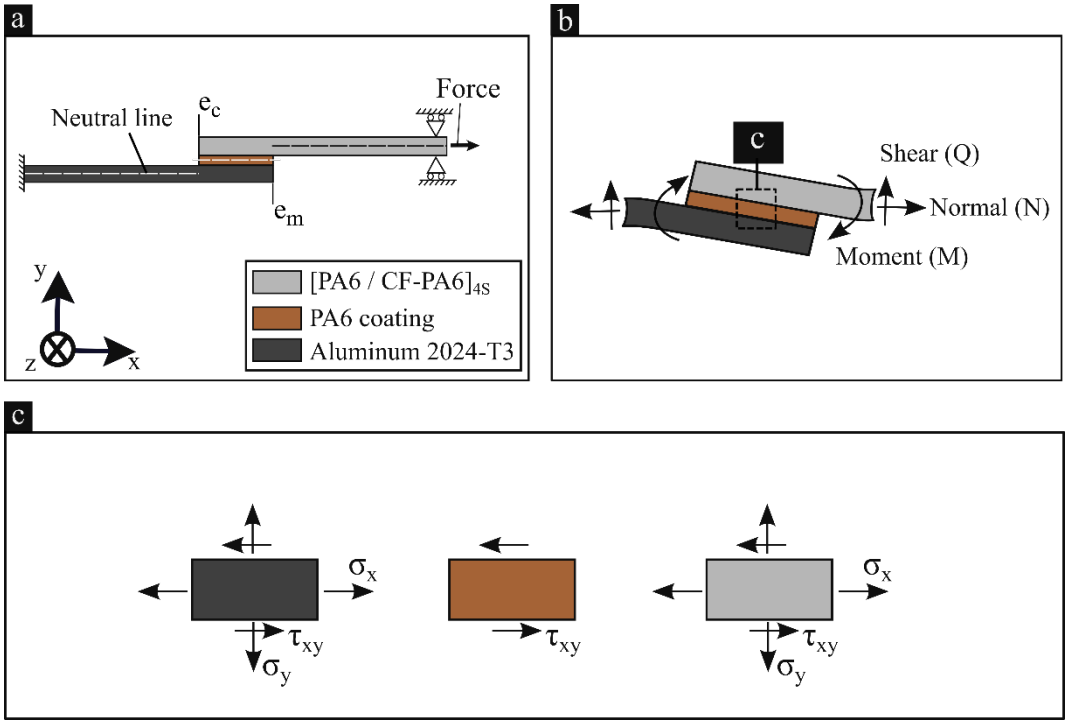

Figure 7-1 Schematic of (a) AddJoining hybrid joints, indicating possible areas with high deformation e_m and e_c, (b) overlap joint deformation with (c) free bocy diagrams of the overlap (adapated from [253]).

From the SB evaluation, the out-of-plane displacements shown in Figure 7-2 were evaluated by a digital image correlation (DIC) system. At first the out-of-plane displacement varies linearly through the bonding area. The dissimilarity of material stiffness is clearly seen in the measured maximum out-of-plane displacement during this test. SB was evaluated for three different load levels during the mechanical performance tests, e.g. at 10 %, 50% and 90% of ULSF (Figure 7-2). From the DIC images in Figure 7-3, it can be seen the PA6 coating holds both parts together, withstanding maximum deformation prior to delamination of the composite [PA6/CF-PA6]$_{4S}$ part. At 10 % of ULSF, i.e. 1.23 kN, the initial deformation corresponds to 0.03 mm for the aluminum 2024-T3 part and 0.23 mm for the composite [PA6/CF-PA6]$_{4S}$ part (Figure 7-3 (i)). At 50 % of ULSF, i.e. 6.15 kN, the out-of-plane displacement increases by a factor of four (0.12 mm) in the metal part and by a factor of 2.3 (0.53 mm) in the composite part (Figure 7-3(ii)). At the third level 90 % of ULSF, i.e. 11.1 kN, the relatively low displacement corresponds to 0.16 mm in the aluminum 2024-T3 part and 0.74 mm in the composite [PA6/CF-PA6]$_{4S}$ part (Figure 7-3(iii)). Given the higher metal stiffness of on average 76 GPa, the low transversal displacement is no surprise. However, the high deformation is driven by the composite part, which has an average stiffness of 35.7 GPa. It is also interesting to note that a reduction of the SB effect is achieved by increasing the overlap length, as presented in Appendix A.5. By increasing the overlap length from 12.5 mm to 25.5 mm, a decrease of 62.5 % of the out-of-plane displacement was observed with aluminum 2024-T3. The overlap length helps to distribute the shear distribution effectively, causing an increase in the ULSF [259,260]. According to Zou, Shahin and Taheri [261], the stress concentrations on the overlapping ends decrease by increasing the overlap length due to redistribution of stresses along the overlap length and width. Therefore, in this PhD work, based on an engineering approach, the maximum ULSF for the largest overlap length of 25.5 mm was selected for thorough investigation into the mechanical performance, as shown in Appendix A.5.

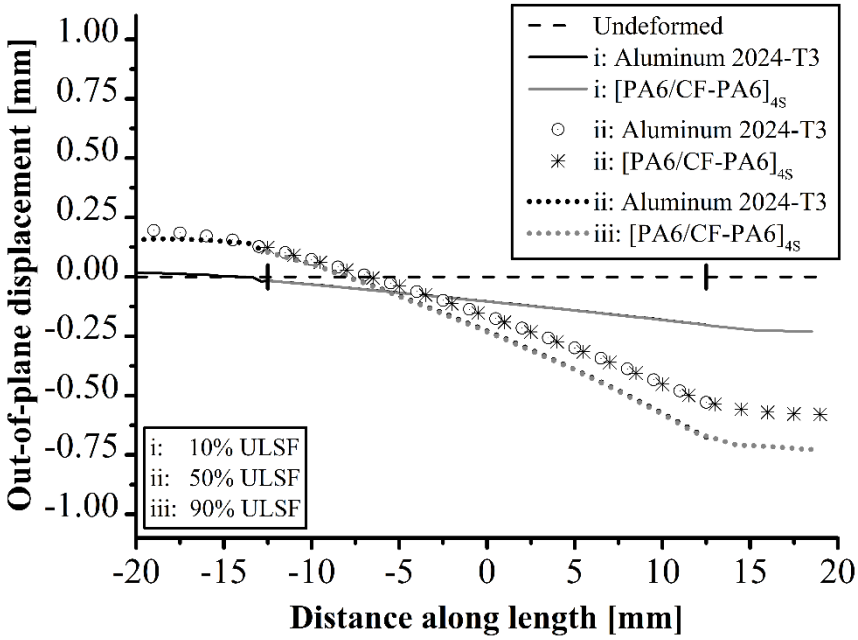

Figure 7-2 Profile for the out-of-plane displacements under lap shear quasi-static loading measured by a digital image correlation (DIC) system for three different loading levels at 10%, 50% and 90% of ULSF.

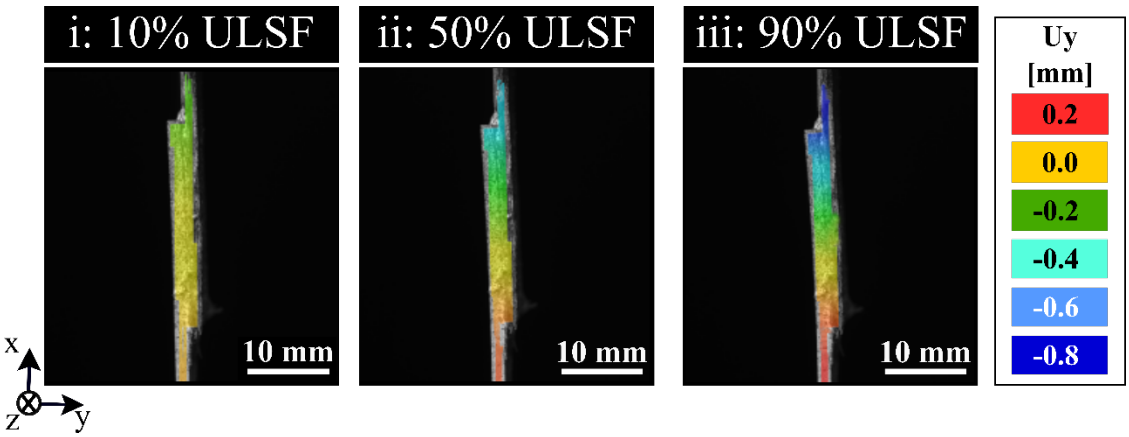

Figure 7-3 Images from the out-of-plane displacements under lap shear quasi-static loading measured by a digital image correlation (DIC) system for three different loading levels at 10%, 50% and 90% of ULSF

7.1.2 Stress distribution in the overlap area

The results can be further analyzed by stress distribution in the overlapping area using an FEA model. The model is briefly described and its validation is presented in Appendix A.8. Figure 7-4(a) shows three locations in the overlap joining area: (*Left*) closest to the composite $[PA6/CF\text{-}PA6]_{4S}$ part's edge, (*Middle*) at the center of the composite, and (*Right*) closest to the aluminum 2024-T3 part's edge. At these three locations, the axial stress distribution (in the X-direction) was obtained through the thickness (in the Y-direction) and this helped to identify the locations with high stresses. In all three locations, the reinforced CF-PA6 layer carried most of the load in the composite $[PA6/CF\text{-}PA6]_{4S}$ as is presented for *Left* (Figure 7-4(b)), *Middle* (Figure 7-4(c)), and *Right* (Figure 7-4(d)).

Another observation confirms the SB phenomena by comparing the stress distribution at the three locations. The axial stress distribution is nearly constant (300 MPa) at the center of the overlap area, as shown in Figure 7-4(c). The SB phenomena are easily observed by comparing the stress distribution at the edges in Figure 7-4(b) and Figure 7-4(d), representing the stress flow from loading end to unloading end. Due to the SB effects at the unloading end the aluminum 2024-T3 only withstood a stress magnitude of 305 MPa (Figure 7-4(e)), which is below its base material yield strength of 350 MPa [189].

For instance, at the loading end in Figure 7-4(d) on the bottom surface (distance -2 mm in the Y-direction) of the aluminum 2024-T3 part, the axial stress is compressive with a magnitude of 1.4 MPa (Figure 7-4(f)). The axial stresses in the aluminum 2024-T3 part change from compressive to tensile closer to the PA6 coating (0.19 MPa). The stress then gradually increases as the ends of the overlap are approached [260,262]. In this regard, the axial stress reached 17 MPa gradually increases to 85 MPa from the PA6 coating to PA6 layer of the composite $[PA6/CF\text{-}PA6]_{4S}$ (Figure 7-4(g)). The axial stress is significantly higher for the PA6 layer with a base material ultimate strength of 54 MPa [192]. Moreover, in the second layer the CF-PA6 reached 1254 MPa, which is also high compared to its base material strength of 700 MPa [192]. It seems that the high stresses in the composite part are due to the simplified FEA model, because it is not possible to consider in a two-dimensional plane the stress at different orientations ±45°. Therefore, the PA6 layer is modeled as an isotropic polymer, as described in the Appendix A.8. However, for the purpose of the model, it shows the large gradient in the stresses in the Y-direction, especially near the end of the overlap. This also gives qualitative hints for a possible failure location to help in the fracture analysis (Section 7.3).

Figure 7-5(a) is a schematic of the joining region used to evaluate the shear and out-of-plane stress along the overlap length. According to Tsai and Morton [252], the peak shear stress and out-of-plane stresses towards the edges of the overlap are caused by a variation in tensile deformation along the overlap length of the parts within single lap joints. A similar result can be seen in the stress profiles of shear stress along the overlap length in Figure 7-5(b) and out-of-plane stress in Figure 7-5(c).

Due to the SB effect, the out-of-plane stress (Figure 7-5(c)) distribution was almost symmetrical and peak stress is reached at the end of the overlap length, followed by a compressive region in the center of the overlap join area [263–265]. A lack of symmetrical peak stress and shear stress is attributed to the mismatch in stiffness of the materials of the aluminum 2024-T3 part and composite $[PA6/CF\text{-}PA6]_{4S}$ part [266]. Figure 7-5(b) shows the shear stress profiles with a fairly symmetrical behavior caused by bending with eccentricity of the load path. The CF-PA6 layer shows a high shear stress magnitude with 15.4 MPa in the center of the overlap joining area, which is 103 % more than the shear strength of the CF-PA6 base material [267]. It can be seen that in the PA6 coating (20.3 MPa) and PA6 layer (16.4 MPa) shear stress is relatively lower than for the PA6 base material (60 MPa, [192]). This analysis suggests that interfacial transverse shear stresses do not influence failure of the PA6 coating and PA6 layer, rather it indicates failure of the CF-PA6 layer.

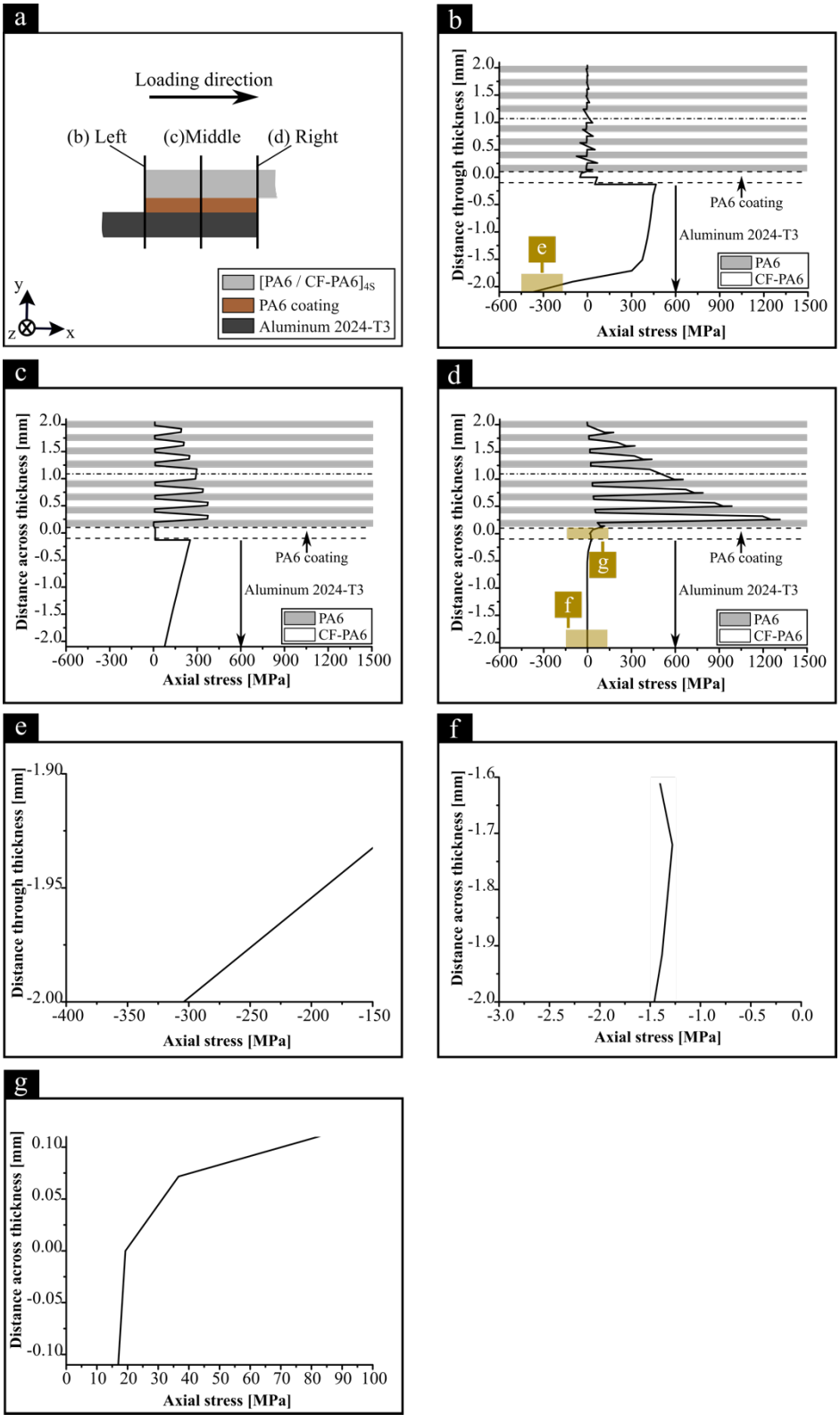

Figure 7-4 (a) Schematic of three different locations in the overlap joining area, axial stress distributions: (b) left, (c) middle, and (d) right; (e) Inset graph for the region marked in (b); (f) and (g) Inset graphs for the regions marked in (d).

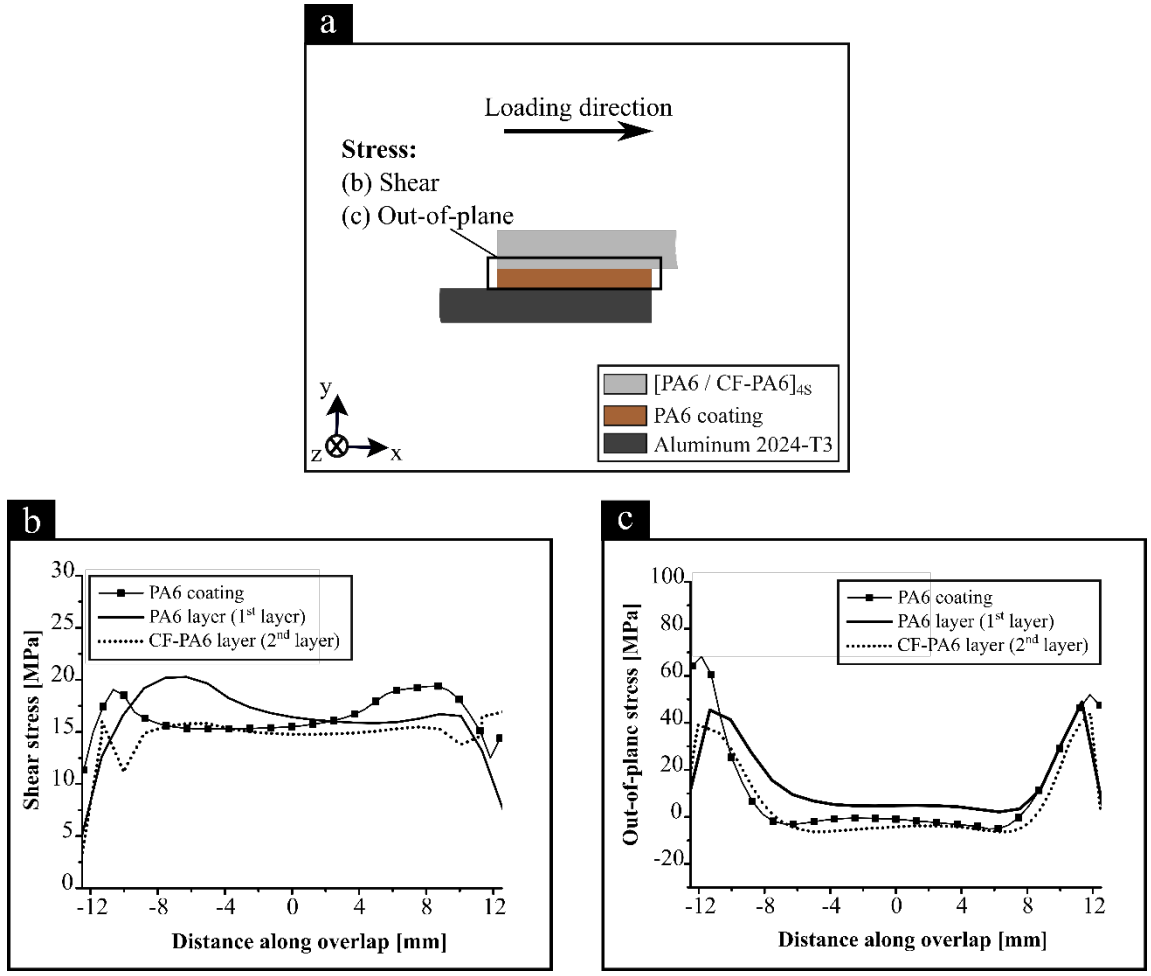

Figure 7-5 (a) Schematic of the joining region, comparing (b) shear stress, and (c) out-of-plane stress for the PA6 coating, PA6 layer (first layer), and CF-PA6 layer (second layer) along the overlap length.

For the out-of-plane stresses, Figure 7-5(c) shows the stress decreases from the edge to a certain distance near to the center of the overlap joining area. Afterwards, it decreases gradually from the outer edges to the inner overlap area. As can be seen, in the PA6 coating it was 64.1 MPa on the composite edge (-12.5 mm in the X-direction) and the stress increased 6.2 % at -11 mm in X-direction followed by a large descending gradient until reaching a compressive region with 0.6 MPa in the center of the overlap joining area. The stress distribution is roughly symmetrical for the PA6 coating. A similar trend is observed for both the PA6 layer and the CF-PA6 layer, but with different stress magnitudes, as shown in Figure 7-5(c). According to the literature, out-of-plane mechanical strength is on average 33 MPa and 31 MPa, for CF-PA6 and PA6, respectively [192,193]. It is worth noting that the out-of-plane mechanical properties are sensitive to peel stresses, due to extensive fiber-matrix separation in composites [268]. Therefore, as was observed in this study, the PA6 and CF-PA6 layer could also fail by peel stress due to the bending effect during quasi-static loading in the AddJoining hybrid joints. In fact, this observation will help to assess the failure region during the fracture analysis in Section 7.3.

7.1.3 Mechanical performance and failure mechanisms

The results presented in Figure 7-6(a) are typical for mechanical tests of AddJoining hybrid joints under lap shear quasi-static loading. Figure 7-6(b) shows the failure path representing an interfacial intralaminar failure of a fracture in the composite $[PA6/CF\text{-}PA6]_{4S}$ part (to be discussed in Section 7.3). Furthermore, the strain fields were evaluated at three different stages, corresponding to 10 % of ULSF (1.23 kN), 50 % of ULSF (6.15 kN) and 90 % of ULSF (11.1 kN). These strains were measured using the DIC system on the surfaces in the overlap area of the composite $[PA6/CF\text{-}PA6]_{4S}$ (Figure 7-7(a)) and aluminum 2024-T3 (Figure 7-7(b)). The major strains were found at points near to the edges of the overlap, and this will help evaluating damage initiation and propagation during mechanical testing. The major strains are also quantitatively plotted as graphs from their values at the four end points of the overlapping area, as presented in Appendix A.9. The intention is to verify asymmetric strain evolution during quasi-static loading that is caused by a 90° road orientation contour and the SB effect, and this is further discussed in this section.

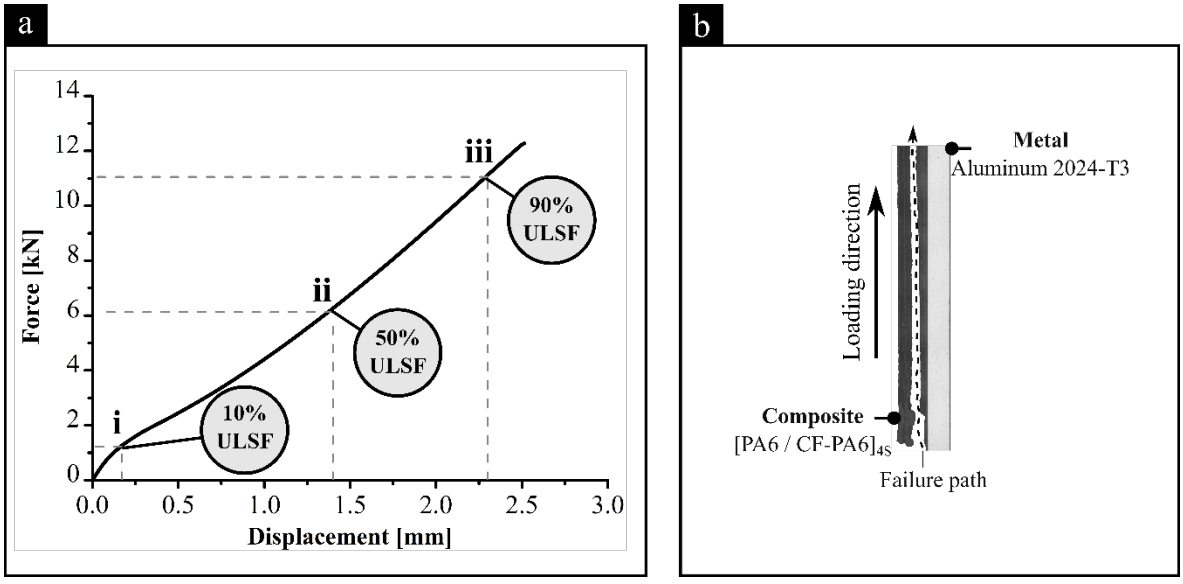

Figure 7-6 (a) Representative force-displacement curve with the (b) typical failure mode of the AddJoining hybrid joints.

A rough linear elastic behavior was observed in the AddJoining hybrid joint until 10 % of the ULSF was reached. The highest deformation took place at the end of overlapping area, corresponding to the composite $[PA6/CF\text{-}PA6]_{4S}$ edge. At this location, a contour is formed with a 90° orientation, creating a weak link for load transferability. The explanation for this lies in the distribution of road orientation, where road deposition at 90° is inevitably formed in the overlap area (a limitation of the used 3D-printer), which is perpendicular to the testing loading direction and this is known to be detrimental. During 3D printing the nozzle trajectory forms a road deposition at 45° that creates a region with a lack of material when it reaches the outer contour. Eiliat and Urbanic [269] reported a similar observation, but by applying an algorithm to change the trajectory of road deposition it was possible to minimize voids in these regions. In terms of microstructure the elastic regime is overcome by breaking adhesive forces in the fiber matrix, where the deformation takes place. This observation is discussed further in Section 7.3.

At load levels, greater than 10 % of ULSF the decreasing stiffness is caused by damage evolution during quasi-static loading (Figure 7-8). The stiffness measured by the force-displacement is displayed in Table 7-1. At 50 % of ULSF stiffness is 69 % lower compared to stiffness at 10 % of ULSF. At 50 % of ULSF the SB starts to be visible, as shown by comparing the deformation on the composite surface (Figure 7-7(a)) with deformation on the metal surface (Figure 7-7(b)). From the DIC image shown in Figure 7-7(a), the damage propagates asymmetrically from the end of the composite overlap towards the opposite edge in the load direction. The strain is quantitatively lower on the metal side due to its higher stiffness. However, the composite side is marked by high deformation. At this point the strain is further distributed over the edges of the composite in the overlap area.

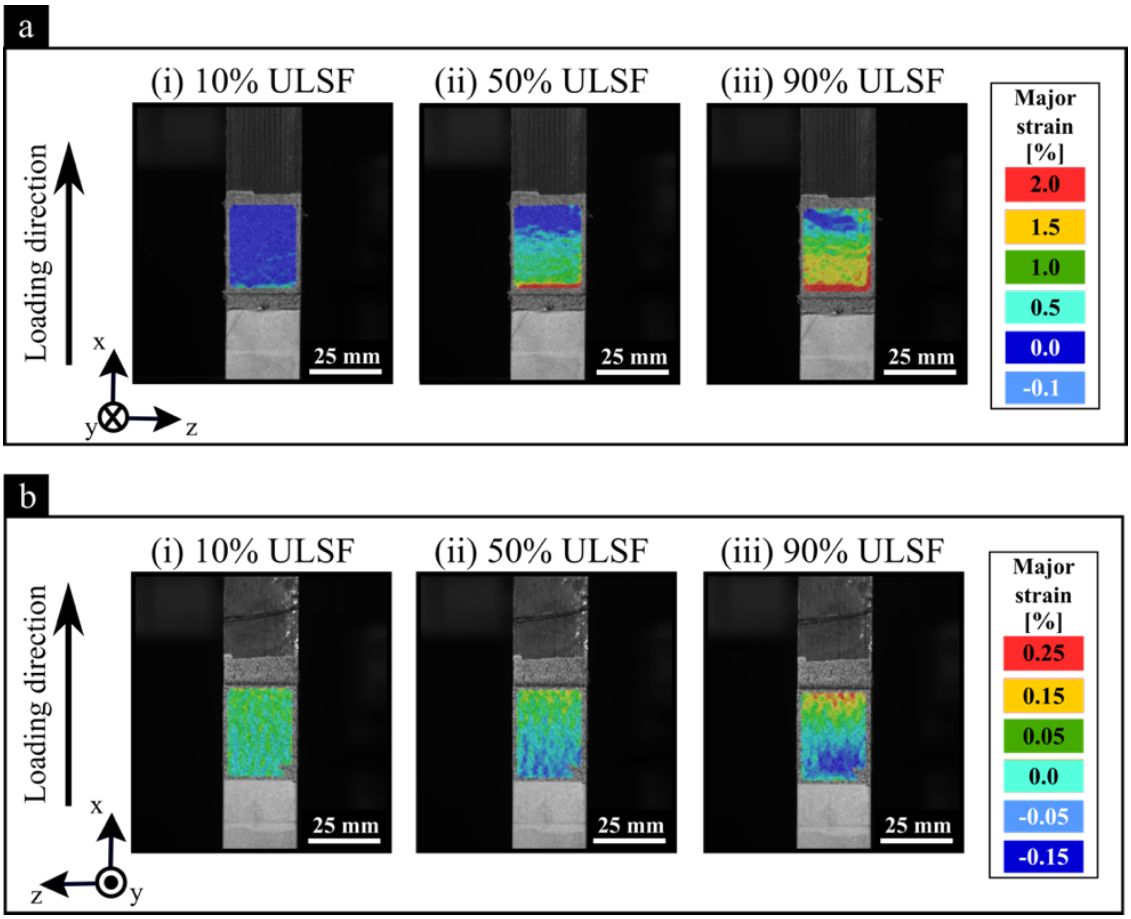

Figure 7-7 Strain fields measured by a digital image correlation system on the overlap area (a) composite [PA6/CF-PA6]$_{4S}$ surface, and (b) aluminum 2024-T3 surface of AddJoining hybrid joints under lap shear quasi-static loading.

At load levels above 50 % of the failure load, damage propagates through the composite part. The strain further increases, as shown at 90 % of ULSF. The force-displacement curves show unchanged stiffness between 50 % of ULSF (5.9 kN/mm) and 90 % of ULSF (5.4 kN/mm), as is also shown in Figure 7-8. It is common for gradual failure of the central layers of composites, by multiple fiber breakages and consequently a dispersal of delamination through the composite part. Thus, it leads to unchanged stiffness caused by unidirectional fibers that have fragmented into lengths close to their critical length [270]. Moreover, if the AddJoining hybrid joint is loaded above 90 % of ULSF, the damage saturation eventually leads to failure.

Table 7-1 Stiffness for the three load levels selected from the force-displacement curve of representative AddJoining hybrid joints under lap shear quasi-static loading.

Stage	Fraction of ULSF [%]	Force [kN]	Stiffness [kN/mm]
i	10	1.23	8.7
ii	50	6.15	5.9
iii	90	11.1	5.4

Figure 7-8 shows the results of loading-unloading experiments at the three selected load levels. Hysteresis evolves and this helps to evaluate the damage initiation and evolution during quasi-static loading. The same graph shows permanent deformation develops, which is caused by initial debonding of the fiber-matrix and delamination between the layers. The difference between the monotonic and load-unload cyclic loading behavior is due to molecular rearrangement at the microscopic level [271]. The presence of pores within the composite part can cause a variation in stiffness that do not match the monotonic curve. The increasing loading causes the plastic deformation to extend from 0.02 % at 10 % of ULSF to 1.12 % at 90 % of ULSF. To further explore the damage, Figure 7-9 shows the microstructure and non-destructive testing used, as described in Section 4.3.4 and Section 4.3.9, respectively.

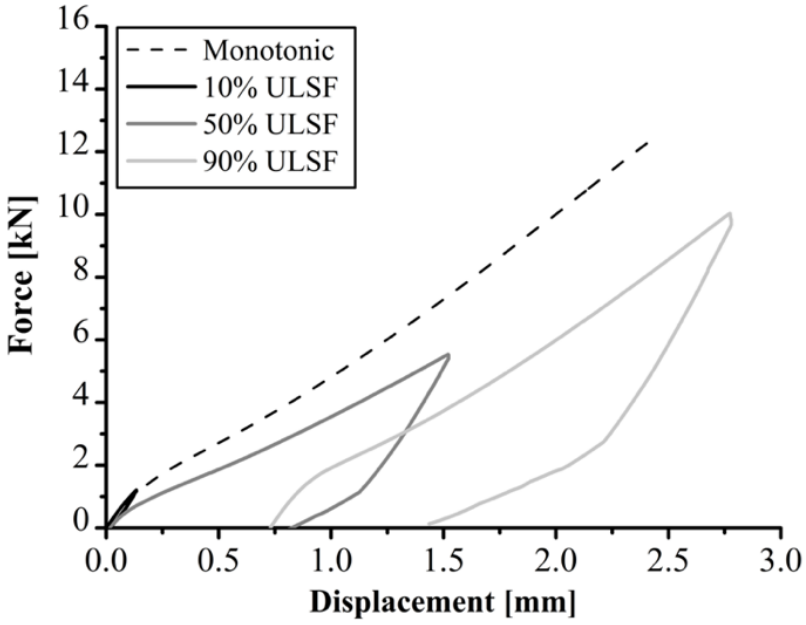

Figure 7-8 Loading-unloading at the three load levels selected from the force-displacement curve of representative AddJoining hybrid joints under lap shear quasi-static loading.,

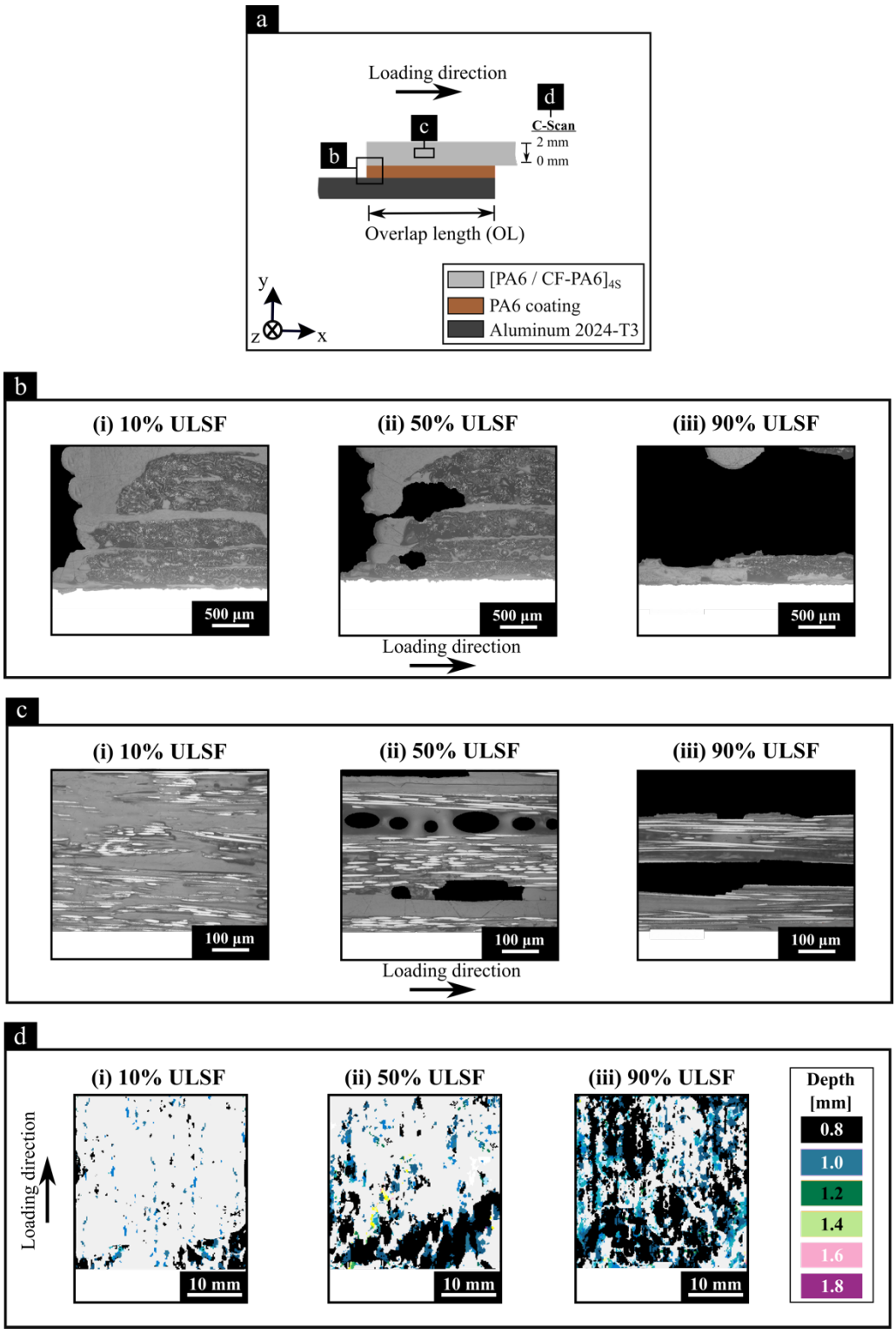

Figure 7-9 (a) Schematic of the locations to investigate damage evolution at the three selected load levels obtained from loading-unloading experiments; RLOM micrographs of the composite [PA6/CF-PA6]$_{4S}$ part (b) at the overlap ending, and (c) at the center; (d) C-Scan images from the overlapping section of the composite [PA6/CF-PA6]$_{4S}$ part. 0 mm is the interface of aluminum 2024-T3 and PA6 coating / [PA6/CF-PA6]$_{4S}$.

Figure 7-9(a) indicates the locations of interest for investigation of the damage evolution at the three loading levels. After testing, the AddJoining hybrid joints were characterized by RLOM and C-Scan. For the C-Scan measurements, the defect depth was considered as 0.0 mm as the interface of aluminum 2024-T3 and PA6 coating / $[PA6/CF\text{-}PA6]_{4S}$ (as shown Figure 4-13 in Section 4.3.9.1). Furthermore, it is important to note that each loading-unloading cycle was performed with a different replicate. The purpose of this is to avoid any damage accumulation from the previous cycle. From the microstructure after these tests, as shown in Figure 7-9(b) and Figure 7-9(c), it is not possible to identify any visual damage at 10 % of ULSF (Figure 7-9(b-i)). However, the loading-unloading curve indicates initial permanent deformation is caused by damage. From the C-Scan image in Figure 7-9(d-i)) it is possible to identify an area of damage (represented by black color voids) that is 9.1 ± 0.5 % at 10 % of ULSF. During AddJoining procedure this was stressed by the presence of intrinsic pores in the CF-PA6 layers, caused by a lack of fusion between resin and fiber. Those areas with a lack of resin can cause stress concentrations and may produce initial damage [272]. Despite this, the excellent mechanical performance of AddJoining hybrid joints results from strong mechanical interlocking that is achieved between the PA6 coating and the metal substrate. The PA6 coating remains undeformed, as is shown in the fracture analysis in Section 7.3. Moreover, the optimal bonding formation of subsequent 3D printed layers is achieved by intermolecular diffusion, counteracting the effects of pores in the CF-PA6 layers. At 50 % of ULSF the damage becomes visible on the contour, due to debonding of the CF-PA6 layer with 90° orientation (Figure 7-9(b-ii)). Toward the central layers it suffers multiple delamination failures between the PA6 layer and CF-PA6, governed by shear deformation (Figure 7-9(c-ii)). The extent of permanent deformation is also confirmed by an increase in damage area to 36.3 ± 0.8 % as shown in Figure 7-9(d-ii). The damage further propagates through the composite and delamination of the central layers takes place as shown in Figure 7-9(c-ii) at 50 % of ULSF and in Figure 7-9(c-iii) at 90 % of ULSF. At this stage, the damage area has reached 66.1 ± 1.4 % as illustrated in Figure 7-9(d-iii). The final failure mode, namely is a interfacial-intralaminar failure mode [273,274], was shown in Figure 7-6(b).

This type of failure mode is a combination of interlaminar and intralaminar failure modes. It is caused by the presence of intrinsic voids in an intralayer of the CF-PA6 layer, leading to high stress concentration zones [275]. Moreover, the high stress transfer from the reinforced layer (CF-PA6) to the unreinforced layer (PA6) promotes a high stresses distribution and causes interfacial delamination between the CF-PA6 and PA6 layers as shown in Figure 7-4. Furthermore, it is also governed by high shear deformation and out-of-plane deformation due to the voids and weaknesses of the layers within the composite $[PA6/CF\text{-}PA6]_{4S}$ part as it was explained for Figure 6-4 (Section 6.1.1.2). To further the failure, a detailed evaluation of fracture mechanisms suggests is discussed in Section 7.3.

7.2 Effect on mechanical properties at different temperatures

Previously, the mechanical performance was evaluated at room temperature (20 °C). Nonetheless, it is well known that polymeric materials can exhibit a significant temperature dependency of their mechanical properties. For instance, when subjected to temperature above glass-transition temperature, thermoplastic-based composites can significant decrease the stiffness and strength whereas the failure strain increases [276–278]. Therefore, in this section, a preliminary investigation on the effect of temperature was evaluated for the AddJoining hybrid joints. To investigate the effects of temperature, the AddJoining hybrid joints were submitted to three alternative temperature levels, specifically -55 °C, 70 °C and 120 °C. The mechanical testing described in Section 4.3.8.1 was then

carried out. Figure 7-10(a) shows representative the force-displacement curves after these different temperatures. For a better visualization, the ULSF and DaB depicted in Figure 7-10(b) were obtained from the force-displacement curves (Appendix A.10). At the lowest temperature of -55 °C the mechanical performance had 32 % less strength with ULSF 8.3 ± 0.6 kN and 64 % less ductility with a DaB of 0.89 ± 0.04 mm compared to room temperature with ULSF of 12.3 ± 0.1 kN and DaB of 2.48 ± 0.05 mm.

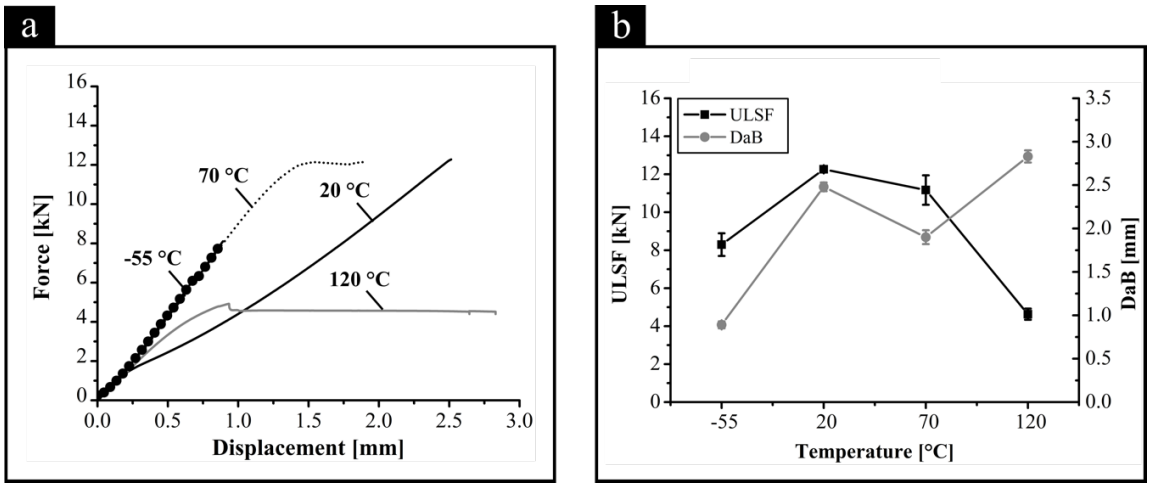

Figure 7-10 Mechanical performance of the AddJoining hybrid joints as a function of the selected temperature range: (a) representative force-displacement curves, and (b) average ULSF and DaB.

In this PhD work, the reduction in mechanical performance of the AddJoining hybrid joints was found to be caused by two main reasons at low temperature: First the PA6 coating is compromised due to the formation of microcracks due to the hard and brittle state caused by amorphous phase [279–281], as previously discussed in Chapter 6. Second, high thermal residual stresses may cause interfacial microcracks in the PA6 coating due to contraction of the aluminum part leading to a possible tensile reaction of the composite due to the different coefficient of thermal expansion [282,283]. The composite used has unidirectional carbon fiber, where the coefficient of thermal expansion is negative ($\alpha_1 = -0.9 \times 10^{-6}\ K^{-1}$) in the fiber direction and positive ($\alpha_2 = 27 \times 10^{-6}\ K^{-1}$) in the transverse direction [284]. Other authors have reported a reduction of mechanical performance for CFRP at cryogenic temperatures below its glass transition temperature [278]. For the material selected in this PhD work, the glass transition temperature of the polymer is on average 57 °C. At temperatures between -55 °C and 20 °C, the mechanical behavior of the AddJoining hybrid joints was a linear response before an abrupt failure as illustrated in Figure 7-10(a). At 70 °C in this figure the representative force-displacement curves mostly exhibit a linear behavior until failure followed by a non-linear response closely before failure at a temperature above glass transition [285]. These phenomena are caused by molecular mobility in the polymer at temperatures above its glass transition temperature, i.e. the molecules become mobile leading to softening and flexibility of the material [6,286]. That is why at 70 °C these mechanical properties had slightly lower values, with strength reduced by 9 % and ductility by 23 % compared to room temperature, ULSF of 11.2 ± 0.7 kN and DaB with 1.9 ± 0.08 mm. At the higher temperature of 120 °C the strength decreased drastically by 62 % with ULSF of 4.6 ± 0.3 kN and DaB increased 14 % to 2.83 ± 0.07 mm in comparison with the performance at room temperature. For the selected temperature series, details of the fracture surface images are depicted in Section 7.3.

The average energy absorbed during testing is presented in Figure 7-11 that was used for analysis of the mechanical performance at the selected temperatures cited in this chapter. This considers the area beneath the curve from the force-displacement curves, because temperature dependence is a characteristic of polymer and the material is a part from the AddJoining hybrid joints. It is possible to observe the variation in energy absorption within the selected range of temperatures. At the lowest temperature -55 °C the energy absorbed was 3.5 ± 0.2 J, corresponding to 76 % less energy absorption compared to room temperature. The fracture surface at this temperature indicates adhesive-cohesive failure caused by severe cracking of the PA6 coating and matrix within the composite part (Figure 7-16, discussed in Section 7.3). At room temperature, the energy absorbed was the highest (14.8 ± 0.2 J) in the range of selected temperatures used in this PhD work. This time the fracture surface indicates an interfacial-intralaminar failure mode by delamination of the composite part. At 70 °C the energy absorbed reduced by 2 % (14.5 ± 0.1 J) compared to the highest absorption at room temperature. The fracture surface shows no significant changes on the fracture mechanisms. At the highest temperature of 120 °C a reduction in load carrying occurred and the energy absorbed fell to 11.4 ± 0.2 J.

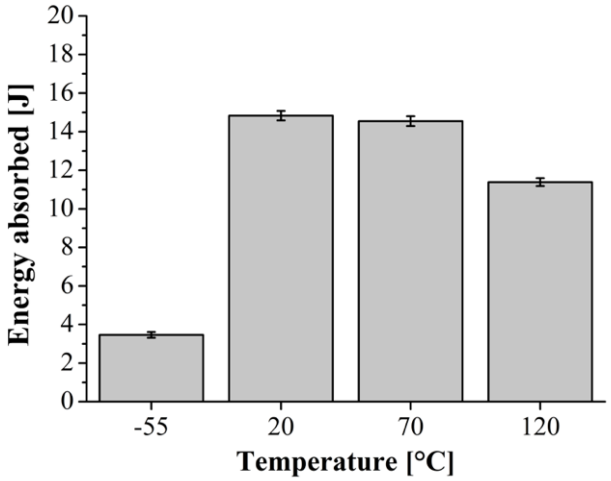

Figure 7-11 Average energy absorbed during mechanical performance testing of the AddJoining hybrid joints as a function of the selected temperature series.

To summarize, under cryogenic conditions at -55 °C the micromechanisms of damage are characterized by fiber-matrix interface weakness, which causes delamination and the amorphous matrix to crack, thereby reducing the mechanical performance. At room temperature, linear response is caused by the low mobility of the polymer chains leading to abrupt failure. The micromechanisms of damage observed at room temperature are a combination of stresses leading to interfacial-intralaminar failure mode by delamination of the composite part. For 70 °C and 120 °C, a non-linear behavior becomes pronounced and stiffness decreases with increasing temperature as the strength decreases. At 120 °C, the failure resulted from extensive plastic deformation of the polymer. This was observed by the presence crazing indicating ductile failure (as it will be discussed in Section 7.3, Figure 7-17). Crazes are easier to identify by the formation of cavitation microvoids, as it was clearly seen for the fracture surface of the AddJoining hybrid joint tested at 120 °C. Therefore, it seems that the composite part stiffness is more sensitive to higher temperatures within this temperature range, as PA6's glass transition temperature (57 °C) is substantially exceeded.

7.3 Fracture surface analysis

Before moving on to the discussion, closer examination of fracture is required. A failure macrograph using RLOM is displayed in Figure 7-12(a) and the predicted damage pattern using FEA in Figure 7-12(b). The stress distribution obtained from this simulation indicates excessive out-of-plane and shear stresses, as previously observed, leading to delamination of the composite. In this regard, the simulation qualitatively shows the damage path is similar to the experimental results. The predicted damage progression is presented using Hashin criteria in Appendix A.8. The delamination observed in loading-unloading experiments was discussed in Section 7.1.3. To further characterize the failure, fracture morphologies were analyzed using SEM. The strain evolution observed in Section 7.1.3 and Appendix A.9 indicates macro damage at the edge of the overlap in the composite $[PA6/CF\text{-}PA6]_{4S}$ part, as previously reported. As strain distribution is asymmetric, damage propagation is not only caused by delamination. The AddJoining hybrid joint is rather complex, due to the high degree of interaction between individual failure mechanisms [20]. The micromechanisms involved in failure were determined by evaluating the SEM surface fractures in metal part (Figure 7-13 and Figure 7-14) as well as in the composite $[PA6/CF\text{-}PA6]_{4S}$ part (Figure 7-15) at room temperature. Furthermore, in this section, failure mechanisms for the fracture at low temperature (at -55 °C, Figure 7-16) and high temperature (at 120 °C, Figure 7-17) are briefly discussed.

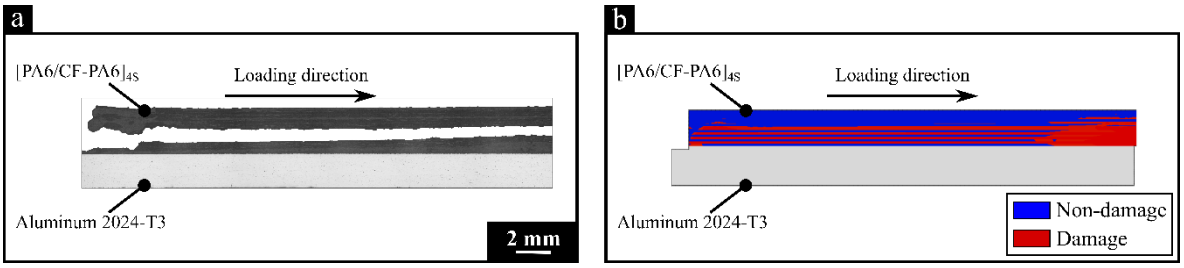

Figure 7-12 Overview of a fractured AddJoining hybrid joint, and (b) predicted damage pattern applying Hashin criteria using FEA.

Figure 7-13(a) illustrates an overview of fractured composite that remains attached to the aluminum 2024-T3. The interfacial-intralaminar failure mode indicates strong mechanical interlocking between the PA6 coating layer and the surface of the aluminum 2024-T3, and between the 3D printed composite $[PA6/CF\text{-}PA6]_{4S}$ and the PA6 coating. As previously reported, the damage is a combination of matrix failure and fiber failure. Nonetheless, some further small features can be observed in the SEM image. Figure 7-13(b) shows a contour with carbon fibers orientated 90° (highlighted by blue arrows). The carbon fiber is detached from the PA6 contour, also orientated 90°, leaving a plastically deformed PA6 matrix, also known as elongated fibrils, i.e. ductile feature, that are deformed in loading direction (Figure 7-13(c)). Towards the center of the overlap region in Figure 7-13(d) there are fiber bundles buckles in-plane phase, caused by compressive stresses resulting from the SB effect. From the image, it can be seen that the fiber bundles buckle in a lateral direction surrounded by fiber-matrix that remains attached. During damage progression, fiber breakage of compression fractures appears as shown in Figure 7-13(e). This feature is better seen in Figure 7-14, where the features of the fracture exhibit the morphological evidence of microbuckling failure mechanisms. The presence of a chop mark on the fiber ends [287,288] is caused by a combination of tension and compressive stresses that are caused by bending, forming a region of transition.

Interfacial failure is observed in the magnified image in Figure 7-13(f). Such a feature occurs due to differences in the stiffness between fiber and matrix within the CF-PA6 layer. This mismatch causes high local stresses around the fiber-matrix interface. For that reason transverse stresses and shear stresses are significantly present in the matrix, leading to debonding due to the lower strength of the matrix [20]. Under quasi-static tensile loading, local fiber fracture can transfer significant stress levels to the matrix and induce cracks. Figure 7-13(g) shows relatively large transverse cracks. According to Greenhalgh [289], transverse cracking is caused by weak strength of the matrix under tension, where relatively low stresses initiate a brittle matrix failure or even fiber-matrix interface debonding. In addition, local deformation of the first 3D printed PA6 layer is confirmation of the strong adhesive forces in the PA6 coating layer on the surface of the aluminum 2024-T3. The matrix is locally deformed in an out-of-plane direction, as shown in Figure 7-13(h), due to high peeling stresses on the overlap edges as previously discussed about stress distribution. Furthermore, it can observe no significant deformation of the PA6 coating (highlighted with black arrow) immediately below the deformed PA6 layer (indicated with white arrow). This is probably caused by the strong adhesive forces and mechanical interlocking in the interface between the PA6 coating layer and the surface of the aluminum 2024-T3.

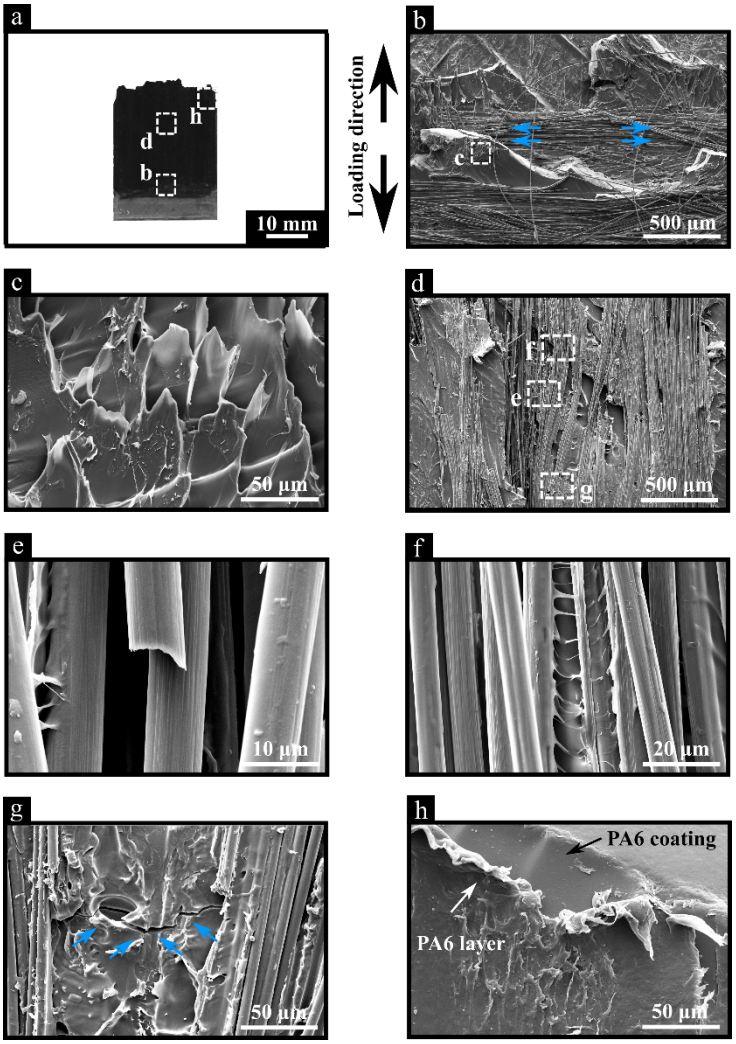

Figure 7-13 Fracture surface of the AddJoining hybrid joints after failure under quasi-static shear testing at room temperature: (a) overview of aluminum 2024-T3 and fractured composite $[PA6/CF\text{-}PA6]_{4S}$, (b) at the overlap edge with the contour (indicated by blue arrows), (c) local fibrils indicating high deformation on the PA6 matrix, (d) region of interfacial-intralaminar failure, (e) fiber breakage at 45° caused by compressive stresses, (f) interfacial failure between fiber and matrix, (g) PA6 matrix crack (blue arrows) propagating in transverse direction to the load application, (h) cohesive failure with PA6 tearing in out-of-plane direction. The direction of load applied during the test is indicated by the arrows beside (b).

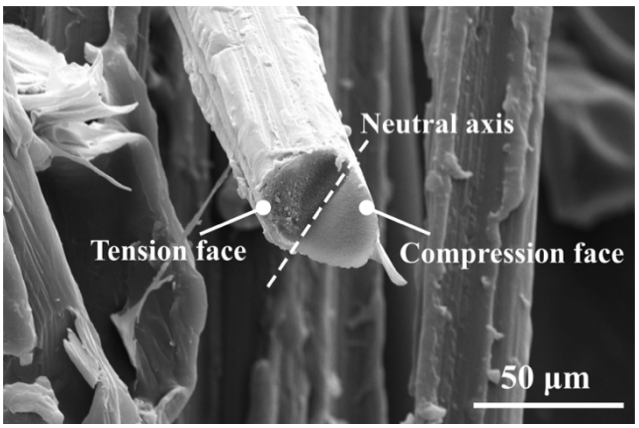

Figure 7-14 Carbon fiber end after tension and compression fracture at 45°, as evidence of the microbuckling failure mechanism of the AddJoining hybrid joints under quasi-static shear testing at room temperature.

The main features observed on the metal side of the fracture were also confirmed on the ruptured composite side, as shown in Figure 7-15. An overview of the interfacial-intralaminar fracture is illustrated in Figure 7-15(a). It reveals a PA6 layer contour orientated 90° (indicated by blue arrows in Figure 7-15(b)) was deformed due to detachment of the CF-PA6 layer. Scarps also formed on the polymeric matrix contour. Such a fracture feature is easily identified by the formation of distinctly aligned steps, as can be seen in Figure 7-15(c). The literature reports that scarps are formed adjacent to the fiber-matrix interface during out-of-plane and shear stresses [290,291]. A similar stress state is the driving force behind detachment of the fiber from the matrix, as shown in Figure 7-15(c) and indicated by black arrows. Usually it is difficult to identify the cause of debonding when it is primarily caused by poor adhesion between the fiber and matrix [292,293]. Another possibility is a lack of fusion between the fiber and matrix at the microscopic level, as previous shown in in Section 4.1.2, Figure 4-2(c). According to Ma *et al.* [193], the polymer matrix, PA6 in this PhD work, may have been polymerized during the fiber impregnation process, creating a barrier to infiltration of fiber bundles and causing a lack of fusion and non-uniform fiber distribution.

Other regions were also explored on the fractured composite part to further identify fracture features. Figure 7-15(d) shows the center of the overlap area with interfacial-intralaminar failure. The presence of voids (blue arrows) attached to carbon fiber without matrix bundles (black arrows) are visible in Figure 7-15(e). Their presence is inherently related to the 3D printing process and the lack of matrix fusion, as previously mentioned in Section 4.1.2, Figure 4-2(c). Furthermore, Figure 7-13(f) shows a failure caused at the interface between the fibers and the matrix (as previously discussed in Figure 7-13(f)). It occurs mainly when fibers are subjected to stresses perpendicularly to fiber direction [289].

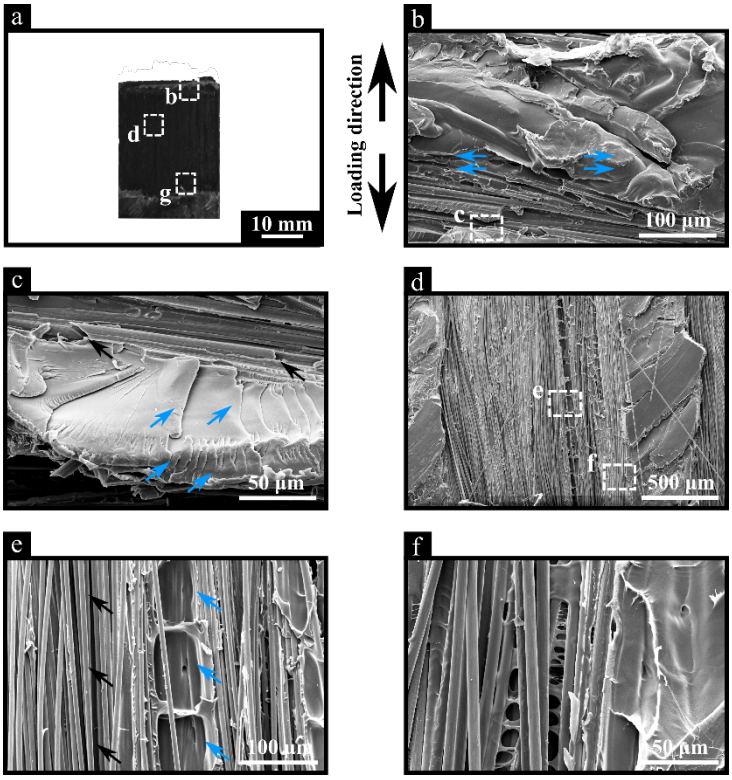

Figure 7-15 Fracture surface of the AddJoining hybrid joints after failure under quasi-static shear testing at room temperature: (a) overview of fractured composite [PA6/CF-PA6]$_{4S}$, (b) overlap edge highlighting a contour (indicated by blue arrows), (c) presence of scarps (blue arrows) and broken fibers in the contour (black arrows), (d) region of interfacial-intralaminar failure, (e) carbon fibers exposed (black arrows) without matrix and presence of pores (blue arrows), (f) high magnification of location with interfacial failure between fiber and matrix. The direction of the load applied during the test is indicated by the arrows beside (b).

When considering the influence of temperature during mechanical testing, the fracture mechanisms were slightly different. The SEM fractographic images are presented here for the lowest (-55 °C) and the highest (120 °C) temperatures within the selected range studied in this PhD work. At the lowest temperature failure changed to adhesive-cohesive mode (Figure 7-16(a-c)). Horiguchi *et al.*[294] reported resin embrittlement dominates under low temperature. Similar fracture mechanism were identified in this PhD by the presence of microcracks in the PA6 coating and PA6 matrix, causing brittle fracture (Figure 7-16(d)) [283,295]. However, on the micro-scale plasticity occurred (Figure 7-16(e)) within this brittle fracture with local ductile fracture (Figure 7-16(f)). This mechanism is indicated by drawing of fibrils (highlighted with a blue box) with resin-dominant failure with textured microflow (indicating with a blue arrow). This fracture mechanisms is possible interpret the damage growth direction [296,297]. The main features observed on the metal side of the fracture were also confirmed on the ruptured composite side. Therefore, no discussion is presented for the composite side.

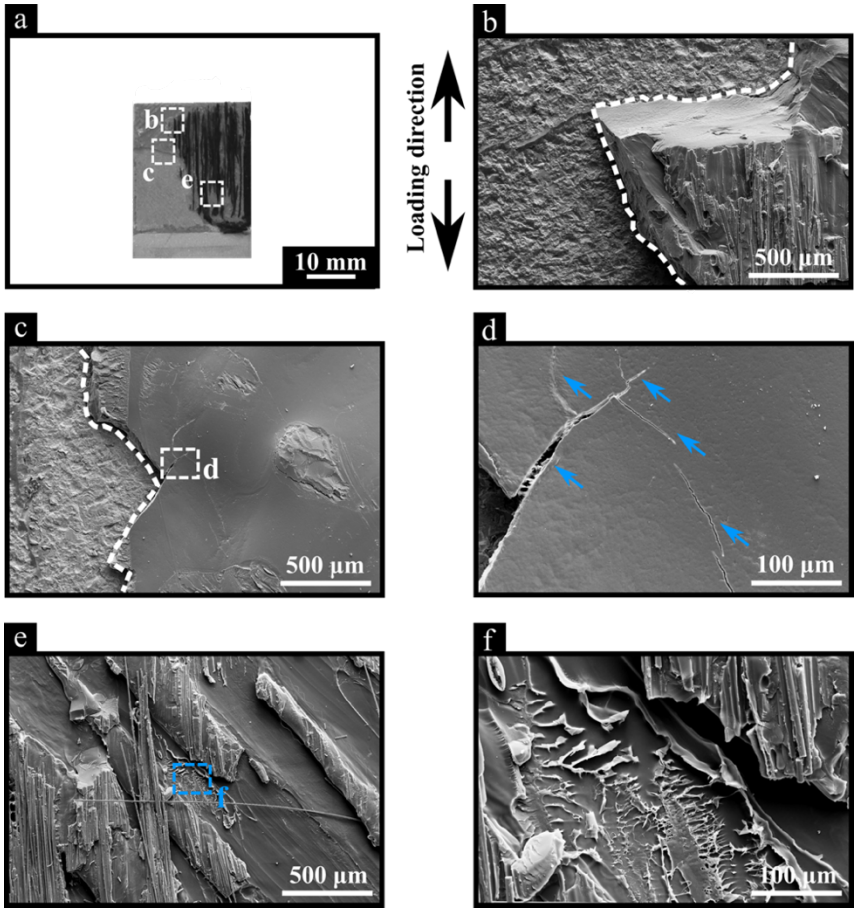

Figure 7-16 Fracture surface of the AddJoining hybrid joints after failure under quasi-static shear testing at -55 °C: (a) overview of aluminum 2024-T3 with the adhesive-cohesive fractured composite $[PA6/CF\text{-}PA6]_{4S}$, (b) mixed of adhesive-cohesive failure with region of interfacial-intralaminar failure, (c) adhesive-cohesive failure with (d) micro-cracks on the PA6 coating (indicated by the blue arrows); (e) low plastic deformation at break with short peaks of fibrils within the PA6 layers indicated by (f) local fibrils features deformed in out-of-plane direction. Direction of the load application during test is indicated by the arrows in (b).

At room temperature and up to 120 °C there is an interfacial-intralaminar failure mode. However, at 120 °C, Figure 7-17(a), new fracture features were observed and these are closely related to a coupling effect of force and high temperature under quasi-static shear testing. The polymer becomes softer and more ductile with increasing temperature, as discussed in Section 7.2. One feature observed was the presence of micro-voids extending in the loading direction, which is an indication of open crazes (Figure 7-17(b-c)). Such features are also known as cavitation and occur due to the excessive deformation. They are often associated with void formation in tension [291,297–299], where the shear stresses cause a distortion of the voids. Another fracture feature observed was formation of riverlines on the PA6 matrix (Figure 7-17(d)). According to the literature [291], riverlines are a natural development of scarps can indicate damage growth direction. Such phenomenon is highlighted with blue arrow in Figure 7-17(e) between fiber imprints (indicated by black arrows). This phenomenon is attributed to tough polymers, which will undergo fracture through ductile drawing [297–299]. Furthermore, Figure 7-17(f) revealed fiber imprints, i.e. PA6 matrix with ribbon of matrix orientated in out-of-plane direction. The main features observed on the metal side of the fracture were also confirmed on the ruptured composite side. Therefore, no discussion is presented for the composite side.

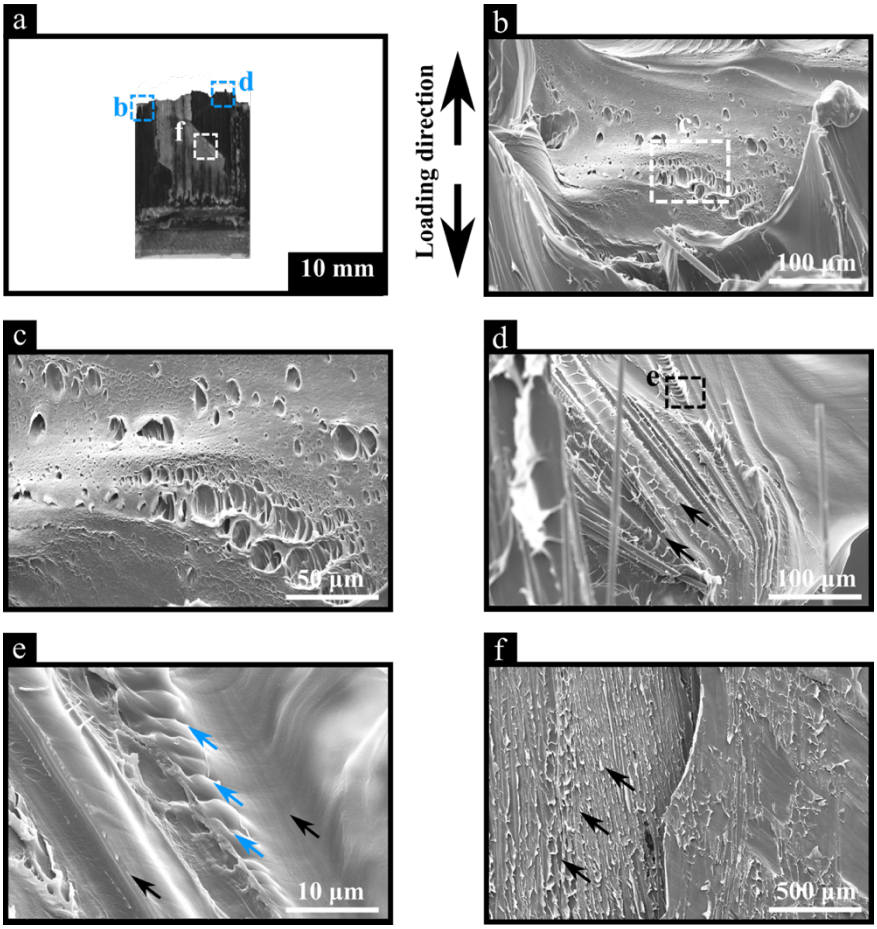

Figure 7-17 Fracture surface of the AddJoining hybrid joints after failure under quasi-static shear testing at 120 °C: (a) overview of aluminum 2024-T3 with the interfacial-intralaminar fractured composite $[PA6/CF\text{-}PA6]_{4S}$, (b) open crazes indicates the formation of (c) micro-voids extended in loading direction, (d) riverlines features (indicated by the back arrows) and (e) scarps (indicated by the blue arrows) of PA6 matrix formed at the adjacent fiber imprints (indicated by the black arrows); (f) carbon fiber imprints in the PA6 matrix with ribbon of matrix (indicated by the black arrows) deformed in out-of-plane direction. Direction of the load application during test is indicated by the arrows in (b).

In this way, the correlations between RLOM failure analysis and the predicted damage pattern using FEA shown in Figure 7-12 helped to elucidate the global failure mechanisms of the AddJoining hybrid joints. Moreover, the evaluation of the failure micromechanisms of the AddJoining hybrid joints further supported the interpretation of global hybrid joint mechanical failure. A complex mixture of ductile and brittle fractures under quasi-static shear loading could be observed, whereby the effect of temperature changed the micromechanisms of failure from adhesive to interfacial-interlaminar. The embrittlement of the polymer at -55 ^{o}C led primarily to adhesive failure with microcracking of polymer coating and matrix. The failure changed from adhesive failure to interfacial-intralaminar microfailure at room temperature and 120 °C - e.g. represented by visible open crazes - due to the excessive deformation - as the polymer becomes softer and ductile. All in all the precise and detailed determination of micromechanisms were essential to support the understanding of hybrid joint failure under quasi-static lap shear testing.

Chapter 8. Fatigue behavior of hybrid joints

To increase maturity of the AddJoining technique, this chapter deals with the fatigue performance of AddJoining hybrid joints. S-N curves were employed to characterize the fatigue resistance of the single lap joints obtained after a number of fatigue tests. Assessment of fatigue life was performed using a two-parameter Weibull distribution. This method is used to evaluate the scattering of fatigue data and predict the S-N curves of different reliability levels. During fatigue cycling, stiffness degradation was monitored to help understand the development of fatigue damage. Moreover, a failure analysis of AddJoining hybrid joints after cyclic loading and the typical features of fracture surfaces is provided. The terminology S-N is used, because this is common practice in the literature, but the fatigue life data presented in this chapter is actually a function of Load-Life (F-N) and not Stress-Life (S-N).

8.1 Fatigue life assessment

The AddJoining hybrid joints were systematically tested at different load levels to obtain their fatigue response, i.e. the S-N_f curve. According to ASTM E739 [214] the replication of fatigue samples for research and development purposes should be between 33 % and 50 %. The replication level required is defined in Equation (8-1), where n_t is the total number of load levels and n_i is the total number of fatigue samples. For this PhD work 66.7 % replication was arrived at, which provides a higher degree of certainty for design approaches. This way the AddJoining hybrid joints were characterized with adequate replication for testing and for gaining a reliable understanding the fatigue behavior of case-study joints made with this new technology.

$$replication\ level = \frac{1 - n_t}{n_i} \tag{8-1}$$

The fatigue tests were performed at five load levels until final failure with three replicates for each load level. Three replicates per level were tested to derive the S-N curve shown in Figure 8-1. This graph shows the relationship between fatigue cycles to failure and maximum force. The load level was selected ranging from 70 % of ULSF (F_{max}: 8.6 kN), to 30 % of ULSF (F_{max}: 3.7 kN) and in order to cover low cycle fatigue (LCF) and high cycle fatigue (HCF) life from 10^3 to 10^6 cycles, respectively [271]. Furthermore, the tests were stopped upon reaching10^6 cycles and samples that survived this fatigue limit are known as run-outs, as indicated by black arrows. In the case of the AddJoining hybrid joints, there were run-outs at 30 % of ULSF (F_{max}: 3.7 kN).

The fatigue data for the AddJoining hybrid joints were analyzed using three different statistical models to evaluate the experimental scatter and formulate the S-N curves. The most common method to describe the dependence of fatigue life and load is linear regression, also known as exponential (log-linear) recommend by ASTM E739 [214]. Another recommendation is the power law (log-log) fit. The standard also suggests, in cases where there is no linear fit, a nonlinear model should be considered for the analysis, such as the two-parameter Weibull distribution (2-P WD) [215].

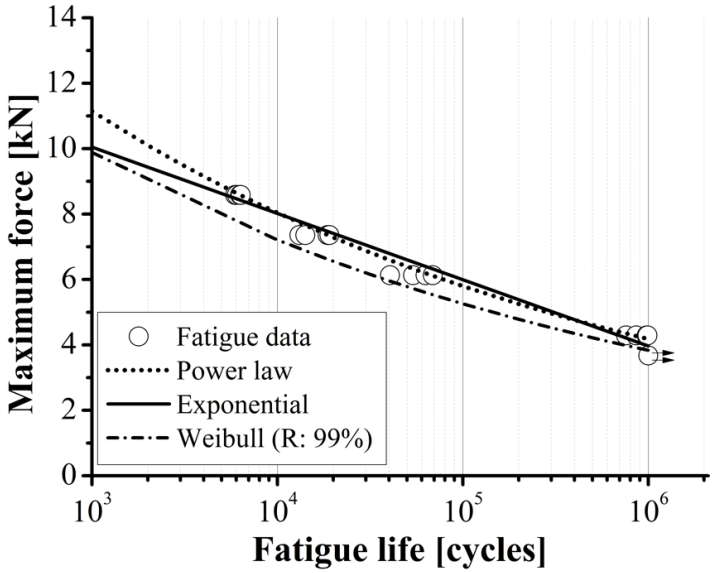

Figure 8-1 Fatigue data scatter plot for a AddJoining hybrid joints and fitted, statistically derived S-N curves according to power law, exponential, and two-parameter Weibull models (the latter with reliability level of 99 %).

Table 8-1 summarizes the fatigue life prediction using the three proposed models. The predicted fatigue life was evaluated at three selected regions from the statistically derived S-N curves presented in Figure 8-1. The three regions are at 10^3 cycles (LCF), at 10^5 cycles, and at 10^6 cycles (HCF). The fatigue life at 10^5 cycles is used by the aerospace industry as a conservative approach for initial design principles [213]. It should be noted that when predicting S-N curves for future structural applications, being conservative is a priority for reasons of safety. According to Schijve [213], to reduce the uncertainties for aircraft during routine operation it is recommended for fatigue life with a low probability of failure as a design principle. For this purpose, Weibull was applied as an example in this section with a reliability of 99 %, which is a 1 % probability of failure. The exponential model predicted higher forces for the three chosen regions compared to the power law and Weibull method. Therefore, the exponential model is less conservative within the evaluated range. The power law has potential similarities in terms of predictability to the Weibull method (for different reliability levels). The statistically tested and validated models for exponential and power law methods are described in Appendix A.12, where the procedure adopted is also briefly described. In the next section the two-parameter Weibull is further discussed.

Table 8-1 Fatigue life predicted at three cycle levels by each of the fitting formulas studied in this work.

Model	At 10^3 cycles		At 10^5 cycles		At 10^6 cycles	
	Force [kN]	ULSF [%]	Force [kN]	ULSF [%]	Force [kN]	ULSF [%]
Exponential	11.2	91	5.8	47	4.2	34
Power law	10.1	82	6.0	49	3.9	32
Weibull (R = 99%)	9.9	81	5.3	43	3.8	31

8.1.1 Statistical analysis using the two-parameter Weibull distribution

In order to understand the fatigue data scatter further, the statistical meaning of the data was evaluated using the Weibull distribution [300,301]. The Weibull distribution function has received much attention in the literature for metals [302,303]. It has also provided useful evaluations of fatigue data with reliability curves for composite materials [304,305]. A two-parameter Weibull distribution (2P-WD) is a highly conservative way to predict S-N curves [306,307]. The statistically derived S-N curves obtained at different reliability levels are presented in Figure 8-2. As previously mentioned, for aerospace structural parts the design principles focus on fatigue reliability and statistically derived S-N curves are used to fit with a high reliability safety level. The reliability levels normally used for aerospace structural parts range from 95 % to 99 % [213]. For a basic understanding of the 2-P WD, the mathematical aspects are presented in Appendix A.13, where the statistically derived S-N curves are described with the associated calculations and graphical analysis used in this PhD work.

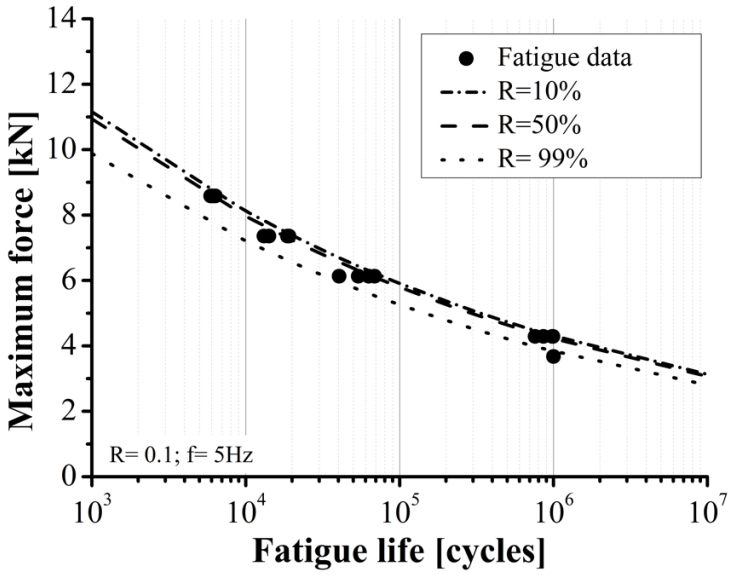

Figure 8-2 Statistically derived S-N curves at different reliability levels using the two-parameter Weibull method.

As described in the previous section, three regions were evaluated to predict fatigue life at 10^3 cycles, at 10^5 cycles, and at 10^6 cycles and the derived S-N curves fitted for three chosen reliability levels (10 %, 50 %, and 99 %). Table 8-2 shows the fatigue life for the three different regions. At 10^5 cycles, the ULSF of the AddJoining hybrid joints corresponds to 48 % (R = 10%) and 43 % (R = 99%). The predicted fatigue life fits well for reliability levels of 50 % or lower, where during the experiment it was validated by testing three replicates at 47 % of ULSF (F_{max}: 5.8 kN) for (101,000 ± 1,500) cycles, i.e. 10^5 cycles. This latter result is further discussed under damage monitoring (Section 8.1.3). At the lower load level, as suggested by the results at a reliability of 99 %, could lead to a higher number of cycles. Thus, it is worth noting the applicability of the 2P WD for analyzing data scattering when evaluating fatigue data. Also, these statistically derived S-N curves provide the reliability of fatigue life needed for initial design in the aerospace sector for this case-study joints.

Table 8-2 Fatigue life predicted at three different cycles and three different reliability levels.

Reliability [%]	At 10^3 cycles		At 10^5 cycles		At 10^6 cycles	
	Force [kN]	ULSF [%]	Force [kN]	ULSF [%]	Force [kN]	ULSF [%]
10	11.2	91	5.9	48	4.3	35
50	10.9	89	5.8	47	4.2	34
99	9.9	81	5.3	43	3.8	31

8.1.2 Residual strength after one million cycles

The fatigue limit can vary between one and 100 million cycles, depending on the technology and materials. For the development and understanding of a new technology, the fatigue limit is often defined when the sample does not fail after 10^6 cycles [308,309]. Therefore, for this PhD work the fatigue limit was defined as one million cycles and the test was then stopped. Moreover, it was assumed that the tested loading level would not promote failure by fatigue. To assess this assumption, the fatigued specimens were also subsequently mechanically tested under quasi-static loading, as described in Section 4.3.8.1. Figure 8-3(a) illustrates the comparison of mechanical performance between the initial unfatigued quasi-static samples and run-out specimens after one million cycles. An insignificant change in stiffness was observed with average stiffness of 8.8 kN/mm and 8.9 kN/mm for initial samples and after one million cycles, respectively (Table 8-3).

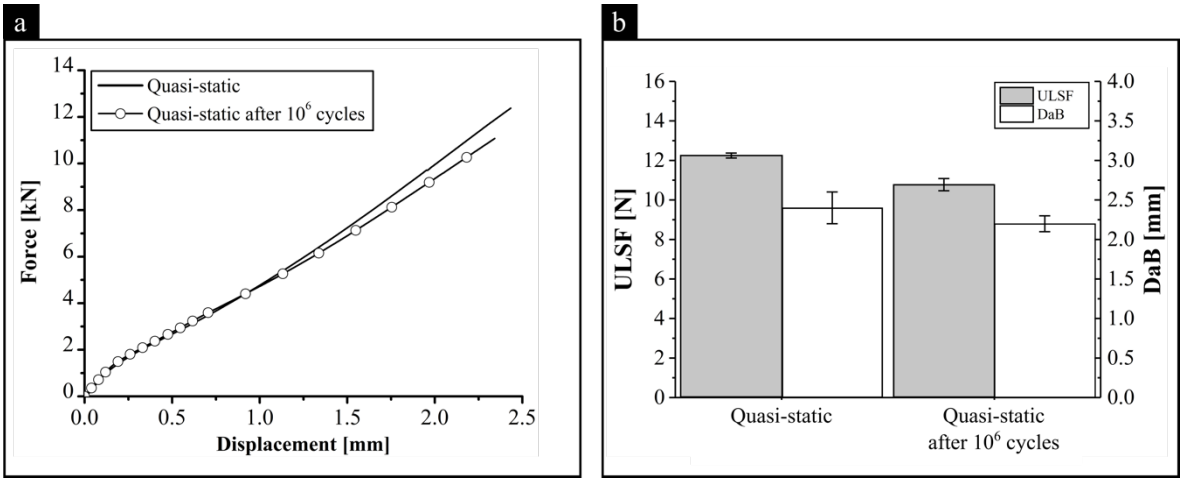

Figure 8-3 Comparison of mechanical performance of initial quasi-static samples and after one million cycles: (a) representative force-displacement curves, and (b) average ULSF and DaB.

The average ULSF and DaB shown in Figure 8-3(b) were obtained from the force-displacement curves provided in Appendix A.11. When comparing the average ULSF and DaB, after 10^6 cycles the strength decreased by 9.9 % with a difference in ULSF of 11.1 ± 0.2 kN and ductility by 7.3 % with DaB to 2.3 ± 0.07 mm less than the initial mechanical performance, with ULSF of 12.3 ± 0.1 kN and DaB of 2.48 ± 0.05 mm. This decrease in fatigue performed is believed to be related to the well-known damage accumulation during cyclic loading, which usually promotes a reduction in mechanical performance in composite single lap joints [310].

Table 8-3 Stiffness obtained from the force-displacement curves and damage area from C-Scan measurements for initial quasi-static samples and after one million cycles.

	Stiffness	Damage area	
	[kN.mm^{-1}]	[%]	[mm^2]
Quasi-static	8.8 ± 0.09	20.6 ± 1.3	4.7 ± 0.4
Quasi-static after 10^6 cycles	8.9 ± 0.07	29.7 ± 2.1	6.5 ± 0.2

Before quasi-static mechanical testing, another investigation approach was considered to further understand the damage accumulation during fatigue testing. Knowing the loading level that corresponds to the fatigue limit, the test was stopped at 90 % of fatigue life, i.e. 900,000 cycles at 30 % of the ULSF. The damage was measured by quality inspection using ultrasound C-Scan, as described in Section 4.3.9.1, and compared with the sample before fatigue cyclic loading as shown in Figure 8-4.

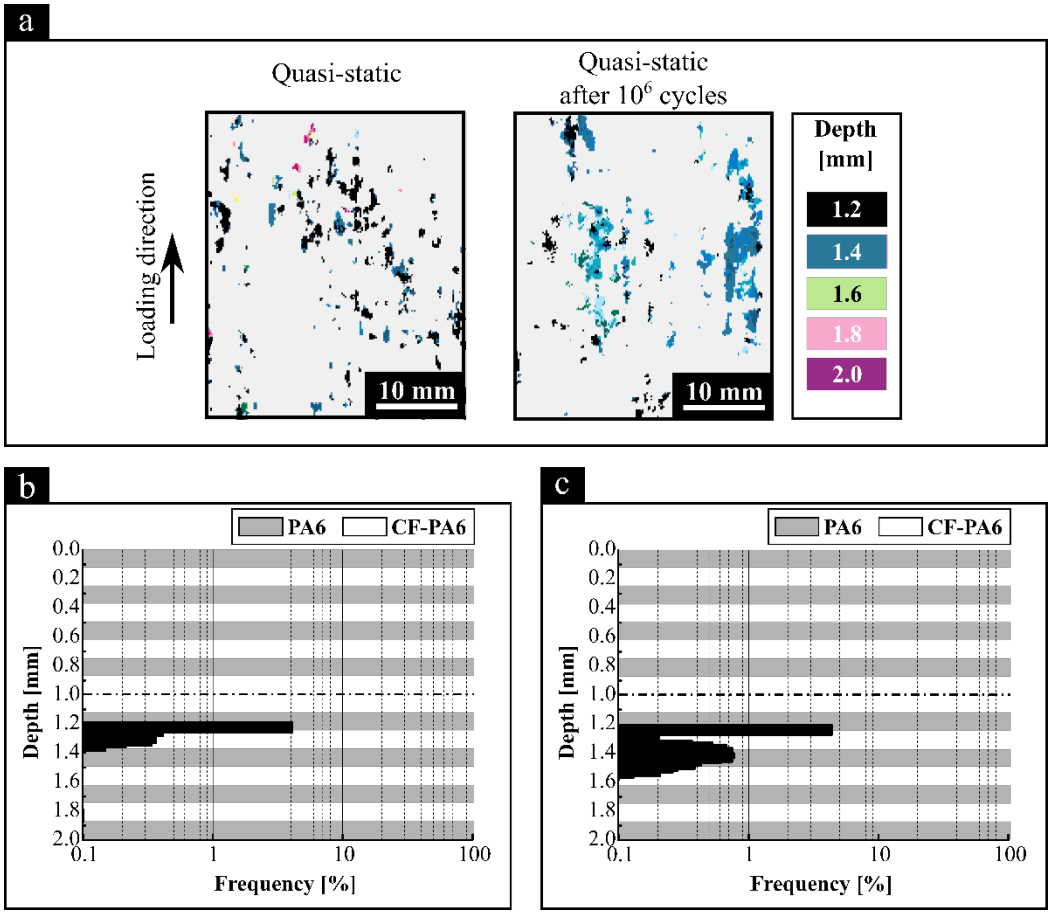

Figure 8-4 (a) C-Scan graphs for initial quasi-static samples and after one million cycles; corresponding damage distribution histograms of (b) initial quasi-static, and (c) after one million cycles. 0 mm is the interface of aluminum 2024-T3 and PA6 coating / $[PA6/CF\text{-}PA6]_{4S}$.

As it can be seen in the C-Scan graphs, damage was detected in the interior of the overlap region (Figure 8-4(a)). By observing the damage distribution in the histograms presented in Figure 8-4(b)

and Figure 8-4(c) the frequency quantifies the damage obtained from C-Scan. The frequency on the X-axis is plotted on a logarithmic scale to highlight the variation in damage. In this chart, the damage is concentrated on the interior of the center (in depth 1.2 mm and 1.4 mm) of the printed composite part. In this region, the frequency of damage the initial quasi-static sample and quasi-static after one million cycles is 4.1 % and 4.3 %, respectively. This indicates that it is this region that could lead to failure. It also corroborates the observed interfacial-intralaminar failure mode by delamination of the middle of the composite thickness (corroborates with Figure 7-9(c) and discussed in Section 7.1.3). The chart in Figure 8-4(c) also shows that the effect of cyclic loading tends to increase the damage in composite materials, even with load levels that survive the fatigue limit. Moreover, Table 8-3 also depicts that compared to the initial samples the damage after 10^6 cycles increased by 31 % in area fraction (from 20.6 % to 29.7 %) and by 28 % in area (from 4.7 mm^2 to 6.5 mm^2). Thus, damage propagation is relatively slow for the loading level at 30 % of ULSF, where the total damage area corresponds on average to 1 % of the overlap area. This PhD work has found the damage is primarily caused by an accumulation of delamination that follows initial damage caused by the existence of multiple intrinsic manufacturing defects (i.e., voids) within the composite [PA6/CF-PA6] part, as previously discussed. Thus, it is the delamination evolution through the composite part that accounts for the damage. Furthermore, in order to assess the damage evolution, the analysis was experimentally evaluated by monitoring the stiffness degradation, an approach discussed further in Section 8.1.3.

8.1.3 Damage monitoring in fatigue

During the cyclic loading, stiffness reduction can be used as a method to monitor damage progression in the AddJoining hybrid joints. Stiffness monitoring is commonly used for the fatigue testing of composites, where stiffness changes are due to stress redistribution, which correlates to internal damage development in the composite [311–314]. To further understand the fatigue life of the AddJoining hybrid joints, four loading levels were used to evaluate stiffness degradation. For initial design principles, the fatigue life at 10^5 cycles is used by the aerospace industry as a conservative approach [213]. Therefore, in this section only reports the results for loading level 47 % of ULSF (F_{max}: 5.8 kN) at 10^5 cycles. However, the full results are presented with the other three loading levels in Appendix A.14. Figure 8-5 depicts the stiffness and damage curves, where the data is plotted against the fatigue life. In this regard, the latter represents the ratio of fatigue life to fatigue life at fracture. It is a common approach for clearly visualizing the variations in stiffness and damage at different loading levels [311–313]. Figure 8-5(a) shows a decrease of 1.5 % in stiffness (i.e. the secant modulus, E= 2557 MPa) at 10 % fatigue life compared to the stiffness of the initial fatigue cycle (E_0= 2594 MPa). A small reduction in stiffness to 1 % of the original stiffness was observed until 60 % of the fatigue life. Thereafter the stiffness reduction slowly decreased, until reaching 4 % (E= 2490 MPa) at 70 % of the fatigue life. From this stage on, the stiffness varied in an approximately linear fashion, without distinctly abrupt stiffness reductions. By then the stiffness had reduced to 18 % (E= 2132 MPa) of the original stiffness at the failure stage. A similar observation is seen for damage in Figure 8-5(b). The variable D represents the damage measured by the ratio of stiffness E for each measured fatigue cycle to stiffness E_0 for the initial fatigue cycle [315]. D varies between zero and one, and a low damage value means a low variation in modulus due to cyclic loading. At 90 % of fatigue life, damage increased to 18 %, corresponding to stages of fiber breakage and unstable delamination growth [316]. Schulte [317] reported for the first time a three-stage stiffness reduction during fatigue loading of a composite, referred to as a characteristic damage state (CDS). According

to Highsmith and Reifsnider [311] and Gamstedt, Redon and Brøndsted [318], the presence of a continuous fiber orientation, e.g. at 0°, dominates the laminate stiffness in composites are too small to clearly identify stiffness degradation. Similar results were obtained in this PhD work, where it was difficult to observe a clear definition of the three stages of stiffness reduction in the unidirectional composite.

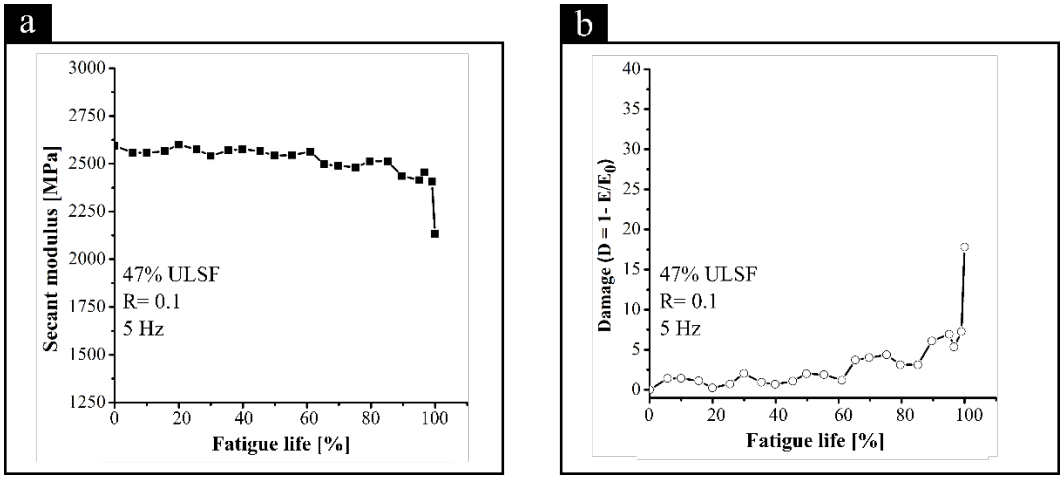

Figure 8-5 Measured (a) stiffness variation, and (b) damage variation as a function of fatigue life during cyclic loading at 47 % of the ULSF, corresponding to a maximum force of 5.8 kN.

Moreover, the cyclic fatigue loading represented by force-displacement curve (Figure 8-6) shows similar stiffness behavior and remarkably similar to the hysteresis loops observed from the fatigue cyclic loading. Figure 8-6 shows the cyclic fatigue loading behavior at 47 % of the ULSF. In these graphs, representative force-displacement hysteresis loops are presented in Figure 8-6(a), and the first nine full cycles of loading are shown to highlight the variation of displacement. Figure 8-6(b) shows the two curves for loading level 47 % of ULSF at 10 % and 99 % of fatigue life. It appears hysteresis heating is negligible, as no significant variation in dissipated energy occurs during cyclic loading [319,320]. Another indication of low or insignificant thermal-induced cyclic damage during fatigue testing is the low variation in width of the cyclic hysteresis loops, which suggests slow damage deformation per cycle [321]. According to Robert, Moulinjeune, and Houba [322], the presence of fibers in a thermoplastic exert an influence on the fast stabilization of hysteresis loops. The authors did not report the reason for the stabilization in their work. However, as previously discussed here, the presence of unidirectional fiber in loading direction contributes positively to decrease stiffness degradation. Therefore, it explains the stable performance with no drastic decrease in the slope of the hysteresis loops. Thus, the expected cyclic softening of ductile polymer, in this case the PA6, was not observed and the cyclic softening presented instead a propeller-like shape during cyclic loading [271]. This suggests that micro-damage initiation is dominated for most of the fatigue life by the high stiffness stability observed during damage monitoring [321], instead of thermal-induced cyclic damaging.

In this PhD work, the stabilization phase was investigated by calculating the dissipated energy per cycle during a complete cycle. For better visualization of this the energy dissipation per cycle is presented in Figure 8-7 for all four loading levels selected in this PhD. In this image, the curves are considered for 10 %, 60 %, 80 % and 99 % of fatigue life. It is worth noting that the dissipated energy per cycle is stable, but in the final stages of fatigue life increases rapidly (refer to Figure 8-7). At

99 % of the fatigue life and at LCF, represented by 70 % and 60 % of the ULSF, the energy dissipation per cycle reached 0.12 J and 0.11 J, respectively. At 47 % of the ULSF, the magnitude decreased to 64 % compared to the loading level at 70 % of the ULSF with an energy dissipation of 0.04 J. Consequently, a dependence is observed on the energy dissipation per cycle for the loading level. For a loading level near the fatigue limit at 35 % of the ULSF, the energy is 83 % (0.02 J) lower compared to the LCF loading level. Thus, at a high loading level the damage tends to coalescence rapidly and leads to fracture without further extensive growth. Conversely, the lower the loading level the lower the dissipated energy and consequently lower the damage formation. These observations were further rationalized on the basis of damage evolution for all four loading levels using C-Scan measurements, as presented from Figure A.42 to Figure A.44 and at 47% of the ULSF in this section (Figure 8-8).

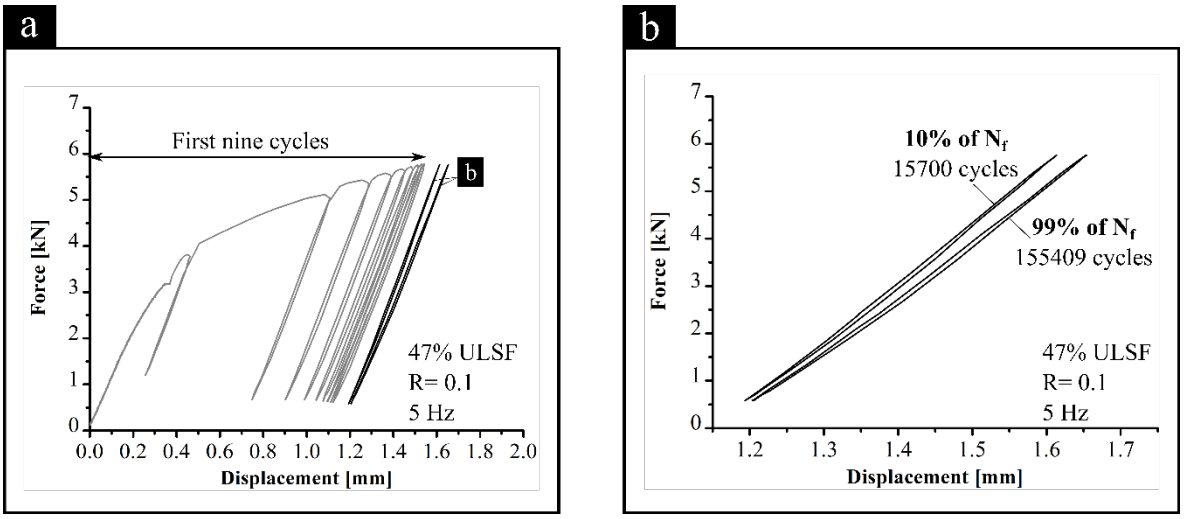

Figure 8-6 Representative force-displacement curves at 47 % of the ULSF corresponding to a maximum force of 5.8 kN (a) with hysteresis loops during cyclic loading, and (b) at two selected levels of fatigue life.

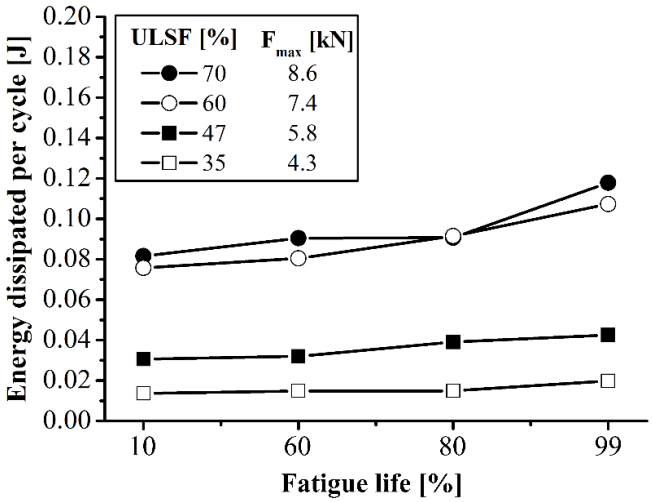

Figure 8-7 Energy dissipated per cycle stiffness in function of four selected fatigue life during cyclic loading at four different loading levels.

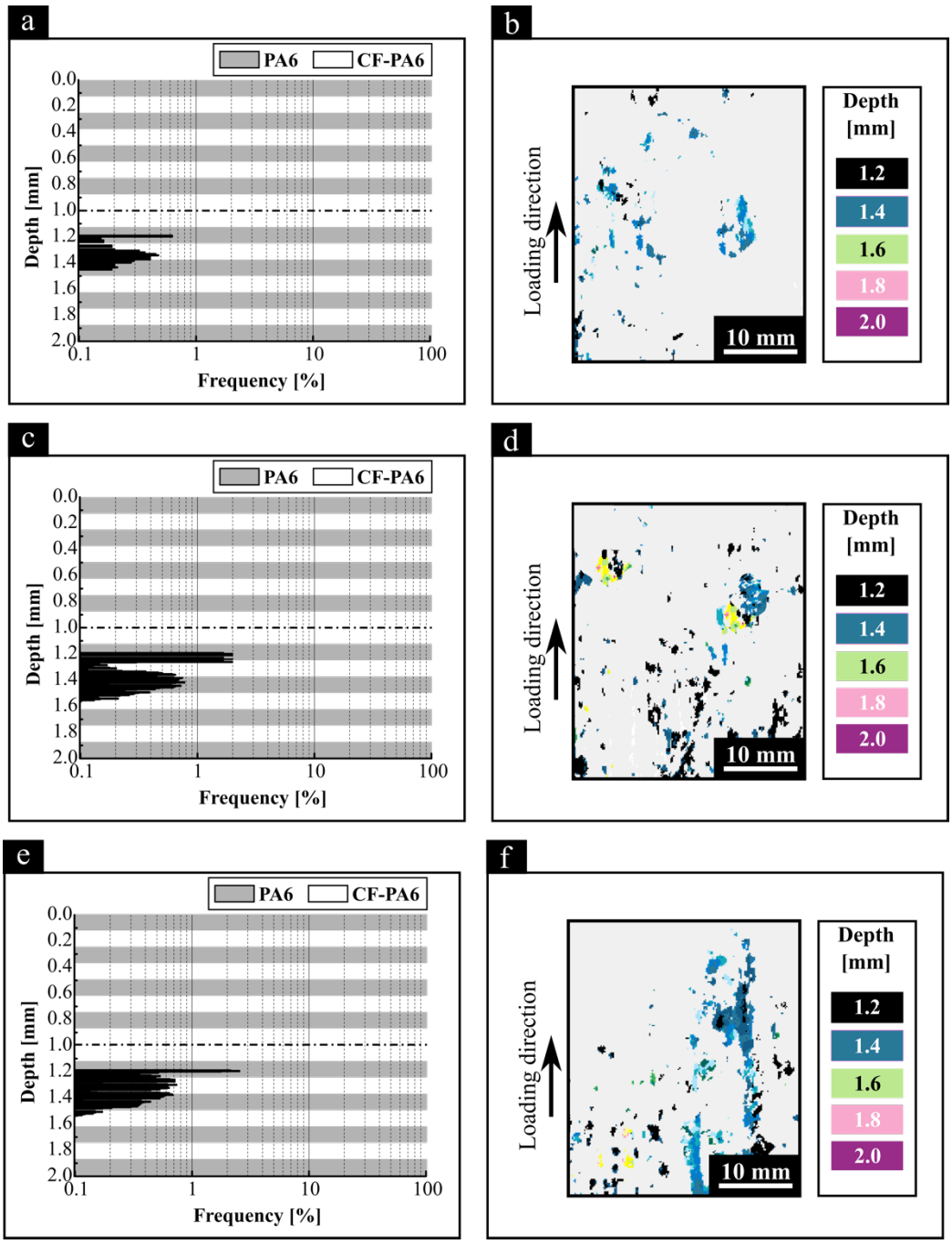

Figure 8-8 Damage distribution histograms in (a), (c), and (e) corresponding to C-scan graphs (b), (d), and (f) measured for 10 %, 60 % and 80 % of the fatigue life, respectively, for cyclic loading at 47 % of the ULSF, corresponding to a maximum force of 5.8 kN. 0 mm is the interface of aluminum 2024-T3 and PA6 coating / $[PA6/CF\text{-}PA6]_{4S}$.

The damage evolution is evaluated at 47 % of the ULSF. Figure 8-8 shows damage distribution with histograms presented on the left and C-Scan graphs on the right. In this investigation three different levels of fatigue life were selected to evaluate the damage. At 10 % of the fatigue life the damage is shown quantitatively in Figure 8-8(a) and visually in the C-Scan image in Figure 8-8(b). The same follows for 60 % of the fatigue life in Figure 8-8(c) and Figure 8-8(d) and for 80 % of the fatigue life in Figure 8-8(e) and Figure 8-8(f). The damage is concentrated in the center of the interior of the

printed composite part, as previously discussed. The histograms indicate that damage increases during the fatigue life. However, for a better overview the size of the damage area is tabulated in Table 8-4 at the three selected levels of fatigue life. The damage after 10 % of the fatigue life reached 6.9 % of the overlap area, corresponding to a total area of 44.9 mm^2. During cyclic loading the size of damage had increased twofold at 60 % of the fatigue life. However, damage remains fairly stable at 80 % of the fatigue life with nearly 20 % of overlap area, a damage area with an average size of 123 mm^2. Moreover, at LCF for loading level at 70 % and 60 % of the ULSF, the damage propagates faster (as presented in Table A.12, Appendix A.14). The opposite is observed for loading levels nearing the fatigue limit.

Table 8-4 Damage area for three selected levels of fatigue life at 47 % of the ULSF, corresponding to a maximum force of 5.8 kN (obtained from C-Scan measurements).

F_{max} [kN]	ULSF [%]	N_i [cycles]	N_i/N_f [%]	Damage area [%]	Damage area [mm^2]
5.8	47	15700	10	6.9 ± 1.5	44.9 ± 2.7
		94200	60	14.5 ± 1.9	90.8 ± 11.1
		125609	80	19.7 ± 0.2	123.2 ± 15.8

To conclude, it seems that fiber rupture controls composite failure in the unidirectional fiber orientation, due to the high damage stabilization observed during damage monitoring and C-Scan measurements [323]. It was found that the presence of continuous fiber orientation (at 0°) dominated the stiffness in the composite, whereby changes in stiffness were relatively small. Another observation was rather the negligible hysteresis heating, due to a low variation in dissipated energy during cyclic loading. This suggested that damage is dominated mostly by fiber rupture caused by fatigue loading, due to the strong stiffness stability observed during damage monitoring. It is important to emphasize that the failure modes for composite materials are more complex [20,32]. The damage mechanisms in composites are based on interaction between matrix failure and fiber failure. Therefore it is difficult to identify the early stage of the damage. Although, the fiber dominates the stiffness in the composite, the fiber failure is rather abrupt, whereas fiber-matrix debonding is a progressive damage resulting in matrix cracking. Therefore, the failure mechanisms observed and evaluated in Section 8.2 was focused on the polymer matrix to understand fatigue failure mechanisms.

8.2 Failure mechanism and fracture surface analysis

The loading level at 47 % of the ULSF was also chosen to investigate the proposed failure mechanisms of AddJoining hybrid joints under cyclic loading. As for quasi-static loading, the overall aspects of failure resemble a high degree of interaction between the individual micromechanisms of failure. Following the same principles used to determine the failure mechanisms under quasi-static loading, fatigue was investigated by evaluating the SEM surface fractures of the material attached to the metal part (Figure 8-9) followed by the composite $[PA6/CF\text{-}PA6]_{4S}$ part (Figure 8-10).

The fractured composite attached to the aluminum 2024-T3 is shown as an overview in Figure 8-9(a). On a macroscopic level, the interfacial-intralaminar failure mode of the fatigue specimens appears similar to specimens from quasi-static loading tests. However, at a microscopic level the fracture

features associated with their interfacial-intralaminar fatigue failure indicate different morphologies to those associated with cyclic loading (Figure 8-9(b)). As previously reported, the damage is an interaction between matrix failure and fiber failure. Nonetheless, small features can be observed in the SEM image evaluation. One interesting fatigue failure mechanism is presented in Figure 8-9(c) (highlighted with blue arrows). It resembles fatigue striations, but these extremely small ridges lead to a different micromechanism of failure, such as shear cusps [290,291]. The formation of shear cusps are associated with fiber imprints due to fracture of the fiber-matrix interface [296,324]. This mechanism is caused by cyclic loading, leading to plasticity of the matrix fracture. This is a combination of microcracks adjacent to the carbon fiber extend into the matrix over different paths. However, Figure 8-9(d) shows a fiber imprint (marked with black arrows) with evidence of local ductile fracture, a matrix pattern formed probably by crazing, void coalescence and fibrillation [289,291,296]. As a consequence, high damage propagation can form the matrix cleavage mechanisms (indicated with black arrow) observed in Figure 8-9(e). Another observation is the formation of shear cusps between the fiber imprint as shown in Figure 8-9(f) as indicated by the black arrows, with a change of the morphology highlighted by blue arrows. These out-of-plane features of orientation are precursors in the formation of a fracture feature known as matrix rollers [291]. This is a strong indication of intralaminar failure [290,291], and it is identified by the underlying fibrils exhibiting strong elongation, due to their high degree of ductility. Furthermore, one key observation is of the sharp shear cusps, which indicate the deterioration stage of the cusps and correspond to elongation of the matrix. Such micromechanisms of failure are also identified clearly on the other side of the composite fracture shown in Figure 8-10. Furthermore, Figure 8-9(g) shows the overlap edge, and a high magnification image of this is presented in Figure 8-9(h). Similar to facture after quasi-static loading, it resembles a ductile PA6 coating fracture failure, i.e dimples. According to Khan *et al.* [325], the dimple size corresponds to the loading level under cyclic loading. This means that the localized plastic deformation promotes a stretching of the dimples that depends on the applied stress.

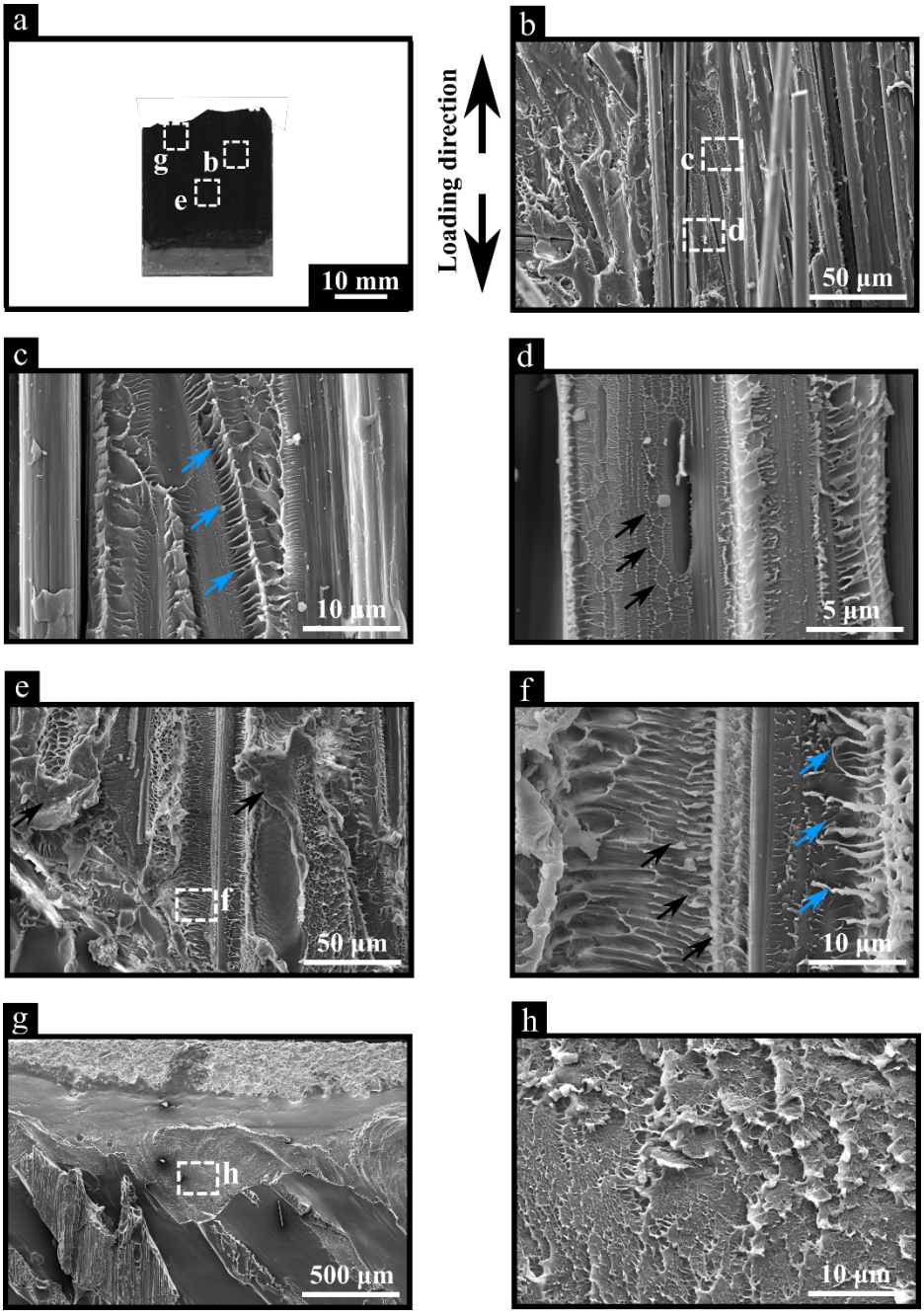

Figure 8-9 Fracture surface of metal side of the AddJoining hybrid joints after failure from cyclic loading at 47 % of ULSF: (a) overview of aluminum 2024-T3 with fractured composite [PA6/CF-PA6]$_{4S}$ attached, (b) high magnification of multiple fatigue fracture features, (c) formation of shear cusps (blue arrows), (d) ductile failure caused by the coalescence of voids (black arrows) on fiber imprints; (e) indication of matrix cleavage (black arrows), (f) formation of cusps in loading direction (black arrows) and nearly deteriorated shear cusps (also known as "matrix rollers", indicated by blue arrows); (g) overlap edge, (h) formation of dimples in the out-of-plane direction. Direction of the load application during the test is indicated by the arrows beside (b).

The main features of details observed on the metal side were also confirmed on the composite side of the fracture as shown in Figure 8-10. The interfacial-intralaminar failure is easily identified and an overview of the fracture is presented in Figure 8-10(a). It reveals several micromechanisms of failure at the center of the fracture (Figure 8-10(b)). As the literature reports [296,324], the formation of

cusps in Figure 8-10(c) tilts away in the opposite direction to the damage growth (in blue arrows). The cusps are easily identified, adjacent to or between fibers, as indicated on the fiber imprint (white arrows). As previously noted, voids (blue arrows) beside a carbon fiber and without matrix bundles (black arrows) are visible in Figure 7-15(c). Their presence is inherently related to the 3D printing process and to the lack of matrix fusion as previously mentioned. Figure 8-10(d) also shows the presence of sharp shear cusps, which reveals the deterioration stage of such fracture features as precursors of matrix rollers [291]. This feature has out-of-plane orientation and is the last stage of shear cusp formation, suggested by elongation of the matrix. Following a change to the morphology, Figure 8-10(e) shows matrix rollers, as indicated by blue arrows (as previously discussed in Figure 8-9(f)). Black arrows in Figure 8-10(e) shows intralaminar fracture features. This fracture mechanism was discussed for the quasi-static shear testing in Figure 7-13(f) (Section 7.3). That occurs due to differences in stiffness between the fiber and matrix in the CF-PA6 layer. As it was previously described for quasi-static loading tests (Figure 7-13, Section 7.3) this mismatch causes high local stresses around the fiber-matrix interface. This means transverse stresses and shear stresses are significantly present on the matrix and this leads to debonding due to the lower relative strength of the matrix.

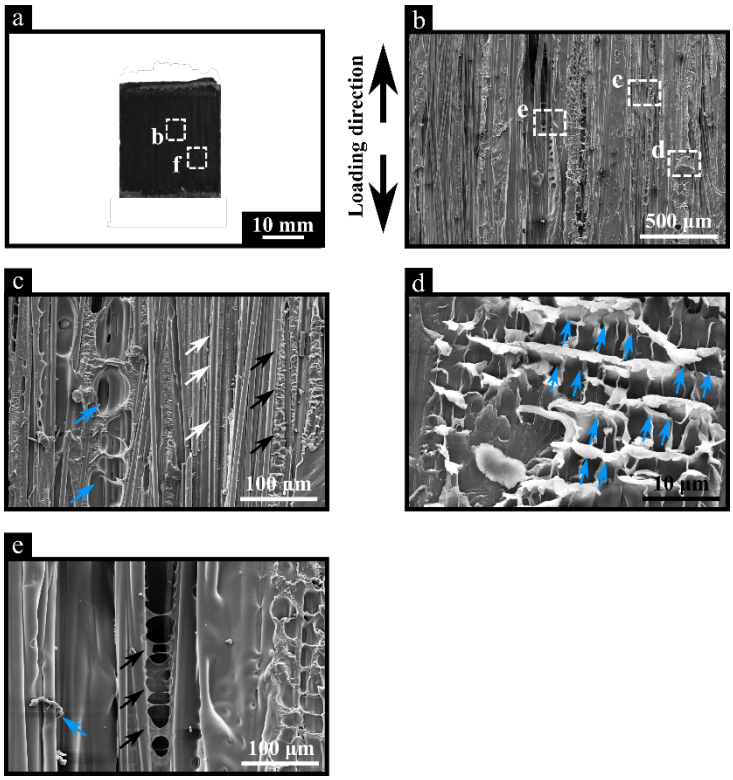

Figure 8-10 Fracture surface of the composite side of the AddJoining hybrid joints after failure from cyclic loading at 47 % of ULSF: (a) overview of fractured composite $[PA6/CF\text{-}PA6]_{4S}$, (b) high magnification region multiple fatigue fracture features, (c) formation of cusps (black arrows) in the polymer matrix, fiber imprint with high polymer deformation (white arrows) and presence of voids (blue arrows), (d) nearly deteriorated cusps (blue arrows) leading to the formation of (e) matrix rollers (blue arrow), and interfacial and interlaminar failure by the debonding between fiber and matrix (black arrows). Direction of the load application during test is indicated by the arrows beside (b).

In summary, the fatigue damage evolves similarly to quasi-static loading tests and propagates through the composite. All in all, AddJoining hybrid joints' failure micro-mechanisms under cyclic loading

showed a complex combination of fracture micromechanisms involving a mixture of brittle (e.g. evidenced by cleavage) and ductile (e.g. by matrix rollers) micromechanisms. As for the case of quasi-static loading, the detailed analysis of micromechanisms of fracture assisted the understanding of the hybrid joint global mechanisms of failure under cyclic fatigue loading.

Chapter 9. Summary of results and conclusions

The new AddJoining technique was introduced and thoroughly discussed for layered hybrid structures in this doctoral thesis for the first time in the literature. The thesis aimed to describe the principles of the technique, its main process parameters, while process variants were identified and explored. The work also highlighted its advantages, limitations, and potential engineering applications. Furthermore, the work provided an in-depth understanding of the bonding mechanisms, microstructural changes, physicochemical thermal properties, and phase identification changes in the selected material combination used in this work.

In this context, this chapter summarizes the main findings of this PhD work, along with the technological and scientific aspects of the AddJoining technique. Major findings were drawn from the development of AddJoining and the results obtained with respect to the defined goals of the work, as follows:

Introduction to the AddJoining process

The AddJoining concept was introduced as a novel approach for producing layered hybrid structures. The process is a fusion of additive manufacturing (AM) and the principles of joining technology to add layers of polymer or composite onto a metal substrate. The principles of the process are presented in Section 5.1 with an approach to increase the roughness for better adhesion between the joining parts, allowing the formation of micromechanical interlocking. Following the steps of the process, the 3D printed composite $[PA6/CF\text{-}PA6]_{4S}$ is manufactured layer by layer on the aluminum 2024-T3 surface. There is a wide range of process parameters possible for AddJoining, depending on the 3D printer selected (Section 5.2). In this case, three process variants were identified and are presented in Section 5.3. Their advantages, limitations and potential applications are highlighted in Section 5.4. Therefore Chapter 5 thoroughly described for the first time the new process' principles.

Development of the AddJoining process

To understand process-induced changes in the selected material combination (aluminum 2024-T3 and the composite $[PA6/CF\text{-}PA6]_{4S}$), three combinations of process parameters were used in this investigation through the variation on the process parameters, namely coating temperature (CT) and heating bed temperature (HBT). In this regard, from the DoE (available on Appendix A.4, see Table A.5 and Figure A.21), the optimized CT at 229 °C and HBT at 77 °C were fixed and the minimum and maximum values of CT selected to help evaluate the results, at 20 °C and 150 °C, respectively.

The stepwise approach (Section 6.1.1.1) helped to support the understanding of the bonding, which influenced the microstructure of the joined composite part (Section 6.1.1.2). A strong bonding of polymer-to-polymer is promoted purely by temperature, leading to strong adhesion. Therefore, the variability of heating bed temperature greatly varies the surface morphology and strongly influences the quality of the bonding formation. It suggests the importance of controlling the temperature to promote a continuing autohesion process and fusion of the surfaces. It was presumed that the rough surface and presence of fault lines at low temperature is associated with a lack of softening of the polymer and that this restricts polymer bond formation. For instance, the lack of smooth surface and presence of fault lines for HBT at 20 °C led to formation of gaps on the AddJoining hybrid joints. Another example is the misalignment of the carbon fiber reinforcement for HBT at 150 °C, where

during the AddJoining process the fiber nozzle drags and distorts the deposited fiber bundles due to low viscosity of the previous polymer layers.

The heat factor used during the AddJoining process significantly influenced the local mechanical properties closer to the metal surface, i.e. the PA6 coating and PA6 first layer. The hardness distributions of the metal part of the overlap joint configuration were affected by the changing in heating bed temperature (HBT). For HBT at 77 °C and 150 °C, hardness increased by 1 % (143.9 ± 2.2 HV) and by 2 % (146.1 ± 3.8 HV), respectively. The temperature increased the hardness and this indicates a precipitation of strengthening particles occurred. However by visual inspection of microstructural aspects in Figure 6-5, it was difficult to distinguish many differences between the three HBT. The changes in the local mechanical properties, e.g. microhardness (Section 6.1.2.1 and nanohardness (Section 6.1.2.2)) suggested that an increase of precipitate reinforcement took place, whereby precipitation of particles once solubilized in the base material (the base material alloy was only in T3 condition) may have taken place at higher HBT, thereby locally increasing hardness.

Within the composite $[PA6/CF\text{-}PA6]_{4S}$ the process induced a global modification of the polymer, the subsequent deposition of polymeric layers in the AddJoining process caused a change to the chain configuration from random (amorphous) to an ordered (crystalline). As it was observed from the thermal properties evaluation, a partial conclusion can be drawn: the effect of HBT slightly changed the thermal properties of the composite part. However, the results have given a basic understanding of the effects of HBT. Therefore, a stepwise approach was carried out to combine the phase-identification (Section 6.1.4) and nanohardness investigations (Section 6.1.2.2) of the polymer. The investigations offered a more comprehensive understanding of the local variations in material properties by means of the phase-changes in each layer. It indicates the presence of two polymorphs of α-PA6 and γ-PA6. Such variation of polymer phase, it is associated with the presence of a thermal history of AddJoining, which can affect the crystallinity locally and decrease in hardness compared to the base material.

From the global mechanical performance analysis, it seems that a reduction in secondary bending influenced by the strong bonding formation on the joined composite is a reasonable explanation to the better quasi-static mechanical performance of AddJoining hybrid joints with HBT at 77 °C. This is believed to be related with a reduction in out-of-plane stresses. Furthermore, towards the end of the chapter, the mechanical behavior of a DoE/ANOVA optimized AddJoining hybrid joint (joint optimization in Appendix A.4) was compared with conventional adhesive bonding. An average improvement of 76 % was observed in ultimate lap shear force (ULSF) with 7.24 ± 0.4 kN and 5.5 ± 0.8 kN for the optimized joint and the adhesively bonded joint, respectively. This gave an indication of the efficiency of AddJoining in bonding the materials by the formation of interlocking on the micro scale (Figure 6-15(b)). By contrast, gaps were visible between the adhesive and the first 3D printed layer of PA6 (Figure 6-15(a)). Whereas in AddJoining hybrid joints the primary bonding mechanisms between the printed layers are thermal fusion and interlayer bonding. This result shows the effectiveness of the optimization procedure employed to obtain the best set of joining parameters for the material combination used in this PhD work.

Quasi-static behavior of hybrid joints

The eccentricity of the load path under single lap shear quasi-static loading affected the mechanical performance of AddJoining hybrid joints. The secondary bending phenomenon was confirmed by the stress distribution obtained with the help of a finite element model (FEM). The FEM was used to

validate and evaluate the stress distribution on the overlap area and gave qualitative hints for the possible failure location as near to the edge of the overlap with a large gradient of stresses in an out-of-plane direction. Another observation was a lack of symmetry in peak stress and shear stress, attributed to the mismatch in material stiffness between aluminum 2024-T3 and composite $[PA6/CF\text{-}PA6]_{4S}$ parts.

Under quasi-static tensile loading at room temperature, it was possible to observe in the fracture surface (Figure 7-13 and Figure 7-15) that interfacial failure occurred due to the differences in stiffness between the fiber and matrix within the CF-PA6 layer. Local deformation of the first 3D printed PA6 layer was also observed on the fracture surface, confirming the strong adhesion forces binding the PA6 coating layer to the surface of the aluminum 2024-T3. The presence of voids beside carbon fibers without matrix bundles were visible, inherently related to the 3D printing process and a lack of matrix fusion. Furthermore, the major strain measured during experiments confirmed asymmetrical damage evolution caused by road deposition at 90° towards the edge of the overlap area (Figure 7-7), resulting in an interfacial-intralaminar failure of the fractured composite $[PA6/CF\text{-}PA6]_{4S}$ part (Figure 7-6). This type of failure combines interlaminar and intralaminar failure modes caused by the presence of intralayer voids in the CF-PA6 layer, leading to high stress concentration zones. In addition, it is also governed by high shear deformation and out-of-plane deformation due to the voids and weaknesses of the layers within the composite $[PA6/CF\text{-}PA6]_{4S}$ part. Hence, a gradual failure in the central layers was observed by C-Scan measurements (Figure 7-9). It also seems that delamination evolved throughout the composite part by multiple fiber breakages.

When considering the influence of temperature during mechanical testing, under cryogenic conditions at -55 °C, the failure changed to adhesive-cohesive mode with the presence of a microcrack in the PA6 coating and PA6 matrix. The micromechanisms of damage are characterized by fiber-matrix interface weakness, which causes delamination and the amorphous matrix to crack, thereby reducing the mechanical performance. At 120 °C, the failure resulted from extensive plastic deformation of the polymer proved by the presence of crazes (i.e., polymeric microcavitation defects) indicating ductile failure. The polymer softening at 120 °C leads to interfacial-intralaminar new fracture features caused by ductile, e.g. visible open crazes due to the excessive deformation. Therefore, it seems that the composite part stiffness is more sensitive to high temperature within this temperature range, as PA6's glass transition temperature (57 °C) is substantially exceeded.

Using scanning electron microscopy (SEM), the AddJoining hybrid joints showed a complex mixture of ductile and brittle fractures under quasi-static shear loading in an evaluation of the failure micromechanisms. The correlations between RLOM failure analysis and the predicted damage pattern using FEA shown in Figure 7-12 helped to elucidate the global failure mechanisms of the AddJoining hybrid joints. All in all the precise and detailed determination of micromechanisms were essential to support the understanding of hybrid joint failure under quasi-static lap shear testing.

Fatigue behavior of hybrid joints

The fatigue performance of the AddJoining hybrid joints was systematically tested by cyclic tension-tension loading. In this study, the fatigue limit was defined as the load level below which no failure would occur until 10^6 cycles. AddJoining hybrid joints were found not to fail after 10^6 cycles of loading at 30 % of the ULSF, 3.7 kN. Three different statistical models were applied to evaluate the scatter of experimental data and formulate S-N curves, these included linear models recommended by the ASTM standard and a two-parameter Weibull distribution (Figure 8-1). The exponential model

predicted high forces in three different regions compared to power law and Weibull method. Therefore, the exponential model was found to exhibit low conservatism within the evaluated range. Power law had a potential similarity in predictability to the Weibull method (see the reliability levels in Figure 8-2). Therefore, a potential analysis provided statistically derived S-N curves using the Weibull method was successfully able to predict with the reliability of fatigue life needed for initial design in the aerospace sector.

To evaluate their residual strength, AddJoining hybrid joints that survived the fatigue limit 10^6 cycles were also mechanically tested. Although it was assumed that the tested loading level of 30 % of ULSF would not promote failure by fatigue, it is known that damage accumulation under cyclic loading can promote a reduction in mechanical performance in composite single lap joints. From C-Scan measurement (Figure 8-4), the damage propagation was found to be relatively slow, corresponding on average to 1 % of the overlap area for the hybrid joints that survived the fatigue limit 10^6 cycles. This PhD work has found the damage is primarily caused by accumulation of delamination that follows initial damage caused by the existence of multiple intrinsic manufacturing defects (i.e., voids) within the composite $[PA6/CF\text{-}PA6]_{4S}$ part. Also, it proves that the damage is primarily caused by an accumulation of delamination that follows initial damage caused by the existence of multiple intrinsic manufacturing defects (i.e., voids) within the composite [PA6/CF-PA6] part.

By studying damage evolution, it seems that fiber rupture controls composite failure in the unidirectional fiber orientation, due to the high damage stabilization observed during damage monitoring and C-Scan measurements. Furthermore, it was found that the presence of continuous fiber orientation (at 0°) dominated the stiffness in the composite, whereby changes in stiffness were relatively small. From another observation, there was rather a negligible hysteresis heating, due to a low variation in dissipated energy during cyclic loading. This suggested that damage is dominated mostly by fiber rupture caused by fatigue loading, due to the strong stiffness stability observed during damage monitoring.

As for the case of quasi-static loading, the detailed analysis of micromechanisms of fracture assisted the understanding of the hybrid joint global mechanisms of failure under cyclic fatigue loading. Therefore, the fatigue failure micromechanisms presented in Section 8.2 helped to understand that the fatigue damage evolves similarly to quasi-static loading tests and propagates through the composite part. To summarize, AddJoining hybrid joints' failure micro-mechanisms under cyclic loading showed a complex combination of fracture micromechanisms involving a mixture of brittle, e.g. evidenced by cleavage, and ductile fracture, e.g. by matrix rollers, micromechanisms.

Therefore, this PhD work has been successful in fulfilling its objectives. The results achieved in this work contributed to introduce and describe the fundamentals of the AddJoining technique. In addition, it contributed to understand the influence of process parameters on the 3D-printed materials by means of the bonding formation, microstructural changes, physical-chemical properties, and phase identification. A detailed mechanical characterization was achieved for the AddJoining hybrid joints. The generation of this knowledge is fundamental to enable the industrial transfer of AddJoining. Finally, this work demonstrated the potential for the AddJoining technique in manufacturing future multi-material complex parts for structural applications with tailoring design aspect to improve damage tolerance and carrying load.

Chapter 10. Recommendations for future work

An important step was taken by this PhD work, which has for the first time covered the principles, fundamentals and potential development of the AddJoining process. Many aspects remain open for future investigation, although process variants, process parameters and mechanical properties have been successfully addressed and explained. Therefore, this chapter recommends potential topics for further development of the AddJoining technique.

AddJoining has the potential to join a wide range of material combinations. The investigation of a high performance polymers such as PEEK and high strength alloys such as Ti-6Al-4V, are certainly valuable materials worth considering. In addition, a combination of post-printing steps, including thermomechanical treatment such as hot isostatic pressing, could be applied to diminish the presence of intrinsic voids in the polymer component. Another possible variant of the AddJoining technique would be to guide a laser beam with an intensity control to reheat the polymer as it leaves the extruder head nozzle. Moreover, a thorough investigation of the mechanical performance, including impact, stress relaxation, damage tolerance, artificial and natural ageing of AddJoining layered samples is necessary to prove the potential of that technique. In this PhD work, difficulties in measuring the temperature during the AddJoining process were reported. It is strongly recommended to develop an in-situ measurement device that makes it possible to record the temperature on the surface layer and between the 3D printed layers. This would help to better substantiate the explanations of thermal changes in the joined materials.

A deeper investigation of mechanical performance would complement understanding of the process. First of all, the development of analytical models is recommended that is capable of predicting the progress of damage in the stiffness-based fatigue experiments [323,326,327]. This could contribute to the investigation of fatigue performance with different stress ratios, also covering tension-compression and compression-compression regimes. AddJoining has the potential to be applied in structural applications, therefore it is extremely important to understand the fatigue performance with variable amplitudes, such as overload cases. An approach like this would cover realistic service loads and this is key to fatigue analysis and design principles for the aircraft industry. Finally, the study of corrosion behavior of AddJoining hybrid joints under various corrosive environments or thermo-oxidative conditions would improve the process knowledge.

References

[1] K. Anderson, A. Bows, S. Mander, From long-term targets to cumulative emission pathways: Reframing UK climate policy, Energy Policy. 36 (2008) 3714–3722.

[2] J.M. Allwood, M.F. Ashby, T.G. Gutowski, E. Worrell, Material efficiency: A white paper, Resour. Conserv. Recycl. 55 (2011) 362–381.

[3] J.K. Steinberger, F. Krausmann, N. Eisenmenger, Global patterns of materials use: A socioeconomic and geophysical analysis, Ecol. Econ. 69 (2010) 1148–1158.

[4] A.M. Lewis, J.C. Kelly, G.A. Keoleian, Vehicle lightweighting vs. electrification: Life cycle energy and GHG emissions results for diverse powertrain vehicles, Appl. Energy. 126 (2014) 13–20.

[5] P.K. Mallick, Joining for lightweight vehicles, in: P.K. Mallick (Ed.), Mater. Des. Manuf. Light. Veh., Woodhead Publishing, 2010: pp. 275–308.

[6] S.T. Amancio Filho, L.-A. Blaga, Joining of polymer-metal hybrid structures : principles and applications, John Wiley & Sons, Inc, 2017.

[7] S. Amancio-Filho, FRICTION RIVETING: development and analysis of a new joining technique for polymer-metal multi-material structures, Weld. World. 55 (2011) 13–24.

[8] S.M. Goushegir, J.F. Santos, S.T. Amancio-Filho, Influence of process parameters on mechanical performance and bonding area of AA2024 / carbon-fiber-reinforced poly (phenylene sulfide) friction spot single lap joints, Mater. Des. 83 (2015) 431–442.

[9] S.M. Goushegir, J.F. Santos, S.T. Amancio-Filho, Friction Spot Joining of aluminum AA2024 / carbon-fiber reinforced poly (phenylene sulfide) composite single lap joints : Microstructure and mechanical performance, Mater. Des. 54 (2014) 196–206.

[10] A.B. Abibe, M. Sônego, J.F. Santos, L.B. Canto, S.T. Amancio-Filho, On the feasibility of a friction-based staking joining method for polymer – metal hybrid structures, Mater. Des. 92 (2016) 632–642.

[11] A.B. Abibe, S.T. Amancio-Filho, J.F. Santos, E.H. Jr, Mechanical and failure behaviour of hybrid polymer – metal staked joints, Mater. Des. 46 (2013) 338–347.

[12] E.E. Feistauer, R.P.M. Guimarães, T. Ebel, J.F. Dos Santos, S.T. Amancio-Filho, Ultrasonic joining: A novel direct-assembly technique for metal-composite hybrid structures, Mater. Lett. 170 (2016) 1–4.

[13] E.E. Feistauer, T. Ebel, J.F. Dos Santos, S.T. Amancio-Filho, Ultrasonic joining of through-the-thickness reinforced TI-4AL-6V and polyetherimide hybrid joints, in: Soc. Plast. Eng. (ANTEC 2017), Anaheim, 2017: pp. 1718–1724.

[14] B.F. Balle, G. Wagner, D. Eifler, Ultrasonic metal welding of aluminium sheets to carbon fibre Reinforced thermoplastic composites, (2009) 35–39.

[15] D. Balle, F., Wagner, G., Eifler, Ultrasonic spot welding of aluminum sheet / carbon fiber reinforced polymer – joints, Mat.-Wiss. u. Werkstofftech. (2007) 934–938.

[16] M. Mitschang, Peter, Velthuis, Rudi, Emrich, Stefan, Kopnarski, Induction Heated Joining of Aluminum and Carbon Fiber Reinforced, Thermoplast. Compos. Mater. 22 (2008) 17–27.

[17] R. Falck, S.M. Goushegir, J.F. dos Santos, S.T. Amancio-Filho, AddJoining: a novel additive manufacturing approach for layered metal-polymer hybrid structures, Mater. Lett. (2018).

[18] F.L. Matthews, R.D. Rawlings, Composite Materials: Engineering and Science, Elsevier Science, 1999.

[19] P. Morgan, Carbon Fibers and Their Composites, CRC Press, 2005.

[20] D. Hull, T.W. Clyne, D.R. Clarke, I.M. Ward, S. Suresh, An Introduction to Composite Materials, Cambridge University Press, 1996.

[21] G. Staab, Laminar Composites, Elsevier Science, 1999.

[22] T.W. Chou, A. Kelly, A. Okurat, Fibre-reinforced metal-matrix composites, Composites. 16 (1985) 184–184.

[23] J.M. Hodgkinson, Mechanical Testing of Advanced Fibre Composites, Elsevier Science, 2000.

[24] B. Fiedler, F.H. Gojny, M.H.G. Wichmann, M.C.M. Nolte, K. Schulte, Fundamental aspects of nano-reinforced composites, Compos. Sci. Technol. 66 (2006) 3115–3125.

[25] F.H. Gojny, M.H.G. Wichmann, U. Köpke, B. Fiedler, K. Schulte, Carbon nanotube-reinforced epoxy-composites: Enhanced stiffness and fracture toughness at low nanotube content, Compos. Sci. Technol. 64 (2004) 2363–2371.

[26] F.H. Gojny, M.H.G. Wichmann, B. Fiedler, K. Schulte, Influence of different carbon nanotubes on the mechanical properties of epoxy matrix composites - A comparative study, Compos. Sci. Technol. 65 (2005) 2300–2313.

[27] M.H.G. Wichmann, J. Sumfleth, F.H. Gojny, M. Quaresimin, B. Fiedler, K. Schulte, Glass-fibre-reinforced composites with enhanced mechanical and electrical properties - Benefits and limitations of a nanoparticle modified matrix, Eng. Fract. Mech. 73 (2006) 2346–2359.

[28] L.B. Vogelesang, A. Vlot, Development of fibre metal laminates for advanced aerospace structures, J. Mater. Process. Technol. 103 (2000) 1–5.

[29] A. Asundi, A.Y.N. Choi, Fiber metal laminates: An advanced material for future aircraft, J. Mater. Process. Technol. 63 (1997) 384–394.

[30] A. Vlot, J.W. Gunnink, Fibre metal laminates: an introduction, Springer Science, 2011.

[31] K.L. Reifsnider, A. Talug, Analysis of fatigue damage in composite laminates, Int. J. Fatigue. 2 (1980) 3–11.

[32] D. Hull, Y.B. Shi, Damage mechanism characterization in composite damage tolerance investigations, Compos. Struct. 23 (1993) 99–120.

[33] S.R. Finn, G.S. Springer, Delaminations in composite plates under transverse static or impact loads - A model, Compos. Struct. 23 (1993) 177–190.

[34] B. Audoly, B. Roman, A. Pocheau, Secondary buckling patterns of a thin plate under in-plane compression, Eur. Phys. J. B. 27 (2002) 7–10.

[35] S.K. Panigrahi, B. Pradhan, Through-the-width delamination damage propagation characteristics in single-lap laminated FRP composite joints, Int. J. Adhes. Adhes. 29 (2009) 114–124.

[36] K.G. Satyanarayana, G.G.C. Arizaga, F. Wypych, Biodegradable composites based on lignocellulosic fibers-An overview, Prog. Polym. Sci. 34 (2009) 982–1021.

[37] M. Mohd Tahir, W.X. Wang, T. Matsubara, Failure behavior of quasi-isotropic carbon fiber-reinforced polyamide composites under tension, Adv. Compos. Mater. 3046 (2017) 1–15.

[38] C. Niu, M.C.Y. Niu, Airframe Stress Analysis and Sizing, Conmilit Press, 1999.

[39] C. Niu, M.C.Y. Niu, Airframe Structural Design: Practical Design Information and Data on Aircraft Structures, Adaso Adastra Engineering Center, 1999.

[40] D.H.J.A. Lukaszewicz, C. Ward, K.D. Potter, The engineering aspects of automated prepreg layup: History, present and future, Compos. Part B Eng. 43 (2012) 997–1009.

[41] R. DeVlieg, K. Jeffries, P. Vogeli, High-Speed Fiber Placement on Large Complex Structures, Proc. Aerosp. Technol. Conf. Expo. (2007) 1–5.

[42] B. Denkena, C. Schmidt, P. Weber, Automated Fiber Placement Head for Manufacturing of Innovative Aerospace Stiffening Structures, Procedia Manuf. 6 (2016) 96–104.

[43] C.M. Stokes-Griffin, S. Ehard, A. Kollmannsberger, P. Compston, K. Drechsler, A laser tape placement process for selective reinforcement of steel with CF/PA6 composites: Effects of surface preparation and laser angle, Mater. Des. 116 (2017) 545–553.

[44] C.M. Stokes-Griffin, P. Compston, Investigation of sub-melt temperature bonding of carbon-fibre/PEEK in an automated laser tape placement process, Compos. Part A Appl. Sci. Manuf. 84 (2016) 17–25.

[45] H. Sarrazin, G.S. Springer, Thermochemical and mechanical aspects of composite tape laying, Compos. Mater. 29 (1995) 1908–1943.

[46] P.M. Schaefer, D. Gierszewski, A. Kollmannsberger, S. Zaremba, K. Drechsler, Analysis and improved process response prediction of laser- assisted automated tape placement with PA-6/carbon tapes using Design of Experiments and numerical simulations, Compos. Part A Appl. Sci. Manuf. 96 (2017) 137–146.

[47] J.S. Colton, J. Baxter, J. Behlendorf, T. Halim, B. Harris, G. Kiesler, K. Tung Lu, S. Sammons, W. Savage-Moore, The automation of the lay-up and consolidation of peek/graphite fiber composites, Adv. Manuf. Process. 2 (1987) 1–22.

[48] M.A. Lamontia, M.B. Gruber, B.J. Waibel, R.D. Cope, A. Systems, S. Drive, Comformable compaction system used in automated fiber plcament of large composite aerospace structures, 23rd SAMPE Eur. Conf. Paris. (2002) 9–11.

[49] T. Orth, C. Weimer, M. Krahl, N. Modler, A review of radiative heating in automated layup and its modelling Automated, J. Plast. Technol. 11 (2015).

[50] H. Janssen, T. Peters, C. Brecher, Efficient Production of Tailored Structural Thermoplastic Composite Parts by Combining Tape Placement and 3d Printing, Procedia CIRP. 66 (2017) 91–95.

[51] G. Clancy, D. Peeters, V. Oliveri, D. Jones, R.M. O'Higgins, P.M. Weaver, A study of the influence of processing parameters on steering of carbon Fibre/PEEK tapes using laser-assisted tape placement, Compos. Part B Eng. 163 (2018) 243–251.

[52] M. Lamontia, S.B. Funck, M.B. Gruber, R.D. Cope, B.J. Waibel, N.M. Gopez, Manufacturing

flat and cylindrical laminates and built up structure using automated thermoplastic tape laying, fiber placement, and filament winding, SAMPE J. 39 (2003) 30–38.

[53] Z. Qureshi, T. Swait, R. Scaife, H.M. El-Dessouky, In-situ consolidation of thermoplastic prepreg tape using automated tape placement technology: Potential and possibilities, Compos. Part B Eng. 66 (2014) 255–267.

[54] R.H. Rizzolo, D.F. Walczyk, Ultrasonic consolidation of thermoplastic composite prepreg for automated fiber placement, J. Thermoplast. Compos. Mater. 29 (2016) 1480–1497.

[55] D. Ray, A.J. Comer, J. Lyons, W. Obande, D. Jones, R.M.O. Higgins, M.A. McCarthy, Fracture toughness of carbon fiber/polyether ether ketone composites manufactured by autoclave and laser-assisted automated tape placement, Appl. Polym. Sci. 132 (2015).

[56] F.L. Di Scalea, A hybrid non-contact ultrasonic system for sensing bond quality in tow-placed thermoplastic composites, Compos. Mater. 34 (2000) 1860–1880.

[57] W.J.B. Grouve, L. Warnet, R. Akkerman, S. Wijskamp, J.S.M. Kok, Weld strength assessment for tape placement, Int. J. Mater. Form. 3 (2010) 707–710.

[58] C. Brecher, T. Peters, M. Emonts, Cost-effective high speed production of multi-material components by selective tape placement, in: A.L. Araújo, J.R. Correia, C.M. Mota Soares (Eds.), 10th Int. Conf. Compos. Sci. Technol., 2015.

[59] D. Modi, M.A. McCarthy, A.J. Comer, Investigation of laser assisted automated tape placement process, in: 34th Int. Tech. Conf. Forum, Paris, 2013.

[60] C.M. Stokes-Griffin, P. Compston, T.I. Matuszyk, M.J. Cardew-Hall, Thermal modelling of the laser-assisted thermoplastic tape placement process, J. Thermoplast. Compos. Mater. 28 (2015) 1445–1462.

[61] E. Beyeler, W. Phillips, S.I. Güçeri, Experimental Investigation of Laser-Assisted Thermoplastic Tape Consolidation, J. Thermoplast. Compos. Mater. 1 (1988) 107–121.

[62] V.A. Kagan, G.P. Pinho, Laser Transmission Welding of Semicrystalline Thermoplastics - Part II: Analysis of Mechanical Performance of Welded Nylon, J. Reinf. Plast. Compos. 23 (2004) 95–107.

[63] H. Potente, J. Korte, F. Becker, Laser transmission welding of thermoplastics: Analysis of the heating phase, J. Reinf. Plast. Compos. 10 (1999) 914–920.

[64] M. a Lamontia, M.B. Gruber, Remaining developments required for commerzializing in situ thermoplastic ATP, in: Proc. 2007 SAMPE Conf. Exhib., 2007: pp. 1–15.

[65] B.J. Jensen, M.C. Kinney, R.J. Cano, B.W. Grimsley, Materials for heated head automated thermoplastic tape placement, in: Proc. 2012 SAMPE Conf. Exhib., 2012.

[66] A.J. Comer, D. Ray, W.O. Obande, D. Jones, J. Lyons, I. Rosca, R.M. O'Higgins, M.A. McCarthy, Mechanical characterisation of carbon fibre-PEEK manufactured by laser-assisted automated-tape-placement and autoclave, Compos. Part A Appl. Sci. Manuf. 69 (2015) 10–20.

[67] C.M. Stokes-Griffin, P. Compston, The effect of processing temperature and placement rate on the short beam strength of carbon fibre–PEEK manufactured using a laser tape placement process, Compos. Part A Appl. Sci. Manuf. 78 (2015) 274–283.

[68] F.O. Sonmez, M. Akbulut, Process optimization of tape placement for thermoplastic composites, Compos. Part A Appl. Sci. Manuf. 38 (2007) 2013–2023.

[69] K. Croft, L. Lessard, D. Pasini, M. Hojjati, J. Chen, A. Yousefpour, Experimental study of the effect of automated fiber placement induced defects on performance of composite laminates, Compos. Part A Appl. Sci. Manuf. 42 (2011) 484–491.

[70] A. Sawicki, P. Minguett, The effect of intraply overlaps and gaps upon the compression strength of composite laminates, 39th AIAA/ASME/ASCE/AHS/ASC Struct. Struct. Dyn. Mater. Conf. Exhib. (1998) 744–754.

[71] W. Woigk, S.R. Hallett, M.I. Jones, M. Kuhtz, A. Hornig, M. Gude, Experimental investigation of the effect of defects in Automated Fibre Placement produced composite laminates, Compos. Struct. 201 (2018) 1004–1017.

[72] M. Rakhshbahar, M. Sinapius, A Novel Approach: Combination of Automated Fiber Placement (AFP) and Additive Layer Manufacturing (ALM), J. Compos. Sci. 2 (2018) 42.

[73] M.A. Khan, P. Mitschang, R. Schledjewski, Parametric study on processing parameters and resulting part quality through thermoplastic tape placement process, J. Compos. Mater. 47 (2013) 485–499.

[74] S. Rajan, M.A. Sutton, R. Wehbe, B. Tatting, Z. Gürdal, A. Kidane, R. Harik, Experimental investigation of prepreg slit tape wrinkling during automated fiber placement process using StereoDIC, Compos. Part B Eng. 160 (2018) 546–557.

[75] M. Arhant, C. Briançon, C. Burtin, P. Davies, Carbon/polyamide 6 thermoplastic composite cylinders for deep sea applications, Compos. Struct. 212 (2019) 535–546.

[76] S. Van Hoa, M. Duc Hoang, J. Simpson, Manufacturing procedure to make flat thermoplastic composite laminates by automated fibre placement and their mechanical properties, J. Thermoplast. Compos. Mater. 30 (2017) 1693–1712.

[77] J.-P. Kruth, M.C. Leu, T. Nakagawa, Progress in Additive Manufacturing and Rapid Prototyping, CIRP Ann. - Manuf. Technol. 47 (1998) 525–540.

[78] ASTM F2792-12, Standard Terminology for Additive Manufacturing Technologies, ASTM Int. West Consh (2012) 1–3. http://www.astm.org.

[79] S.H. Huang, P. Liu, A. Mokasdar, L. Hou, Additive manufacturing and its societal impact: A literature review, Int. J. Adv. Manuf. Technol. 67 (2013) 1191–1203.

[80] H. Bikas, P. Stavropoulos, G. Chryssolouris, Additive manufacturing methods and modelling approaches: a critical review, Int. J. Adv. Manuf. Technol. (2015).

[81] L. Novakova-Marcincinova, I. Kuric, Basic and Advanced Materials for Fused Deposition Modeling Rapid Prototyping Technology, Manuf. Ind. Eng. 11 (2012) 24–27.

[82] S.S. Crump, Apparatus and Method for Creating Three-Dimensional Objects, US5340433, 1992.

[83] Stratasys, Manufacturing Auto Jigs and Fixtures with 3D Printing, Direct Digit. Manuf. BMW. (2016). http://www.stratasys.com/resources/case-studies/automotive/bmw (accessed July 5, 2016).

[84] K. V. Wong, A. Hernandez, K. V. Wong, A. Hernandez, A Review of Additive

Manufacturing, A Review of Additive Manufacturing, Int. Sch. Res. Not. Int. Sch. Res. Not. 2012, 2012 (2012) e208760.

[85] Brian N. Turner, Robert Strong, Scott A. Gold, A review of melt extrusion additive manufacturing processes: I. Process design and modeling, Rapid Prototyp. J. 20 (2014) 192–204.

[86] T. Campbell, C. Williams, I. Olga, B. Garrett, Could 3D Printing Change the World?, Technol. Potential, Implic. Addit. Manuf. Atl. Counc. Washington, DC. (2011) 15. http://3dprintingindustry.com/wp-content/uploads/2013/05/Atlantis-Report-on-3D-printing.pdf (accessed January 11, 2016).

[87] S.H. Ahn, C. Baek, S. Lee, I.S. Ahn, c, Int. J. Mod. Phys. B. 17 (2003) 1510–1516.

[88] R. Anitha, S. Arunachalam, P. Radhakrishnan, Critical parameters influencing the quality of prototypes in fused deposition modelling, J. Mater. Process. Technol. 118 (2001) 385–388.

[89] F. Górski, W. Kuczko, R. Wichniarek, Influence of Process Parameters on Dimensional Accuracy of Parts Manufactured Using Fused Deposition Modelling Technology, Adv. Sci. Technol. – Res. J. 7 (2013) 27–35.

[90] L. Novakova-Marcincinova and J. Novak-Marcincin, Testing of Materials for Rapid Prototyping Fused Deposition Modelling Technology, Int. J. Mech. Aerospace, Ind. Mechatron. Manuf. Eng. 6 (2012) 2081–2085.

[91] Q. Sun, G.M. Rizvi, C.T. Bellehumeur, P. Gu, Effect of processing conditions on the bonding quality of FDM polymer filaments, Rapid Prototyp. J. 14 (2008) 72–80.

[92] A.K. Sood, R.K. Ohdar, S.S. Mahapatra, Improving dimensional accuracy of Fused Deposition Modelling processed part using grey Taguchi method, Mater. Des. 30 (2009) 4243–4252.

[93] R. Van Weeren, M. Agarwala, V.R. Jamalabad, A. Bandyophadyay, R. Vaidyanathan, N. Langrana, A. Safari, P. Whalen, S.C. Danforth, C. Ballard, Quality of parts processed by fused deposition, in: 1995: pp. 314–21.

[94] M. Domingo-Espin, J.M. Puigoriol-Forcada, A.A. Garcia-Granada, J. Llumà, S. Borros, G. Reyes, Mechanical property characterization and simulation of fused deposition modeling Polycarbonate parts, Mater. Des. 83 (2015) 670–677.

[95] A.W. Fatimatuzahraa, B. Farahaina, W.A.Y. Yusoff, The effect of employing different raster orientations on the mechanical properties and microstructure of Fused Deposition Modeling parts, in: 2011 IEEE Symp. Business, Eng. Ind. Appl. ISBEIA, 2011: pp. 22–27.

[96] R. Falck, J.F. Dos Santos, S.T. Amancio-Filho, An overview on the materials and mechanical behavior used in fused deposition modeling, in: Soc. Plast. Eng. (ANTEC 2017), Society of Plastics Engineers, Anaheim, 2017: pp. 1689–1695.

[97] Mukesh K. Agarwala, Vikram R. Jamalabad, Noshir A. Langrana, Ahmad Safari, Philip J. Whalen, Stephen C. Danforth, Structural quality of parts processed by fused deposition, Rapid Prototyp. J. 2 (1996) 4–19.

[98] C. Bellehumeur, L. Li, Q. Sun, P. Gu, Modeling of Bond Formation Between Polymer Filaments in the Fused Deposition Modeling Process, J. Manuf. Process. 6 (2004) 170–178.

[99] J.F. Rodríguez, J.P. Thomas, J.E. Renaud, Mechanical behavior of acrylonitrile butadiene

styrene fused deposition materials modeling, Rapid Prototyp. J. 9 (2003) 219–230.

[100] A.K. Sood, R.K. Ohdar, S.S. Mahapatra, Parametric appraisal of mechanical property of fused deposition modelling processed parts, Mater. Des. 31 (2010) 287–295.

[101] N. Hill, M. Haghi, Deposition direction-dependent failure criteria for fused deposition modeling polycarbonate, Rapid Prototyp. J. 20 (2014) 221–227.

[102] C. Ziemian, M. Sharma, S. Ziemian, Anisotropic mechanical properties of ABS parts fabricated by fused deposition modelling, in: M. Gokcek (Ed.), Mech. Eng., InTech, 2012: pp. 159–180.

[103] O.S. Es-Said, J. Foyos, R. Noorani, M. Mendelson, R. Marloth, B.A. Pregger, Effect of Layer Orientation on Mechanical Properties of Rapid Prototyped Samples, Mater. Manuf. Process. 15 (2000) 107–122.

[104] A. Bellini, S. Güçeri, Mechanical characterization of parts fabricated using fused deposition modeling, Rapid Prototyp. J. 9 (2003) 252–264.

[105] J. Lee, A. Huang, Fatigue analysis of FDM materials, Rapid Prototyp. J. 19 (2013) 291–299.

[106] A. Bagsik, V. Schöoppner, Mechanical Properties of Fused Deposition Modeling Parts Manufactured with ULTEM 9085, Proc. ANTEC (Vol. 2011). (2011) 1294–1298.

[107] A.Q. Pan, Z.F. Huang, R.J. Guo, J. Liu, Effect of FDM Process on Adhesive Strength of Polylactic Acid(PLA) Filament, Key Eng. Mater. 667 (2015) 181–186.

[108] F. Ning, W. Cong, Y. Hu, H. Wang, Additive manufacturing of carbon fiber-reinforced plastic composites using fused deposition modeling: Effects of process parameters on tensile properties, J. Compos. Mater. (2016).

[109] W. Wu, P. Geng, G. Li, D. Zhao, H. Zhang, J. Zhao, Influence of Layer Thickness and Raster Angle on the Mechanical Properties of 3D-Printed PEEK and a Comparative Mechanical Study between PEEK and ABS, Materials. 8 (2015).

[110] S. Hertle, M. Drexler, D. Drummer, Additive Manufacturing of Poly(propylene) by Means of Melt Extrusion, Macromol. Mater. Eng. (2016) 1482–1493.

[111] S.S. Voyutskii, V.L. Vakula, The role of diffusion phenomena in polymer-to-polymer adhesion, J. Appl. Polym. Sci. 7 (1963) 475–491.

[112] H.L. Tekinalp, V. Kunc, G.M. Velez-Garcia, C.E. Duty, L.J. Love, A.K. Naskar, C.A. Blue, S. Ozcan, Highly oriented carbon fiber-polymer composites via additive manufacturing, Compos. Sci. Technol. 105 (2014) 144–150.

[113] W. Zhong, F. Li, Z. Zhang, L. Song, Z. Li, Short fiber reinforced composites for fused deposition modeling, Mater. Sci. Eng. A. 301 (2001) 125–130.

[114] M.L. Shofner, K. Lozano, F.J. Rodríguez-Macías, E. V. Barrera, Nanofiber-reinforced polymers prepared by fused deposition modeling, J. Appl. Polym. Sci. 89 (2003) 3081–3090.

[115] H. Prüß, T. Vietor, Design for Fiber-Reinforced Additive Manufacturing, J. Mech. Des. 137 (2015) 111409.

[116] MarkForged, The Mark Two: Industrial Strength 3D Printer, (2016). http://markforged.com/mark-two/.

[117] A. Fischer, S. Rommel, R. Geiger, S. Weber, Tool and method for sheating and elongate product available by the meter, WO214026762A3, 2011.

[118] A. Fischer, S. Rommel, T. Bauernhansl, New fiber matrix process with 3D fiber printer – A strategic in-process integration of endless fibers using fused deposition modeling (FDM), in: G.L. Kóvacs, D. Kochan (Eds.), IFIP Adv. Inf. Commun. Technol., Dresden, 2013: pp. 167–175.

[119] F. Baumann, J. Scholz, J. Fleischer, Investigation of a New Approach for Additively Manufactured Continuous Fiber-reinforced Polymers, Procedia CIRP. 66 (2017) 323–328.

[120] Desktop Metal, Desktop Metal - Fiber™, (2019). www.desktopmetal.com/products/fiber/ (accessed November 15, 2019).

[121] A. Essop, Desktop Metal reveals Fiber, a new desktop 3D printer for continuous fiber composites, (n.d.). https://3dprintingindustry.com/news/desktop-metal-reveals-fiber-a-new-desktop-3d-printer-for-continuous-fiber-composites-164109/ (accessed November 15, 2019).

[122] M. Burlington, Desktop Metal Set to Transform Continuous Fiber 3D Printing, (2019).

[123] Y. Su, M. de Rooij, W. Grouve, R. Akkerman, The effect of titanium surface treatment on the interfacial strength of titanium – Thermoplastic composite joints, Int. J. Adhes. Adhes. 72 (2017) 98–108.

[124] M.-S. Seong, T.-H. Kim, K.-H. Nguyen, J.-H. Kweon, J.-H. Choi, A parametric study on the failure of bonded single-lap joints of carbon composite and aluminum, Compos. Struct. 86 (2008) 135–145.

[125] Y. Zhai, D. Li, X. Li, L. Wang, An experimental study on the effect of joining interface condition on bearing response of single-lap, countersunk composite-aluminum bolted joints, Compos. Struct. 134 (2015) 190–198.

[126] G. Di Franco, L. Fratini, A. Pasta, Analysis of the mechanical performance of hybrid (SPR/bonded) single-lap joints between CFRP panels and aluminum blanks, Int. J. Adhes. Adhes. 41 (2013) 24–32.

[127] P. Lopez-Cruz, J. Laliberté, L. Lessard, Investigation of bolted/bonded composite joint behaviour using design of experiments, Compos. Struct. 170 (2017) 192–201.

[128] J.-H. Kweon, J.-W. Jung, T.-H. Kim, J.-H. Choi, D.-H. Kim, Failure of carbon composite-to-aluminum joints with combined mechanical fastening and adhesive bonding, Compos. Struct. 75 (2006) 192–198.

[129] K. Bodjona, L. Lessard, Hybrid bonded-fastened joints and their application in composite structures: A general review, J. Reinf. Plast. Compos. 35 (2016) 764–781.

[130] P. Mitschang, R. Velthuis, M. Didi, Induction Spot Welding of Metal/CFRPC Hybrid Joints, Adv. Eng. Mater. 15 (2013) 804–813.

[131] S.M. Goushegir, J.F. dos Santos, S.T. Amancio-Filho, Friction Spot Joining of aluminum AA2024/carbon-fiber reinforced poly(phenylene sulfide) composite single lap joints: Microstructure and mechanical performance, Mater. Des. 54 (2014) 196–206.

[132] S.T. Amancio-Filho, J.F. dos Santos, Joining of polymers and polymer–metal hybrid structures: Recent developments and trends, Polym. Eng. Sci. 49 (2009) 1461–1476.

[133] A. Higgins, Adhesive bonding of aircraft structures, Int. J. Adhes. Adhes. 20 (2000) 367–376.

[134] Y. Ciupack, H. Pasternak, C. Mette, E. Stammen, K. Dilger, Adhesive bonding in steel construction -Challenge and innovation, Procedia Eng. 172 (2017) 186–193.

[135] A. Kwakernaak, J. Hofstede, J.A. Poulis, R. Benedictus, Improvements in bonding metals for aerospace and other applications, Weld. Join. Aerosp. Mater. (2012) 235–287.

[136] A.B. Abibe, S.T. Amancio-Filho, J.F. dos Santos, E. Hage Jr., Mechanical and failure behaviour of hybrid polymer–metal staked joints, Mater. Des. 46 (2013) 338–347.

[137] A.B. Abibe, M. Sônego, J.F. dos Santos, L.B. Canto, S.T. Amancio-Filho, On the feasibility of a friction-based staking joining method for polymer–metal hybrid structures, Mater. Des. 92 (2016) 632–642.

[138] S.T. Amancio-Filho, Henry Granjon Prize Competition 2009 Winner Category A: "Joining and Fabrication Technology" Friction Riveting: development and analysis of a new joining technique for polymer-metal multi-material structures, Weld. World. 55 (2011) 13–24.

[139] N.Z. Borba, L. Blaga, J.F. dos Santos, S.T. Amancio-Filho, Direct-Friction Riveting of polymer composite laminates for aircraft applications, Mater. Lett. 215 (2018) 31–34.

[140] P. Mitschang, R. Velthuis, S. Emrich, M. Kopnarski, Induction Heated Joining of Aluminum and Carbon Fiber Reinforced Nylon 66, J. Thermoplast. Compos. Mater. 22 (2009) 767–801.

[141] C. Ageorges, L. Ye, Resistance welding of thermosetting composite/thermoplastic composite joints, Compos. - Part A Appl. Sci. Manuf. 32 (2001) 1603–1612.

[142] K.W. Jung, Y. Kawahito, M. Takahashi, S. Katayama, Laser direct joining of carbon fiber reinforced plastic to zinc-coated steel, Mater. Des. 47 (2013) 179–188.

[143] F.I. Hussein, E. Akman, B. Genc Oztoprak, M. Gunes, O. Gundogdu, E. Kacar, K.I. Hajim, A. Demir, Evaluation of PMMA joining to stainless steel 304 using pulsed Nd:YAG laser, Opt. Laser Technol. 49 (2013) 143–152.

[144] N.M. André, S.M. Goushegir, J.F. dos Santos, L.B. Canto, S.T. Amancio-Filho, Friction Spot Joining of aluminum alloy 2024-T3 and carbon-fiber-reinforced poly(phenylene sulfide) laminate with additional PPS film interlayer: Microstructure, mechanical strength and failure mechanisms, Compos. Part B Eng. 94 (2016) 197–208.

[145] S.T. Amancio-Filho, A.B. Abibe, J.F. Dos Santos, Joining: Mechanical Fastening of Polymers, Composites, and Polymer–Metal Hybrid Structures, Wiley Encycl. Compos. (2012).

[146] M. Grujicic, V. Sellappan, G. Arakere, N. Seyr, A. Obieglo, M. Erdmann, J. Holzleitner, The Potential of a Clinch-Lock Polymer Metal Hybrid Technology for Use in Load-Bearing Automotive Components, J. Mater. Eng. Perform. 18 (2009) 893–902.

[147] E.E. Feistauer, J.F. dos Santos, S.T. Amancio-Filho, A Review on Direct Assembly of Through-the-Thickness Reinforced Metal-Polymer Composite Hybrid Structures, Polym. Eng. Sci. (2018) 1–14.

[148] S.T. Peters, Handbook of composites, 2nd ed., Chapman & Hall, Springer, US, 1998.

[149] ASM International Handbook Committee, ASM Volume 21 - Handbook of Composites, ASM International, 2001.

[150] A. Heinz, A. Haszler, C. Keidel, S. Moldenhauer, R. Benedictus, W.S. Miller, Recent development in aluminium alloys for aerospace applications, Mater. Sci. Eng. A. 280 (2000) 102–107.

[151] I.J. Polmear, Recent developments in light alloys, Mater. Trans. 37 (1996) 12–31.

[152] F. Mansfeld, J. V Kenkel, Laboratory Studies of Galvanic Corrosion of Aluminum Alloys, in: R. Baboian, W. France, L. Rowe, J. Rynewicz (Eds.), Galvanic Pitting Corros. Lab. Stud., ASTM International, West Conshohocken, PA, 1976: pp. 20–47.

[153] L.F. Mondolfo, Aluminum Alloys: Structure and Properties, Elsevier Science, 2013.

[154] G. Mathers, The Welding of Aluminium and Its Alloys, Elsevier Science, 2002.

[155] C. Genevois, A. Deschamps, P. Vacher, Comparative study on local and global mechanical properties of 2024 T351, 2024 T6 and 5251 O friction stir welds, Mater. Sci. Eng. A. 415 (2006) 162–170.

[156] P. Cavaliere, R. Nobile, F.W. Panella, A. Squillace, Mechanical and microstructural behaviour of 2024–7075 aluminium alloy sheets joined by friction stir welding, Int. J. Mach. Tools Manuf. 46 (2006) 588–594.

[157] P. Sadeesh, K.M. Venkatesh, V. Rajkumar, P. Avinash, N. Arivazhagan, R.K. Devendranath, S. Narayanan, Studies on friction stir welding of aa 2024 and aa 6061 dissimilar metals, Procedia Eng. 75 (2014) 145–149.

[158] S.T. Amancio-Filho, A.P.C. Camillo, L. Bergmann, J.F. dos Santos, S.E. Kury, N.G.A. Machado, Preliminary Investigation of the Microstructure and Mechanical Behaviour of 2024 Aluminium Alloy Friction Spot Welds, Mater. Trans. 52 (2011) 985–991.

[159] Global Industry Analysts, Nylon - Market analysis, trends, and forecasts by global industry analysts, 2018. https://www.strategyr.com/market-report-nylon-forecasts-global-industry-analysts-inc.asp.

[160] E.C. Botelho, J.C. Bravim Júnior, M. Leali Costa, M.C. Magalhaes De Faria, Environmental Effects on Thermal Properties of PEI/Glass Fiber Composite Materials, J. Aerosp. Technol. 5 (2013) 241–254.

[161] S. Boria, A. Scattina, G. Belingardi, Impact behavior of a fully thermoplastic composite, Compos. Struct. 167 (2017) 63–75.

[162] E.C. Botelho, L. Figiel, M.C. Rezende, B. Lauke, Mechanical behavior of carbon fiber reinforced polyamide composites, Compos. Sci. Technol. 63 (2003) 1843–1855.

[163] M.I. Kohan, M.I. Kohan, Nylon Plastics Handbook, Hanser Publishers, 1995.

[164] F.W. Billmeyer, Textbook of Polymer Science, 3rd ed., Wiley, 2007.

[165] N.S. Murthy, R.G. Bray, Structure and properties of polyamide 6 and 4-aminomethylcyclohexane carboxylic acid copolymers with an unusually short helical pitch for nylons, Polymer (Guildf). 44 (2003) 5387–5396.

[166] Y. Li, W.A. Goddard, N.S. Murthy, Crystal structure and properties of N6/AMCC copolymer from theory and fiber XRD, Macromolecules. 36 (2003) 900–907.

[167] N.S. Murthy, Hydrogen Bonding, Mobility, and Structural Transitions in Aliphatic Polyamides, J. Polym. Sci. Part B Polym. Phys. 44 (2006) 1763–1782.

[168] H. Batzer, U.T. Kreibich, Influence of water on thermal transitions in natural polymers and synthetic polyamides, Polym. Bull. 5 (1981) 585–590.

[169] BASF, Mechanical Performance of Polyamides with Influence of Moisture and Temperature –Accurate Evaluation and Better Understanding, (2001).

[170] S.S. Yao, F.L. Jin, K.Y. Rhee, D. Hui, S.J. Park, Recent advances in carbon-fiber-reinforced thermoplastic composites: A review, Compos. Part B Eng. 142 (2018) 241–250.

[171] R. Cai, T. Jin, The effect of microstructure of unidirectional fibre-reinforced composites on mechanical properties under transverse loading: A review, J. Reinf. Plast. Compos. 37 (2018) 1360–1377.

[172] C. Oztan, R. Karkkainen, M. Fittipaldi, G. Nygren, L. Roberson, M. Lane, E. Celik, Microstructure and mechanical properties of three dimensional-printed continuous fiber composites, in: J. Compos. Mater., 2018.

[173] G.W. Melenka, B.K.O. Cheung, J.S. Schofield, M.R. Dawson, J.P. Carey, Evaluation and prediction of the tensile properties of continuous fiber-reinforced 3D printed structures, Compos. Struct. 153 (2016) 866–875.

[174] F. Van Der Klift, Y. Koga, A. Todoroki, M. Ueda, Y. Hirano, 3D Printing of Continuous Carbon Fibre Reinforced Thermo-Plastic (CFRTP) Tensile Test Specimens, Open J Compos Mater. 6 (2016) 18–27.

[175] A.N. Dickson, J.N. Barry, K.A. Mcdonnell, D.P. Dowling, Fabrication of continuous carbon , glass and Kevlar fibre reinforced polymer composites using additive manufacturing, Addit. Manuf. 16 (2017) 146–152.

[176] H.J. An, J.S. Kim, K.-Y. Kim, Y. Lim, D.H. Kim, Mechanical and Thermal Properties of Long Carbon Fiber-reinforced Polyamide 6 Composites, Fibers Polym. 15 (2014) 2355–2359.

[177] J. Wang, L. Li, Y. He, H. Song, X. Chen, J. Guo, The effect of thermo-oxidative ageing on crystallization, dynamic and static mechanical properties of long glass fibre-reinforced polyamide 10T composites, R. Soc. Open Sci. 5 (2018).

[178] P.A. Eriksson, P. Boydell, K. Eriksson, J.A.E. Månson, A.C. Albertsson, Effect of thermal-oxidative aging on mechanical, chemical, and thermal properties of recycled polyamide 66, J. Appl. Polym. Sci. 65 (1997) 1619–1630.

[179] H. Li, Y. Wang, C. Zhang, B. Zhang, Effects of thermal histories on interfacial properties of carbon fiber/polyamide 6 composites: Thickness, modulus, adhesion and shear strength, Compos. Part A Appl. Sci. Manuf. 85 (2016) 31–39.

[180] D. Kada, A. Koubaa, G. Tabak, S. Migneault, B. Garnier, Tensile Properties, Thermal Conductivity , and Thermal Stability of Short Carbon Fiber Reinforced Polypropylene Composites, Polym. Compos. (2016) 1–7.

[181] C. Ouyang, W. Xue, D. Zhang, Q. Gao, X. Li, K. Zheng, Influence of a Synthetic Ureido Nucleating Agent on Crystallization Behavior and Mechanical Properties of Polyamide 6, Polym. Eng. Sci. (2015).

[182] J. Liang, Y. Xu, Z. Wei, P. Song, G. Chen, W. Zhang, Mechanical properties, crystallization and melting behaviors of carbon fiber-reinforced PA6 composites, J. Therm. Anal. Calorim. 115 (2014) 209–218.

[183] B. Yalcin, D. Valladares, M. Cakmak, Amplification effect of platelet type nanoparticles on the orientation behavior of injection molded nylon 6 composites, Polymer (Guildf). 44 (2003) 6913–6925.

[184] T.D. Fornes, D.R. Paul, Crystallization behavior of nylon 6 nanocomposites, Polymer (Guildf). 44 (2003) 3945–3961.

[185] G.D. Goh, Y.L. Yap, S. Agarwala, W.Y. Yeong, Recent Progress in Additive Manufacturing of Fiber Reinforced Polymer Composite, Adv. Mater. Technol. 1800271 (2018) 1–22.

[186] R. Falck, J. dos Santos, S.T. Amancio-Filho, Microstructure and Mechanical Performance of Additively Manufactured Aluminum 2024-T3/Acrylonitrile Butadiene Styrene Hybrid Joints Using an AddJoining Technique, Materials. 12 (2019).

[187] R. Falck, S.T. Amancio-Filho, The influence of coating and adhesive layers on the mechanical performance of acrylonitrile butadiene styrene/aluminum hybrid joints manufactured by AddJoining, in: Annu. Assem. Int. Inst. Weld. – IIW 2020, Comm. XVI, Online Conference (https://iiw2020.online/), 2020.

[188] Aluminum AA2024-T3 technical datasheet. Constellium France, (2012).

[189] H. Boyer, T. Gall, Metals Handbook, American Society for Metals, Ohio, 1985.

[190] R.K.W. Marceau, G. Sha, R.N. Lumley, S.P. Ringer, Evolution of solute clustering in Al–Cu–Mg alloys during secondary ageing, Acta Mater. 58 (2010) 1795–1805.

[191] S. Abis, M. Massazza, P. Mengucci, G. Riontino, Early ageing mechanisms in a high-copper AlCuMg alloy, Scr. Mater. 45 (2001) 685–691.

[192] MarkForged, Material datasheet and descriptions - composites, (2018). https://static.markforged.com/markforged_composites_datasheet.pdf (accessed October 1, 2018).

[193] Y. Ma, M. Ueda, T. Yokozeki, T. Sugahara, Y. Yang, Investigation of the Flexural Properties and Failure Behavior of Unidirectional CF / Nylon 6 and CF / Epoxy Composites, (2017) 227–249.

[194] A. Grozdanov, G. Bogoeva-Gaceva, Carbon Fibers/Polyamide 6 Composites Based on Hybrid Yarns, J. Thermoplast. Compos. Mater. 23 (2010) 99–110.

[195] I. Boukal, Effect of water on the mechanism of deformation of nylon 6, J. Appl. Polym. Sci. 11 (2018) 1483–1494.

[196] V. Miri, O. Persyn, J.M. Lefebvre, R. Seguela, Effect of water absorption on the plastic deformation behavior of nylon 6, Eur. Polym. J. 45 (2009) 757–762.

[197] ASTM D570-98, Standard Test Method for Water Absorption of Plastics, ASTM Stand. 16 (1985) 1–4.

[198] D.C. Montgomery, G.C. Runger, Applied statistics and probability for engineers, 3rd ed., John Wiley & Sons, 2003.

[199] T. Wember, Technische Statistik und statistische Versuchsplanung: Einführung in statistische Methoden mit Anwendungsschwerpunkt in der Analyse technischer Daten für Techniker, Ingenieure und Naturwissenschaftler, P & P Informationstechnologie GmbH, 1999.

[200] ISO 4287:1997 - Geometrical Product Specifications (GPS) - Surface texture: Profile method

-Terms, definitions and surface texture parameters, ISO. (1997).

[201] G.W. Ehrenstein, G. Riedel, P. Trawiel, Thermal Analysis of Plastics: Theory and Practice, Carl Hanser Verlag, Munich, 2004.

[202] C. Millot, L.-A. Fillot, O. Lame, P. Sotta, R. Seguela, Assessment of polyamide-6 crystallinity by DSC: Temperature dependence of the melting enthalpy, J. Therm. Anal. Calorim. (2015).

[203] K.-H. Illers, Polymorphie, kristallinität und schmelzwärme von poly(ε-caprolactam), 2. Kalorimetrische untersuchungen, Die Makromol. Chemie. 179 (n.d.) 497–507.

[204] B. Wunderlich, Macromolecular physics, Academic Press, New York, 1971.

[205] S. Zhou, Q. Zhang, J. Huang, D. Ding, Friction and wear behaviors of polyamide-based composites blended with polyphenylene sulfide, J. Thermoplast. Compos. Mater. 27 (2014) 977–991.

[206] ASTM E384-10e1, Standard Test Method for Knoop and Vickers Hardness of Materials, (2010). http://www.astm.org.

[207] X. Li, B. Bhushan, A review of nanoindentation continuous stiffness measurement technique and its applications, Mater. Charact. 48 (2002) 11–36.

[208] W.C. Oliver, G.M. Pharr, I. Introduction, An improved technique for determing hardness and elastic modulus using load and displacement sensing indentation experiments, Mater. Res. 7 (1992) 1564–1583.

[209] S. Homaeigohar, J. Koll, E.T. Lilleodden, M. Elbahri, The solvent induced interfiber adhesion and its influence on the mechanical and filtration properties of polyethersulfone electrospun nanofibrous microfiltration membranes, Sep. Purif. Technol. 98 (2012) 456–463.

[210] B.J. Briscoe, L. Fiori, E. Pelillo, Nano-indentation of polymeric surfaces, J. Phys. D. Appl. Phys. 31 (1998) 2395–2405.

[211] ASTM D3163-01, Standard Test Method for Determining Strength of Ad hesively Bonded Rigid Plastic Lap-Shear Joints in Shear by Tension Loading, (2014). www.astm.org.

[212] ASTM E466-15, Standard Practice for Conducting Force Controlled Constant Amplitude Axial Fatigue Tests of Metallic Materials, (n.d.). www.astm.org.

[213] J. Schijve, Fatigue of Structures and Materials, Springer Netherlands, 2008.

[214] ASTM E739-10, Standard Practice for Statistical Analysis of Linear or Linearized Stress-Life (S-N) and Strain-Life (ε-N) Fatigue Data, ASTM Stand. (2015). www.astm.org.

[215] DIN 50100, Schwingfestigkeitsversuch - Durchführung und Auswertung von zyklischen Versuchen mit konstanter Lastamplitude für metallische Werkstoffproben und Bauteile, (2016). www.din.de.

[216] A. Fahr, A.Y. Kandeil, Ultrasonic C-scan inspection of composite materials, Eng. J. Qatar Univ. 5 (1992) 201–222.

[217] H.T. Hahn, R.Y. Kim, Fatigue behaviour of composite laminate, J. Compos. Mater. 10 (1976) 156–180.

[218] S.M. Goushegir, J.F. dos Santos, S.T. Amancio-Filho, Influence of aluminum surface pre-treatments on the bonding mechanisms and mechanical performance of metal-composite

single-lap joints, Weld. World. 61 (2017) 1099–1115.

[219] A.K. Ravi, A. Deshpande, K.H. Hsu, An in-process laser localized pre-deposition heating approach to inter-layer bond strengthening in extrusion based polymer additive manufacturing, J. Manuf. Process. 24 (2016) 179–185.

[220] S.K. Mazumdar, Composites Manufacturing: Materials, Product and Process Engineering, 2002.

[221] R. Falck, J.F. dos Santos, S.T. Amancio-Filho, Case studies on topology optimization for AddJoining metal-polymer hybrid structures, in: 12th Int. Semin. Numer. Anal. Weldability, 2018.

[222] A. Zosel, The effect of bond formation on the tack of polymers, J. Adhes. Sci. Technol. 11 (1997) 1447–1457.

[223] F. Awaja, Autohesion of polymers, Polymer (Guildf). 97 (2016) 387–407.

[224] A. Baldan, Adhesion phenomena in bonded joints, Int. J. Adhes. Adhes. 38 (2012) 95–116.

[225] Z. Huda, N.I. Taib, T. Zaharinie, Characterization of 2024-T3: An aerospace aluminum alloy, Mater. Chem. Phys. 113 (2009) 515–517.

[226] S.T. Amancio-Filho, S. Sheikhi, J.F. dos Santos, C. Bolfarini, Preliminary study on the microstructure and mechanical properties of dissimilar friction stir welds in aircraft aluminium alloys 2024-T351 and 6056-T4, J. Mater. Process. Technol. 206 (2008) 132–142.

[227] Y.C. Lin, Y.C. Xia, Y.Q. Jiang, H.M. Zhou, L.T. Li, Precipitation hardening of 2024-T3 aluminum alloy during creep aging, Mater. Sci. Eng. A. 565 (2013) 420–429.

[228] R.W. Hertzberg, Deformation and fracture mechanics of engineering materials, J. Wiley & Sons, 1996.

[229] W.D. Callister, D.G. Rethwisch, Materials Science and Engineering: An Introduction, 9th Edition: Ninth Edition, John Wiley and Sons, Incorporated, 2013.

[230] W.F. Smith, J. Hashemi, Foundations of Materials Science and Engineering, McGraw-Hill, 2003.

[231] J.L. Murray, A.J. McAlister, The Al-Si (Aluminum-Silicon) system, Bull. Alloy Phase Diagrams. 5 (1984) 74–84.

[232] S.P. Ringer, K. Hono, Microstructural Evolution and Age Hardening in Aluminium Alloys, Mater. Charact. 44 (2000) 101–131.

[233] Y.S. Sato, H. Kokawa, Distribution of tensile property and microstructure in friction stir weld of 6063 aluminum, Metall. Mater. Trans. A Phys. Metall. Mater. Sci. 32 (2001) 3023–3031.

[234] J.Q. Su, T.W. Nelson, R. Mishra, M. Mahoney, Microstructural investigation of friction stir welded 7050-T651 aluminium, Acta Mater. 51 (2003) 713–729.

[235] R.M. Mahamood, E.T. Akinlabi, Heat affected zone Relationship with processing parameter in Additive Manufacturing Process, Mater. Today Proc. 5 (2018) 18362–18367.

[236] G. Engkvist, Investigation of microstructure and mechanical properties of 3D printed Nylon, Master thesis, Lulea University of Technology, 2017. http://ltu.diva-portal.org/smash/get/diva2:1153278/FULLTEXT01.pdf.

[237] M.N. Bureau, J. Denault, K.C. Cole, G.D. Einright, The role of crystallinity and reinforcerment in the mechanical behavior of Polyamide-6/Clay Nanocomposites, Polym. Eng. Sci. 42 (2002) 1897–1906.

[238] D. Forsström, B. Terselius, Thermo oxidative stability of polyamide 6 films I. Mechanical and chemical characterisation, Polym. Degrad. Stab. 67 (2000) 69–78.

[239] T. Gates, The physical and chemical ageing of polymeric composites, Ageing Compos. (2008) 3–33.

[240] T.K. Tsotsis, Thermo-Oxidative Aging of Composite Materials, J. Compos. Mater. 29 (1995) 410–422.

[241] L. Sang, C. Wang, Y. Wang, Z. Wei, Thermo-oxidative ageing effect on mechanical properties and morphology of short fibre reinforced polyamide composites – comparison of carbon and glass fibres, RSC Adv. 7 (2017) 43334–43344.

[242] X. Wen, Y. Wang, J. Gong, J. Liu, N. Tian, Y. Wang, Z. Jiang, J. Qiu, T. Tang, Thermal and flammability properties of polypropylene/carbon black nanocomposites, Polym. Degrad. Stab. 97 (2012) 793–801.

[243] X. Yan, Y. Imai, D. Shimamoto, Y. Hotta, Relationship study between crystal structure and thermal/mechanical properties of polyamide 6 reinforced and unreinforced by carbon fiber from macro and local view, Polymer (Guildf). 55 (2014) 6186–6194.

[244] T. Liu, I.Y. Phang, L. Shen, S.Y. Chow, W.-D. Zhang, Morphology and Mechanical Properties of Multiwalled Carbon Nanotubes Reinforced Nylon-6 Composites, Macromolecules. 37 (2004) 7214–7222.

[245] N. Dencheva, Z. Denchev, M.J. Oliveira, S.S. Funari, Relationship between crystalline structure and mechanical behavior in isotropic and oriented polyamide 6, Appl. Polym. Sci. 103 (2007) 2242–2252.

[246] N. Mahmood, M. Islam, A. Hameed, S. Saeed, Polyamide 6/multiwalled carbon nanotubes nanocomposites with modified morphology and thermal properties, Polymers. 5 (2013) 1380–1391.

[247] N.S. Murthy, Metastable crystalline phases in nylon 6, Polym. Commun. 32 (1991) 301–305.

[248] N.S. Murthy, R.G. Bray, S.T. Correale, R.A.F. Moore, Drawing and annealing of nylon-6 fibres: studies of crystal growth, orientation of amorphous and crystalline domains and their influence on properties, Polymer (Guildf). 36 (1995) 3863–3873.

[249] P. Bernadó, C. Alemán, J. Puiggalí, Relative stability between the α and γ forms of even nylons based on group contributions, Eur. Polym. J. 35 (1999) 835–847.

[250] Y. Boutar, S. Naïmi, S. Mezlini, L.F.M. Da Silva, M. Hamdaoui, M. Ben Sik Ali, Effect of adhesive thickness and surface roughness on the shear strength of aluminium one-component polyurethane adhesive single-lap joints for automotive applications, J. Adhes. Sci. Technol. 30 (2016) 1913–1929.

[251] D.M. Gleich, M.J.L. Van Tooren, A. Beukers, Analysis and evaluation of bondline thickness effects on failure load in adhesively bonded structures, J. Adhes. Sci. Technol. 15 (2001) 1091–1101.

[252] M.Y. Tsai, J. Morton, F.L. Matthews, Experimental and Numerical Studies of a Laminated

Composite Single-Lap Adhesive Joint, J. Compos. Mater. 29 (1995) 1254–1275.

[253] Q. Luo, L. Tong, Fully-coupled nonlinear analysis of single lap adhesive joints, Int. J. Solids Struct. 44 (2007) 2349–2370.

[254] I.U. Ojalvo, H.L. Eidinoff, Bond Thickness Effects upon Stresses in Single-Lap Adhesive Joints, AIAA J. 16 (1978) 204–211.

[255] Y. Pekbey, Numerical elastoplastic analysis of the shear stress distribution in the adhesive layer for single-lap joints, Sci. Eng. Compos. Mater. 21 (2014) 389–400.

[256] L. Jarfall, Shear loaded fastener installations, Int. J. Veh. Des. 7 (1986) 337–380.

[257] J. Schijve, Some Elementary Calculations on Secondary Bending in Simple Lap Joints, Nationaal Lucht- en Ruimtevaartlaboratorium, 1977.

[258] J. Schijve, G. Campoli, A. Monaco, Fatigue of structures and secondary bending in structural elements, Int. J. Fatigue. 31 (2009) 1111–1123.

[259] R.R.D.S.G. Campilho, M.M.F.S.F. de Moura, J.J.M.S. Domingues, Modelling single and double-lap repairs on composite materials, Compos. Sci. Technol. 65 (2005) 1948–1958.

[260] A. Özel, M.D. Aydin, Ş. Temiz, The effects of overlap length and adherend thickness on the strength of adhesively bonded joints subjected to bending moment, J. Adhes. Sci. Technol. 18 (2004) 313–325.

[261] G.P. Zou, K. Shahin, F. Taheri, An analytical solution for the analysis of symmetric composite adhesively bonded joints, Compos. Struct. 65 (2004) 499–510.

[262] T.P. Lang, P.K. Mallick, Effect of spew geometry on stresses in single lap adhesive joints, Int. J. Adhes. Adhes. 18 (1998) 167–177.

[263] E.M. Moya-Sanz, I. Ivañez, S.K. Garcia-Castillo, Effect of the geometry in the strength of single-lap adhesive joints of composite laminates under uniaxial tensile load, Int. J. Adhes. Adhes. 72 (2017) 23–29.

[264] R.D.S.G. Campilho, M.D. Banea, A.M.G. Pinto, L.F.M. Da Silva, A.M.P. De Jesus, Strength prediction of single- and double-lap joints by standard and extended finite element modelling, Int. J. Adhes. Adhes. 31 (2011) 363–372.

[265] T.E.A. Ribeiro, R.D.S.G. Campilho, L.F.M. da Silva, L. Goglio, Damage analysis of composite-aluminium adhesively-bonded single-lap joints, Compos. Struct. 136 (2016) 25–33.

[266] N.J. Al-Ramahi, R. Joffe, J. Varna, Investigation of end and edge effects on results of numerical simulation of single lap adhesive joint with non-linear materials, Int. J. Adhes. Adhes. 87 (2018) 191–204.

[267] Y. Ma, M. Ueda, T. Yokozeki, T. Sugahara, Y. Yang, H. Hamada, A comparative study of the mechanical properties and failure behavior of carbon fiber / epoxy and carbon fiber / polyamide 6 unidirectional composites, Compos. Struct. 160 (2017) 89–99.

[268] M.S. Madhukar, L.T. Drzal, Fiber-Matrix Adhesion and Its Effect on Composite Mechanical Properties : Tensile and Flexure Behavior of Graphite / Epoxy Composites, J. Compos. Mater. 25 (1991) 958–991.

[269] H. Eiliat, R.J. Urbanic, Minimizing voids for a material extrusion based process, Rapid

Prototyp. J. 24 (2018) 485–500.

[270] J.D. Fuller, M.R. Wisnom, Ductility and pseudo-ductility of thin ply angle-ply CFRP laminates under quasi-static cyclic loading, Compos. Part A Appl. Sci. Manuf. 107 (2018) 31–38.

[271] S. Suresh, Fatigue of Materials, Cambridge University Press, 1998.

[272] S. Yamashita, K. Hashimoto, Experimental characterization of the tensile failure mode of ultra-thin chopped carbon fiber tape-reinforced thermoplastics, (2016).

[273] I.N. Dyson, A.J. Kinloch, A. Okada, The interlaminar failure behaviour of carbon fibre/polyetheretherketone composites, Composites. 25 (1994) 189–196.

[274] N. Sato, M. Hojo, M. Nishikawa, Intralaminar fatigue crack growth properties of conventional and interlayer toughened CFRP laminate under mode i loading, Compos. Part A Appl. Sci. Manuf. 68 (2015) 202–211.

[275] W. V. Liebig, C. Leopold, K. Schulte, Photoelastic study of stresses in the vicinity of a unique void in a fibre-reinforced model composite under compression, Compos. Sci. Technol. 84 (2013) 72–77.

[276] M.G. Kim, S.G. Kang, C.G. Kim, C.W. Kong, Tensile response of graphite/epoxy composites at low temperatures, Compos. Struct. 79 (2007) 84–89.

[277] A.G. Gibson, M.E.O. Torres, T.N.A. Browne, S. Feih, A.P. Mouritz, High temperature and fire behaviour of continuous glass fibre/polypropylene laminates, Compos. Part A Appl. Sci. Manuf. 41 (2010) 1219–1231.

[278] S. Sánchez-Sáez, T. Gómez-Del Río, E. Barbero, R. Zaera, C. Navarro, Static behavior of CFRPs at low temperatures, Compos. Part BEngineering. 33 (2002) 383–390.

[279] J.J.M. Machado, E.A.S. Marques, L.F.M. da Silva, Influence of low and high temperature on mixed adhesive joints under quasi-static and impact conditions, Compos. Struct. 194 (2018) 68–79.

[280] J.J.M. Machado, E.A.S. Marques, L.F.M. da Silva, Mechanical behaviour of adhesively bonded composite single lap joints under quasi-static and impact conditions with variation of temperature and overlap, J. Compos. Mater. (2018).

[281] J.J.M. Machado, P.D.P. Nunes, E.A.S. Marques, L.F.M. da Silva, Adhesive joints using aluminium and CFRP substrates tested at low and high temperatures under quasi-static and impact conditions for the automotive industry, Compos. Part B Eng. 158 (2019) 102–116.

[282] P.E. Irving, C. Soutis, Polymer Composites in the Aerospace Industry, Elsevier Science, 2014.

[283] S. Kalia, S.-Y. Fu, Polymers at Cryogenic Temperatures, Springer, 2013.

[284] K.C. Shin, J.J. Lee, Effects of thermal residual stresses on failure of co-cured lap joints with steel and carbon fiber-epoxy composite adherends under static and fatigue tensile loads, Compos. Part A Appl. Sci. Manuf. 37 (2006) 476–487.

[285] Y. Zhang, A.P. Vassilopoulos, T. Keller, Effects of low and high temperatures on tensile behavior of adhesively-bonded GFRP joints, Compos. Struct. 92 (2010) 1631–1639.

[286] K. Van De Velde, P. Kiekens, Thermoplastic polymers: Overview of several properties and their consequences in flax fibre reinforced composites, Polym. Test. 20 (2001) 885–893.

[287] L. Shikhmanter, B. Cina, I. Eldror, Fractography of multidirectional CFRP composites tested statically, Composites. 22 (1991) 437–444.

[288] A. Jumahat, C. Soutis, F.R. Jones, A. Hodzic, Fracture mechanisms and failure analysis of carbon fibre/toughened epoxy composites subjected to compressive loading, Compos. Struct. 92 (2010) 295–305.

[289] E.S. Greenhalgh, Delamination growth in carbon-fibre composite structures, Compos. Struct. 23 (1993) 165–175.

[290] L. Engel, An Atlas of polymer damage: surface examination by scanning electron microscope, Prentice-Hall, 1981.

[291] E. Greenhalgh, Failure Analysis and Fractography of Polymer Composites, Elsevier Science, 2009.

[292] M.S. Madhukar, L.T. Drzal, Fiber-Matrix Adhesion and Its Effect on Composite Mechanical Properties: IV. Mode I and Mode II Fracture Toughness of Graphite/Epoxy Composites, J. Compos. Mater. 26 (1992) 936–968.

[293] L.T. Drzal, Adhesion of Graphite FIbres to Epoxy Matrices: I. The Role of Fibre Surface Treatment, J. Adhes. 16 (1982) 1–30.

[294] K. Horiguchi, Y. Shindo, H. Kudo, S. Kumagai, End-Notched Flexure Testing and Analysis of Mode II Interlaminar Fracture Behavior of Glass-Cloth/Epoxy Laminates at Cryogenic Temperatures, J. Compos. Technol. Res. 24 (2002) 239–245.

[295] J.J. Horst, J.L. Spoormaker, Fatigue fracture mechanisms and fractography of short-glassfibre-reinforced polyamide 6, J. Mater. Sci. 32 (1997) 3641–3651.

[296] M.J. Hiley, Fractographic study of static and fatigue failures in polymer composites, Plast. Rubber Compos. 28 (1999) 210–227.

[297] D. Purslow, Matrix fractography of fibre-reinforced epoxy composites, Composites. 17 (1986) 289–303.

[298] K. Friedrich, R. Walter, L.A. Carlsson, A.J. Smiley, J.W. Gillespie, Mechanisms for rate effects on interlaminar fracture toughness of carbon/epoxy and carbon/PEEK composites, J. Mater. Sci. 24 (1989) 3387–3398.

[299] E.A. Chakachery, W.L. Bradley, A comparison of the crack tip damage zone for fracture of Hexcel F185 neat resin and T6T145/F185 composite, Polym. Eng. Sci. 27 (1987) 33–40.

[300] J.J. Xiong, R.A. Shenoi, Fatigue and Fracture Reliability Engineering, Springer, 2011.

[301] W. Weibull, A statistical distribution function of wide applicability, J. Appl. Mech. (1951) 293–299.

[302] R.C. Brzostek, U. Suhuddin, J.F. Dos Santos, Fatigue assessment of refill friction stir spot weld in AA 2024-T3 similar joints, Fatigue Fract. Eng. Mater. Struct. 41 (2017).

[303] X.D. Ren, Y.K. Zhang, D.W. Jiang, T. Zhang, G.F. Sun, A model for reliability and confidence level in fatigue statistical calculation, Theor. Appl. Fract. Mech. 59 (2012) 29–33.

[304] R. Sakin, I. Ay, Statistical analysis of bending fatigue life data using Weibull distribution in glass-fiber reinforced polyester composites, Mater. Des. 29 (2008) 1170–1181.

[305] U.A. Khashaba, Fatigue and Reliability Analysis of Unidirectional GFRP Composites under Rotating Bending Loads, J. Compos. Mater. 37 (2003) 317–331.

[306] Y.X. Zhao, H.B. Liu, Weibull modeling of the probabilistic S-N curves for rolling contact fatigue, Int. J. Fatigue. 66 (2014) 47–54.

[307] M. Alqam, R.M. Bennett, A.H. Zureick, Three-parameter vs. two-parameter Weibull distribution for pultruded composite material properties, Compos. Struct. 58 (2002) 497–503.

[308] S.M. Ahmadi, R. Hedayati, Y. Li, K. Lietaert, N. Tümer, A. Fatemi, C.D. Rans, B. Pouran, H. Weinans, A.A. Zadpoor, Fatigue performance of additively manufactured meta-biomaterials: The effects of topology and material type, Acta Biomater. 65 (2018) 292–304.

[309] J.A. Suresh, G. Saravana Kumar, P. Ramu, J. Rengaswamy, Fatigue Life Characterization of Additively Manufactured Acrylic like Poly-Jet Printed Parts, in: R. Prakash, V. Jayaram, A. Saxena (Eds.), Adv. Struct. Integr., Springer Singapore, Singapore, 2018: pp. 623–632.

[310] M. Dubé, P. Hubert, J.N.A.H. Gallet, D. Stavrov, H.E.N. Bersee, A. Yousefpour, Fatigue performance characterisation of resistance-welded thermoplastic composites, Compos. Sci. Technol. 68 (2008) 1759–1765.

[311] A.L. Highsmith, K.L. Reifsnider, Stiffness-Reduction Mechanisms in Composite Laminates, in: K.L. Reifsnider (Ed.), Damage Compos. Mater., ASTM International, 1982: pp. 103–290.

[312] P. Brøndsted, S.I. Andersen, Fatigue performance of glass/polyester laminates and the monitoring of material degradation, Mech. Compos. Mater. 32 (1996) 32–41.

[313] J.B. Knoll, B.T. Riecken, N. Kosmann, S. Chandrasekaran, K. Schulte, B. Fiedler, The effect of carbon nanoparticles on the fatigue performance of carbon fibre reinforced epoxy, Compos. Part A Appl. Sci. Manuf. 67 (2014) 233–240.

[314] I.M. Daniel, A. Charewicz, Fatigue damage mechanisms and residual properties of graphite/epoxy laminates, Eng. Fract. Mech. 25 (1986) 793–808.

[315] D. Krajcinovic, J. Lemaître, Continuum Damage Mechanics: Theory and Applications, Springer-Verlag Kg, 1987.

[316] R.M. Guedes, Time-dependent failure criteria for lifetime prediction of polymer matrix composite structures, Woodhead Publishing Limited, 2010.

[317] K. Schulte, Stiffness Reduction and Development of Longitudinal Cracks during Fatigue Loading of Composite Laminates, in: A.H. Cardon, G. Verchery (Eds.), Mech. Characterisation Load Bear. Fibre Compos. Laminates, Springer, 1985: pp. 36–54.

[318] E.K. Gamstedt, O. Redon, P. Brøndsted, Fatigue Dissipation and Failure in Unidirectional and Angle-Ply Glass Fibre/Carbon Fibre Hybrid Laminates, Key Eng. Mater. 221–222 (2002) 35–48.

[319] A.K. Bledzki, J. Gassan, K. Kurek, The accumulated dissipated energy of composites under cyclic-dynamic stress, Exp. Mech. 37 (1997) 324–327.

[320] P.T. Curtis, The fatigue behaviour of fibrous composite materials, J. Strain Anal. 24 (1989) 235–244.

[321] H. Jiang, T. Luo, G. Li, X. Zhang, J. Cui, Fatigue life assessment of electromagnetic riveted carbon fiber reinforce plastic/aluminum alloy lap joints using Weibull distribution, Int. J.

Fatigue. 105 (2017) 180–189.

[322] M. Houba, G. Robert, O. Moulinjeune, Fatigue of glass fibers reinforced polyamides: Mean stress effects as a function of glass fiber orientation, 20th Int. Conf. Compos. Mater. (2015).

[323] F. Wu, W.X. Yao, A fatigue damage model of composite materials, Int. J. Fatigue. 32 (2010) 134–138.

[324] A. Sjögren, L.E. Asp, Effects of temperature on delamination growth in a carbon/epoxy composite under fatigue loading, Int. J. Fatigue. 24 (2002) 179–184.

[325] S.U. Khan, A. Munir, R. Hussain, J.K. Kim, Fatigue damage behaviors of carbon fiber-reinforced epoxy composites containing nanoclay, Compos. Sci. Technol. 70 (2010) 2077–2085.

[326] S. Shiri, M. Yazdani, M. Pourgol-Mohammad, A fatigue damage accumulation model based on stiffness degradation of composite materials, Mater. Des. 88 (2015) 1290–1295.

[327] W. Van Paepegem, J. Degrieck, A new coupled approach of residual stiffness and strength for fatigue of fibre-reinforced composites, Int. J. Fatigue. 24 (2002) 747–762.

[328] T. R. Crompton, Practical Polymer Analysis, Springer US, 1993.

[329] R. Zbinden, Infrared Spectroscopy of High Polymers, Academic Press, New York, 1964.

[330] G.H. Lopes, J. Junges, R. Fiorio, M. Zeni, A.J. Zattera, Thermoplastic polyurethane synthesis using POSS as a chain modifier, Mater. Res. 15 (2012) 698–704.

[331] S. Yuan, J. Bai, C. Kai Chua, K. Zhou, J. Wei, Characterization of Creeping and Shape Memory Effect in Laser Sintered Thermoplastic Polyurethane, J. Comput. Inf. Sci. Eng. 16 (2016) 041007.

[332] R. Zhang, K. Huang, S. Hu, Q. Liu, X. Zhao, Y. Liu, Improved cell morphology and reduced shrinkage ratio of ETPU beads by reactive blending, Polym. Test. 63 (2017) 38–46.

[333] T. Zhang, Y. Zhao, H. Li, B. Zhang, Effect of polyurethane sizing on carbon fibers surface and interfacial adhesion of fiber/polyamide 6 composites, J. Appl. Polym. Sci. 135 (2018) 1–10.

[334] Q. Wu, M. Li, Y. Gu, S. Wang, X. Wang, Z. Zhang, Reaction of carbon fiber sizing and its influence on the interphase region of composites, J. Appl. Polym. Sci. 132 (2015) 1–8.

[335] T. Brocks, M.O.H. Cioffi, H.J.C. Voorwald, Effect of fiber surface on flexural strength in carbon fabric reinforced epoxy composites, Appl. Surf. Sci. 274 (2013) 210–216.

[336] C. Pradere, J.C. Batsale, J.M. Goyhe, Thermal properties of carbon fibers at very high temperature, Carbon N. Y. 47 (2009) 737–743.

[337] R.E. Taylor, Specific heat of carbon/carbon composites, West Lafayette, 1980. http://www.dtic.mil/dtic/tr/fulltext/u2/a106709.pdf.

[338] K.. Bacon, A.W. Sisko, Differential Thermal Analysis of High Polymers. III. Polyamides, Polym. Sci. L (1961) 87–98.

[339] C. Ochoa-Putman, U.K. Vaidya, Mechanisms of interfacial adhesion in metal-polymer composites - Effect of chemical treatment, Compos. Part A Appl. Sci. Manuf. 42 (2011) 906–915.

[340] J. Rotheiser, Joining of plastics: handbook for designers and engineers, Hanser, Munich, 1999.

[341] H.M.S. Iqbal, S. Bhowmik, R. Benedictus, Surface modification of high performance polymers by atmospheric pressure plasma and failure mechanism of adhesive bonded joints, Int. J. Adhes. Adhes. 30 (2010) 418–424.

[342] A. Baldan, Adhesively-bonded joints and repairs in metallic alloys, polymers and composite materials: Adhesives, adhesion theories and surface pretreatment, J. Mater. Sci. 39 (2004) 1–49.

[343] R.A. Mendelson, A generalized melt viscosity-temperature dependence for styrene and styrene-acrylonitrile based polymers, Polym. Eng. Sci. 16 (1976) 690–696.

[344] N. Rosenzweig, M. Narkis, Sintering rheology of amorphous polymers, Polym. Eng. Sci. 21 (1981) 1167–1170.

[345] J.H. Kweon, J.W. Jung, T.H. Kim, J.H. Choi, D.H. Kim, Failure of carbon composite-to-aluminum joints with combined mechanical fastening and adhesive bonding, Compos. Struct. 75 (2006) 192–198.

[346] K.S. Kim, J.S. Yoo, Y.M. Yi, C.G. Kim, Failure mode and strength of uni-directional composite single lap bonded joints with different bonding methods, Compos. Struct. 72 (2006) 477–485.

[347] S.K. Mazumdar, P.K. Mallick, Static and fatigue behavior of adhesive joints in SMC-SMC composites, Polym. Compos. 19 (1998) 139–146.

[348] S.A. Tronvoll, T. Welo, C.W. Elverum, The effects of voids on structural properties of fused deposition modelled parts: a probabilistic approach, Int. J. Adv. Manuf. Technol. 97 (2018) 3607–3618.

[349] R.F. Gibson, A review of recent research on nanoindentation of polymer composites and their constituents, Compos. Sci. Technol. 105 (2014) 51–65.

[350] A.M. Díez-Pascual, M.A. Gómez-Fatou, F. Ania, A. Flores, Nanoindentation in polymer nanocomposites, Prog. Mater. Sci. 67 (2015) 1–94.

[351] Z. Hashin, Failure Criteria for Unidirectional Fiber Composites, J. Appl. Mech. 47 (1980) 329–334.

[352] A.D. Crocombe, C.Y. Ong, C.M. Chan, M.M. Abdel Wahab, I.A. Ashcroft, Investigating fatigue damage evolution in adhesively bonded structures using backface strain measurement, J. Adhes. 78 (2002) 745–776.

[353] V. Shenoy, I.A. Ashcroft, G.W. Critchlow, A.D. Crocombe, M.M. Abdel Wahab, An investigation into the crack initiation and propagation behaviour of bonded single-lap joints using backface strain, Int. J. Adhes. Adhes. 29 (2009) 361–371.

[354] Z. Zhang, J.K. Shang, F. V. Lawrence, A Backface Strain Technique for Detecting Fatigue Crack Initiation in Adhesive Joints, J. Adhes. 49 (1995) 23–36.

[355] A.G. Solana, A.D. Crocombe, M.M.A. Wahab, I.A. Ashcroft, Fatigue initiation in adhesively-bonded single-lap joints, J. Adhes. Sci. Technol. 21 (2007) 1343–1357.

[356] T. Adam, R.F. Dickson, J. Jones, H. Reiter, B. Harris, A power law fatigue damage model for fiber-reinforced plastic laminates, Part C J. Mech. Eng. Sci. 200 (1986) 155–166.

[357] W. Weibull, A Statistical Theory of the Strength of Materials, Generalstabens Litografiska Anstalts Förlag, Stockholm, 1939.

[358] P.S. Effertz, V. Infante, L. Quintino, U. Suhuddin, S. Hanke, J.F. Santos, Fatigue life assessment of friction spot welded 7050-T76 aluminium alloy using Weibull distribution, Int. J. Fatigue. (2016).

List of Figures

List of Tables

Appendices

Appendix A.1 AddJoining patent

(19) Deutsches Patent- und Markenamt

(10) **DE 10 2016 121 267 A1** 2018.05.09

(12) **Offenlegungsschrift**

(21) Aktenzeichen: **10 2016 121 267.9**
(22) Anmeldetag: **07.11.2016**
(43) Offenlegungstag: **09.05.2018**

(51) Int Cl.: ***B29C 70/38*** (2006.01)
B29C 70/20 (2006.01)
B29C 70/78 (2006.01)
B33Y 10/00 (2015.01)
B29C 64/106 (2017.01)

(71) Anmelder:
Helmholtz-Zentrum Geesthacht Zentrum für Material- und Küstenforschung GmbH, 21502 Geesthacht, DE

(74) Vertreter:
Bird & Bird LLP, 20457 Hamburg, DE

(72) Erfinder:
Traglia Amancio Filho, Sergio de, Prof. Dr., 21039 Börnsen, DE; Miler Moreira Falck, Rielson, 22085 Hamburg, DE

(56) Ermittelter Stand der Technik:

DE	**10 2013 021 672**	**A1**
DE	**10 2015 215 669**	**A1**
DE	**11 2012 005 634**	**T5**

Prüfungsantrag gemäß § 44 PatG ist gestellt.

Die folgenden Angaben sind den vom Anmelder eingereichten Unterlagen entnommen.

(54) Bezeichnung: **Verfahren zum Herstellen eines schichtförmigen Bauteils**

Figure A.1 AddJoining German patent application DE 10 2016 121 267 A1.

Appendix A.2 Base material characterization of CF-PA6 and PA6

MarkForged materials are not provided with the exact specification. Markforged trade the unreinforced polymer as *Nylon* and the reinforced polymer as *carbon fiber* [192]. The investigations performed in this work identified that the *Nylon* grade is a PA6 and the *carbon fiber* is reinforced in PA6 matrix. The outcome of this conclusion is provided below along this investigation.

The *carbon fiber* bundles are infused with a resin resulting in a filament bundle of 0.34 mm in diameter. Moreover, the *Nylon* is provided with 1.74 mm in filament diameter. Both base materials were characterized among different methods. First of all, an EDS (Energy-dispersive X-ray spectroscopy) was used with 15 kV energy and the working distance to sample set to 10 mm to identify qualitatively the composition of the resin. From the EDS spectrum, it can be seen that major elements of carbon (92.8%), oxygen (6.1%) and gold (1.1%) exhibit stronger peaks (Figure A.2(a)) for *carbon fiber*. The unreinforced *Nylon* has 63% and 56% lower quantity of carbon (30.6%) and oxygen (6.3%) respectively in comparison with the *carbon fiber* base material (Figure A.2(b)). The presence of gold is due to the gold sputtered used prior the measurements as described in Section 4.3.4.

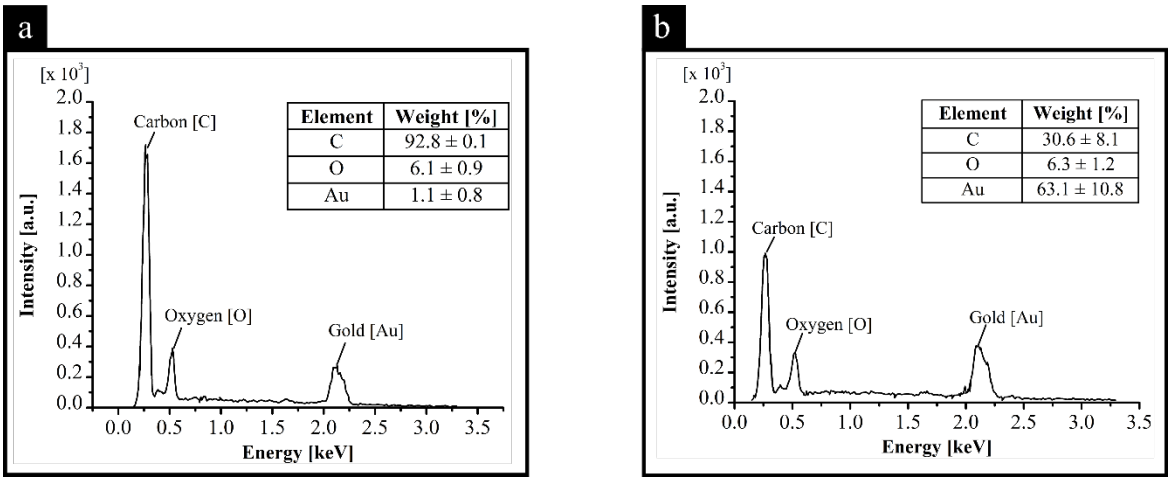

Figure A.2 Chemical composition of base material: (a) CF-PA6 and (b) PA6.

From the EDS measurement, the high presence of carbon and oxygen present in the *carbon fiber* resin indicates an inorganic resin material [328]. The base materials were further analyzed using FTIR based on the parameters described in Section 4.3.6. Based on the presence on the absorption bands, the *carbon fiber* spectrum has similar shape in comparison to *Nylon* (Figure A.3). The chemical structure changed along with different vibration bands. The intensity of the vibration bands for the *carbon fiber* spectrum is less pronounce when compared to *Nylon*. An explanation is the low presence of resin (53% in volume) in the fiber bundle.

Attenuated total reflection fourier transform infrared (ATR-FTIR) spectrophotometry was used to compare variations in functional groups [329]. This technique was carried out using an Equinox 55 (Bruker, Germany) to identify the chemical structures of the base material and the joints after thermo-

oxidative ageing. The solid samples each weighing 9 ± 1 mg were placed in a standard pellet holder. The analysis was performed at 0.1/cm resolution in a wave-number range from 4400/cm to 400/cm.

The characteristic of polyamide infrared spectrum is the presence of the functional group amine represented by –NH vibration with bands in two vibration range type as stretching (from 3250 cm^{-1} to 3300 cm^{-1}) and bending (from 3105 cm^{-1} to 3075 cm^{-1}). The second most important group is aliphatic -CH_2- with bands representing antisymmetric stretching (around 2940 cm^{-1} to 2910 cm^{-1}) and symmetric stretching (from 2870 cm^{-1} and 2840 cm^{-1}). Moreover, the C=O (amide I) absorption at 1640 cm^{-1} and the -NH (amide II) absorption at 1540 cm^{-1} can be observed. The spectrum of the carbon fiber was nearly the same as the Nylon. After a detailed comparison from both spectra (Figure A.3), the *carbon fiber* spectrum shows peaks of urethane (C=O) range from 1732 cm^{-1} to 1702 cm^{-1} [330–332]. It is an indication of polyurethane sizing in the carbon fiber base materials. According to Zahn *et al.* [333], the effect of thermoplastic polyurethane improves the adhesion of carbon fiber and polyamide 6. The author also observed the presence of urethane vibration bands of 1730 cm^{-1} in their spectrum.

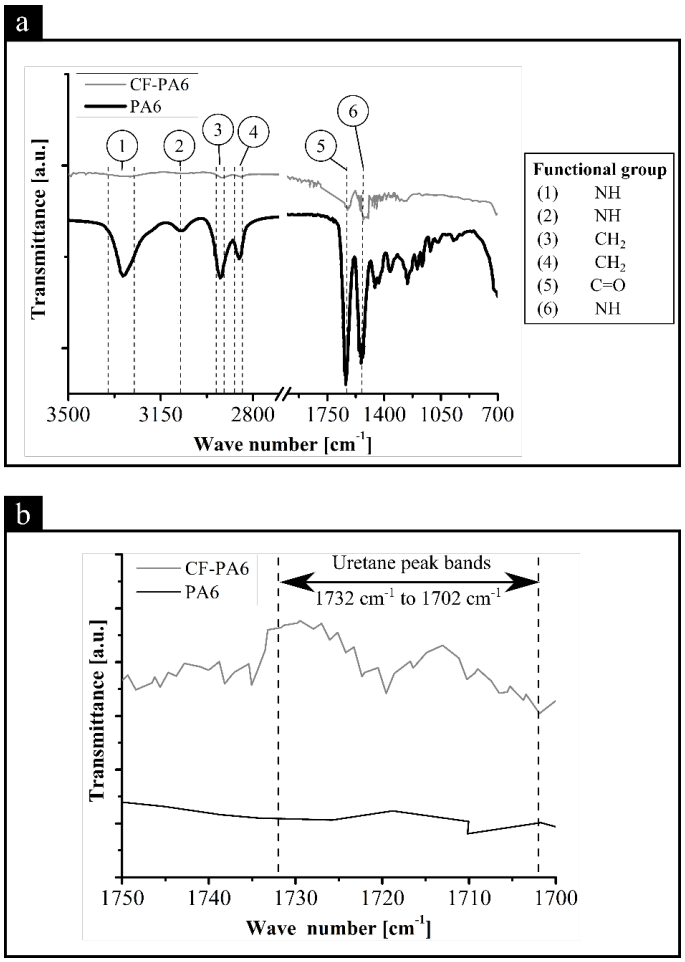

Figure A.3 ATR-FTIR spectrum of (a) base material CF-PA6 and PA6 and (b) highlighting the presence of uretane peak bands.

Furthermore, for comparison, the surface from *glass fiber* and *carbon fiber* were investigated by SEM (Figure A.4). The *carbon fiber* surface is visible with significantly roughness (Figure A.4(a)). On the contrary, glass fiber appears with a smooth and neat surface (Figure A.4(b)). The presence of sizing

increases the roughness of the *carbon fiber* [333–335]. In fact, the sizing effect forms a very thin coating layer [334]. The sizing thickness was measured by comparing the filament bundle diameter between both fibers. The carbon fiber diameter (0.38 ± 0.02 mm) filament is 25 µm larger than the glass fiber (0.35 ± 0.01 mm).

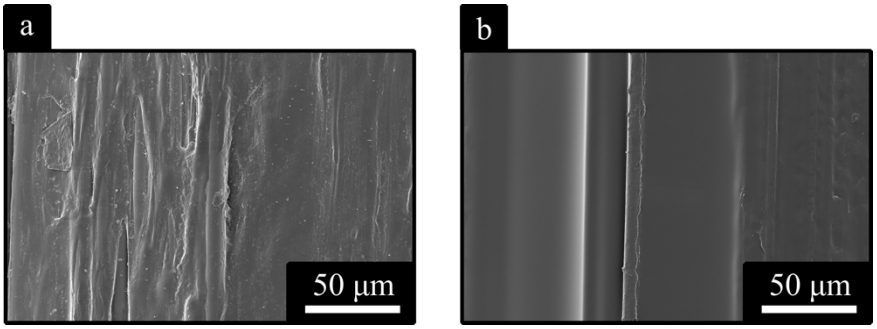

Figure A.4 Surface images from (a) carbon fiber and (b) glass fiber using SEM

Moreover, thermal analysis was carried out to identify the physical-chemical changes in the material. DSC analyses were performed as described in Section 4.3.5.1. DSC analysis shows the second cycle heating and cooling curves for the carbon fiber base material (Figure A.5(a)) and for *Nylon* (Figure A.5(b)). The heating curves representing the energy required to melt the material. At this curve, the T_g and T_m temperatures are identified as 57.1 ± 1.1 °C and 233.1 ± 0.5 °C, respectively for the CF-PA6. Polyamide 6 (PA6) is the closest *Nylon* grade in comparison to the data available in the literature [176], with a glass transition at 55.9 ± 0.7 °C and melting point of 201.2 ± 1.2 °C. At the cooling curve, the crystallization peak temperature, T_{cc}, of the CF-PA6 shows 157 ± 0.7 °C, nearly 3% higher than that for the PA6 (152.7 ± 0.5 °C). The crystallinity index was 27.3 ± 0.9 % and 1.3 ± 0.4 % for PA6 and CF-PA6, respectively. The decomposition temperature (T_d) is obtained by differential analysis of the TGA and DTG thermograms. DTG curves show that the CF-PA6 and PA6 were decomposed in a single step (Figure A.6). The CF-PA6 starts to degrade at around 476 ± 2.5 °C (Figure A.6(a)) and PA6 at 456 ± 1.4 °C (Figure A.6(b)).

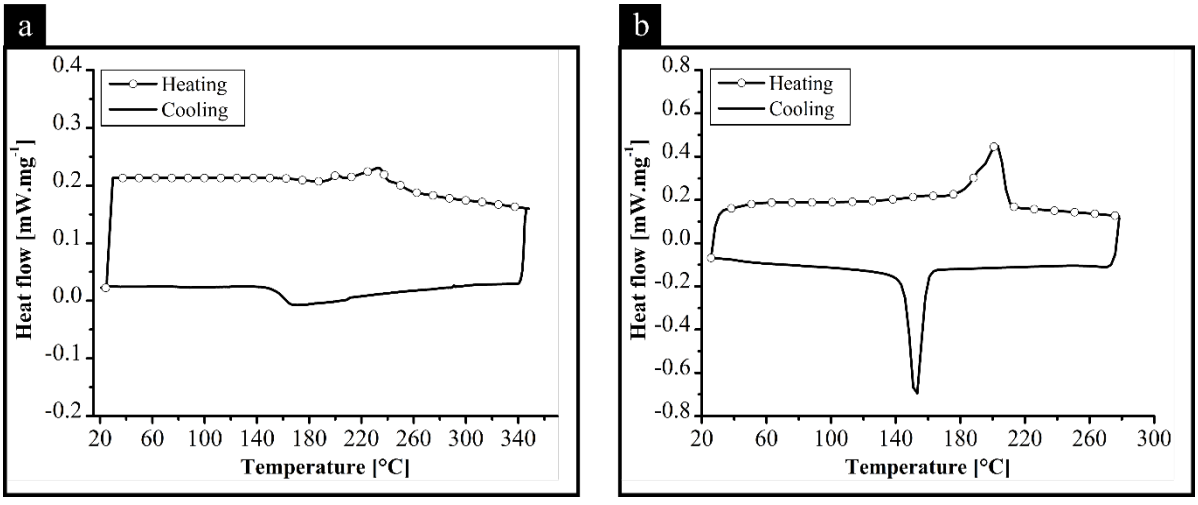

Figure A.5 DSC cruves used to identify the base mterials: (a) CF-PA6 and (b) PA6 by determination of thermal properties temperatures.

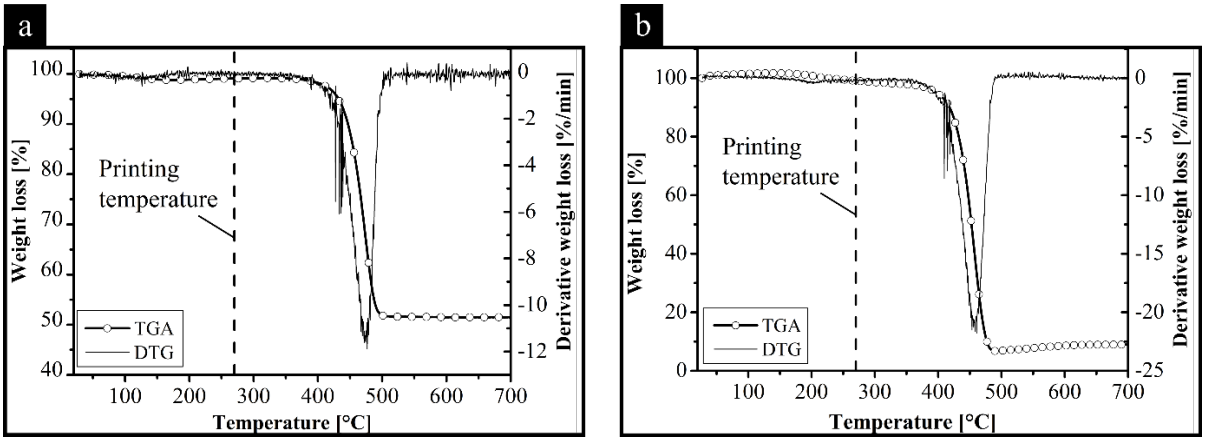

Figure A.6 TGA curves used to identify the decomposition temperature of the base mterials: (a) CF-PA6 and (b) PA6.

From thermal analysis, the thermal properties for both base materials are summarized in Figure A.7. The thermal properties here investigated move to higher temperature zone in comparison with neat PA6. The presence of fiber influenced the thermal stability of the base material resin, which it caused the increasing in thermal properties in comparison with PA6 [176,180]. Moreover, the changing in thermal properties is caused by the heat absorption capacity of carbon fiber [336,337] being higher than that for the PA6 (C_p = 1500 $J.kg^{-1}.K^{-1}$) [202,338]. Another explanation, it is the effect of nucleation and growth of PA6 crystals affected by the presence of carbon fibers [181].

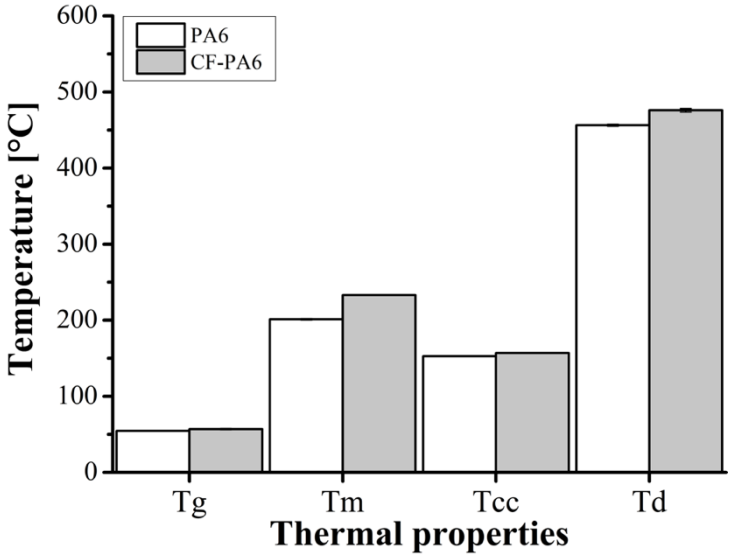

Figure A.7 Thermal properties of the base materials CF-PA6 and PA6.

Based on the exploratory investigation, the PA6 stored inside the drybox was dried every three months. PA6 was dried for 22h at 80 °C to avoid the hydrolyzing effects of humidity on the material. The accumulation of moisture was increasing the PA6 mass in 1.3% and causing slightly a reduction on the thermal properties of the PA6. The presence of moisture acts as plasticizing action, which change the mobility of the amorphous phase present in the PA6 [165–167], thus exposing the material to experience a reduction in the mechanical properties and thermal properties [167,168]. Figure A.8 shows a summary on the overall thermal properties already discussed in this section.

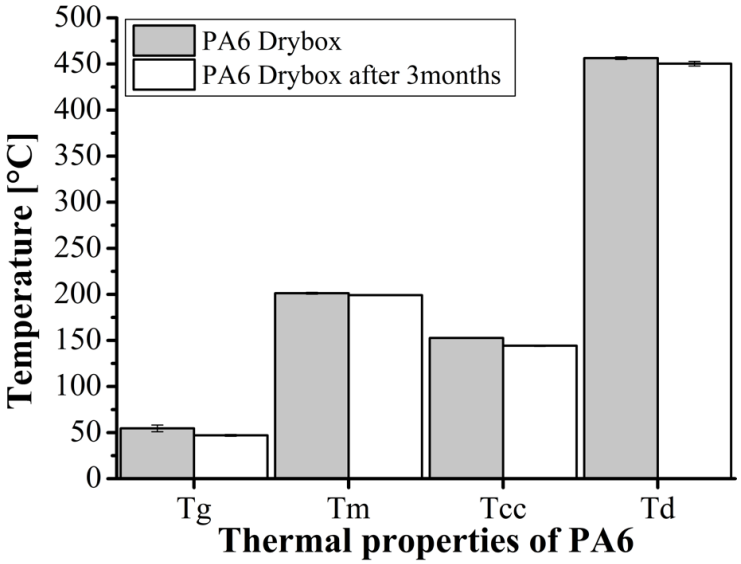

Figure A.8 Thermal properties of the base materials PA6 Drybox and PA6 Drybox after three months.

Appendix A.3 AddJoining process variants

There are three AddJoining process-variants investigated during the feasibility study of the technology development process. The fourth variant briefly described was not developed, which demand an extensive investigation and project development of laser and instrument installations, such as optical and temperature sensors to be interconnected with the desktop 3D printer.

To allow the adhesion of the polymer on the metal surface, the AddJoining process variants were investigated by using the material combination aluminum 2024-T3 with acrylonitrile butadiene styrene (ABS). The process variants were tested under single-lap joint configuration and were briefly described in Section 5.3. Note that this preliminary investigation was carried out without optimizing each process variant, but rather to obtain the first understanding of the AddJoining technique. This exploratory study was based on the selected parameters described in Section 5.2, such as printing temperature of 255 °C, road thickness of 0.2 mm, deposition speed of 40 mm/s, and 2 contours.

The first variant of the process was tested using an epoxy-based adhesive, DP490 from 3M (USA). The curing procedure was applied following the supplier procedure in two cycles, where the adhesive joints were kept one day in room temperature and subjected to the second cycle in the air-circulating oven from Nabertherm TR60 (Germany) at 80 °C for 1 hour. Second variant was identified using an heating-control system, where the ABS coating was applied by indirect heating as follows: (1) printing a stand-alone layer of ABS (13 mm x 26 mm x 0.2 mm); (2) heating the aluminum part with the stand-alone ABS printed layer using an external hot plate at 250°C for one minute (to remelt and homogenize the stand-alone printed layer); (3) allowing a two-minutes consolidation time to form the coating. This variant opened space to the development of the heating-control system, previously described in Section 4.2.2. The third variant is to form a thin polymeric coating similar using an adapted dip-coating method. To perform the coating, first ABS filament was dissolved in pure acetone at room temperature for 24 hours. 15 wt.% ABS solution was applied with a customized tool to spread it manually on the aluminum surface. The samples were subsequently dried in the horizontal position for five minutes at room temperature.

The overall mechanical performance is shown in Figure A.9. The stiffness among the process variants are similar (Figure A.9(a)). The force-displacement curves of the different process variants showed a linear elastic behavior and similarity on the stiffness prior to failure. The variant using adhesive showed limited displacement at break (DaB: 0.67 ± 0.04 mm) representing the low-ductility of the adhesive. In constrast to process variant using heating control, the displacement at break was 79% higher than the variant using adhesive (DaB: 1.21 ± 0.16 mm). Figure A.9(b) compares the peak force (ULSF) obtained from force-displacement curves. The process variant two displayed an average ULSF of 1.2 ± 0.05 kN. Hence, the process variant one and three showed lower mechanical performance compared to the heating control variant, 42% (ULSF: 0.7 ± 0.1 kN) and 8.3% (ULSF: 1.1 ± 0.06 kN), respectively.

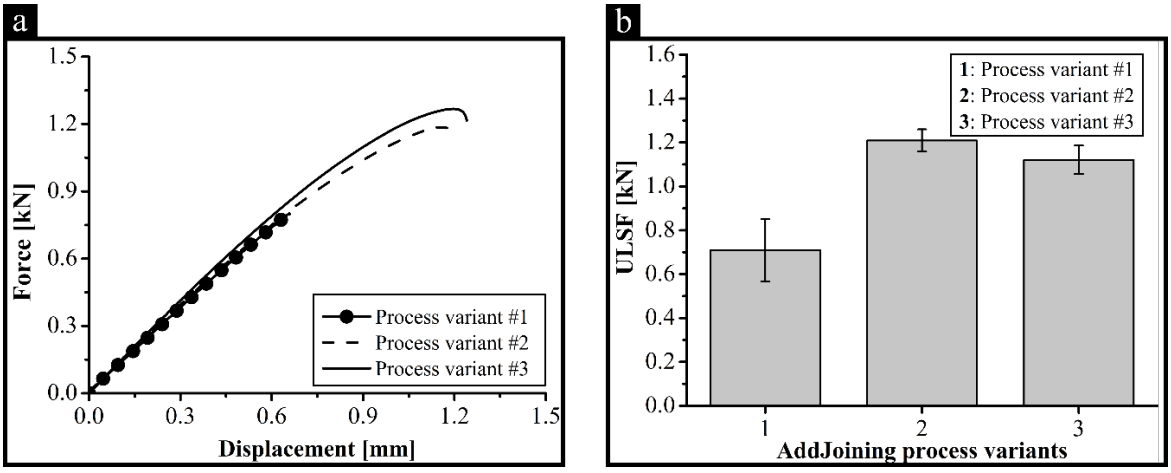

Figure A.9 Mechnical performance of the AddJoining process variants: (a) representative force-displacement curves for process variant one (with adhesive), variant two (with heating control) and variant three (with thin-coating layer). (b) average ULSF for each process variant.

For the process variant one, the poor mechanical performance using commercial adhesive can be explained by the difficulties of bonding thermoplastics because of their low surface tension. Thermoplastics requires surface treatment applied by physical or chemical means to produce high performance adhesively bonded joints [6,339–342]. Although, the adhesive thickness applied in the metallic surface was in average 200 µm. During the AddJoining process, the extruder head movement was 3D printing the ABS causing to remove the uncured adhesive from the metallic due to the contact of the nozzle. Affecting the bond line, the adhesive final thickness of 32 ± 2 µm was achieved thickness between ABS and adhesive (Figure A.10(a)). According to Boutar *et al.* [250], the ideal bond line thickness using structural adhesive is in average between 200 µm to 500 µm. The authors reported that interface stresses are higher with thin bond line adhesive thickness, which might reduce the carry load capability of the adhesive [250,251].

The process variant two and three, Figure A.10(b) and Figure A.10(c), respectively, an intimate contact could be achieved between the coating layer and the surface of the aluminum, and between the deposited polymer and coating layer. For process variant three, the presence of voids in the ABS coating is caused due to the evaporation of residual acetone, from the coating solution, during the AddJoining printing stage. Such phenomenon was not present in the process variant two, where the ABS coating was formed by heating control approach. Therefore, in this variant, the primary bonding mechanisms between the printed layers are by thermal fusion and interlayer bonding. Mendelson [343] correlated the melt viscosity dependence of ABS with temperature. The author reported that a variation in temperature reduced the melt viscosity up to 50% (4600 Pa-s (230 °C) and 2500 Pa-s (260 °C)), where the bonding between the layers is activated because the sintering process is thermally driven by the polymer viscous flow process [344]. Keeping the temperature above the glass transition temperature assures us that there would be good bonding between successively deposited layers.

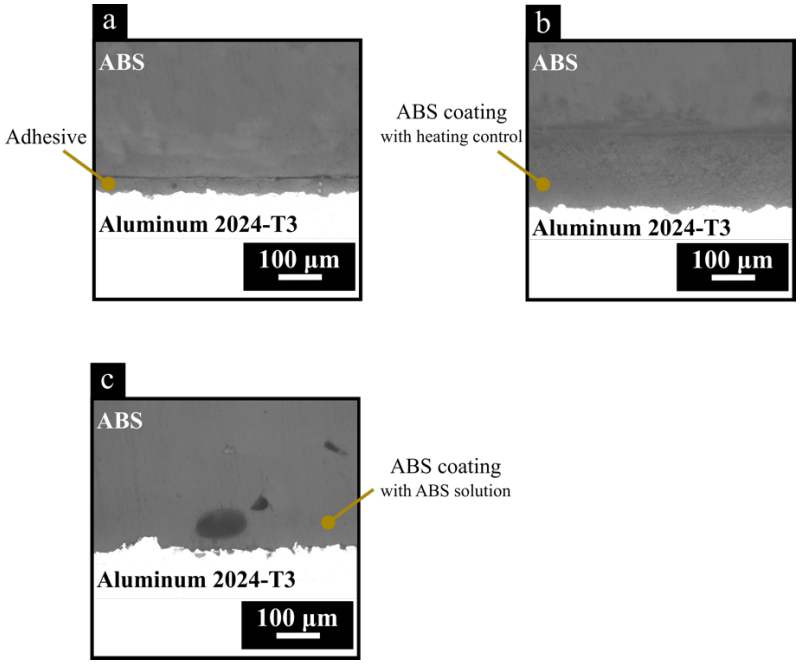

Figure A.10 Microstructure of the overalp joint obtained from the AddJoining process variants: (a) process variant one (with adhesive), (b) variant two (with heating control) and (c) variant three (with thin-coating layer) obtained with RLOM.

The fracture surfaces for each process variant were not further analyzed in this PhD work for each process variant. Figure A.11 illustrates the fracture surface of the process variant (1) with adhesive layer, (2) ABS coating obtained with heating control and (3) ABS coating achieved with ABS solution. There are clearly three different failure types among the AddJoining process variants. The three different failure types are a result from the different bonding mechanisms among the process variants. Figure A.11(a) illustrates the mixed mode failure type obtained for the process variant one due to the lack of bonding between the 3D-printed ABS and the adhesive presented in the surface of the aluminum 2024-T3. This means that adhesive remains attached to both parts also known as adhesive-cohesive failure [345,346]. On the contrary, the strong bonding formation obtained with the heating control approach. Stock-break failure occurred by tensile failure outside of the overlap joint area across the width of the 3D-printed ABS (Figure A.11(b)) [347]. This typical failure is rarely reported for hybrid joints, and it is mainly caused by the strong interface between the adherends (aluminum 2024-T3 and the 3D-printed ABS), where the failure is driven to possible area with stress concentrations. AddJoining uses FFF process as main backbone to produce the hybrid joints and it is well-known the presence of voids in the 3D-printed FFF parts [93,95,109,112,348]. The voids act as stress concentrations and contributing to anisotropy of the mechanical properties. Thus, for the process variant using heating control, the strong interface drives the failure to the 3D-printed part to fail at lower stresses. Figure A.11(c) shows an adhesive failure, where very thin layer of ABS coating remains attached to the metallic surface. The presence of voids in the ABS coating is caused due to the evaporation of residual acetone. Nevertheless, at the microscopic level, the presence of voids in the ABS coating was not sufficient to extremely decrease the overall mechanical performance of the AddJoining hybrid joints, where a good mechanical interlocking was achieved between the coated metal substrate and the 3D-printed polymer.

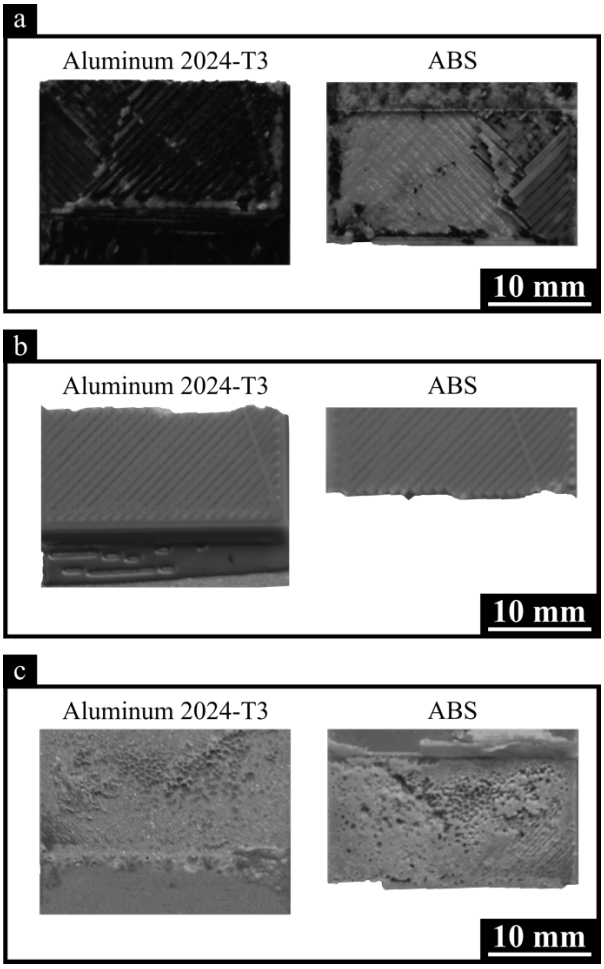

Figure A.11 Fracture surface from the AddJoining hybrid joints for (a) process variant one (with adhesive), (b) variant two (with heating control) and (c) variant three (with thin-coating layer).

The different AddJoining process variants was successfully demonstrated using the most common materials applied in the transportation industry. This new process has proven suitable to produce hybrid single-lap joints and has potential to upscale to produce future layered metal-polymer structures.

Appendix A.4 Statistical modeling

In this appendix, the influence of the controlled structural parameters and heating control process parameters on the mechanical performance of hybrid joints were evaluated using statistical modelling. Two statistical modeling were evaluated and correlated with the parameters shown in each section.

The current investigation aims to evaluate the influence of different parameters on the mechanical behavior of hybrid joints made by AddJoining. This study facilitates the first insights into the understanding and improvement of hybrid joints by AM means. Therefore, two well-established materials were selected for this study: aluminum alloy 2024-T3 and unreinforced polyamide 6 (PA6) and carbon-fiber-reinforced polyamide 6 (CF-PA6). The geometry selected to perform mechanical testing (lap shear test) was single-lap joint configuration (described in Section 4.3.8.1) with an overlap area of 12.5 mm x 25.5 mm. The joints were evaluated under quasi-static loading to assess the mechanical performance. Based on ASTM D3163-01, the single-lap shear test was performed in the universal testing machine Zwick/Roell 1478 at room temperature with a transverse speed of 1.27 mm/min. As a result of this study, the set of optimized parameters used in this PhD work was attained for the chosen combination of materials.

Indirect heating approach

An effect of the structural parameters on the mechanical performance of single-lap joint was evaluated using an indirect heating approach. This method was used first as a feasibility study to identify possible constrains on the development of the heating system (described in Section 4.2.2).

First of all, a PA6 coating was applied by indirect heating after the sandblasting as follows: (1) printing a stand-alone layer of PA6 (13 mm x 26 mm x 0.2 mm); (2) heating the aluminum 2024-T3 part with the stand-alone PA6 printed layer using an external hot plate at 270°C for three minutes (to remelt and homogenize the stand-alone printed layer); (3) allowing a ten-minutes consolidation time to cool down in room temperature. This coating permits the adhesion of the printed PA6 on the sandblasted aluminum surface.

In this PhD work, structural parameters were varying as process parameters to produce the single-lap joints using MarkTwo. The structural parameters were previously described in Section 5.2. Again, the three controllable process parameters briefly described as follows:

a) CF-PA6 distribution means the strategy to distribute the CF-PA6 layers along the composite part (shown in Figure 5-4).

b) CF-PA6 layer is the amount of CF-PA6 layer present in the composite part (shown in Figure 5-5).

c) CF-PA6 orientation refers to the orientation in each CF-PA6 layer (shown in Figure 5-6).

Three factors were considered for the DoE with three-level full factorial design with the selected factors. The three levels were varied shown in Table A.1. DoE was proposed to evaluate the mechanical performance of the single-lap joints produced and analysis of variance (ANOVA) were used to evaluate the significance of the selected parameters on the mechanical strength of the joints.

Table A.1 AddJoining structural parameters (factors) used in the three-level full factorial design with three factors with indirect heating approach.

Factor	Unit	Level 1	Level 2	Level 3
CF-PA6 distribution	a.u.	Alternate	Mid-plane top	Mid-plane bottom
CF-PA6 orientation	°	0	45	90
CF-PA6 layers	a.u.	4	6	8

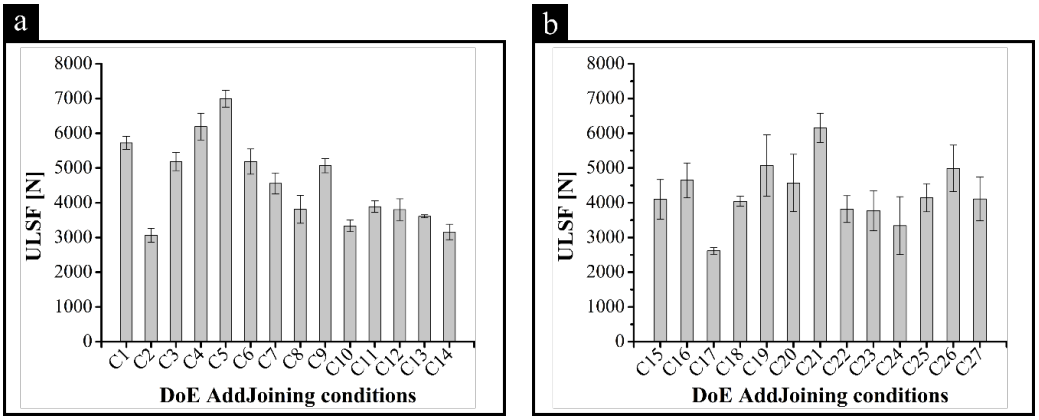

Figure A.12 Effect of different conditions on the ULSF (a) conditions one to 14 and (b) 15 to 27 correspond to the experiments performed during the DoE with indirect heating approach.

Table A.2 ANOVA results for ULSF for AddJoinig hybrid joints used in the three-level full factorial design with three factors (full model) for indirect heating approach.

CF-PA6 Factor	Adj SS	Adj MS	F-value	p-value
Distribution	5636917	4795381	11.45	< 0.05
Orientation	1994088	1994088	8.10	< 0.05
Layers	91051	91051	0.37	0.546
Orientation x Orientation	771485	771485	3.13	0.084
Layers x Layers	1459	1459	0.01	0.934
Layers x Orientation	262504	262504	1.07	0.308
Distribution x Orientation	6109247	3054623	12.41	< 0.05
Distribution x Layers	225998	112999	0.46	0.635
Error				
Lack-of-fit	4633082	308872	1.46	0.189

Table A.3 ANOVA results for ULSF for AddJoinig hybrid joints used in the three-level full factorial design with three factors (reduced model) for indirect heating approach.

CF-PA6 Factor	Adj SS	Adj MS	F-value	p-value
Distribution	25165586	12582793	53.46	< 0.05
Orientation	5917225	5917225	25.14	< 0.05
Layers	7968388	7968388	33.86	< 0.05
Orientation x Orientation	771485	771485	3.28	0.077
Distribution x Orientation	6109247	3054623	12.98	< 0.05
Error				
Lack-of-fit	5123043	268634	1.28	0.257

Table A.4 Regression equations for each CF-PA6 distribution (categorical factor) identified within the the three-level full factorial design with three factors (reduced model) for indirect heating approach.

CF-PA6 distribution (Categorical factor)	Regression equation
Alternate	$ULSF = 4895 + 235.2{\times}B - 34.89{\times}C + 0.1252{\times}C^2$
Mid-plane top	$ULSF = 4895 + 235.2{\times}B - 26.22{\times}C + 0.1252{\times}C^2$
Mid-plane bottom	$ULSF = 2338 + 235.2{\times}B - 12.65{\times}C + 0.1252{\times}C^2$

B: CF-PA6 layers
C: CF-PA6 orientation

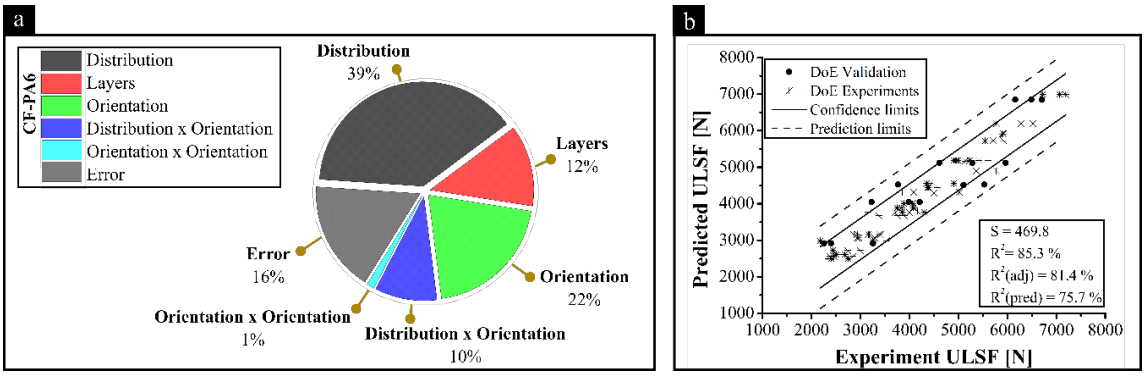

Figure A.13 (a) Effect of each significat factor and interactions and (b) Validation diagram for the ULSF reduced model with indirect heating approach.

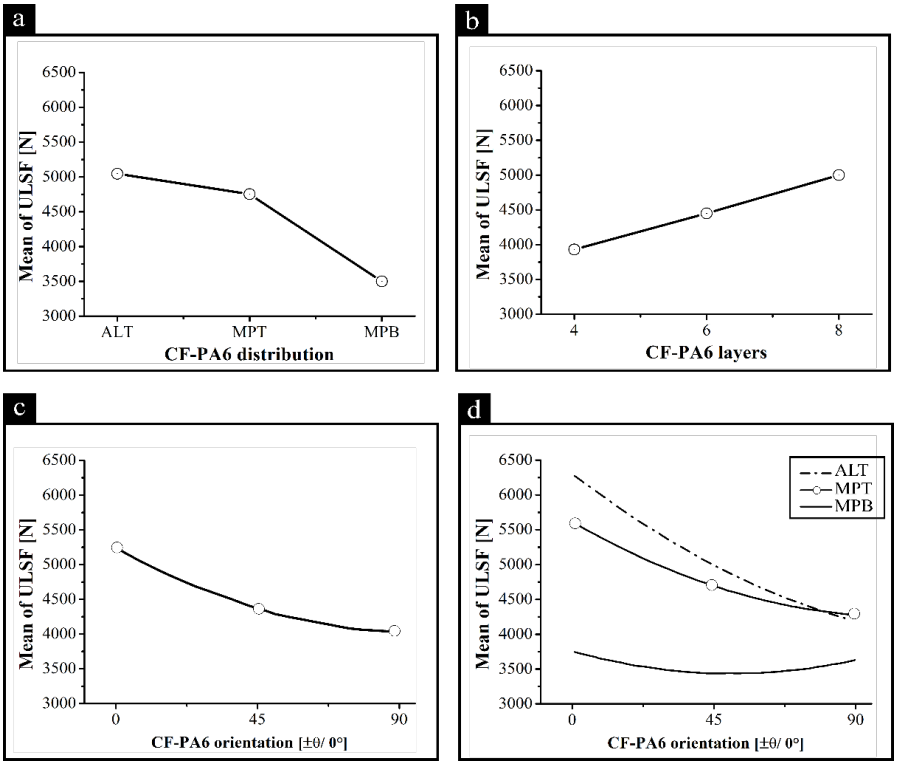

Figure A.14 Effect of the factors (a) CF-PA6 distribution, (b) CF-PA6 layers, (c) CF-PA6 orientation and interaction between CF-PA6 distribution and CF-PA6 orientation on the ULSF with indirect heating approach.

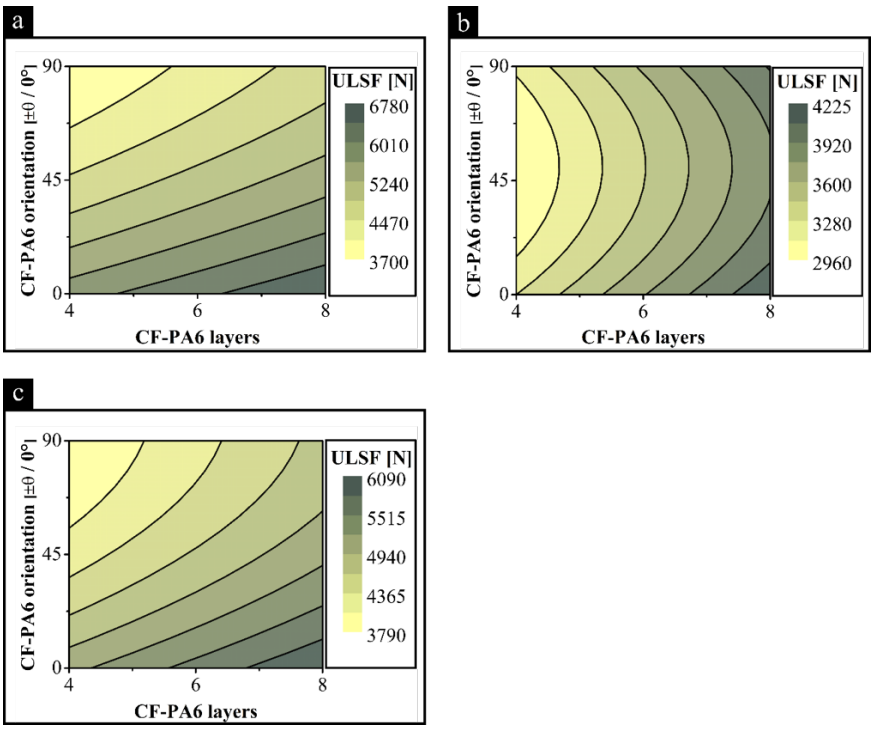

Figure A.15 Contour plot for the each CF-PA6 distribution (a) Alternate, (b) Mid-plane bottom and (c) Mid-plane top for indirect heating approach.

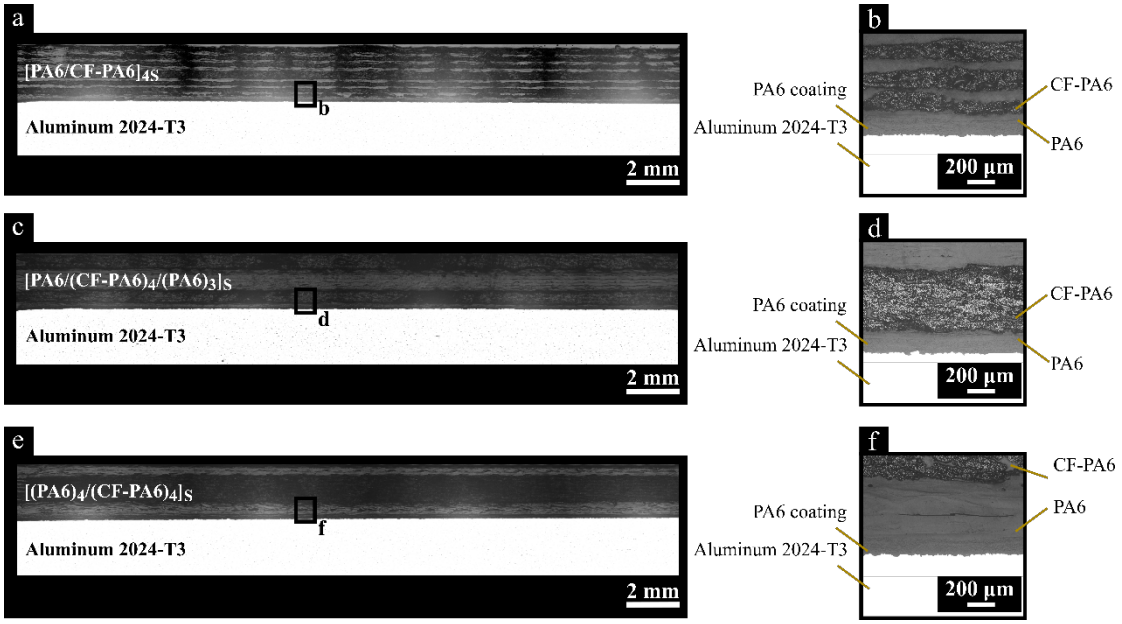

Figure A.16 Cross-sectional microstructure of hybrid joints for eight CF-PA6 layers, 0° CF-PA6 orientation and three different CF-PA6 distribution: (a) Alternate with (b) the interface of aluminum 2024-T3 / PA6 coating / $[PA6/CF\text{-}PA6]_{4S}$, (c) Mid-plane top with (d) the interface of aluminum 2024-T3 / PA6 coating / $[PA6/(CF\text{-}PA6)_4/(PA6)_3]_S$, (e) Mid-plane bottom with (d) the interface of aluminum 2024-T3 / PA6 coating / $[(PA6)_4/(PA6)_4]_S$ obtained with RLOM for indirect heating approach.

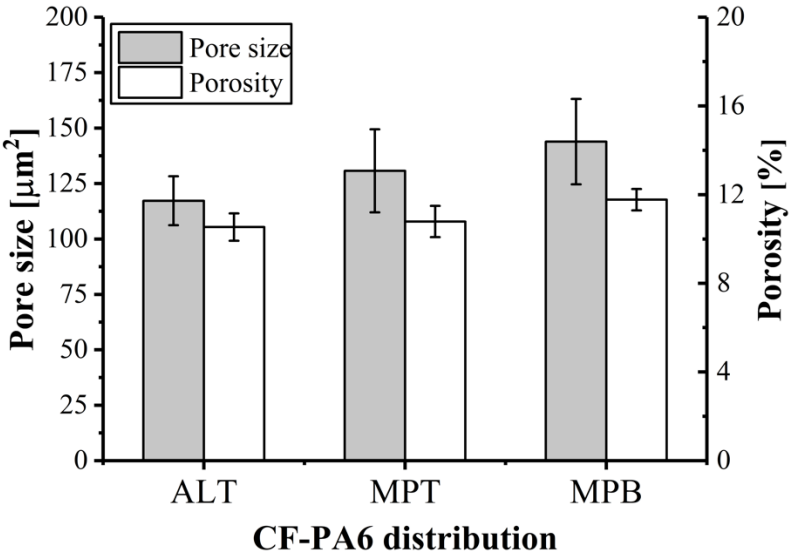

Figure A.17 Pore size and area fraction of hybrid joints for eight CF-PA6 layers, 0° CF-PA6 orientation and three different CF-PA6 distribution: Alternate (ALT), Mid-plane top (MPT) and Mid-plane bottom (MPB) with indirect heating approach.

Direct heating approach

The optimum structural parameters obtained on the previous investigation, such as the Alternate CF-PA6 distribution, eight CF-PA6 layers and 0° CF-PA6 orientation, was used for the further evaluation using direct heating approach. In order to reproduce the parameters from indirect heating approach on the direct heating approach, a parameter setup was defined that corresponds the coating

temperature (CT) and heating bed temperature (HBT), such as 270 °C and 20 °C, respectively. The heating applied to form was 270°C as previously described and as the heating bed has not heating control is considered room temperature with an average temperature of 20 ± 2 °C. Note that the indirect heating approach is not possible to control temperature during the AddJoining 3D-printing method. Due to manufacturing constrains, the system was not feasible to install on the printing bed surface. However, as previously described, the indirect heating approach gave the first insights on the feasibility of the AddJoining process and for the further development on the direct heating approach. The mechanical performance was compared in order to assess possible difference on the hybrid joints behavior between the two approaches (Figure A.18). The indirect heating approach achieved ULSF of 6993 ± 243 N and displacement at break (DaB) of 1.56 ± 0.08 mm. Thus, for direct heating method obtained ULSF of 7098 ± 106 N and DaB of 1.73 ± 0.04 mm. Based on the mechanical performance, statistically, there no difference between the two approaches for the selected process parameters. Thus, to explore the effects of different coating temperatures and heating bed temperatures, this study was further analyzed using direct heating approach.

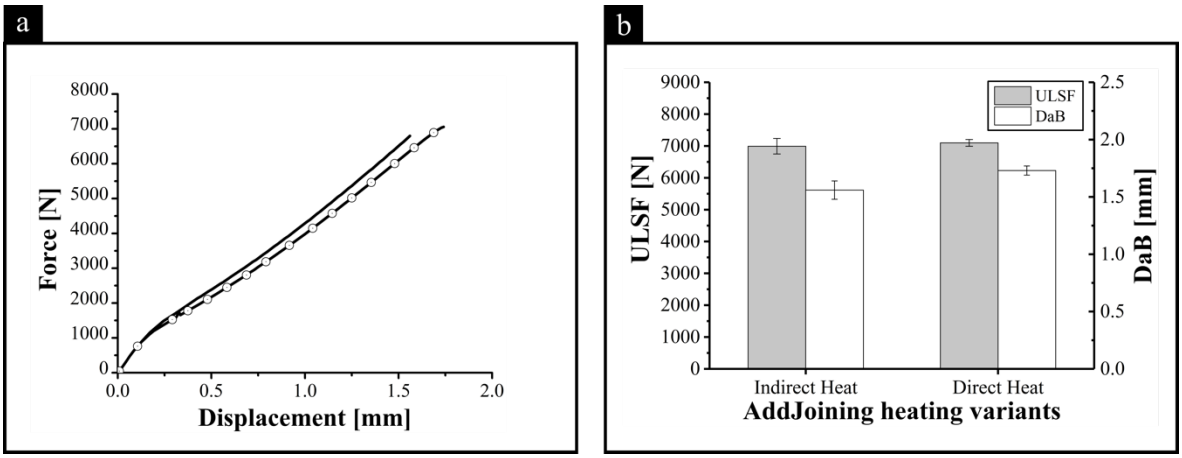

Figure A.18 Mechanical performance of the AddJoining hybrid joints for indirect and direct heating approach (a) representative force-displacement curvs and (b) average ULSF and DaB.

Table A.5 Summary of the ULSF for all nine conditions in the DoE three-level full factorial design with two factors with direct heating approach.

Condition	Factors		ULSF	
	CT [°C]	**HBT** [°C]	**Average**	**Standard deviation**
1	200	20	5401	247
2	235	20	7482	309
3	270	20	7098	106
4	235	85	8254	93
5	235	150	7461	342
6	200	85	6574	387
7	270	85	7163	139
8	200	150	7672	235
9	270	150	5557	247

The final mathematical model used to describe the ULSF, which it is included the significant parameters and interaction, are given in:

$$\mathrm{ULSF} = -28485 + 299.4\times\mathrm{CT} + 65.5\times\mathrm{HBT} - 0.0914\times\mathrm{CT}\times\mathrm{HBT} - 0.638\times\mathrm{CT}^2 - 0.2905\times\mathrm{HBT}^2 \quad \text{(A-1)}$$

The optimized condition was obtained by applying partial derivatives (Equation (A-1) and Equation (A-2)) to the mathematical model (Equation (A-3)). The set of parameters obtained corresponds to optimized condition, i.e. point of maximum for the model.

$$\frac{\partial ULSF}{\partial CT} = 0 \therefore 299.4 - 0.0914\times HBT - 1.276\times CT = 0 \quad \text{(A-2)}$$

$$\frac{\partial ULSF}{\partial HBT} = 0 \therefore 65.5 - 0.0914\times CT - 0.581\times HBT = 0 \quad \text{(A-3)}$$

Equation (A-1) and Equation (A-2) resume to a system of equations with two variables. By solving the system of equation, the CT is equal to 229.2 °C and HBT is equal to 76.68 °C. It is important to notice that the optimized value was rounded to significant numbers, such as 229 °C and 77 °C for CT and HBT, respectively.

Table A.6 ANOVA results for ULSF for AddJoinig hybrid joints used in the three-level full factorial design with two factors (full model) for direct heating approach.

CF-PA6 Factor	Adj SS	Adj MS	F-value	p-value
HBT	3660892	3660892	39.16	< 0.05
CT	3629516	3629516	38.82	< 0.05
HBT x CT	518336	518336	5.54	0.028
CT x CT	3662891	3662891	39.18	< 0.05
HBT x HBT	9038083	9038083	96.67	< 0.05
Error				
Lack-of-fit	486809	162270	1.98	0.153

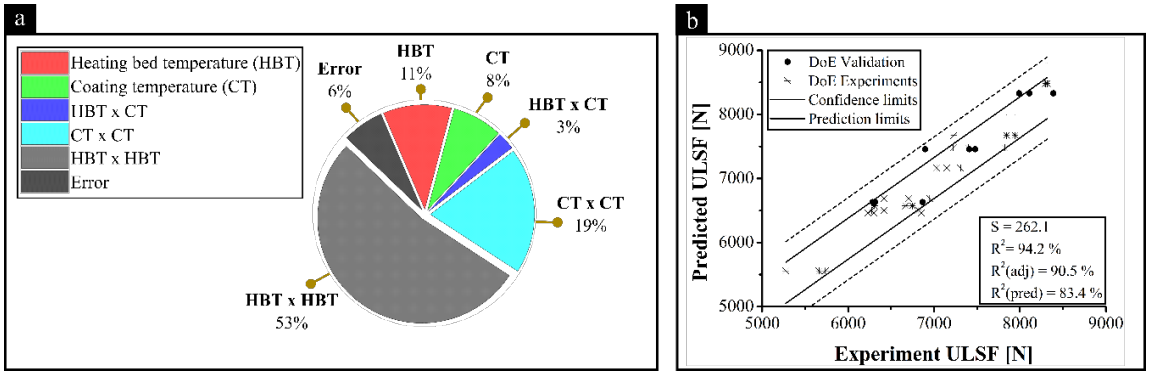

Figure A.19 (a) Effect of each significat factor and interactions and (b) Validation diagram for the ULSF full model with direct heating approach.

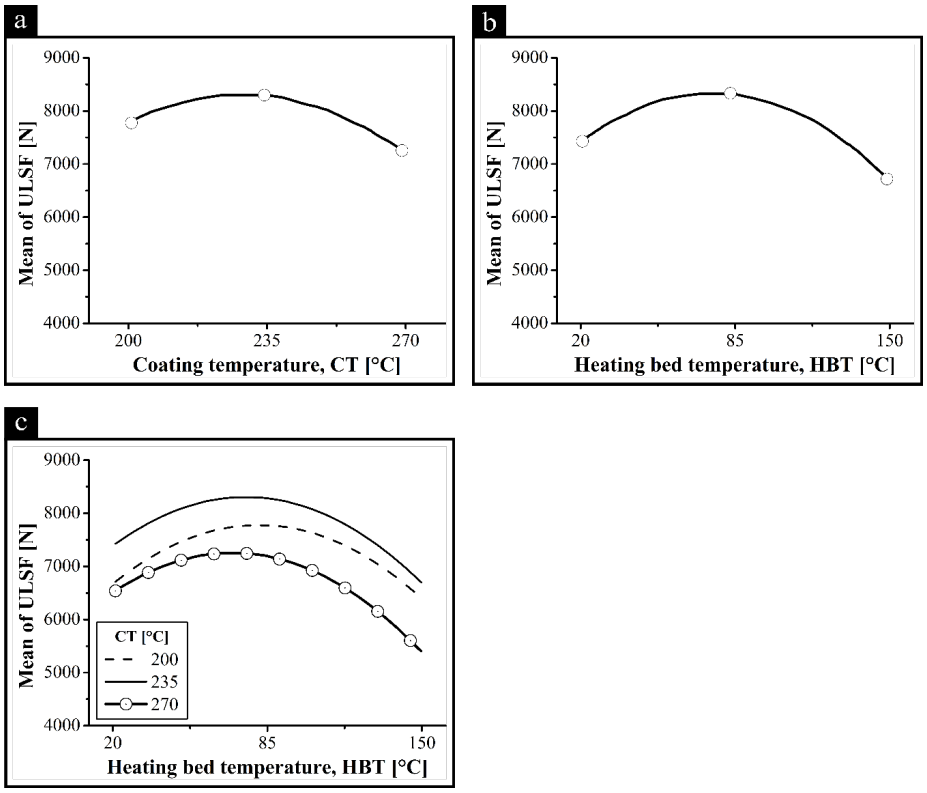

Figure A.20 Effect of the factors (a) CT, (b) HBT, and (c) interaction between CT and HBT on the ULSF with direct heating approach.

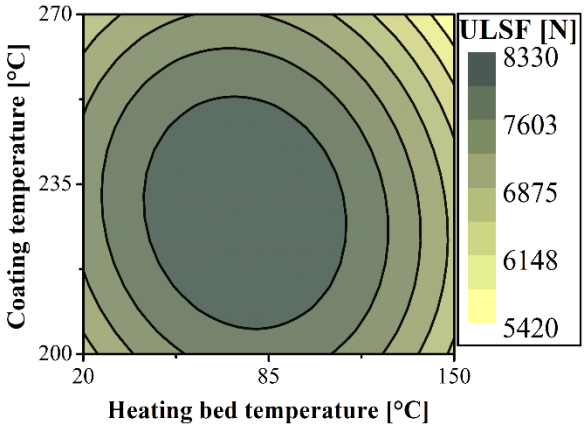

Figure A.21 Contour plot based on the three-level full factorial design with two factors (full model) for direct heating approach.

Appendix A.5 Changing the AddJoining hybrid joint geometry

In this appendix, the AddJoining hybrid overlap length was changing from 12.5 to 25.5 mm as shown in Figure A.22. The width, length and thickness for the metallic and composite part was kept unchanged. The purpose was to reduce the number of variable within the process or structural parameters in this PhD work. According to the ASTM D3163 [211], it is allowed to change the single-lap joint geometry to investigate possible variation in the failure mode. For the three-overlap length shown in the image, the delamination was predominant. Although, the ULSF increased by 66% with increasing in the overlap length from 12.5 mm (ULSF: 8.24 ± 0.4 kN) to 25.5 mm (ULSF: 12.3 ± 0.1 kN). Based on the engineering approach, the maximum response is visible with the help of the contour plot shown in the figure.

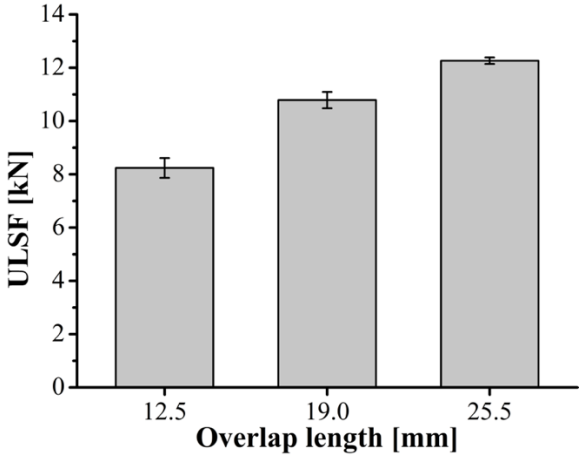

Figure A.22 The effect of overlap length on the ultimate lap shear force (ULSF) for AddJoining hybrid joints under direct heating approach.

From the SB evaluation, the out-of-plane displacement shown in Figure A.23 was evaluated by digital image correlation (DIC) system. The out-of-plane displacement vary linearly through the bonding area. The dissimilarity on the material stiffness is seen on the measured maximum out-of-plane displacement during the test. For the minimum overlap length, the aluminum 2024-T3 displacement corresponded to 0.37 mm and 0.75 mm for the $[PA6/CF\text{-}PA6]_{4S}$ part. As previously discussed in Chapter 7 and Section 7.1.1, the relatively low displacement corresponded to 0.16 mm for the aluminum 2024-T3 part and 0.74 mm for the $[PA6/CF\text{-}PA6]_{4S}$ part. The high metal stiffness in average 76 GPa avoid the large deformation on the metallic part. On the contrary, the high deformation is drive by the composite part with an average stiffness of 35.7 GPa. The overlap length helps to distribute effective the shear distribution causing to raise the ULSF. The reduction of the SB effect is due to the increasing in overlap length. By increasing the overlap length, it was observed a decreased by 62.5% on the out-of-plane displacement for aluminum 2024-T3 from 12.5 mm to 25.5 mm.

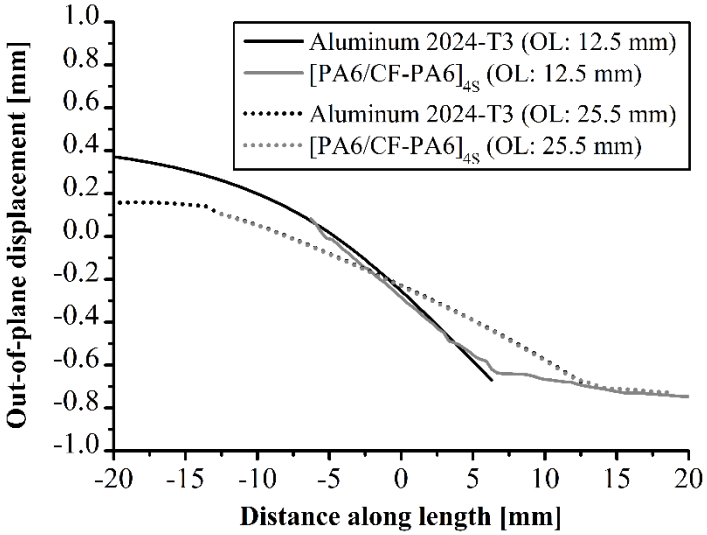

Figure A.23 Out-of-plane displacement profiles for overlap length 12.5 mm and 25.5 mm measured by digital image correlation (DIC) system.

Appendix A.6 Nanoidentation curves

The typical oscillation seen in the modulus curves is attributed to surface roughness of the samples, but an average value was instrumentally calculated from a stable contact depth of between 200 nm and 800 nm. The hardness was also instrumentally calculated from nanoindentation measurements during unloading. However, the purpose here is not to offer a deeper understanding of the nanoindentation technique, for more information please refer to [208,349,350] for a comprehensive overview of the technique.

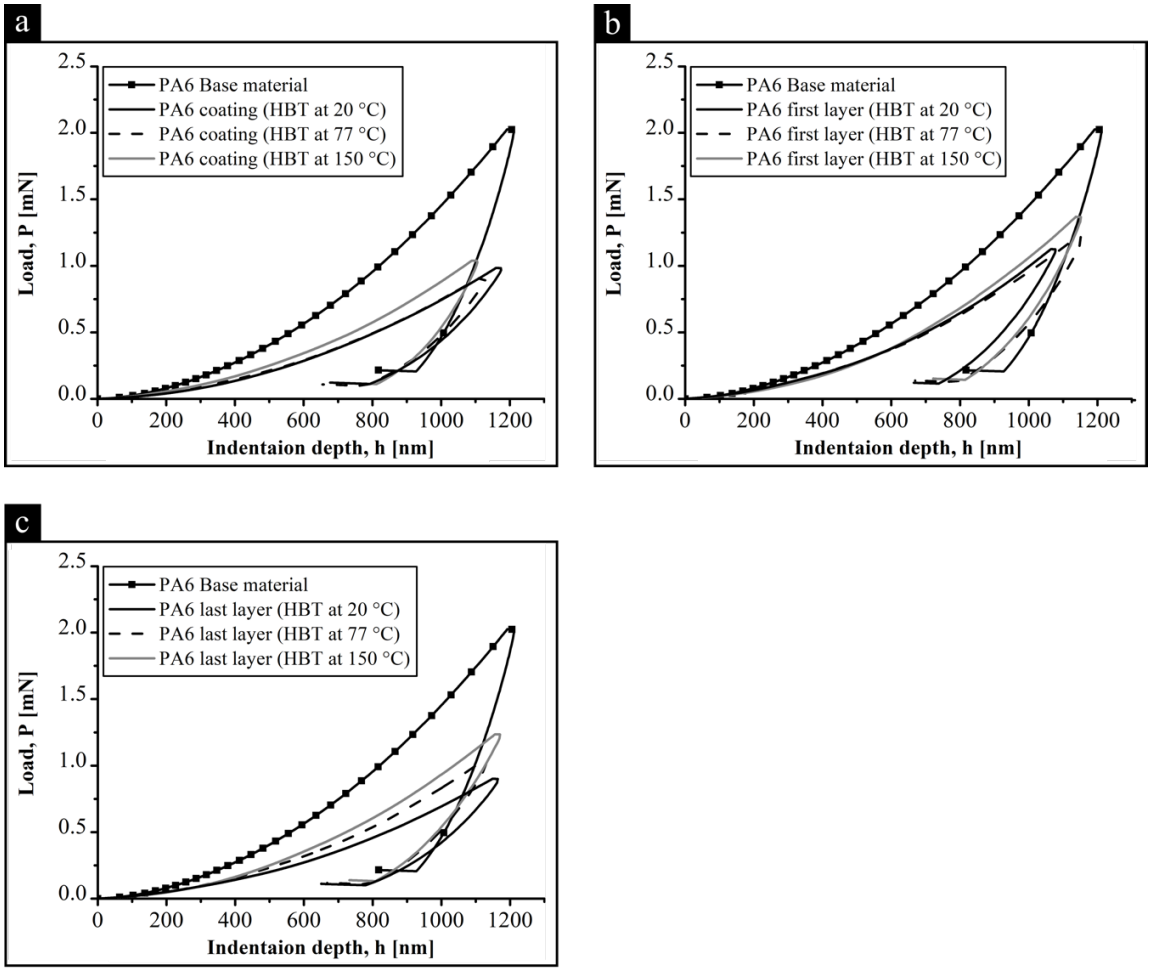

Figure A.24 Representative quasi-static P-h curve obtained for the PA6 coating also (a) PA6 coating, (b) PA6 first layer and (c) PA6 last layer base material within the selected HBT range.

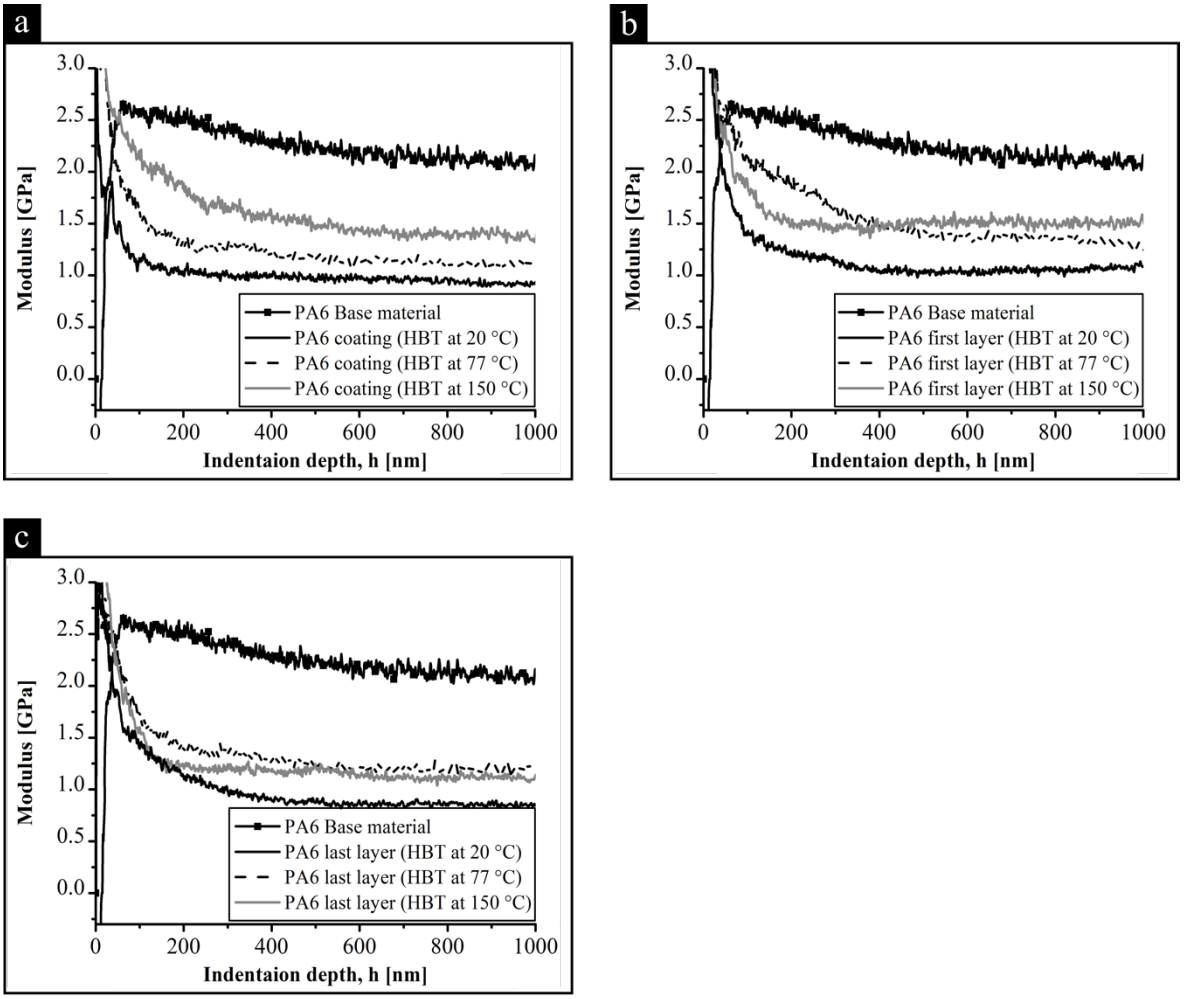

Figure A.25 Representative modulus curve obtained for the PA6 coating also (a) PA6 coating, (b) PA6 first layer and (c) PA6 last layer base material within the selected HBT range.

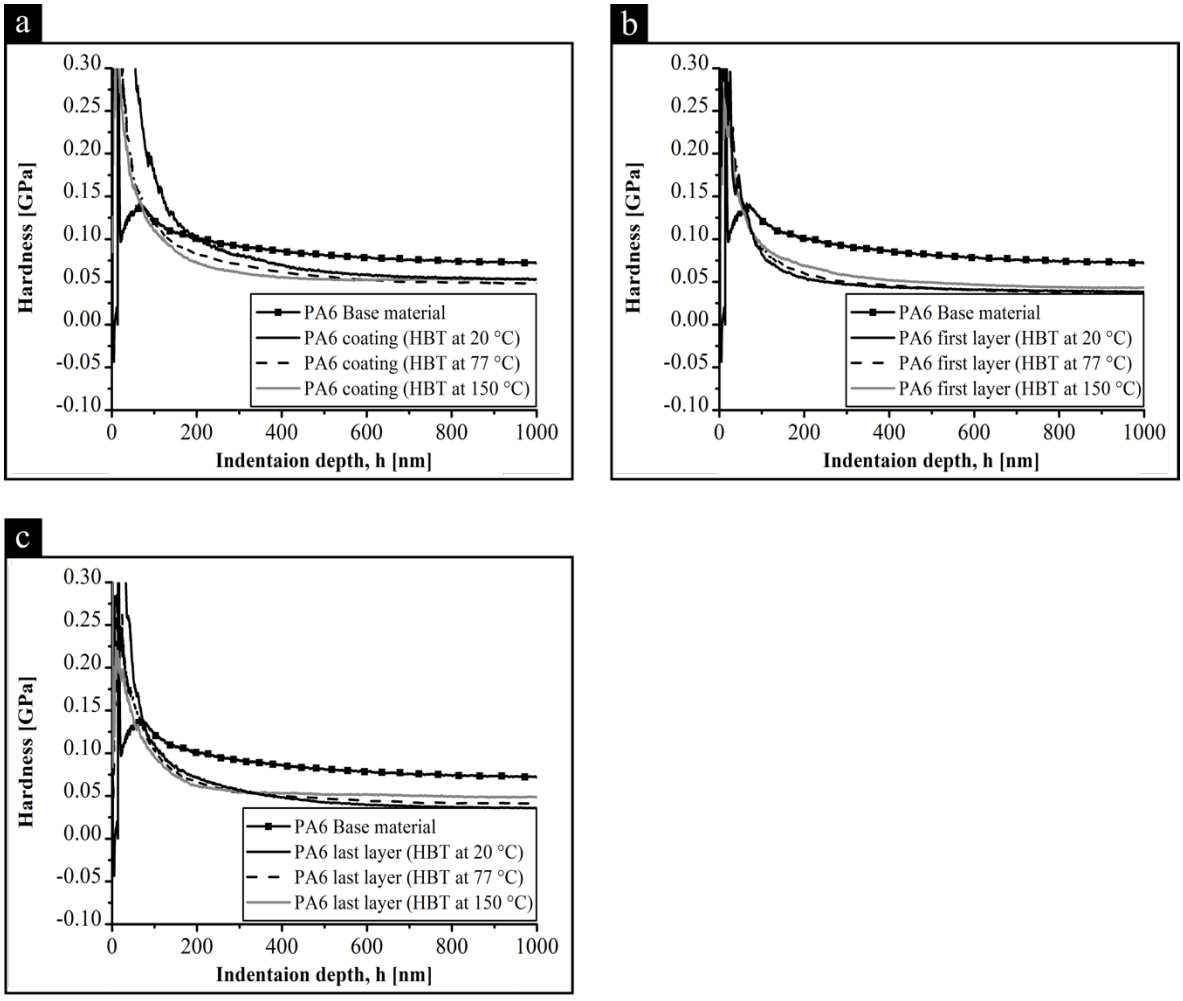

Figure A.26 Representative hardness curve obtained for the PA6 coating also (a) PA6 coating, (b) PA6 first layer and (c) PA6 last layer base material within the selected HBT range.

The first region to evaluate is from the measurements on the aluminum 2024-T3 close to the interface (Figure A.27(1)). Generally speaking, these results show a modulus decrease of 11 % (79.3 ± 3.8 GPa) compared to the base material (89.4 ± 2.6 GPa) for HBT at 20 °C. For the other two HBT values, the modulus also decreased at 77 °C and 150 °C by 6 % (84.2 ± 4.4 GPa) and 3 % (86.9 ± 2.3 GPa), respectively.

By comparing the results in the second region, corresponding to the PA6 coating, the average modulus (Figure A.27(2)) drastically decreased compared to the base material. At 20 °C, the modulus decreased by 56 % (0.96 ± 0.09 GPa) compared with the base material (2.18 ± 0.12 GPa). At a higher HBT the variation in modulus decreased in comparison to the base material, by 50 % (1.09 ± 0.03 GPa) and by 33 % (1.45 ± 0.12 GPa), at 77 °C and 150 °C, respectively. In the measurements of the first layer of PA6 it is difficult to distinguish any differences from the PA6 coating. The average modulus (Figure A.27(3)) are statistically similar to the values presented here. For example, for HBT at 150 °C the modulus decreased 31 % (1.51 ± 0.09 GPa) compared to the base material (2.18 ± 0.12 GPa). For the last region, the average modulus (Figure A.27(4)) of the last layer of PA6 has no significant difference within the selected HBT range, with an average of 1.2 GPa, which is 44 % compared to the base material.

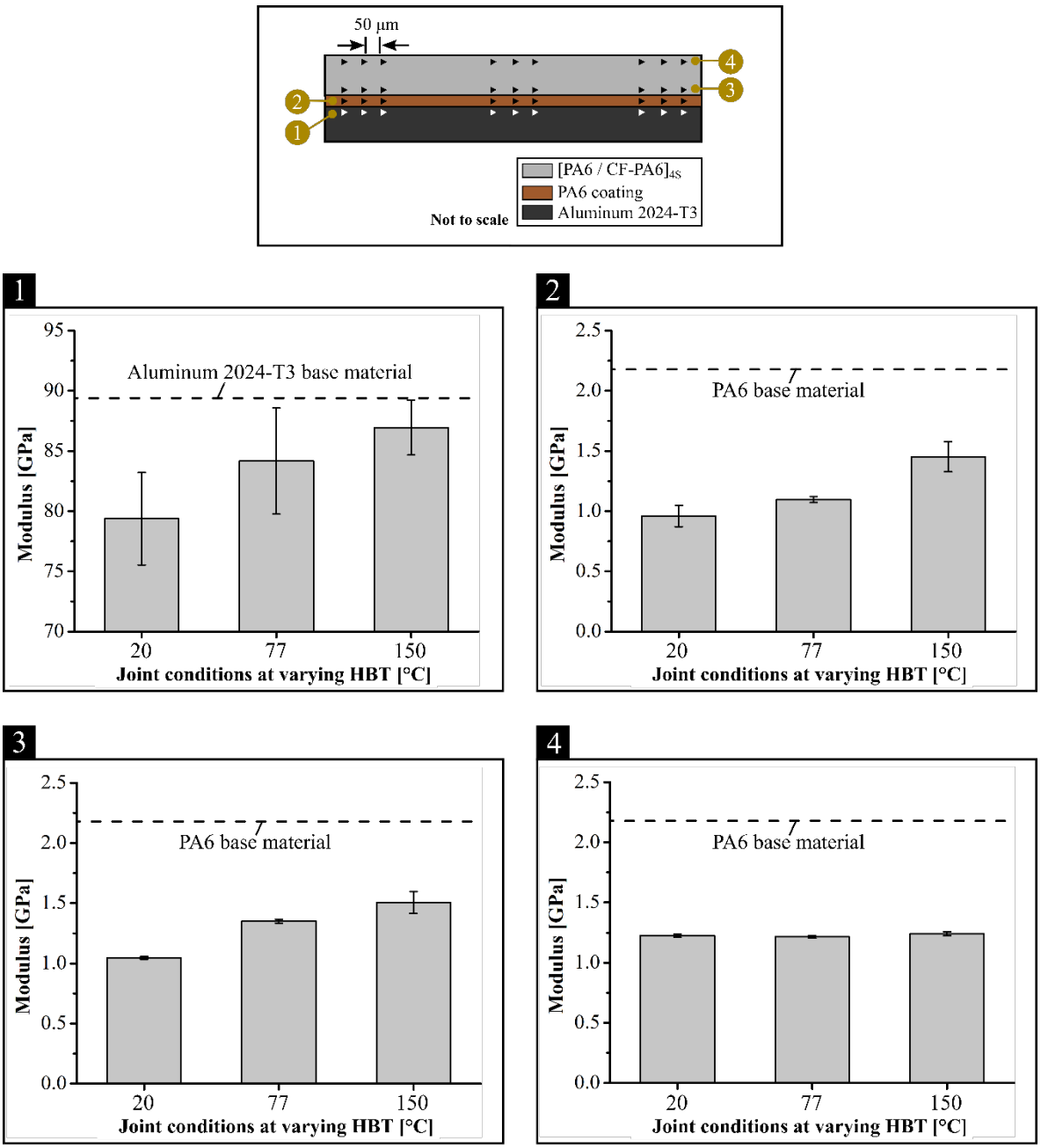

Figure A.27 Schematic of nanoindentation measurement of overlap joint locations on aluminum 2024-T3, on PA6 coating, and on composite [PA6/CF-PA6]$_{4S}$; average nanoindentation modulus of (1) aluminum 2024-T3 close to the interface with the PA6 coating / [PA6/CF-PA6]$_{4S}$, (2) PA6 coating, (3) PA6 first layer, and (4) PA6 last layer. Each at the three different heating bed temperatures (HBT).

Appendix A.7 DSC and TGA curves

From Figure A.28 to Figure A.30, the curves show the first derivatives for the investigation on variation of HBT (Chapter 6 in Section 6.1.3). The sample for DSC and TGA curve were extracted covering the composite $[PA6/CF\text{-}PA6]_{4S}$ full thickness (as described in Section 4.3.5). DSC gave hints on the presence of PA6 crystalline changes by investigating the first derivative on the DSC curves. For HBT at 20 °C and 77 °C, the slope of the curve changed (highlighted with the circle and arrow), Figure A.28 and Figure A.29, respectively. However, no sign of polymorphism was observed on the HBT at 150 °C (Figure A.30). Therefore, the thermal analysis was not enough to understand possible variation on PA6 crystalline changes. A reason is the presence of CF-PA6 on the composite $[PA6/CF\text{-}PA6]_{4S,}$ which it can hinder the crystallinity effect of the PA6 present. By contrast, the investigation on the phase-identification study helped to better understand the phase changes during the AddJoining process by a stepwise approach (Section 6.1.4).

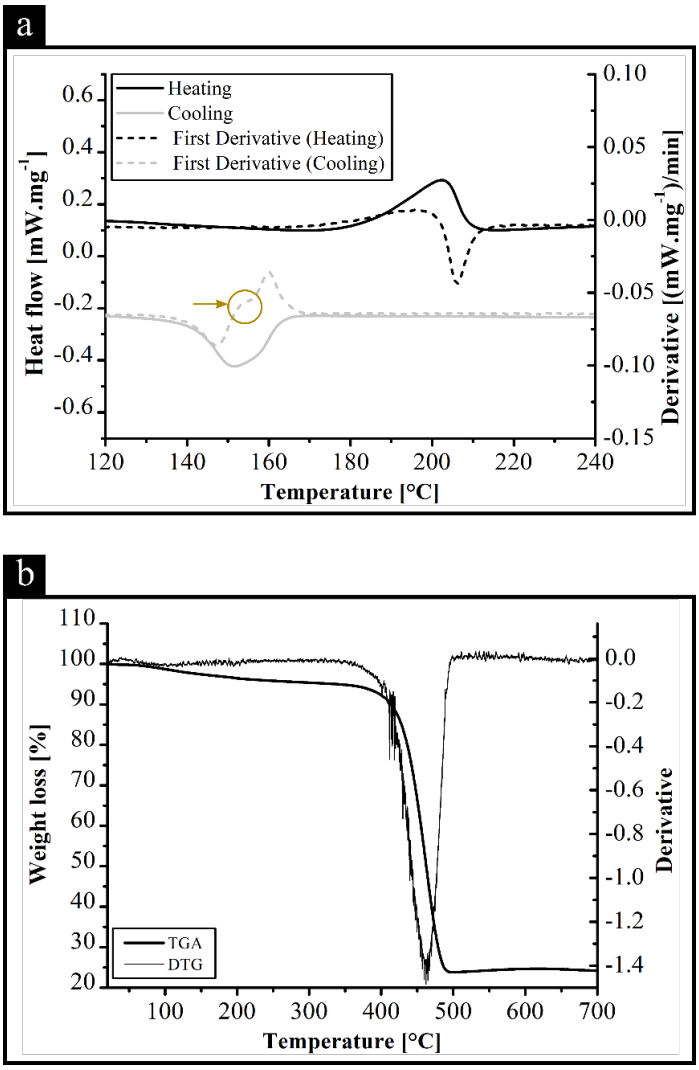

Figure A.28 (a) DSC curve (c) TGA curve with their first derivatives for HBT at 20 °C for the composite $[PA6/CF\text{-}PA6]_{4S}$ part.

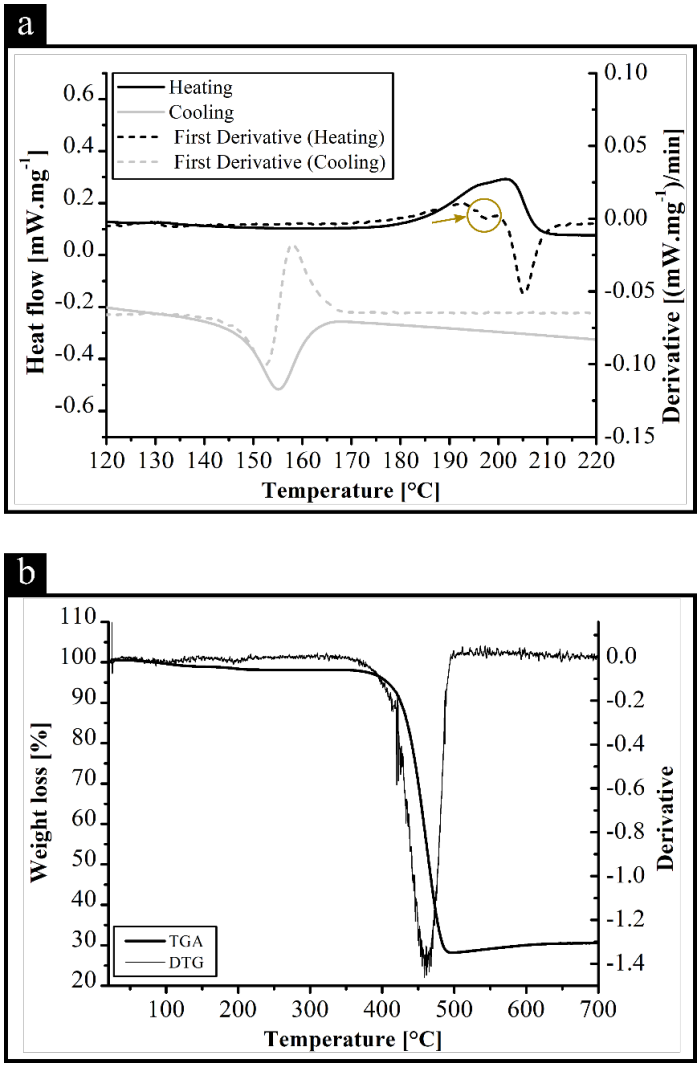

Figure A.29 (a) DSC curve (c) TGA curve with their first derivatives for HBT at 77 °C for the composite $[PA6/CF\text{-}PA6]_{4S}$ part.

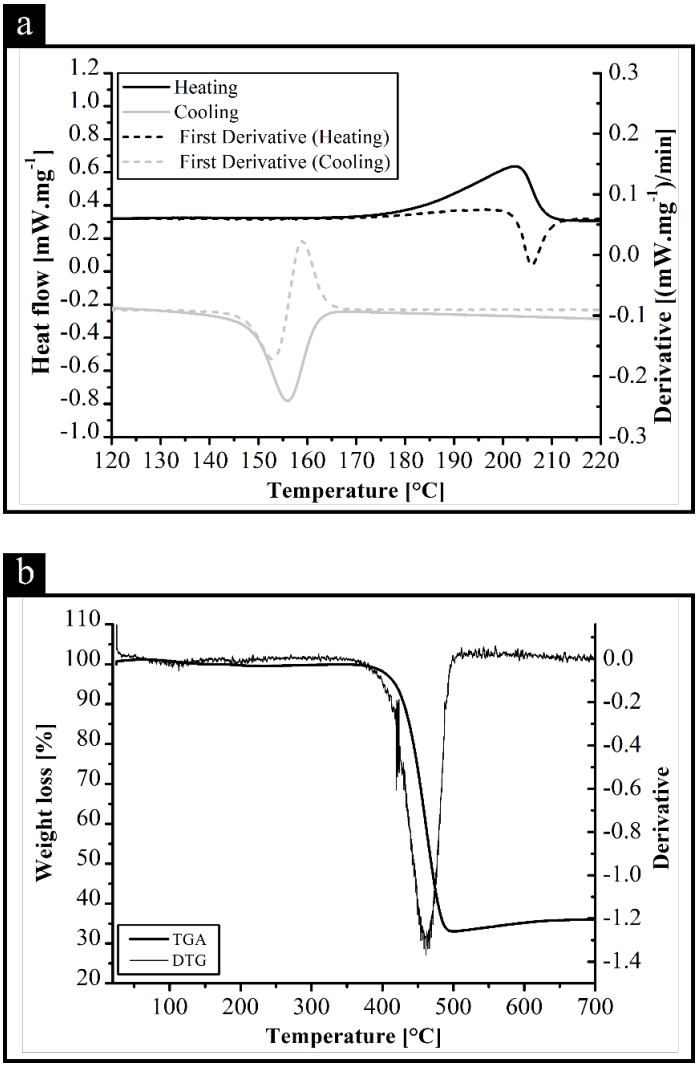

Figure A.30 (a) DSC curve (c) TGA curve with their first derivatives for HBT at 150 °C for the composite $[PA6/CF\text{-}PA6]_{4S}$ part.

Appendix A.8 Finite element analysis of AddJoining hybrid joints

The model was useful to depict the stress distribution of the AddJoining hybrid joints. Figure A.31 shows the schematic representation from the boundary conditions used within the model. The FE analyses were performed using the Abaqus/Standard (version 6.14-2). A length of 25 mm is fixed in all directions on the end of aluminum part on the opposite side from the overlap end. On the contrary, a length of 25 mm is fixed in all directions, except in X-direction on the composite part. The displacement is applied based on the quasi-static shear loading obtained from the experiment, i.e. 2.5 mm. An *EQUATION approach is applied in an offset point in X-direction parallel to the loading application edge. This point is coupled with all nodes within the edge, where the constrained grip length moves in the same direction during the displacement. The CPS8 element type is an 8-node, two-dimensional isotropic stress/displacement plane stress elements. It was used for the aluminum 2024-T3 and composite $[PA6/CF\text{-}PA6]_{4S}$ parts. A total of 5328 elements and 16751 nodes are applied in the model, i.e. a global mesh size of 0.5 mm is considered.

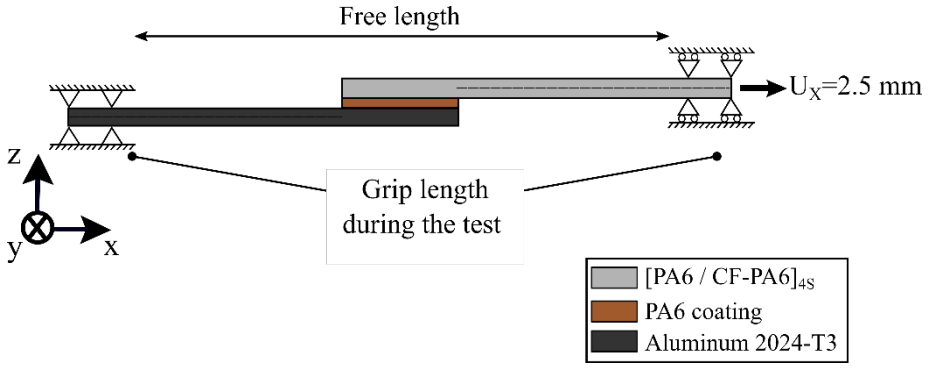

Figure A.31 Schematic representation from the boundary conditions for model used to simulate the single-lap shear testing.

The AddJoining hybrid joints simulation was applied using a merge method, where no need to apply cohesive surface contact or applying a tie method. The merge approach consists to replace two nodes closer within a specified distance for a single new node. The new node location is the average position of the closest node. This method was considered due to type of failure mode obtaining during the experiments. The main advantage is also to reduce the computational time without applying any non-linear contact effect into the simulation.

The aluminum 2024-T3 part was defined using elastic-plastic material properties. The plastic properties is defined as true strain and stresses shown in Table A.7. The PA6 coating was applied as elastic material. The composite $[PA6/CF\text{-}PA6]_{4S}$ part was defined as lamina with discrete alternating layers of PA6 and CF-PA6 layers. In this regard, it was considered elastic and shear stiffness according the properties shown in Table A.8. Moreover, the Hashin failure criteria was applied to obtain the failure region within the composite. According to Hashin [351], the criteria is a two dimensional classical lamination approach. The method uses point stress calculations with ply discounting as the material degradation model. Furthermore, it is interesting to note that failure indices for Hashin criteria are related to fiber or matrix failures.

Table A.7 Platic properties used for aluminum 2024-T3 in the simulation for AddJoining hybrid joint.

True Stress [MPa]	True Strain [%]	True Stress [MPa]	True Strain [%]
343	0.	530	0.0951
370	0.0051	560	0.35
400	0.0151	575	0.155
421	0.0251	595	0.195
440	0.0351	630	0.295
460	0.0451	700	0.495
473	0.0551	730	0.695
490	0.0651	750	0.795
498	0.0751	790	0.995

Table A.8 Properties used for PA6 and CF-PA6 in the simulation for AddJoining hybrid joint [192]**.**

Properites	PA6	CF-PA6
Elastic modulus in the longitudinal direction (E_{11})	0.94 GPa	54 GPa
Elastic modulus in the transverse direction (E_{22})	0.94 GPa	7.4 GPa [a]
In-plane shear modulus (G_{12})	32 GPa	51 GPa
Tension strength in longitudinal direction (X_T)	54 MPa	700 MPa
Tension strength in transverse direction (Y_T)	54 MPa	33 MPa [a]

(a) Data from the literature [267]

The global response of the experiment and simulation are shown in Figure A.32(a) as force-displacement curve. Moreover, the predicted out-of-plane displacement is also compared with the measured by the digital image correlation (Figure A.32(b)). The simulation gives fairly good prediction of the carrying load capacity and the out-of-plane displacement. The predicted force-displacement curve shows a linear behavior with relatively high stiffness. The deviation is 2% in ULSF compared with the experiment results. Furthermore, the out-of-plane displacement is similar on the metallic part with a deviation of 35%, i.e. simulation and experiment reached 0.2 mm and 0.13 mm, respectively. On the contrary, the composite part, the simulation reached -0.57 mm in out-of-plane displacement, consequently a high deviation by 79% compared to the experiment (-0.72 mm) on the composite part is caused by the presence of voids and 3D properties not considered in the model. Nevertheless, for the purpose of the model was considered accurate to describe the AddJoining hybrid joint behavior, and it predicted the stress distribution presented in Chapter 7.

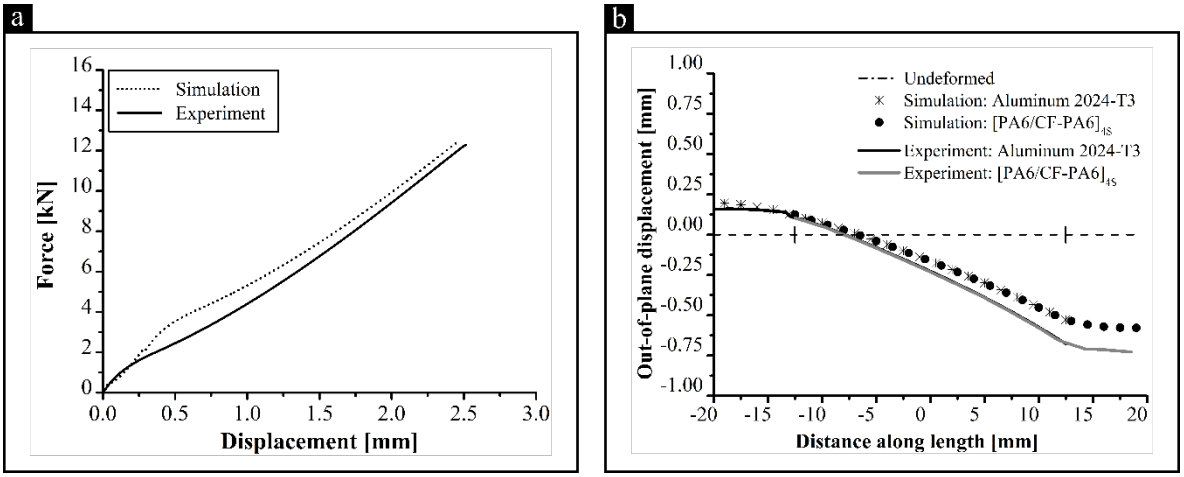

Figure A.32 Comparison between (a) representative force-displacement curve for experiment and simulation, and (b) out-of-plane displacement profiles obtained by digital image correlation system and predicted by the simulation.

The Hashin failure approach suggests according to a semi-emiprical method to address the failure modes in composite. The method defines four failure modes: (1) tensile fiber failure, (2) compressive fiber failure, (3) tensile matrix failure and (4) compressive matrix failure. These failure modes are presented in Figure A.33. The progressive damaged considers the stress state under which each would occur leading in a piecewise failure, i.e. occurs in the composite (highlighted in red), where the material properties continued to degraded in the damaged area. The main failure is shown on the edges due to the eccentricity of the load path (Figure A.33(a) and (Figure A.33(c)). It is interesting to observe failure on the center of the overlap area (Figure A.33(d)) caused by compressive stress during the out-of-plane deformation.

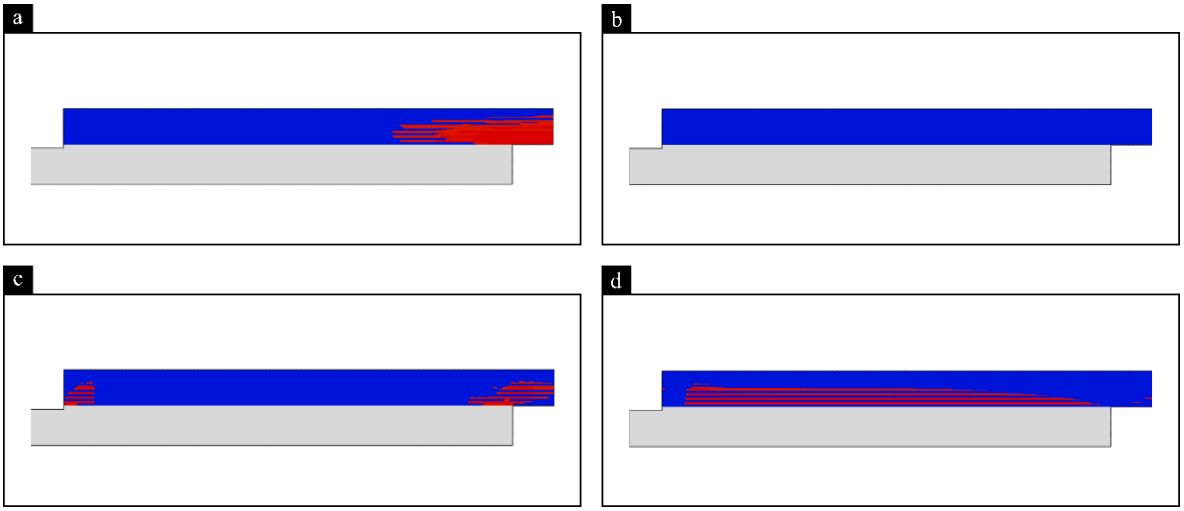

Figure A.33 Four failure mode obtained on the composite [PA6/CF-PA6]$_{4S}$ part using Hashin criteria: (a) tensile fiber failure, (b) compressive fiber failure, (c) tensile matrix failure and (d) compressive matrix failure.

Appendix A.9 Strain evolution under quasi-static lap shear loading

The strain was measured using digital image correlation system on the overlap end. Figure A.34 depicts the region to monitor the strain during quasi-static lap shear loading, such as edge composite (e_c) and edge metal (e_m).

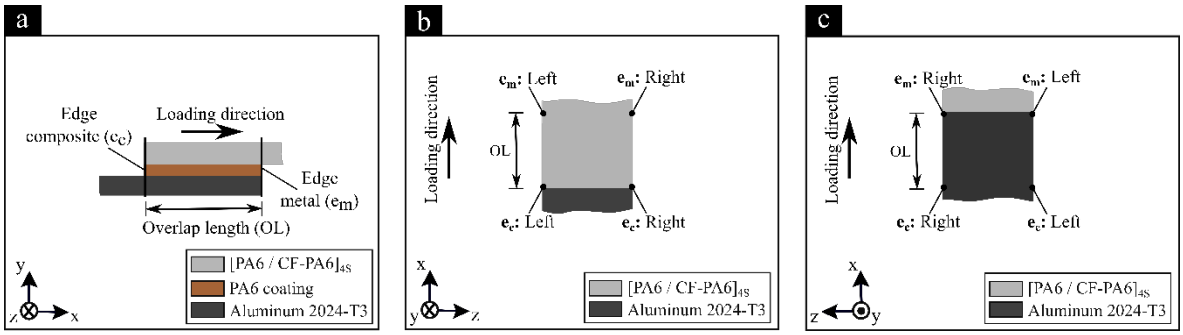

Figure A.34 Strain evolution measurement locations (a) overview, (b) composite [PA6/CF-PA6]$_{4S}$ surface, and (c) aluminum 2024-T3 surface.

The strain was monitored on the surface from each AddJoining hybrid joint member. Scuh technique is named in the literature as backface strain technique and it is widely used to detect fatigue crack initiation in adhesive-bonded single lap joints [352–355]. In this PhD work was applied under quasi-static loading to measure the strain in four different locations on the composite part (Figure A.34(b)) and on the metal part (Figure A.34(c)). The locations are on the opposite edges on each overlap end. The strain is reasonable higher on the composite as an indication of high carrying load part and damage evolution occurring. On the contrary, the metal deformation reflects the high stiffness and stable material.

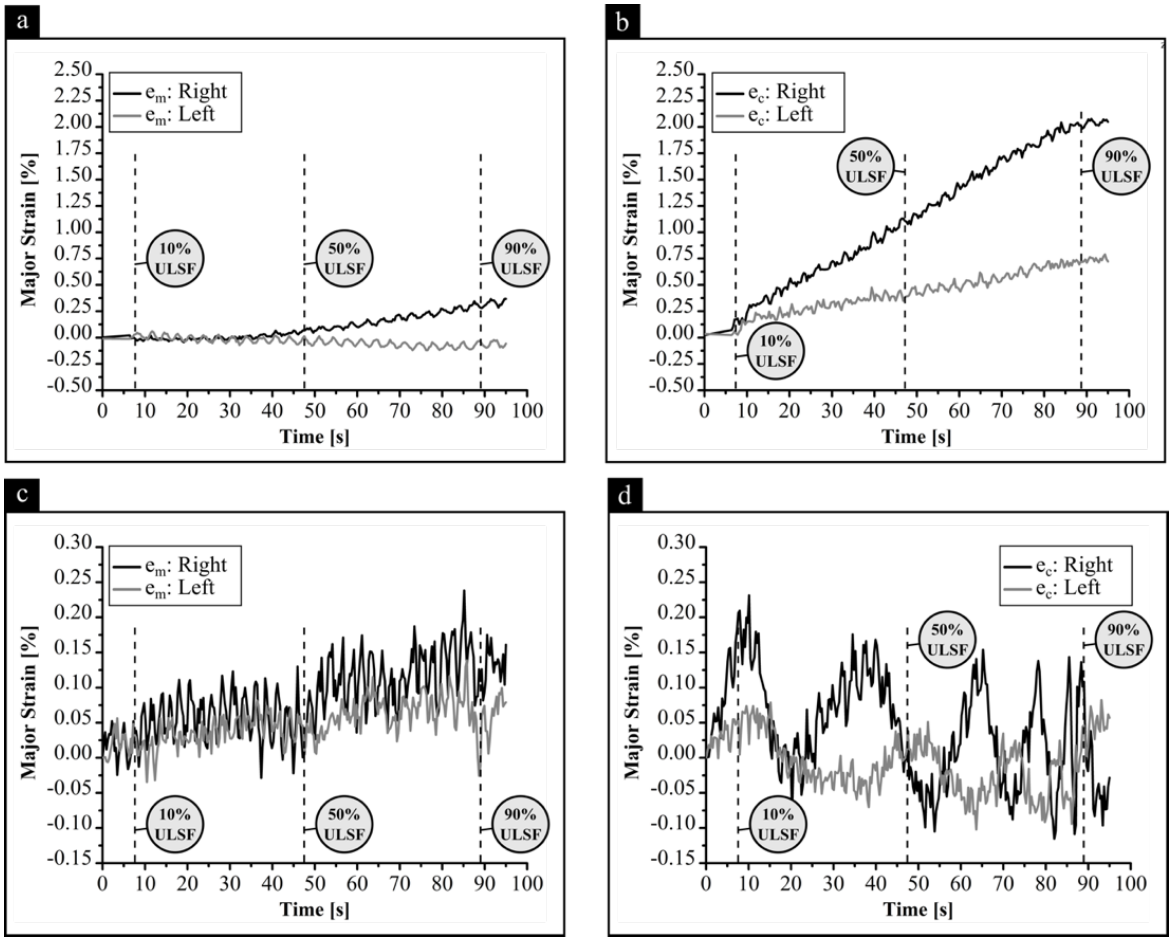

Figure A.35 Strain evolution measure by DIC system on the composite surface on the (a) metal free edge on the overlap endng, (b) composite edge on the overlap endng, and on the metal surface on the (c) metal free edge on the overlap ending, (d) composite edge on the overlap endng.

Appendix A.10 Force-displacement curves for low and high temperature of AddJoining hybrid joints

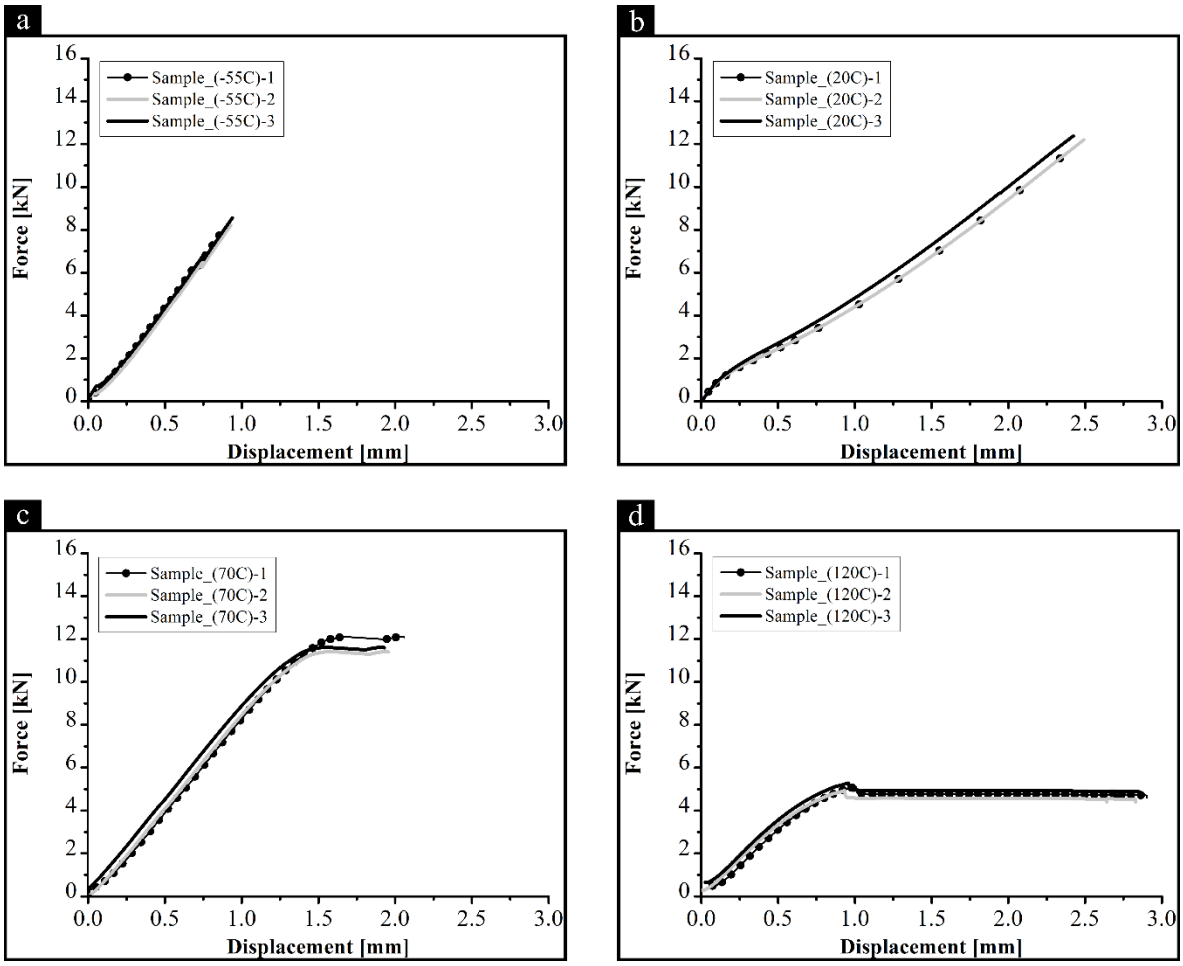

Figure A.36 Force-displacement curves at (a) -55 °C, (b) room temperature, (c) 70 °C, and (d) 120 °C for the AddJoining hybrid joints under quasi-static shear test.

Appendix A.11 Force-displacement curves for quasi-static after one million cycles of AddJoining hybrid joints

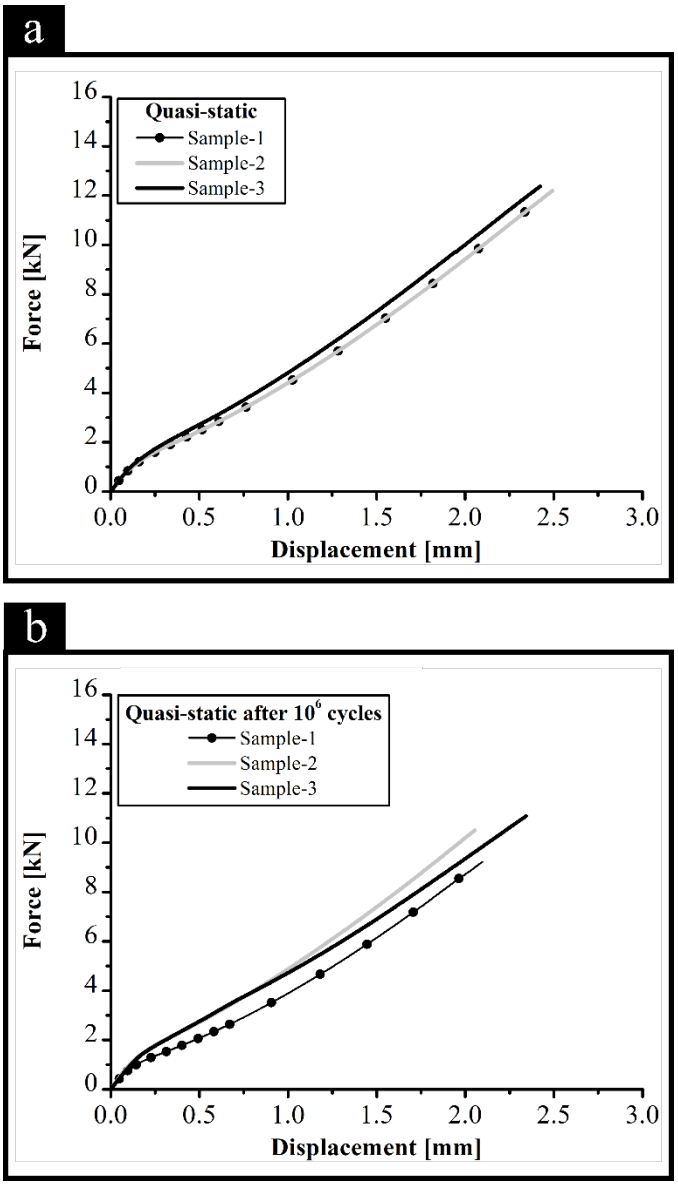

Figure A.37 Force-displacement curves at (a) quasi-static samples and (b) after one million cycles for the AddJoining hybrid joints under quasi-static shear test.

Appendix A.12 Linear statistical analysis of the fatigue data scatter

Two models were used to evaluate fatigue data scatter on the AddJoining hybrid joints. The exponential and power law models are recommended by the ASTM E739-10 [214]. Also, the two methods are used to assess fatigue life of single lap joints [310] and composite [356]. According to the ASTM standard, two different equations shown in Equation (A-4), for exponential, and Equation (A-5), for power law, used to fit the fatigue data.

$$\log(N) = \boldsymbol{a} + \boldsymbol{b}F \tag{A-4}$$

$$\log(N) = \boldsymbol{c} + \boldsymbol{d}log(F) \tag{A-5}$$

Equation (A-4) is used to fit the exponential model, where *N* is the fatigue data, *F* refers to applied force at a constant amplitude, whereas *a* and *b* are the model parameters. Similar, to power law model is employed with Equation (A-5), where *c* and *d* as model parameters. It is worth to note that the fatigue life is assumed by linear formulation proposed by ASTM standard [214], where the *N* is the dependent parameter and the *F* is an independent parameter. Furthermore, the statistical analysis did not employ the run-outs, i.e. the samples that survived 10^6 cycles. In addition, it is considered the normal distribution of the logarithm of fatigue life *N*. As previously mentioned in Chapter 8, during the experimental phase achieved 66.7% of replication, which account for higher degree of certainty for design approaches [214]. From the two models proposed here, $R^2_{(adj)}$, the adjusted R-squared presented reliable values of 0.99 and 0.83 for exponential and power-law, respectively. The model parameters are presented in Table A.9.

Table A.9 Model parameters estimated for exponential and power law.

Exponential		Power law	
a	**b**	**c**	**d**
-2026	16124	29708	-0.142

The validation approach follows the recommendation of the ASTM E739 [214]. The linarity index was calculated and compare with the critical linearity index (F_p) for a significance level of 5%. The validation is shown Table A.10, where the exponential model exceeds the critical linearity index. The lack of linearity might be for strong non-linear distribution, i.e. high scattering of the fatigue data. Such behavior have been observed in [310,356]. On the contrary, the power law is within the linearity hypothesis.

Table A.10 Model parameters estimated for exponential and power law.

Exponential		Power law	
Linearity index	**F_p**	**Linearity index**	**F_p**
23.96	4.459	1.42	4.459

Appendix A.13 Two-parameter Weibull method of the fatigue data scatter

It is essential for the understanding of the statistical aspects of two-parameter Weibull distribution (2-P WD) to give the basis of the method. The fatigue data scattering of the AddJoining hybrid joints follows the 2-P WD extensively discussed in the literature [301,304,305,357,358]. The 2-P WD is defined as a probability density function, *f(x)*, of failure as presented in Equation (A-6**)** and the associated distribution function also known as probability of failure, $P_f(x)$, in Equation (A-7).

$$f(x) = \frac{\beta}{\alpha}\left(\frac{x}{\alpha}\right)^{\beta-1} e^{-\left(\frac{x}{\alpha}\right)^{\beta}} \quad \text{(A-6)}$$

$$P_f(x) = 1 - e^{-\left(\frac{x}{\alpha}\right)^{\beta}} \quad \text{(A-7)}$$

The two-Weibull parameters are α and β are the two Weibull parameters, which describe the characteristic life at a certain selected stress level (scale parameter) and slope (shape parameter) of the Weibull distribution, respectively. Furthermore, the number of cycles to failure represented by x. The probability of survival or reliability is represented by $R = 1 - P_f(x)$ [304]. By rewriting the Equation (A-6**)** and applying a natural logarithm, the Weibull parameters are determined by the following Equation (A-8**)**.

$$\ln\left(\ln\left(\frac{1}{1 - P_f(x)}\right)\right) = \beta \ln(x) - \beta \ln(\alpha) \quad \text{(A-8)}$$

Equation (A-8**)** is a linear equation [304,305] in the form $y = mX + \mathrm{c}$ with $y = \ln(\ln(1/(1 - P_f(x))))$, $X = \ln(x)$, $m = \beta$, and $\mathrm{c} = -\beta \ln(\alpha)$. The further steps for determining the Weibull parameters is to simplify Weibull parameter estimation, so-called Bernard's Median Rank (MR) commonly used in the literaute [304,305], due to the median rank are at 50% confidence level and can be estimated using the Equation (A-9**)**. In equation, i represents the failure serial number and n represents the total number of specimens tested by each loading level. Therefore, the fatigue life (N_f) is organizing by each loading level in an ascending order (Rank (i)) and giving to each of the three specimen a serial number (shown in Table A.11).

$$MR = \frac{i - 0.3}{n + 0.4} \quad \text{(A-9)}$$

The next steps are after calculated $y = \ln(\ln(1/(1 - MR))$ and plotted against the $X = \ln(N)$ of number of cycles *x* for each loading level. This graphic is so-called Weibull lines and is presented in Figure A.38(a) [304,305,357]. Weibull lines are helpful to estimate the parameters by a linear fit of each loading level. By applying a substitution of the fitted equation, the angular coefficient m and c, shown previously, it is possible to obtain the corresponding β and α. Table A.11 shows the Weibull parameters predicted for the AddJoining hybrid joints for the different load levels.

Table A.11 Weibull parameters for AddJoining hybrid joints.

Loading level	ULSF [%]	F_{max} [kN]	N_f [cycles]	Rank	MR	ln(ln(1/1-MR)	c	β	α	MTTF [cycles]
			5913	1	0.2	-1.47				
1	70	8.6	6042	2	0.5	-0.37	-123	14.1	6498	6262
			6874	3	0.8	0.46				
			13134	1	0.2	-1.47				
2	60	7.4	14139	2	0.5	-0.37	-48	4.9	17662	16206
			18659	3	0.8	0.46				
			53865	1	0.2	-1.47				
3	50	6.1	62954	2	0.5	-0.37	-47	4.3	61961	56384
			68779	3	0.8	0.46				
			860323	1	0.2	-1.47				
4	35	4.3	981217	2	0.5	-0.37	-107	7.8	949368	892755
			991453	3	0.8	0.46				
			1000000							
5	30	3.7	1000000							
			1000000							

F_{max}: maximum load, N_f: number of cycles (experimental), MR: Bernard's Median Rank, c, β and α: Weibull parameters, MTTF: mean time to failure.

After the Weibull parameters are known, CV is calculated based on Equation (A-10**)** and is defined as the ratio between the standard deviation (SD) and the mean time to failure (MTTF). According to the Weibull distribution, MTTF represents the expected mean life for a given loading level. Figure A.38(b) presents the CV calculated for each level in function of the MTTF estimation. The CV indicates two regions of high scattering, the first on low cycle fatigue, below 10^3 cycles. It corresponds to the regions with low standard deviation due to the closest to the quasi-static behavior. Furthermore, at region between 10^3-10^5 cycles, the scatter increases associated with uncertainties familiar to fatigue response. At this fatigue life region, data scattering in fatigue experiments is stochastic and unavoidable. The presence of pores on the composite $[PA6/CF\text{-}PA6]_{4S}$ part is one strong factor affecting the high scattering in the fatigue experiment data. Moreover, the last narrowest scatter was observed near to the fatigue limit at 10^6 cycles, whereas the fatigue damage accumulation seems to not reach a critical value to lead failure. The reduction of fatigue scattering at high cycle fatigue have been reported for unidirectional composite materials in the literature [304,305].

$$CV = \frac{SD}{MTTF} = \frac{\alpha\sqrt{\Gamma\left(1+\frac{2}{\beta}\right) - \Gamma^2(1+\frac{1}{\beta})}}{\alpha\Gamma\left(1+\frac{1}{\beta}\right)} \quad \text{(A-10)}$$

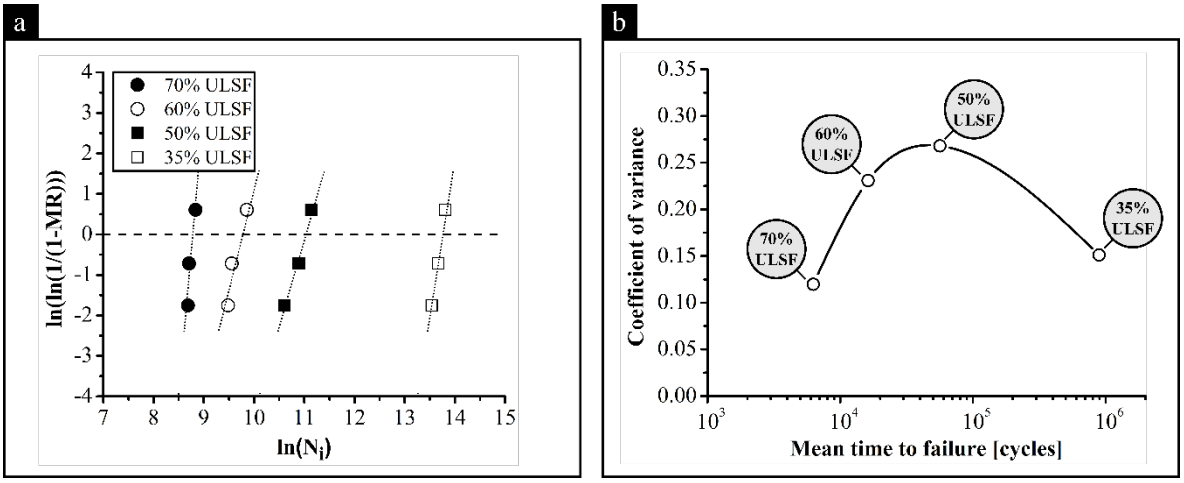

Figure A.38 (a) Weibull lines used for the estimation of the Weibull parameters, and (b) coefficient of variance (CV) in function of mean time to failure (MTTF).

By Weibull distribution, the evaluation of the probability of survival is applied to evaluate the fatigue survival probability based on the fatigue data scattering (Figure A.39). The survival probability is calculated using Equation (A-7), introduced in the beginning of this Appendix. By applying, the two-known Weibull parameters, the probability of survival is calculated for the four-different load levels. At high loading level, i.e. 8.6 kN, corresponding to 70% of ULSF, the predicted fatigue is 6400 cycles for a survival life at 50%. For the same survival life at 50%, at low loading level, i.e. 4.3 kN, at 35% of ULSF, the fatigue life corresponds to 900000 cycles. This tendency is used for the design and application to define design criterion for high performance application [305].

The reliability curves can be applied to predict statistically-derived S-N curves as shown in section 8.1.1. The calculated fatigue life from Equation (A-11) accounts for the reliability level R_x, varying from 10% to 99%. The two-Weibull parameters presented previously and the predicted fatigue life N_{R_x} is obtained.

$$N_{R_x} = \alpha((-\ln(R_x))^{-\frac{1}{\beta}} \quad \text{(A-11)}$$

Considering the predicted fatigue life varying for different loading level, a regression parameters can obtain the a and b from power-law function as shown in Equation (A-12). Therefore, this approach is widely used to predict statistically-derived S-N curves and further used to understand the fatigue data scattering in different loading levels.

$$S_a = a(N_f)^b \quad \text{(A-12)}$$

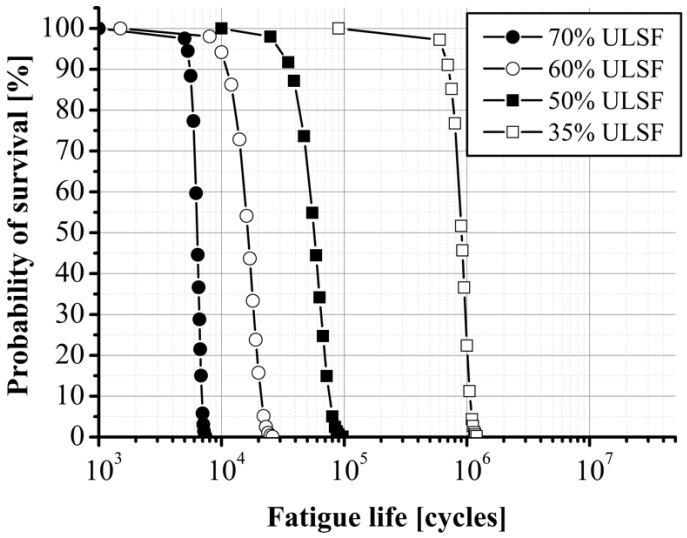

Figure A.39 Probability of survival for four different loading levels.

Appendix A.14 Damage monitoring for different loading levels under cyclic loading

In this Appendix, the stiffness variation and damage variation in function of fatigue life is presented in Figure A.40 and Figure A.41 for each loading level evaluated in this PhD work. The variation is thorough discussed in Section 8.1.3. Moreover, the dissipated energy per cycle is shows a qualitatively comparison among the loading level by evaluating the energy dissipation development at 10%, 60%, 80%, and 99% of the fatigue life (Figure 8-7 in Chapter 8). As explained in Section 8.1.3, the variation in energy dissipation per cycle is dependent on the loading level. Also, in case of variation of energy dissipation indicates damage evolution during cyclic loading.

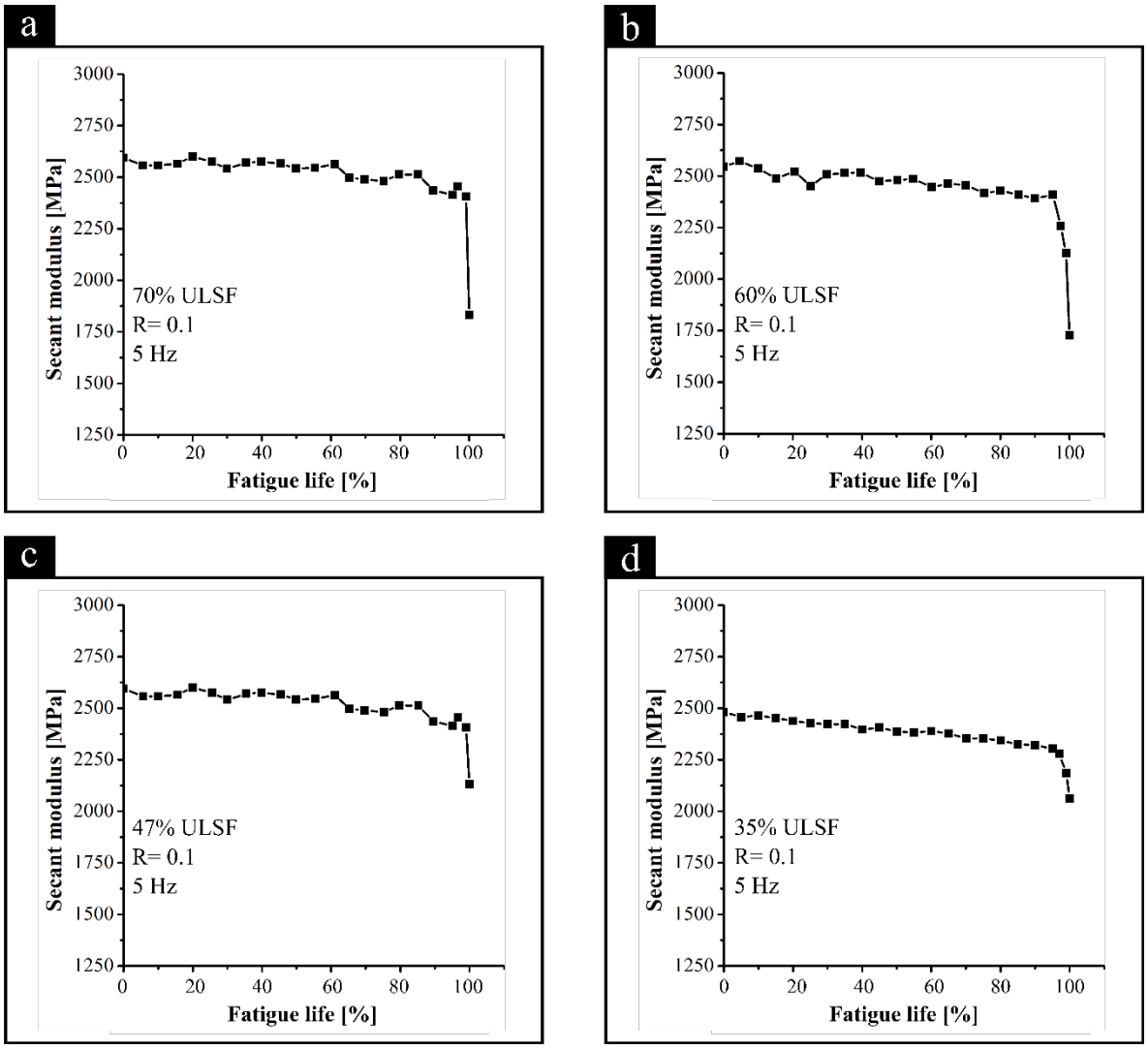

Figure A.40 Measured stiffness variation in function of fatigue life during cyclic loading at four different loading levels.

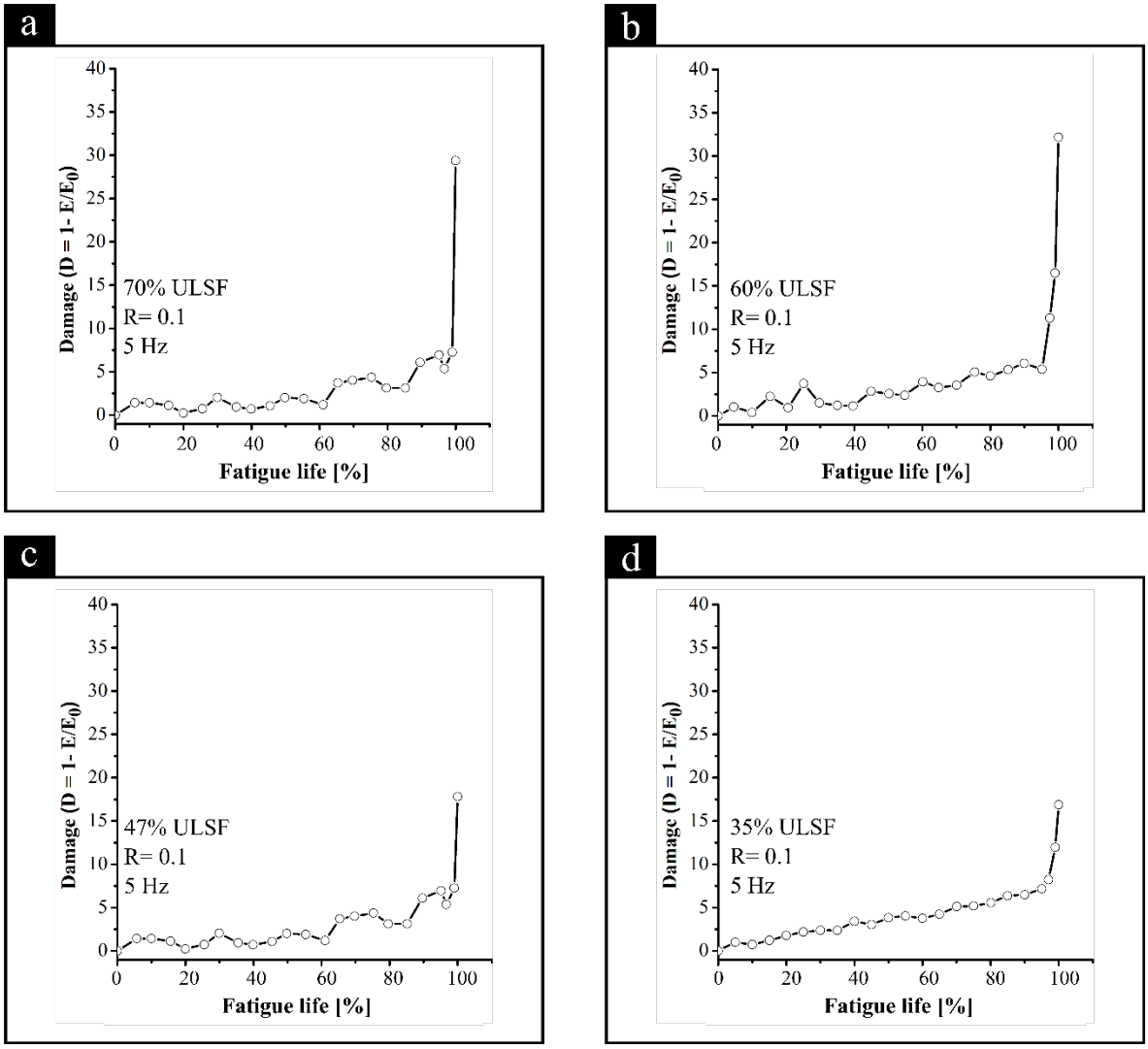

Figure A.41 Measured damage variation in function of fatigue life during cyclic loading at four different loading levels.

Table A.12 summarizes the total damage for the three-selected fatigue life for each loading level. Overall, the damage, at LCF for loading level at 70% and 60% of the ULSF, the damage propagates faster. In contrast is observed for loading level near the fatigue limit. The quantitatively damage data was obtained from the C-Scan graphs from Figure A.42 to Figure A.44 and at 47% of the ULSF previously discussed in Section 8.1.3.

Table A.12 Damage area for three different fatigue life levels at four different loaing level (obtained with C-Scan measurements).

F_{max} [kN]	ULSF [%]	N_i [cycles]	N_i/N_f [%]	Damage area [%]	Damage area [mm^2]
8.6	70	704	10	13.6 ± 0.9	84.8 ± 5.1
		4300	60	20.5 ± 0.6	126.7 ± 10.8
		5609	80	29.7 ± 0.2	134.8 ± 13.2
7.4	60	1309	10	6.9 ± 1.5	44.9 ± 0.7
		7900	60	14.5 ± 1.9	90.8 ± 1.1
		10509	80	19.7 ± 0.2	123.2 ± 0.8
5.8	47	15700	10	6.9 ± 1.5	44.9 ± 2.7
		94200	60	14.5 ± 1.9	90.8 ± 11.1
		125609	80	19.7 ± 0.2	123.2 ± 15.8
4.3	35	78100	10	6.9 ± 1.5	44.9 ± 0.7
		468204	60	14.5 ± 1.9	90.8 ± 1.1
		625000	80	19.7 ± 0.2	123.2 ± 0.8

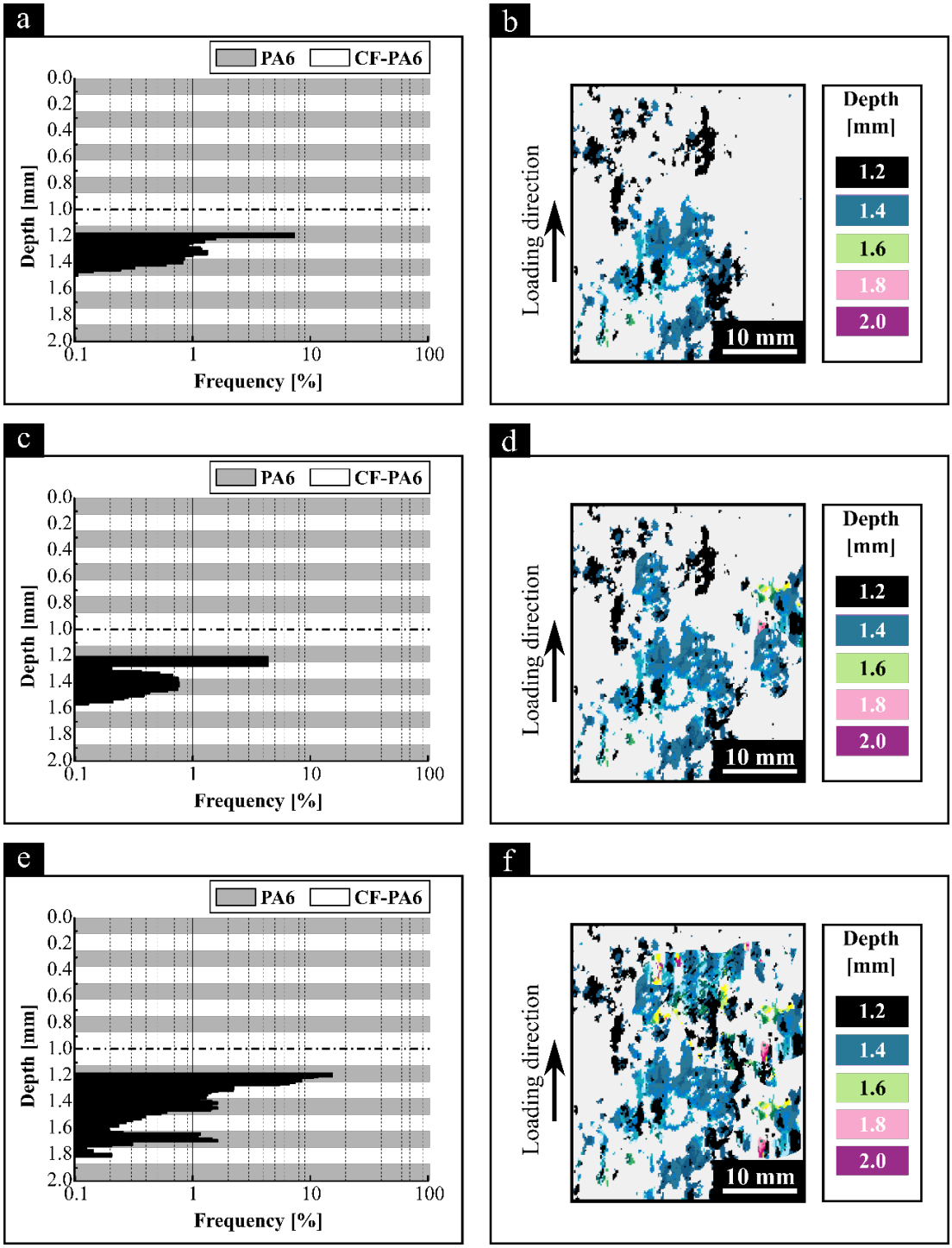

Figure A.42 Damage distribution on histogram (a,c,e) corresponding to C-scan graphs (b,d,f) measured for 10%, 60% and 80% of the fatigue life, respectively for cyclic loading at 70% of the ULSF corresponding to maximum force of 8.6 kN. 0 mm is the interface of aluminum 2024-T3 and PA6 coating / $[PA6/CF\text{-}PA6]_{4S}$.

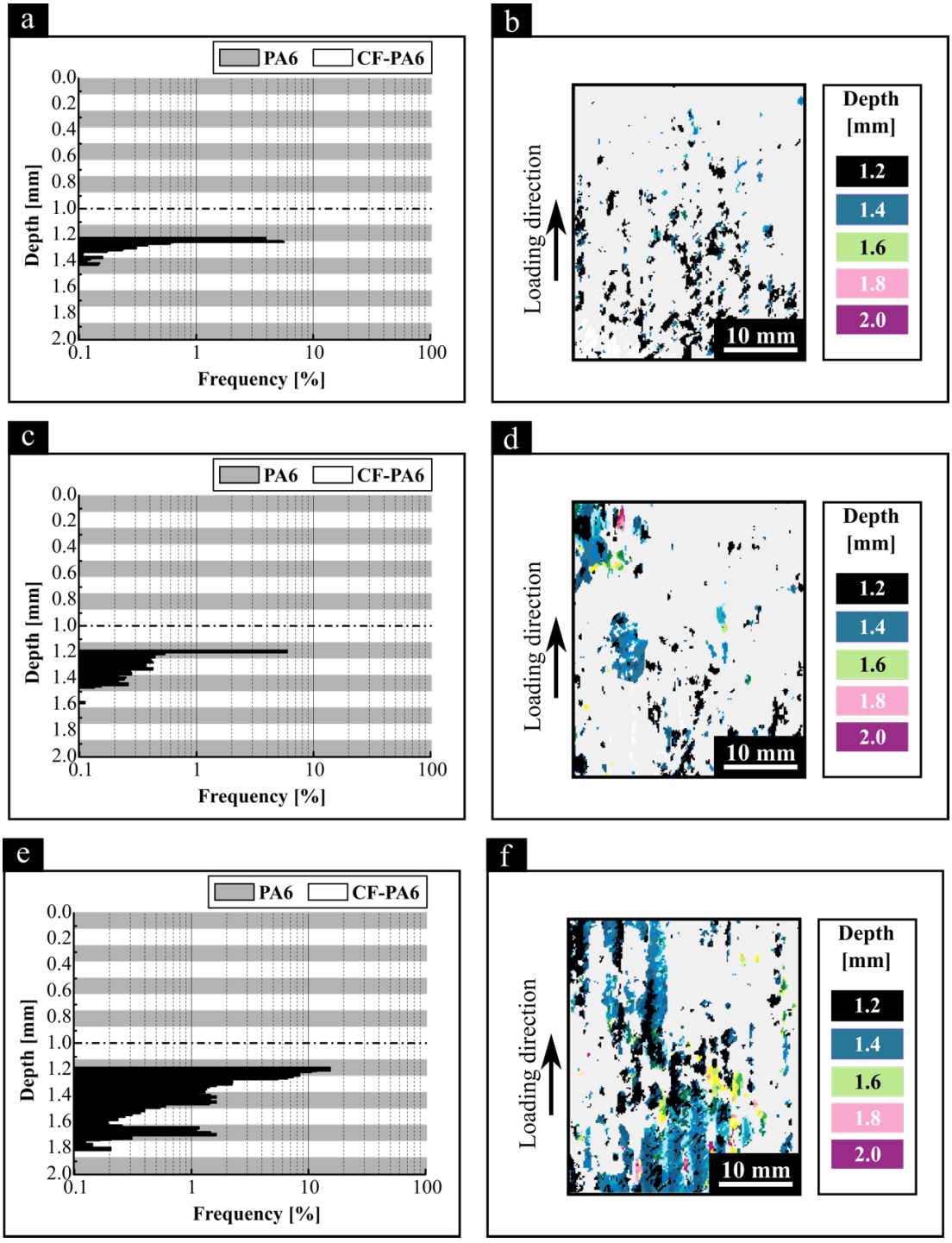

Figure A.43 Damage distribution on histogram (a,c,e) corresponding to C-scan graphs (b,d,f) measured for 10%, 60% and 80% of the fatigue life, respectively for cyclic loading at 60% of the ULSF corresponding to maximum force of 7.4 kN. 0 mm is the interface of aluminum 2024-T3 and PA6 coating / $[PA6/CF\text{-}PA6]_{4S}$.

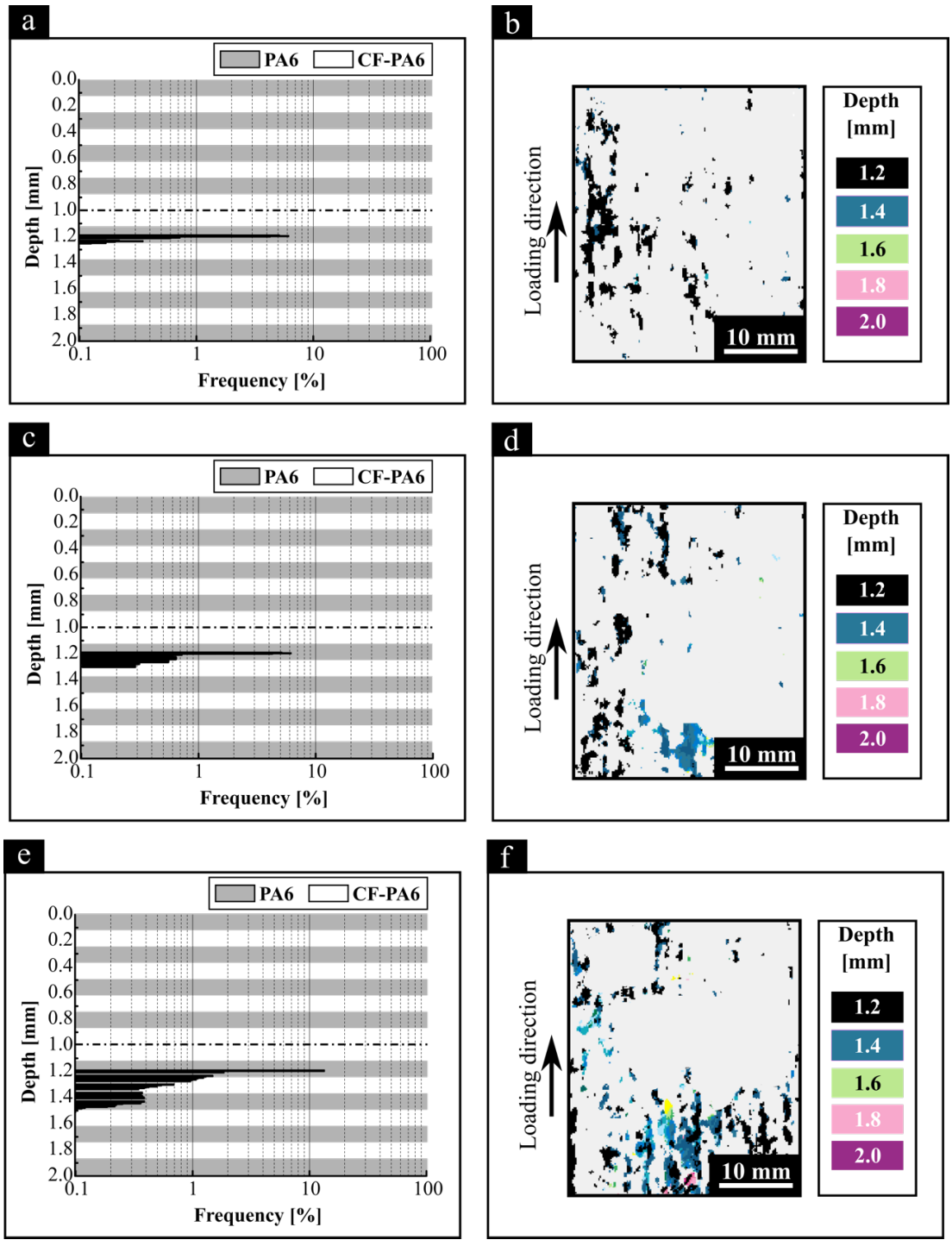

Figure A.44 Damage distribution on histogram (a,c,e) corresponding to C-scan graphs (b,d,f) measured for 10%, 60% and 80% of the fatigue life, respectively for cyclic loading at 35% of the ULSF corresponding to maximum force of 4.3 kN. 0 mm is the interface of aluminum 2024-T3 and PA6 coating / $[PA6/CF\text{-}PA6]_{4S}$.